Investigations on the chemical and the phase stability of oxygen-transporting membranes

Von der Naturwissenschaftlichen Fakultät der
Gottfried Wilhelm Leibniz Universität Hannover
zur Erlangung des Grades

Doktorin der Naturwissenschaften
(Dr. rer. nat.)

genehmigte Dissertation
von

Dipl.-Chem. Olga Ravkina
geboren am 19.07.1983 in Charkow (Ukraine)

2016

Referent: Prof. Dr. Armin Feldhoff
Korreferent: Prof. Dr. Klaus-Dieter Becker
Korreferent: Prof. Dr. Harald Behrens
Tag der Promotion: 08.04.2016

Preface

The presented results of the thesis were carried out from March 2012 until January 2016 during my work as a scientific assistant at the Institute of Physical Chemistry and Electrochemistry at the Gottfried Wilhelm Leibniz Universität Hannover. The project was funded by the Deutsche Forschungsgemeinschaft (DFG, Grant FE 928/4-1) and Chinese-German Center for Science (CDZ, Grant GZ676) under the guidance of Prof. Dr. Armin Feldhoff and Prof. Dr. Jürgen Caro.

Six research articles are presented within this thesis and I am the first author in three of these papers. In the following, my contributions to the articles included in this thesis are illustrated. The encouragement of my co-authors, particularly Prof. Dr. Armin Feldhoff, has been highly beneficial and is greatly aknowledge by me.

The three articles included in Chapter 2 are dealing with the chemical stability of ceramic oxygen-transporting membranes. In the first article *Investigation of carbonates in oxygen-transporting membrane ceramics* scanning electron microscopy (SEM) and transmission electron microscopy (TEM) studies, oxygen permeation measurements, and data interpretation were conducted by me. I am grateful to Prof. Dr. Armin Feldhoff, who performed the energy-loss spectroscopy measurements on the TEM. Furthermore, many thanks go to Dr. Tobias Klande for the assistance during the synthesis of materials and membrane fabrication.

The second article in this chapter, *Effect of A-site lanthanum doping on the* CO_2 *tolerance of* $SrCo_{0.8}Fe_{0.2}O_{3-\delta}$ *oxygen-transporting membranes*, was drawn up in cooperation with Dr. Tobias Klande. I am very glad to contribute to this publication. I have synthesized all materials and provided the fabriactaions of membranes. I also conducted the oxygen permeation measurements and helped by X-ray diffraction (XRD) data interpretation and manuscript preparation.

I appreciate the collaboration with Dr. Yanying Wei from the School of Chemistry and Chemical Engineering of the South China University of Technology in Guangzhou (China). The article *Effect of* CO_2 *and* SO_2 *on oxygen permeation and microstructure of* $(Pr_{0.9}La_{0.1})_2(Ni_{0.74}Cu_{0.21}Ga_{0.05})O_{4+\delta}$ *membranes* was written by Dr. Yanying Wei and myself in equal shares. I carried out the SEM investigations, in-situ XRD measurements and provided support in data interpretation.

Chapter 3 provides an understanding of studies concerning the influence of microstructure and phase compositions on the functionality of the oxygen-transporting membranes. The publication entitled *Influence of different sintering techniques on microstructure and phase composition of oxygen-transporting ceramic* was written by me. I performed all analyses, including temperature-dependent XRD, microscopy and oxygen permeation measurements. I express gratitude to Jan Räthel from the Fraunhofer Institute of Ceramic Technology Dresden, who carried out the field-assisted sintering technique / spark plasma sintering experiments (FAST/SPS).
The article *Effect of microstructure on oxygen permeation of* $Ba_{0.5}Sr_{0.5}Co_{0.8}Fe_{0.2}O_{3-\delta}$ *and* $SrCo_{0.8}Fe_{0.2}O_{3-\delta}$ was prepared in cooperation with Dr. Tobias Klande. I produced the ceramics, conducted all measurements and assisted with data interpretation and manuscript preparation.
The last article of this chapter *Phase separation in BSCF perovskite under elevated oxygen pressures from 1 to 50 bar* arose from the successful cooperation with Dr. Aleksey Yaremchenko from the Department of Materials and Ceramic Engineering of the Universidade de Aveiro (Portugal). The manuscript was written by me and I also provided the SEM and TEM investigations.

Acknowledgment

First and foremost I would like to express my most sincere gratitude to my main supervisor Prof. Dr. Armin Feldhoff for his invaluable guidance, excellent support during the entire thesis and for giving me the opportunity to work on the interesting field of solid state chemistry. I am most grateful to him for sharing his expertise and knowledge in the theory and application of electron microscopy. He always provided me with help and advice, whether in regard to scientific questions or the preparation of manuscripts and conference contributions.

I am especially grateful to Prof. Dr. Jürgen Caro, who established a greatly productive working environment and excellent working conditions for all Ph.D. students.

I would like to express my gratitude to Prof. Dr. Klaus-Dieter Becker from the Institut für Physikalische und Theoretische Chemie of the Technische Universität Braunschweig for his interest in this work and for his readiness to be the second examiner of my doctoral thesis. I would also like to extend thanks to Prof. Dr. Harald Behrens from the Institut für Mineralogie of the Gottfried Wilhelm Leibniz Universität Hannover for his readiness to assess my doctoral thesis as the third examiner. Furthermore, I am very grateful to Prof. Dr. Josef-Christian Buhl from the Institut für Mineralogie of the Gottfried Wilhelm Leibniz Universität Hannover for his willingness to host my thesis defense.

A special thanks goes to my office colleques throughout these three years Dr. Tobias Klande, Benjamin Geppert, Alexander Mundstock, Sebastian Friebe, Michael Bittner, Dr. Kaveh Partovi and Dr. Nanyi Wang who made every day a unique and pleasant working experience. Moreover, I would like to express my gratitude to all members of the Institute of Physical Chemistry and Electrochemisty, particularly to Frank Steinbach for his helpfulness and assistance in the experimental part of my work. I would also like to thank Yvonne Gabbey-Uebe and Kerstin Janze for their important administrative support. I would like to send a special thanks to Peter Mühr, Wilfried Becker and Markus Köhler from the mechanical workshop for their availability and helpfulness in the experimental work.

I would also like to thank my family for their unwavering support and having faith in me. I kindly acknowledge my wonderful parents for their continuous help and love. Very special thanks go to Nurlan for his love, understanding, and always giving me the strength to continue with my work.

Abstract

Oxygen permeable membranes made of mixed oxygen-ionic and electronic conducting (MIEC) ceramic materials can pave the way for energy conversion technologies such as solid oxide fuel cells and oxy-fuel combustion with less environmental pollution than alternative approaches. By using an oxygen-transporting membrane with high selectivity for oxygen not only are the costs of industrial processe lowered, but also the emission of climate-damaging carbon dioxide is reduced. The implementation of the MIEC membrane technology places high demands on ceramic membrane materials. First of all the ceramic should exhibit superior phase stability at working conditions as the oxygen-transporting mechanism is contingent on the crystallographic structure of the material. Another important aspect is the chemical stability against carbon dioxide. The formation of metal carbonates on the contact surface between the membrane and carbon dioxide containing atmosphere can hinder the oxygen flux. Whithin the presented thesis, both of these major issues were extensively studied. Six original research articles concerning the phase and chemical stability of perovskite and Ruddlesden-Popper phase materials were created in the course of this work.

Chapter 2 explains the effect of the partial substitution of alkaline-earth element with rare-earth element on the CO_2 tolerance of $SrCo_{0.8}Fe_{0.2}O_{3-\delta}$ oxygen-transporting membranes in detail. With increasing lanthanum concentration, an elevated stability against carbon dioxide was observed, however the oxygen permeation flux declined at the same time. Thereupon, $La_{0.6}Sr_{0.4}Co_{0.8}Fe_{0.2}O_{3-\delta}$ was established as a CO_2-tolerant material. Moreover, the phase transition from rhombohedral to cubic $La_{0.6}Sr_{0.4}Co_{0.8}Fe_{0.2}O_{3-\delta}$ perovskite was investigated. The formation of metal carbonates in membranes with minor lanthanum content was intensively studied by transmission electron microscopy (TEM), scanning electron microscopy (SEM) and in-situ X-ray diffraction (XRD) techniques. Thermodynamic considerations based on an Ellingham diagram help thereby to clarify the question of the prospective chemical stability of the metal oxide materials under operational conditions. The verification of this thermodynamic approach is also supported by the studies of the Ruddlesden-Popper phase, $(Pr_{0.9}La_{0.1})_2(Ni_{0.74}Cu_{0.21}Ga_{0.05})O_{4+\delta}$, considering the chemical stability in presence of carbon dioxide and a sulfur dioxide environment under experimental conditions.

The influence of the phase composition and microstructure on the permeation performance of mixed ionic electronic materials was studied in chapter 3. By varying the sintering technique for the Ruddlesden-Popper phase La_2NiO_4, a wide distribution of grain size can be achieved. Moreover, the application of the field-assisted sintering technique / spark plasma sintering (FAST/SPS) changes the phase composition and crystallographic structure of the material. In the case of La_2NiO_4, the small grain size, which results from very quick sintering step, has a negative effect on the oxygen-transport performance of the membrane. The investigations on perovskite $Ba_{0.5}Sr_{0.5}Co_{0.8}Fe_{0.2}O_{3-\delta}$ have shown an increasing oxygen permeation flux with increasing grain size. Additionally, the phase transition from a cubic perovskite phase to an ordered $SrCo_{0.8}Fe_{0.2}O_{2.5}$ brownmillerite by-phase on the oxygen-depleted sweep side of the membrane was observed by TEM investigations at 1373 K. Following a treatment in highly oxidizing conditions at intermediate temperatures, the phase composition of $Ba_{0.5}Sr_{0.5}Co_{0.8}Fe_{0.2}O_{3-\delta}$ was furthermore depicted. This was analyzed using thermogravimetry, XRD and TEM to illuminate the decomposition mechanism and to investigate the structure of phases formed during the segregation.

Keywords: oxygen-transporting ceramic membranes, mixed ionic-electronic conductors, chemical and phase stability

Zusammenfassung

Sauerstoffpermeable Membranen aus gemischt ionen- und elektronenleitenden keramischen Materialien (MIEC) ebnen den Weg zu umweltschonenderen Energieumwandlungstechnologien wie Festoffoxid-Brennstoffzellen und Oxy-fuel Verfahren zur Verbrennung kohlenstoffhaltiger Energieträger. Die Verwendung von Sauerstofftransport Membranen mit einer hohen Sauerstoffselektivität ermöglicht nicht nur das Absenken der industriellen Produktionskosten, sondern auch die Reduktion der Kohlenstoffdioxidausstoßes. Bei der Implementierung der Membrantechnologie werden hohe Anforderungen an die keramischen Materialien gestellt. Zum einen sollen die Membranen sich unter den Messbedingungen durch ausgezeichnete Phasenstabilität auszeichnen, da der Sauerstofftransportmechnismus stark von der kristallographischen Struktur abhängt. Zum anderen ist dabei die chemische Stabilität in Kohlenstoffdioxidhaltiger Atmosphäre von großer Bedeutung. Die Bildung der Metallkarbonate an der Grenzfläche zur Kohlenstoffdioxidatmosphäre kann zur Verminderung der Sauerstoffpermeation führen. Im Rahmen der vorliegenden Dissertation werden die genannten zwei Schwerpunkte ausführlich behandelt. Sechs Forschungsartikel, die sich mit den Fragen der chemischen und der Phasenstabilität von Perowskiten und Ruddlesden-Popper Phase beschäftigen, entstanden während der Arbeit an der Dissertation.

In Kapitel 2 wird die Auswirkung der partiellen Substitution der Erdalkalimetalle durch Lanthanoide auf die CO_2-Toleranz von $SrCo_{0.8}Fe_{0.2}O_{3-\delta}$ als Sauerstofftransport Membran detailliert untersucht. Eine erhöhte Stabilität gegenüber CO_2 wird mit steigendem Lanthanumgehalt beobachtet; dabei nimmt jedoch die Sauerstoffpermeation ab. $La_{0.6}Sr_{0.4}Co_{0.8}Fe_{0.2}O_{3-\delta}$ wurde als das CO_2-stabile Material etabliert. Darüber hinaus wurde die Phasenumwandlung vom rhomboedrischen in den kubische Perowskiten $La_{0.6}Sr_{0.4}Co_{0.8}Fe_{0.2}O_{3-\delta}$ untersucht. Die Entstehung der Metallkarbonate bei Membranen mit dem geringeren Lanthangehalt wurde mit Rasterelektronenmikroskopie (REM), Transmissionselektronenmikroskopie (TEM) und insitu Röntgenbeugung (XRD) verfolgt. Die thermodynamische Überlegungen, basierend auf dem Ellingham-Diagramm, erleichtern die Klärung der Frage über die perspektivische CO_2-Stabilität der Metalloxidmaterialien unter den Einsatzbedingungen. Die Gültigkeit des thermodynamischen Ansatzes ist auch durch die Arbeit über die Ruddlesden-Popper Phase $(Pr_{0.9}La_{0.1})_2(Ni_{0.74}Cu_{0.21}Ga_{0.05})O_{4+\delta}$ bestätigt. Die chemische Stabilität in Anwesenheit von Kohlenstoffdioxid und Schwefeldioxid unter Einsatzbedingungen wurde hier analysiert.

Der Einfluss der Phasenzusammensetzung und der Mikrostruktur auf die Permeationsleistung der gemischt ionen- und elektronenleitenden Materialien wird in Kapitel 3 analysiert. Durch das Variiern der Sintertechniken bei der Ruddlesden-Popper Phase La_2NiO_4 konnte eine breite Verteilung der Korngrößen erzielt werden. Darüber hinaus, konnte die kristallographische Struktur und die Phasenzusammensetzung durch Anwendung von Feldaktives Sintern / Spark Plasma Sintern (FAST/SPS)-Technik verändert werden. Im Fall von La_2NiO_4 führen sehr kleine Membrankörner, die aus dem schnellen Sinterschritt resultieren, zu einem negativen Effekt auf den Sauerstoffpermeationfluss. In ähnlicher Weise haben die Untersuchungen an dem Perowskiten $Ba_{0.5}Sr_{0.5}Co_{0.8}Fe_{0.2}O_{3-\delta}$ eine Zunahme des Sauerstofftransportes mit steigender Korngröße gezeigt. Zudem wurde Phasenumwandlung des kubischen Perowskiten in die geordnete $SrCo_{0.8}Fe_{0.2}O_{2.5}$ Brownmillerit-Phase an der sauerstoffarmen Spülgas-Seite der Membran bei 1373 K durch TEM beobachtet. Weiterhin, wurde die Phasenzusammensetzung von $Ba_{0.5}Sr_{0.5}Co_{0.8}Fe_{0.2}O_{3-\delta}$ nach der Behandlung in hochoxidierender Umgebung bei intermediären Temperaturen mit Hilfe der Thermogravimetrie, XRD und TEM untersucht, um den Zersetzungsmechanismus und durch die Zersetzung entstandenen Phase aufzuklären.

Stichwörter: Sauerstoffleitende keramische membranen, gemischte Ionen- und Elektronenleiter, chemische und Phasenstabilität

Abbreviations

BSCF	$Ba_{0.5}Sr_{0.5}Co_{0.8}Fe_{0.2}O_{3-\delta}$
CA	Citric acid Citronensäure
CCS	Carbon capture and storage Kohlenstoffabscheidung und Lagerung
EDTA	Ethylene diamine tetraacetic acid Ethylendiamintetraessigsäure
EDXS	Energy-dispersive X-ray spectroscopy Energiedispersive Röntgenspektroskopie
EELS	Electron-energy loss spectroscopy Elektronenenergieverlustspektroskopie
IT	Intermediate temperatures (500-800 °C) Temperatur im mittleren Bereich (500-800 °C)
FAST/SPS	Field-assisted sintering technique / spark plasma sintering Feldaktives Sintern / Spark Plasma Sintern
LSCF	$La_{1-x}Sr_xCo_{0.8}Fe_{0.2}O_{3-\delta}$
LSCF6482	$La_{0.6}Sr_{0.4}Co_{0.8}Fe_{0.2}O_{3-\delta}$
MIEC	Mixed ionic electronic conductor Gemischt Ionen- und Elektronenleiter
OTM	Oxygen-transporting membrane Sauerstofftransportmembran
SEM	Scanning electron microscopy Rasterelektronenmikroskopie
SOFC	Solid oxide fuel cell Hochtemperaturbrennstoffzelle
TEM	Transmission electron microscopy Transmissionselektronenmikroskopie
XRD	X-ray diffraction Röntgenbeugung

Contents

1 Introduction

1.1 Motivation

In recent years a high demand on clean and efficient energy production from the society and politics was established [1–5]. The worldwide energy demand is expected to grow by 37% by 2040 [6]. In the year of 2014, consumption and production increased for all fuels, reaching record levels for every fuel type except nuclear fuel [7]. Yet about 81% of the world electricity is generated by fossil-fuel power plants [8]. Moreover, in 2014 approximately 43% of the total gross electricity production in Germany was based on coal [9]. Despite the increasing prominence of renewable power, which is expected to rise by around 40% between 2013 and 2018, a complete renunciation of fossil-fuel power plants is not feasible [10, 11]. In this context, the optimization and improvement of current fossil-fuel technologies can make the plants more environmentally sustainable. Energy efficiency plays a key role not only regarding the depletion of natural sources, but also as a way to reduce the carbon dioxide emission [12]. Above 40% of emissions reductions to 2025 can be delivered by end-use energy efficiency. This includes, amongst others, the improving of batteries, fuel cells and gaseous fuels, upgrade of industrial technologies for energy conversion [8].

The elaboration of membrane technology within energy and chemical industries is an area of growing interest [13]. The application of inorganic oxygen-transporting membranes (OTMs) opens up a wide range of possibilities for industrial process modification. The main representatives of OTM, apart from ion conductors like CeO_2, are mixed ionic electronic conducting (MIEC) materials with perovskite or perovskite-related structure [14–16]. These ceramic materials promise high stabilities even under high-temperature conditions. Moreover, a very high oxygen selectivity can be realized by applying dense ceramic membranes. The typical fields of application of MIEC as oxygen-transporting membranes are related to processes, where the supply or removal of oxygen is required. Figure 1 illustrates the schematic principle of the operating of mixed ionic electronic materials as an oxygen-transporting membrane.

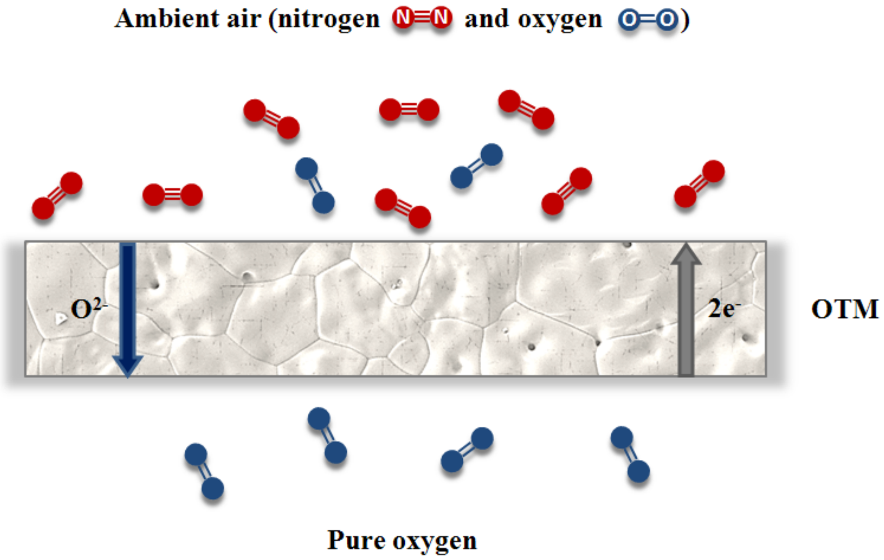

Figure 1: Schematic principle of operating of mixed ionic electronic conducting material as an oxygen-transporting membrane.

The technological application of mixed ionic electronic materials in solid-state electrochemical devices such as oxygen separation units, catalytic membrane reactors or solid oxide fuel cells (SOFCs), have been intensively investigated in the last decades [17–28].

Solid oxide fuel cells are one of the most promising technologies for efficient and clean electricity production [29, 30]. The maximum cell efficiency can exceed 80% [31]. The typical SOFC single cell consists of three main components: a porous cathode (for fuel reduction), a porous anode (for fuel oxidation) and a dense electrolyte (for transport of oxide ions from the cathode to the anode). The main constituents are oxide ceramics which serve typically between 900-1200 °C. The MIEC materials are used as cathode and function as the electrocatalyst. Lowering the operation temperature of SOFC to the intermediate temperature (IT) range between 500-800 °C is one of the main goals in current research. This would help to prevent the high thermal stresses between different components and degradation of materials [32]. At the same time working at intermediate temperatures puts enormous demands on MIEC materials. Shao et al. investigated perovskite $(Ba_{0.5}Sr_{0.5})(Co_{0.8}Fe_{0.2})O_{3-\delta}$ (BSCF) and reported very high values for the oxygen permeation flux for this material [33, 34]. They have also proposed BSCF as a potential cathode material for IT SOFC [35, 36]. Concededly, the material still presents itself as problematic, which hinder its technological implementation. Results concerning the phase stability at intermediate temperatures, which are more oxidative than high temperatures for equal oxygen pressure, are the most limiting factor [37]. Different groups described the phase decomposition of the cubic BSCF perovskite into hexagonal and rhombohedral structures. Herby, the driving force of the decomposition is the temperature dependent valence and spin-state transition of cobalt ions (from Co^{2+} (HS) to Co^{3+} (LS)) and associated decrease of cobalt ionic radius [38–44]. Although, several approaches to stabilze the cubic structure were reported [45–49], a substantial improvement has not been achieved. Understanding of the structure degradation mechanism is in this case of crucial importance. Another problem is the instability under large partial pressure gradient and formation of oxygen-ordered Brownmillerite phase in reducing atmosphere [50]. Additionally, the presence of alkaline-earth metals in perovskites make them unsuitable for further applications with high demand on chemical stability of materials.

In recent years, a new concept of carbon capture and storage (CCS) technologies has been developed [51–55]. There are three technological pathways that can be pursued for CO_2 capture: post-combustion capture, pre-combustion capture and oxyfuel-combustion. In post-combustion capture the carbon dioxide, which is either present in the air or produced by combustion, is separated from other flue gas components. In pre-compustion capture, CO_2 is removed from fuel before combustion. In oxyfuel-combustion, the fuel is burned in an oxygen stream that contains little or no nitrogen [56]. Hence, the flue gas primarily consists of carbon dioxide and water vapour which can be easily condensed [57]. The OTM technolgy can be integrated in the oxyfuel combustion process to generate a pure oxygen stream. The advantages of a membrane separation are its simplicity and low costs; there is no need for an additional rather complex process like in cryogenic oxygen separation. But the membrane materials have to resist all components of the flue gas and at the same time retain the functionality as an oxygen-transporting membrane.

It is known that alkaline-earth metal containing MIEC materials tend to form metal carbonates on the contact surface with carbon dioxide gas, which leads to a dramatic drop of oxygen permeation flux [58]. An increase of the CO_2 tolerance of the material is possible by avoiding the alkaline-earth elements. However, there is a very small variety of perovskite compounds with sufficient oxygen transport performance and concurrently chemically stable structure. Perovskite-related Ruddlesden-Popper phase MIEC compounds can help to solve this problem. $La_2NiO_{4+\delta}$ or $(Pr_{0.9}La_{0.1})_2(Ni_{0.74}Cu_{0.21}Ga_{0.05})O_{4+\delta}$ were investigated in this context and have shown a high tolerance to carbon dioxide environment [59–63]. Another approach is to use dual-phase materials consisting of separate oxygen-ionic conductors and electronic conductors. The so formed percolating network leads to the MIEC properties of dual-phase membrane. According to that concept several materials were developed [64, 65]. Although the chemical stability was reported to be high, the OTM performance was still low.

1.2 Perovskite and perovskite-related structures

1.2.1 Perovskite ABO_3 structure

Perovskite is the name of the structural family with the general stoichiometry ABO_3 and in addition the name for a particular mineral with the composition $CaTiO_3$. The mineral is named after the russian politician and mineral collector, Count Lev Aleksejevich Perovskii, and was discovered by Gustav Rose in 1839 [66, 67]. Due to the large flexibility of the structure, perovskites are the most frequently encounted compounds in solid-state inorganic chemistry.

The ideal cubic perovskite structure can be described as a cubic close-packed array of anions, with one quarter of anions replaced by A cations in an ordered manner. Alternatively, the structure can also be regarded as a pseudo face-centered unit cell with anion or B cation at the origin. The close-packed layers are parallel to the (111) planes of this face-centered cubic cell. A-site cations are typically larger than the B-site cations and similar in size to the anions [68]. Figure 2 illustrates the cubic perovskite structure. For the A-site cations result the cubo-octahedral coordination by twelve anions, whereas the B-site cations are surrounded by six anions in octahedral coordination. The ideal perovskite structure adopts the cubic space group $Pm\overline{3}m$ (Nr. 221), and $SrTiO_3$ is commonly regarded as the archetypical cubic perovskite [69]. The unit cell of $Pm\overline{3}m$ structure has cell edge length a, which is equal to two bond distances between B-site atoms and anion [68]. The cell contains one formula unit (Z) per unit cell.

Woodward and Gallasso have shown, that the majority of simple perovskites are not cubic and have a distorted structure due to a rotation or tilting of the regular octahedra or due to the distorted octahedra themselves [70–72]. The influence of a relative ion size on the structure and properties was recognized by Goldschmidt in 1926 and was summarized in a simple equation, in which the tolerance factor t is expressed as ionic radius ratio of cations r_A, r_B and anion r_O [73, 74].

$$t = (r_A + r_O)/\sqrt{2}(r_B + r_O) \tag{1}$$

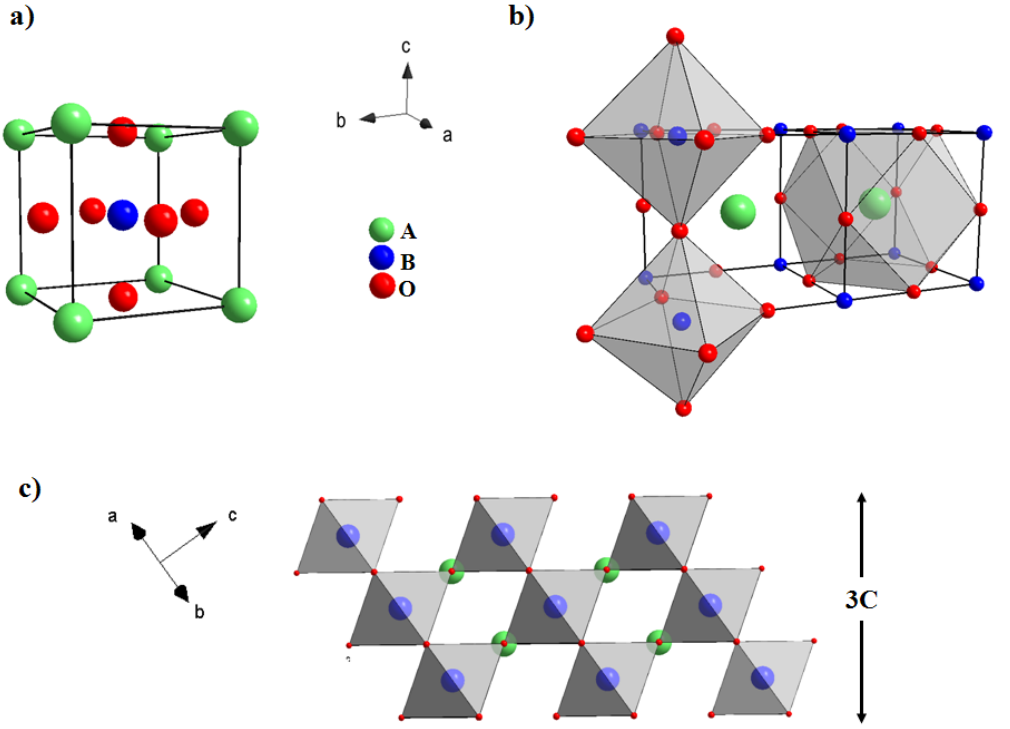

Figure 2: Cubic ABO_3 perovskite structure. (a) Face-centerd cubic unit cell with A cation located at the origin. (b) Two face-centered unit cells showing octahedral coordination of B-site cations and cubo-ocahedral coordination of A-site cations. (c) Projection along [010] on the structure produced by stacking layers of corner-sharing octahedra (*c*-stacking).

The tolerance factor reflects the degree of cubic structure distortion. The closer the structure is to cubic, the closer the value of the tolerance factor is to unity. Goldschmidt has observed, that cubic perovskite structure is formed for $0.8 \leq t \leq 1.0$. Hines et al. proposed that the perovskite will be cubic for $0.9 \leq t \leq 1.0$ and orthorhombic for $0.75 \leq t \leq 0.9$ [75, 76]. The decrease of t to the value below 0.75 will lead to compounds that adopt the hexagonal ilmenite structure, and the increase of t above one results in perovskites with hexagonal symmetry. It should be noted, that the tolerance factor is based on empiric perovskite studies at room temperature and can not be obeyed exactly.

Deviations from the ideal structure with orthorhombic, rhombohedral, tetragonal, monoclinic and triclinic symmetry are well known to occur [77]. Although the distorted structure may exist at room temperature, it transforms to the cubic structure at higher temperatures [15]. A discussion of this phenomena follows in Chapter 2.

Strontium or calcium doped $LaCo_{0.8}Fe_{0.2}O_{3-\delta}$ perovskite with high lanthanum content of 60% adopt rhombohedral $R\overline{3}c$ (Nr. 161) structure [78]. The atomic coordinates in this space group are: A (0,0,1/4), B(0,0,0) and O(x,0,1/4)). Figure 3 shows the transformation of cubic perovskite structure to a rhombohedral one. The tilt angle ω demonstrates the degree of rombohedral strain.

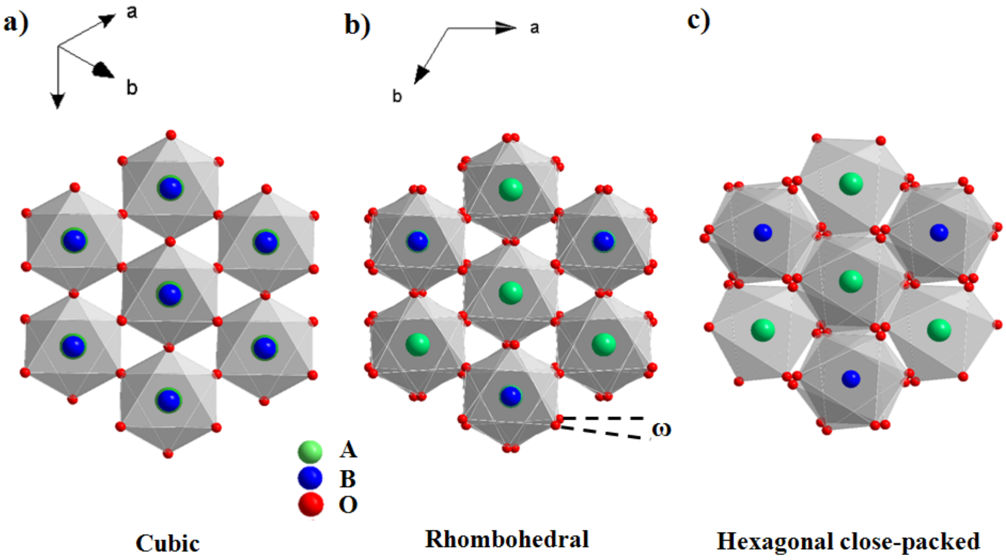

Figure 3: Transformation of (a) cubic perovskite to a (c) hexagonal close-packed structure with increasing rhomboedral tilt angle ω in (b) rhombohedral structure.

The tilt angle, which can vary from 0° to 30°, can be determined using relationships proposed by O´Keeffe and Hyde (Equation 2) [79] and Michel et al. (Equation 3) [80] with the position of the x coordinate of the displaced oxygen atom:

$$tan\omega = \sqrt{3} - (x\sqrt{12}) \tag{2}$$

$$x = 0.5 - [tan\omega/2\sqrt{3}] \tag{3}$$

The limit of 30° tilt angle indicates the hexagonal close-packed arrangement of atoms and the formation of the already mentioned hexagonal ilmenite structure (Fig. 3c), which can be regarded as an extremely distorted or collapsed perovskite structure. Rhombohedral tilt can be treated as positive (anticlockwise) or negative (clock-wise) rotation about the c-axis, depending on the x displacement [68].

The hexagonal perovskite structure plays an important role for the degradation of the cubic $(Ba_{0.5}Sr_{0.5})(Co_{0.8}Fe_{0.2})O_{3-\delta}$ (BSCF) perovskite at intermediate temperatures. The hexagonal symmetry will be adopted, if the A-site cation is too large for the structure, which leads to a tolerance factor greater than one. In this case, a hexagonal perovskite with face-sharing octrahedra, which forms chains along the hexagonal c-axis, can be established (Figure 4). According to Pauling´s Third Rule, structures containing face-sharing octahedra are less stable than those with corner-sharing [81]. However, the hexagonal structure attains additional stabilisation by formation of metal-metal bonds between the B-site cations of the BO_6 octahedra. The majority of hexagonal perovskites contain large alkali- or alkaline earth metals in the A site and transition metals in the B site.

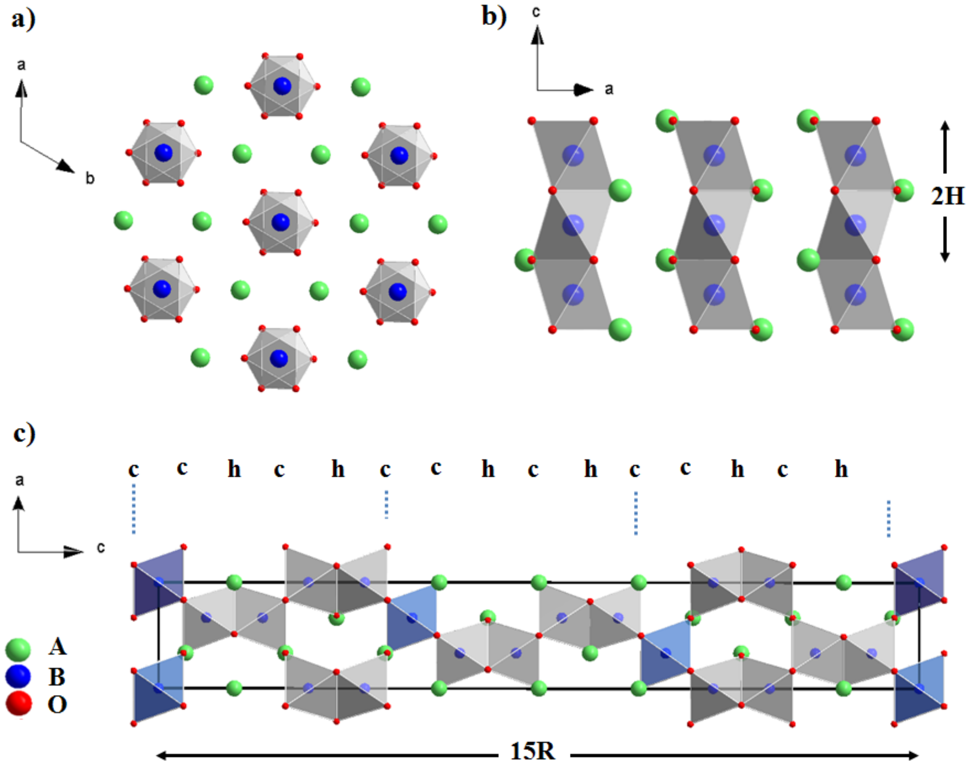

Figure 4: Representation of hexagonal perovskite (a) Clinographic representation of 2H structure (b) Face-sharing octahedra along the c-axis in 2H structure (c) Projection along [010] of 15R polytype produced by stacking layers of corner-sharing (*c*) and face-sharing (*h*).

Ideal hexagonal perovskite structure adopts the space group $P6_3/mmc$ (Nr. 194), also described as 2H structure. The stacking sequence of two face-shared octaedra is commonly named *hh*-stacking [82, 83]. Hexagonal perovskites can adopt a large variety of polytypes. The polytype terms the number of layers stacked along the c-axis and the symmetry resulting from the particular stacking sequence. A mixture of stacking corner-sharing (*c*) and face-sharing (*h*) octahedra is possible. Figure 4c demonstrates the 15R polytype, a structure that was proposed to be a one of the BSCF decomposition products at intermediate temperatures [40]. The more recent investigations demonstrated the formation of $Ba_3Co_{10}O_{17}$ intergrowth cobaltite [84].

1.2.2 Intergrowth cobaltites $Ba_{n+1}Co_nO_{n+3}(Co_8O_8)$

The decomposition process of cubic $(Ba_{0.5}Sr_{0.5})(Co_{0.8}Fe_{0.2})O_{3-\delta}$ (BSCF) perovskite at intermediate temperatures involves beside the hexagonal phase separation, also the separation of rhombohedral $Ba_3Co_{10}O_{17}$ [39, 84]. That compound with a general formual $Ba_{n+1}Co_nO_{n+3}(Co_8O_8)$ belongs to a series of barium cobaltite intergrowth structures with n=2. The structure crystallizes in the space group $R\bar{3}m$ (Nr. 166) and contains perovskite and CdI_2-type layers [85]. The unit cell of $Ba_3Co_{10}O_{17}$ is shown in Figure 5.

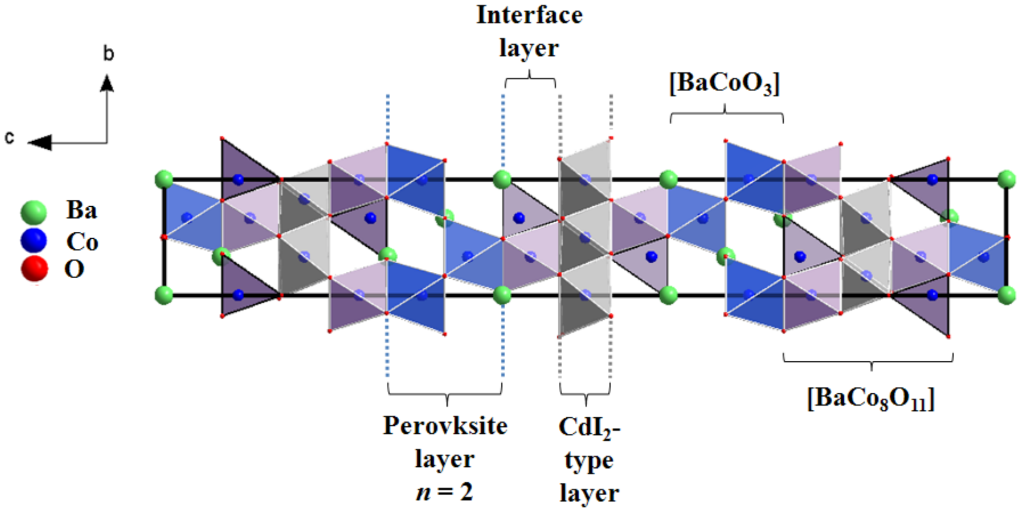

Figure 5: Representation of rhombohedral $Ba_{n+1}Co_nO_{n+3}(Co_8O_8)$ with n=2.

The perovskite (111) blocks $[BaCoO_3]_n$ with double-octahedral layer (n=2) alternate with $[BaCo_8O_{11}]$ blocks that consits of a CdI_2-type layer sandwiched between two interface layers. In other words, the perovskite layer and the CdI_2-type layer are separated from each other by the interface layer. The interface layer contains a close-packed oxygen layer and a $[BaO_3]$ layer. Therefore, there are two types of polyhedral sites, octahedral and tetrahedral sites, all of which are occupied by cobalt ions [85]. In general, the perovksite structure can be described as a close-packed $[BaO_3]$ array in which the octahedral sites are occupied by cobalt ions. Consequently, the structure shown in Figure 5 can be described as mixed close-packing arrays consisting of close-packed oxygen layers and $[BaO_3]$ layers. The octahedral and tetrahedral interstitials in these layers are occupied by cobalt ions [85]. This structure has five different cobalt environments and the average oxidation state of cobalt is +2.8 [85, 86]. The separation processes of $Ba_3Co_{10}O_{17}$ from BSCF is discussed in detail in Chapter 3.

1.2.3 Ruddlesden-Popper Phases

Balz and Plieth in 1955 described the K_2NiO_4 structure formed by melting of KF-NiF_2 and have showed its relation to the perovkite structure [87]. Several years later, Ruddlesden and Popper investigated Sr_2TiO_4, Ca_2MnO_4 and $SrLaAlO_4$ by XRD and determined the structure parameters and the tetragonal *I4/mmm* (Nr. 139) space group [88]. Furthermore, they described the structures of $Sr_3Ti_2O_7$ and $Sr_4Ti_3O_{10}$ and have identify these compounds as a homologous series based on the K_2NiO_4 structure [89].

Homologous intergrowth are ordered arrengements in a crystall with different chemical compositions [90]. Ordered intergrowth with the same chemical composition are called polytypes and are described in Section 1.2.1 on the example of the hexagonal perovskite. Ruddlesden-Popper compounds are homologous series with general composition $A_{n+1}B_nO_{3n+1}$. These compounds can be regarded as perovskite ABO_3 structures to which rock-salt AO units were added. The general formula can be also termed as ($AO+nABO_3$) with n as the number of corner-sharing perovskite layers. Figure 6 represents the different Ruddlesden-Popper phases with increasing n.

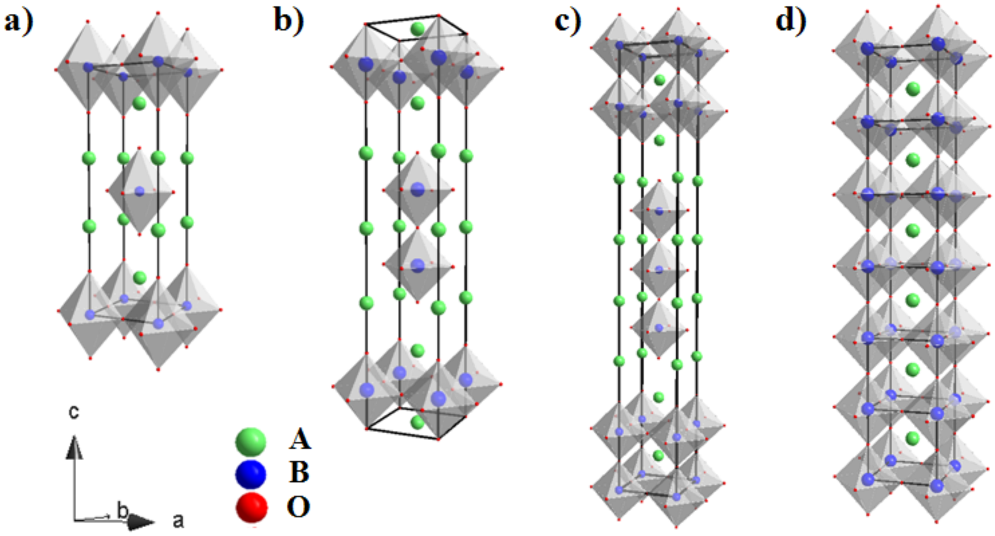

Figure 6: Representation of tetragonal Ruddlesden-Popper phases $A_{n+1}B_nO_{3n+1}$ (a) Unit cell of A_2BO_4 (n=1) (b) Unit cell of $A_3B_2O_7$ (n=2) (c) Unit cell of $A_4B_3O_{10}$ (n=3) (d) Supercell of perovskite ABO_3 ($n=\infty$).

The Ruddlesden-Popper structures can be characterized as perovskite layers in a corner-sharing framework, that are offset from each other by crystallographic shear along the (001) plane with a displacement of (a+b)/2 within the plane. The perovskite lattice is now cut apart at regular intervals, so that the corners, which normally share an oxygen atom, are now separated. The introduction of one rock-salt AO layer eliminates this oxygen deficiency.

Ruddlesden-Popper phases can be formed in the La-Ni-O system. This system was intensively investigated by Petrov et al. who first proposed the phase diagram in the year 1988 [91]. Zinkevich et al. extended the phase diagram using theoretical calculations on the decomposition sequence $LaNiO_3 \rightarrow La_4Ni_3O_{10} \rightarrow La_3Ni_2O_7 \rightarrow La_2NiO_4$ with an increasing oxygen pressure or a lowering temperature [92, 93]. Zhang and Greenblatt have shown that with increasing number of perovskite layers n, the sintering temperature of nickelates decreases from 1200 to 800 °C. The oxidation state of nickel is the reason for this observation, as with increasing n the valence increases ($La_2Ni^{2+}O_4$, $La_3Ni_2^{2.5+}O_7$, $La_4Ni_3^{2.67+}O_{10}$, $LaNi^{3+}O_3$) [94].

The tetragonal body-centered $I4/mmm$ space group of La_2NiO_4 can also be represented as an expanded $\sqrt{2}a \times \sqrt{2}b \times c$ supercell, so that the symmetry is described as face-centered $F4/mmm$ space group [95]. Figure 7 illustrates the structural relation between the two tetragonal space groups.

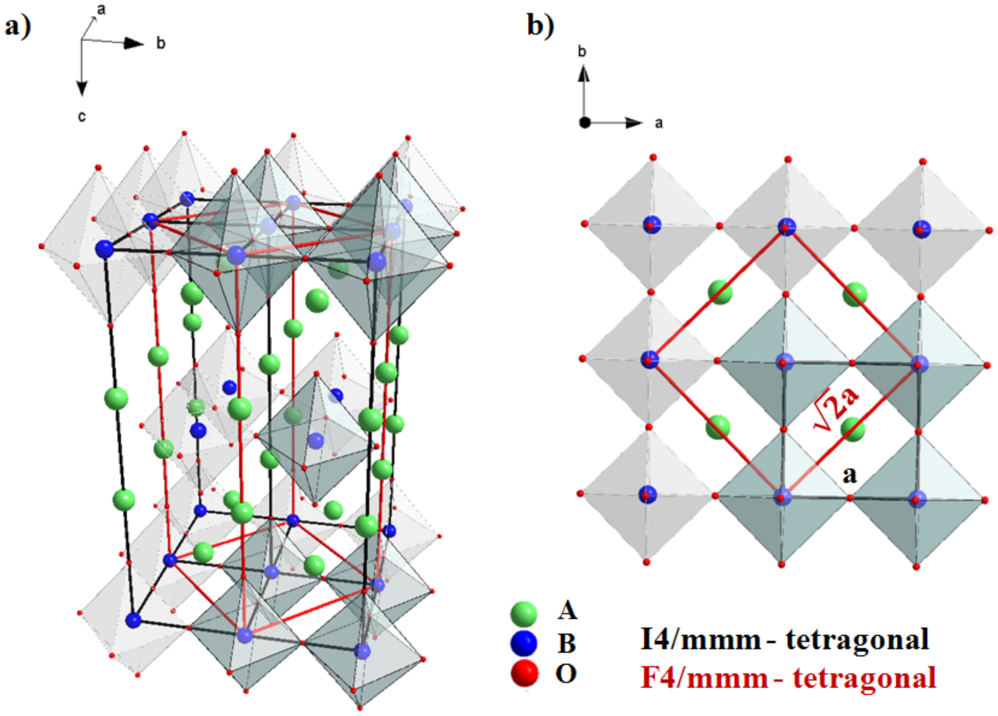

Figure 7: Structural relation between tetragonal space groups $I4/mmm$ and $F4/mmm$ (a) Clinographic projection of supercell with cell borders of $I4/mmm$ (black) and $F4/mmm$ (red) (b) Projection of the cupercell along the c-axis.

The Ruddlesden-Popper compounds are known for incorporating oxygen ion excess δ, which can have influence on the strucure symmetry of the particular phase [96, 97].

For lanthanum nickelate, the structural state depends strongly on the temperature and the oxygen excess δ. Octahedra tilting at low temperatures and small oxygen excess lead to the formation of orthorhombic structure distortion [98–103]. The distorted unit cells, which have a double basal plane area relative to the parent $I4/mmm$ structure, are larger than the undistorted one by $\sqrt{2}$a × $\sqrt{2}$b × c. When comparing the distorted structure with the tetragonal one, it is more convenient to represent the tetragonal $F4/mmm$ instead of $I4/mmm$ [95]. Tranquada and Buttrey et al. proposed a phase diagram for $La_2NiO_{4+\delta}$ with $0.05 \leq \delta \leq 0.11$ [104], wich describe the transition between high-temperature tetragonal phase ($I4/mmm$), low-temperature orthorhombic phase ($Bmab$) and low temperature tetragonal phase ($P4_2/ncm$) in the temperature range from 0 to 350 K. Figure 8 represents the octahedral tilting in *Bmab* space group. The formation of orthorhombic *Bmab* phase will be discussed in Chapter 3.

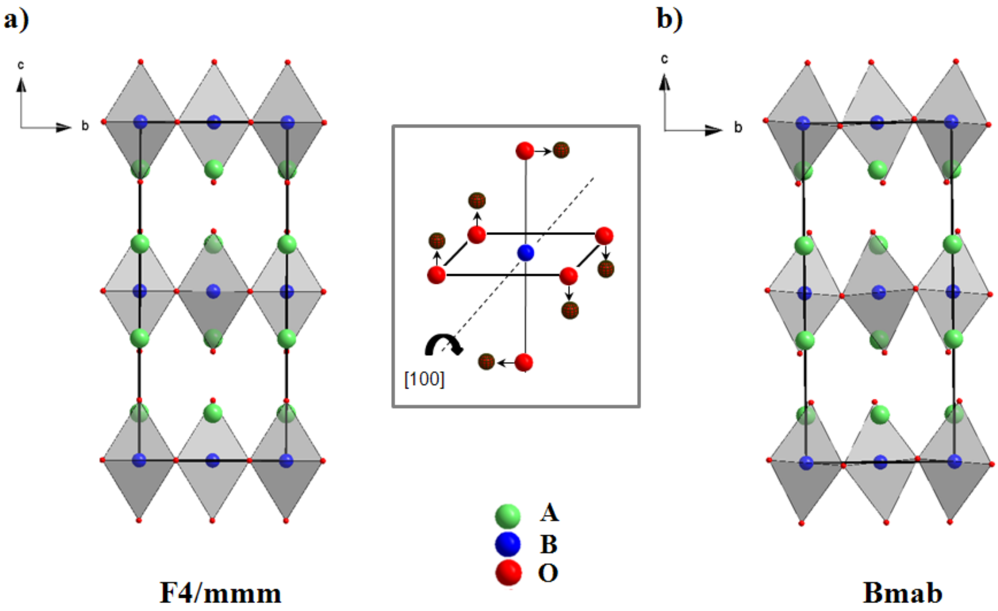

Figure 8: Octahedra tilting in orthorhombic *Bmab* space group. (a) Projection along [100] of tetragonal *F4/mmm* unit cell (b) Projection along [100] of orthorhombic *Bmab* unit cell.

Skinner et al. have shown with the use of in-situ high temperature neutron powder diffraction that La_2NiO_4 adopts tetragonal $I4/mmm$ structure above 423 K and up to at least 1073 K [105]. The oxygen excess dependence of La_2NiO_4 structure symmetry was described by Odier et al. who observed the tetragonal symmetry for samples prepared in oxygen atmosphere and orthorhombic structures for samples prepared in reducing conditions [106].

1.3 Transport properties of MIEC materials

1.3.1 Defect chemistry and conductivity

The MIEC properties of perovksites depend not only on the crystallographic stucture, but also on the structural defects. Creation of defects increases entropy, because there are many possible positions that can be occupied by defects. The driving force of defect formation is the minimizing of the Gibbs free energy ΔG (Gibbs-Helmholz equation) [25, 107].

$$\Delta G = \Delta H - T\Delta S \tag{4}$$

Point defects, are structural defects in the crystal, which only involve a single lattice site and its near environment [108, 109]. Due to the presence of point defects, such as vacancies (Schottky) or interstitials (Frenkel), the oxygen ion diffusion through the crystal lattice can occur. Perovskite materials can accommodate a high degree of disordered oxgen vacancies [110]. This deficit of oxygen ions or the oxygen defect concentration in non-stoichiometric oxide compound depends on temperature and oxygen ambient pressure. With increasing temperature and decreasing oxygen partial pressure oxygen removal from the perovskite lattice takes place, which can be described using the Kröger-Vink defect notation [111].

$$O_O^X + 2B_B^X \rightarrow V_O^{\bullet\bullet} + 2B_B^{'} + \frac{1}{2}O_{2(g)} \tag{5}$$

In this case, the vacancy formation is associated with the formation of electrons (n-type) or electron holes (p-type), which are responsible for the electronic conductivity. The majority of perovskites and Ruddlesden-Popper phases exhibit positive Seebeck coefficients consistent with p-type conduction and electron holes. Resulting from the B-site cation reduction, electron holes can be considered as charge carriers [112]:

$$B_B^X \rightarrow B_B^{'} + h^{\bullet} \tag{6}$$

That mechanism of electron conduction is strongly influenced by temperature and can be seen as thermal excitation of electrons from the valence band to the conduction band [113]. At high temperatures a metal-like conductivity in perovkites can be observed, which is shown by decrease of conductivity with temperature. This behavior can be explained by so called Zerner double exchange process, where the conductivity proceeds through overlapping B-O-B bonds [113, 114]:

$[B^{n+}\text{– } O^{2-}\text{– } B^{(n+1)+}] \rightarrow [B^{(n+1)+}\text{– } O^{1-}\text{– } B^{(n+1)+}] \rightarrow [B^{(n+1)+}\text{– } O^{2-}\text{– } B^{n+}]$

Caused by anion polarization a covalent bond is formed between the oxygen ion and the B-site cation. This process is facilitated by a strong overlap of the $2p_{\pi}$-orbitals of oxygen ion and the $d_{t_{2g}}$-orbitals of B metal ion, which is maximized for the B-O-B angle at 180° (cubic perovksite structure).

The ion and electron transport require an activation energy E_a, which can be described by an Arrhenius approach with k as Boltzmann constant, and C as the pre-exponential factor, which includes carrier concentration and material parameters [22, 115]. The electronic and ionic conductivity increase respectively with increasing temperature.

$$\sigma = \frac{C}{T} exp\left(-\frac{E_a}{kt}\right) \tag{7}$$

1.3.1.1 Ionic transport mechanism in perovskites

Oxygen ion transport through the perovskite structure can be described as an oxygen ion migration from one oxygen vacancy to another [116]. Oxygen ions are sixfold coordinated by four A site and two B site cations, and fill the free octahedral space formed by this cations.

The oxygen migration can be expressed by geometrical appoach considering only the ionic radii of involved ions as proposed by Cook and Sammels [113, 117]. In this case the oxygen ion has to pass a triangle surface, formed by two A-site cations and one B-site cation of two face-shared octahedra (Figure 9). The migration takes place along the [110] edge of the BO_6 octahedron. The saddle point for ionic migration or the critical radius can than be geometrically described as circles touching the radii of these three cations with r_A, r_B as ion radii and a as the lattice parameter.

$$r_{critical} = \frac{r_A^2 + 3/4(a^2) - \sqrt{2}a(r_B) + r_B^2}{2(r_A) + \sqrt{2}a - 2(r_B)} \tag{8}$$

A critical radius is one of three empirical parameters that exhibits strong correlation with activation energy for oxide ion transport introduced by Cook and Sammels. The other two are the average metal-oxygen bond energy and lattice free volumes, defined as the difference between the perovskite unit cell volume and the summed volume of all ions present within the perovskite cell.

Further investigations performed by Cherry and Islam have partly refuted this ge-

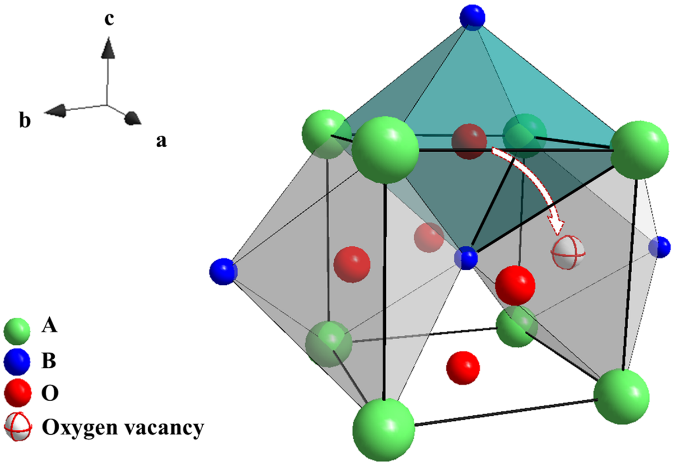

Figure 9: Octahedral oxygen coordination. Transport of an oxygen ion to the oxygen vacany through a triangle surface formed by face-shared octahedra.

ometrical approach [118, 119]. Using computer simulation technique it was shown, that oxygen migration occurs via curved route with saddle point away from the neighboring B site cation. The repulsive interactions between the ions can be reduced by the outward movement of the nearest cations. The lattice relaxation strongly influences the oxygen ion migration. This effect was confirmed for perovskites like $La_{0.6}Sr_{0.4}CoO_{3-\delta}$ [120] and $La_{0.64}Sr_{0.4}Ti_{0.92}Nb_{0.08}O_{2.99}$ [121].

1.3.1.2 Ionic transport in Ruddlesden-Popper Phases

The oxygen ion migration mechanism in Ruddlesden-Popper phases is more complex than in perovskite compounds. The compounds are oxygen-hyperstoichiometric and the oxygen excess is incorporated into an interstitial site. To compensate the oxygen ion excess several mechanisms are possible: formation of oxygen vacancies, cation antisites and oxidizing lattice oxygen ions or nickel ions. Investigations on tetragonal and orthorhombic $La_2NiO_{4+\delta}$ have shown a preference for the formation of oxygen vacancies in the equatorial plane, localized on the **(O1)** site structure. Cleave et al. have reported about formation of anion Frenkel pairs, composed of a vacancy and an interstitial [122, 123]. At the same time Ni^{2+} can be oxidized to Ni^{3+}.

The migration of oxygen ions is highly anisotropic and takes place mainly in the *ab* rock-salt plane [124]. By using the density function theory Frayret et al. predicted, that interstitial oxygen in $La_2NiO_{4+\delta}$ is doubly negatively charged oxygen ion (O^{2-}) [125]. Figure 10a shows double unit cells of a tetragonal body-centered *I4/mmm* structure. Interstitial oxygen ions **(O3)** are at the one hand tetrahedrally coordinated by lanthanum ions, at the other hand also tetrahedrally coordinated by lattice oxygen ions.

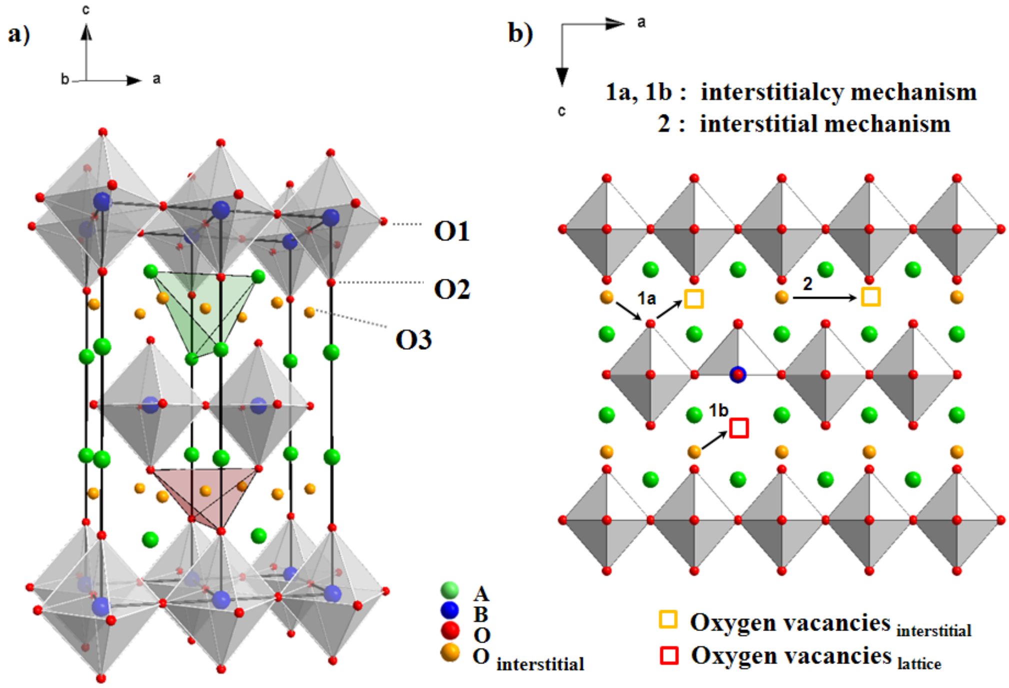

Figure 10: Interstitial oxygen ion in the tetragonal $I4/mmm$ structure. (a) Tetrahedral coordination of interstitial oxygen ion by lattice oxygen and lanthanum cations (b) Simplified presentation of interstitialcy mechanism vs. interstitial mechanism.

Chromeos et al. predicted an interstitialcy mechanism for tetragonal $La_2NiO_{4+\delta}$ in the temperature range 800-1100 K using molecular dynamics calculations [126]. Contradictory, the interstitial mechanism (also denoted as the direct interstitial mechnism) is known, where the defect interstitial oxygen ion simply ”jumps” from one interstitial site to another (Figure 10b). During the interstitialcy mechanism (or indirect interstitial mechanism) in tetragonal $La_2NiO_{4+\delta}$, the oxygen interstitial displaces an apical oxygen ion **(O2)** from the NiO_6 octahedra, which then migrates to a neighboring interstitial site. At the same time a significant tilting of NiO_6 octahedra occurs. This allows either the apical oxygen ion to move towards an unoccupied interstitial site, or to move the existing interstitial oxygen ion towards the formerly occupied site. The correctness of the interstitialcy mechanism could be approved for different Ruddlesden-Popper phases. By using computer simulation studies and the employment both static lattice and molecular dynamics method, Naumovich et al. predicted an anion diffusion mechanism in hypostoichiometric $La_2(M)NiO_{4+\delta}$ (M = Fe, Cu) which includes the **(O2)-(O3)** exchange in the rock-salt layer [127]. Kushima et al. investigated $La_2CoO_{4+\delta}$ [128] and Tealdi et al. analyzed $La_{2-x}Sr_xCoO_{4+\delta}$ [129] and came to the same conclusions in regards to the oxygen migration path.

1.3.2 Oxygen transport through dense MIEC membranes

The oxygen permeation is the oxygen transport through a membrane from one side with high oxygen partial pressure (feed side) to another side with smaller oxygen partial pressure (sweep side). Physically, the oxygen permeation describes the amount of oxygen transported per surface and time. The driving force of oxygen permeation is the gradient of oxygen chemical potential ($\nabla\mu_{O_2}$) across the membrane.

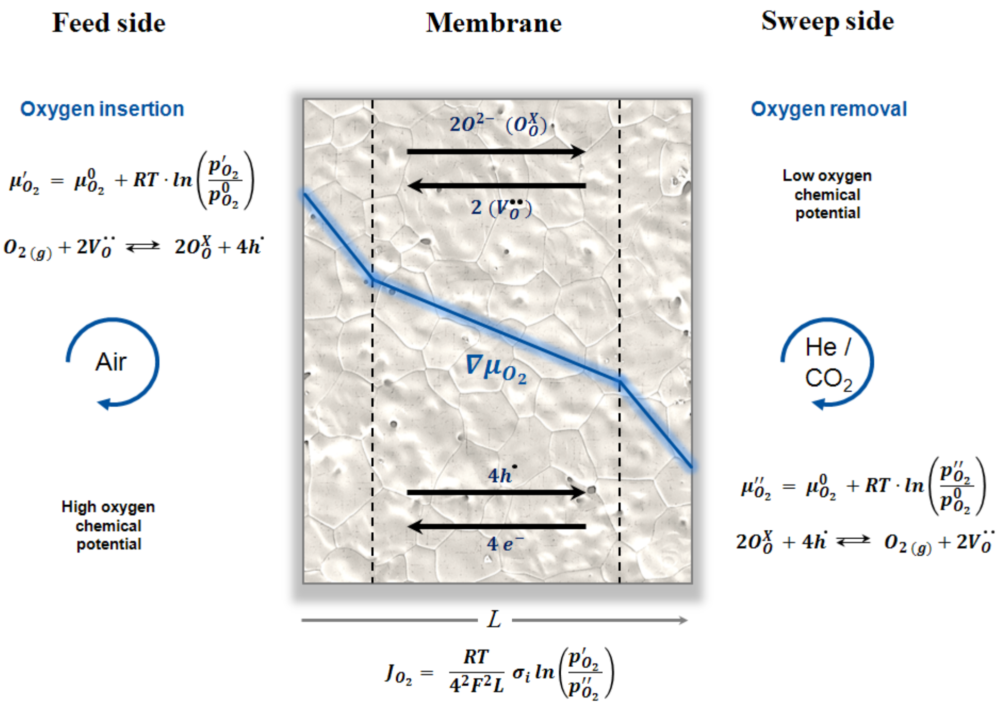

Figure 11: Oxygen permeation through a dense MIEC membrane. The course of the gradient of oxygen chemical potential, oxygen insertion and removal reactions, and bulk diffusion region described by Wagner´s equation are presented.

The oxygen transport mechnism can be simplified by dividing it in three steps: a) surface exchange with gas on the feed side and insertion of oxygen, b) bulk diffusion, c) removal of oxygen and surface exchange on the sweep side of the membrane [130, 131]. The slowest process controls the transport and is the overall rate-limiting step. Characteristic for MIEC materials is the simultaneous transport of oxygen and electrons. Both species migrate in opposite directions in order to maintain local charge neutrality (ambipolar diffusion).

Assuming bulk diffusion as the rate-limiting step (very quick surface reaction or thick membrane), at given temperature and membrane thickness L the oxygen potential gradient then depends only on the oxygen partial pressure on the feed side and sweep side of the membrane:

$$\nabla\mu_{O_2} = \frac{\mu''_{O_2} - \mu'_{O_2}}{L} = \frac{RT}{L} ln \left(\frac{p''_{O_2}}{p'_{O_2}} \right) \tag{9}$$

Considering the ionic and electronic conductivities ($\sigma_i \; and \; \sigma_e$) and the Faraday constant F a term for oxygen permeation, Wagner´s equation, can be obtained [132–134]:

$$J_{O_2} = -\frac{1}{4^2F^2} \cdot \frac{\sigma_i\sigma_e}{\sigma_i + \sigma_e} \cdot \nabla\mu_{O_2} \tag{10}$$

Under the assumption that the oxygen chemical potential varies linearly in space and that ($\nabla\mu_{O_2}$) is locally constant, and after the integration over the membrane thickness L, the Wagner´s equation can be modified:

$$J_{O_2} = \frac{1}{16F^2L} \cdot \int_{p''_{O_2}}^{p'_{O_2}} \frac{\sigma_i\sigma_e}{\sigma_i + \sigma_e} dln \left(\frac{p'_{O_2}}{p''_{O_2}} \right) \tag{11}$$

In perovskites the electronic conduction is much higher than the ionic conduction, so that the conduction term in Equation 11 can be simplified as the following:

$$\frac{\sigma_i\sigma_e}{\sigma_i + \sigma_e} \approx \sigma_i \tag{12}$$

The ionic conductivity depends on the self-diffusion coefficient D_i, the concentration c_i and valence charge z_i of oxygen ions and can be expressed by the Nernst-Einstein relation:

$$\sigma_i = \frac{c_iD_iz_i^2F^2}{RT} \tag{13}$$

Assuming the ionic conductivity remains constant, the Wagner equation, which describes the oxygen permeation in dependence of oxygen partial pressure, ionic conductivity and membrane thickness is obtained:

$$J_{O_2} = \frac{1}{16F^2L} \cdot \sigma_i \cdot ln \left(\frac{p'_{O_2}}{p''_{O_2}} \right) \tag{14}$$

The Wagner equation is only valid for bulk diffusion and does not describe the surface exchange processes. If the oxygen permeation is limited by surface exchange, the oxygen permeation flux can be given as follows:

$$J_{O_2} = kc_i \cdot \left(\sqrt{p\acute{}_{O_2}} - \sqrt{p\acute{}\acute{}_{O_2}} \right) \tag{15}$$

The characteristic thickness L_c introduced by Bouwmeester et al. prowides a way to distinguish which mechanism is controlling the permeation in particular case [135].

$$L_c = \frac{D_i}{k} = \frac{D^*}{k} \tag{16}$$

The characteristic thickness defines the membrane thickness at which the oxygen permeation is equally determined by the bulk diffusion and surface exchange kinetics. The self-diffusion coefficient is assumed to be equal to the tracer diffusion coefficient D^* and can be established simultaneously to the surface exchange coefficient k by ^{18}O - ^{16}O isotope echange experiments.

1.4 Membrane preparation

Membrane preparation can be divided into two steps: material synthesis and dense membrane fabrication. The oxide materials can be synthesized via solid-state reaction, hydrothermal synthesis or spray pyrolysis [136]. Another approach is the sol-gel synthesis, a simple method which offers many advantages and which will be further described. The preparation of dense membranes depends on the membrane architecture. Tube membranes or fiber membranes fabrication use wet spinning/sintering technology [137]. For the preparation of dense disc membranes, the first powder densification step takes place by pressing, followed by a sintering process at elevated temperature. Section 1.4.2 will shortly describe the different sintering techiques relevant for the disc membrane preparation.

1.4.1 Material synthesis via sol-gel process

Sol-gel route is a liquid-phase method, which is most suitable for fabrication of highly pure and homogenous perovskites with complex composition. All syntheses in this thesis were performed via modified Pechini Method using ethylene diamine tetraacetic acid (EDTA) and citric acid (CA), which was intensively studied in the last years [138–141]. The sol formation is provided by building of EDTA-metal complexes. EDTA can be applied for complexation of a wide range of metal cations. The formed chelat-complexes prevent a possible segregation and enhance the solubility in aqueous solution [142]. The citric acid also functions as a chelating agent. Furthermore, a three dimensional network can be formed (gel) after esterification of the citric acid carboxy group. Thereby, the metal ions are homogenously distributed in the whole gel. Further, the sol-gel syntheses also provide a better control on stoichiometry and reduce the synthesis temperature of materials, in comparison to solid-state reactions [143, 144].

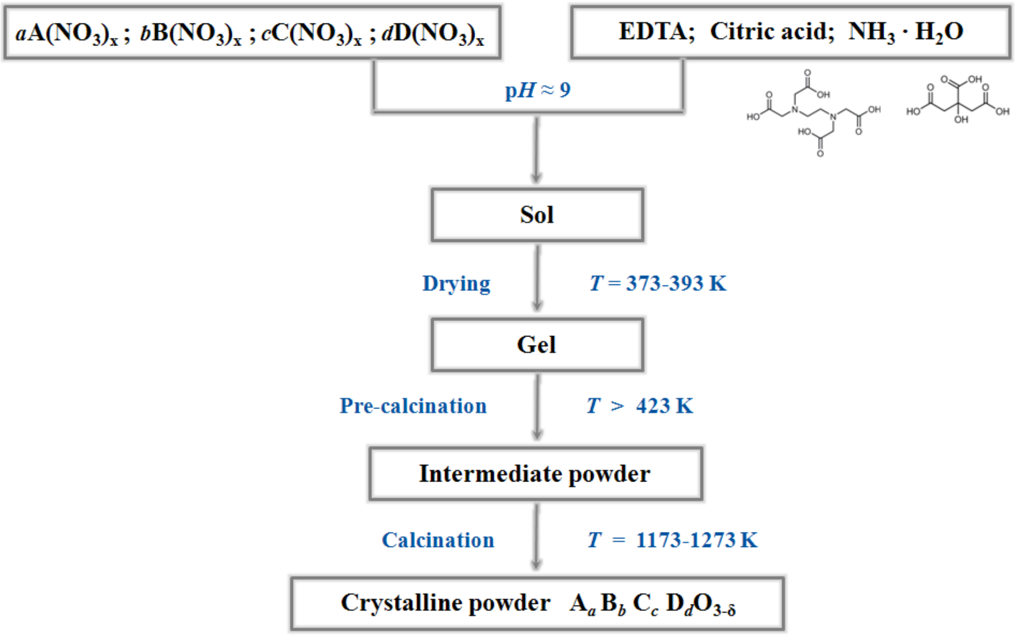

Figure 12: Schematic sol-gel route for oxide materials preparation.

Figure 12 demonstrates a schematic sol-gel route for perovskite oxides preparation. Metals are introduced to the synthesis in the form of metal nitrates in stoichiometric amounts. It is important to adjust the pH value around 9 to ensure a complete dissolvation of precursor powders. Furthermore, the EDTA and citric acid need to be deprotonated before the complexing reaction. The first step of a sol-gel process is the preparation of a sol, which contains highly dispersed solid particles in the size range of 1-100 nm. After sol aging and drying, a pre-calcination step is involed, which yields the intermediate partially amorphous powder. During this step most metal-organic residues are burned out as carbon dioxide and carbon monoxide, so that metal carbonates are left. At the same time the metal nitrates decompose to nitrogen oxides and metal oxides. In the last calcination step, a solid-state reaction of homogenously mixed components occurs. In conclusion, a crystalline powder with given metal stoichiometry is formed.

1.4.2 Preparation of dense membranes

Obtaining dense membranes is of great importance for oxygen permeation experiments. The membrane must be gas-tight to guarantee the exclusivity of oxygen ionic transport through the material. Different techniques like pressure sintering, hot pressing, microwave sintering as well as plasma sintering are possible to achieve that goal [145]. During the work on this thesis two different techniques were applied: powder pressing followed by pressureless sintering and Field-Assisted Sintering Technology/ Spark Plasma Sintering (FAST/SPS).

1.4.2.1 Pressureless sintering and grain growth

The sintering process refers to the densification of powder pellets by a solid-state process at temperatures near the melting point of the material. The pellets or green bodies can be prepared by uniaxial or isostatic pressing to form the material in the desired shape and to press the powder particles closer to each other. The pressureless sintering includes material densification and coarsening, which describes the grain growth (pore growth) and evolution of microstructure. The driving force of the sintering is the effort to reduce the surface energy of the particles caused by decreasing their vapour-solid interfaces. The total energy of the surface and interfaces E can be expressed by Equation 17, where A_{SV} is the solid-vapor interface are and A_{GB} is the grain boundary area. The corresponding interface energies are γ_{SV} and γ_{GB} [145].

$$E = A_{SV} \cdot \gamma_{SV} + A_{GB} \cdot \gamma_{GB} \tag{17}$$

The presence of grain boundaries in a polycrystalline material provides grain growth as an alternative process, by which the powder system can decrease its energy. Moreover, the grain growth and pore growth proceed simultaneously. Sintering of pollycristalline materials occurs by diffusional mass transport and consists of at least six different mechanism: surface diffusion, lattice diffusion (from the surface, vapor transport, grain boundary diffusion, lattice diffusion (from the grain boundary) and plastic flow [145].

The whole sintering process can be divided in three steps effected by different mass transport mechanisms [146]. During the initial stage, a rapid interparticle neck growth by diffusion, vapor transport and plastic flow occurs. The differences in the particle surface curvature are removed. Up to 65% of the maximum density can be achieved at this stage. The initial stage covers the main part of the densification process and ends with approximately 90% of the theoretical density. Densification occurs by pore shrinking and equilibrium pore shape with continuous porosity is formed. In the final stage, the material with isolated porosity is formed. The driving force for the densification is now mainly generated by grain growth, because the solid-vapor interface has already decreased. The density is further increased up to 95-98% [145, 146].

1.4.2.2 FAST/SPS technique

Field-assisted sintering technology/Spark Plasma Sintering is a current and pressure controlled sintering process. In the experimental setup low voltages, typically below 10V, produce high currents (direct current) in the range of 1 to 10 kA, leading to efficient Joule heating [147]. This form of heating is defined as an increase in the specimen temperature from the dissipation of electrical energy [148]. The applied pressure can be huge between 50 and 250 kN. The reduction of sintering process duration can be achieved with heating rates as high as 1000 °C min^{-1} and the maximal attainable temperature up to 2400 °C. The process can be operated under a vacuum or a protective gas atmosphere [147].

Generally, a finer grain size distribution is obtained by applying high pressure during the FAST/SPS process. The pressure influences the sintering step by enhancing the rearrangement of particles, but obviously does not affect the grain growth and coarsening. Application of pressure lowers the sintering temperature, with full density being achieved in a very short time. Due to the reduced sintering time, there is little time for grain growth and resulting grain size is nearby equal to the original particle size in the powder [148].

Another important aspect is the influence of the electric field on the grain growth. The local temperature at the grain boundary becomes higher than in the bulk, because the grain boundaries may posses a higher resistance than the crystal bulk material. This effect would lead to a faster grain boundary diffusion, which controls the grain growth. As a result, an enhancement of grain growth should be observed. Faster diffusion should increase and not hinder the grain growth. The obstruction of the grain growth can be explained by reduction of the local interfacial energy relative to the surrounding material. Ghosh et al. proposed this thermodynamic approach, assuming that the grain boundary energy γ_{GB} corresponds to the Gibbs free energy ΔG [149]. According to the Gibbs-Helmholz equation, the entropic contribution to γ_{GB} will cause the interfacial energy to fall with increasing temperature. A created potential well then hinders the migration of the boundary.

1.5 Stability of MIEC materials

For a successful implementation of ceramic oxygen-transporting membranes in the industrial processes stringent demands on material stability must be ensured. The chemical stability refers to the tolerance of the materials to harsh surrounding environment, like carbon dioxide or sulfur dioxide atmospheres. It is necessary, that the poisoning of the membrane does not occur at working conditions, and that the oxygen-transporting function remains constant. Another important challenge to overcome is the phase stability of the material over the operation time. The long-term stability is essential to guarantee the invariably oxygen flow rates. Material degradation or phase segregation lead to a decline of the oxygen permeation flux, which becomes considerably impaired with an increasing operation time.

In general, the perovskite oxide stability can be estimated using a thermodynamic approach. Yokogawa et al. provided a thermodynamic study on perovskites and K_2NiF_4 compounds stabilization enegy $\Delta_R H^0$, which can be defined as the enthalpy change for formation $\Delta_f H^0$ from the constituent binary oxides [150]. For a general ABO_3 perovskite the stabilization energy can be termed as followed:

$$\Delta_R H^0(ABO_3) = \Delta_f H^0(ABO_3) - \Delta_f H^0(AO_n) - \Delta_f H^0(BO_m) \tag{18}$$

Yokogawa et al. correlated the stabilization energy to the tolerance factor t (Equation 1) and showed the increase in stability with approaching the factor t to unity [150]. Katsura et al. came to the same conclusion through studies of $LnFeO_3$, showing the dependence of the stabilization enegy from the tolerance factor or increasing ionic radius of the lanthanoide cation [151].

The standard enthalpy of formation of a ternary oxide from the binary constituent oxides reflects the strength of the chemical bonds in the ternary oxide relative to those in the binary oxides [152]. Therefore, the enthalpy of formation can be interpreted in terms of factors related to electron transfer between the constituent oxides or with other words acidity or basicity [153]. The larger the difference in acidity of AO_n and BO_m is, the more exothermic is the enthalpy of formation of the ternary oxide from its binary components [152]. The trends of metals within the periodic table of elements to form basic or acid oxides is described in literature [154]. This concept offers an easy way to estimate the stability of perovskite oxides.

Recently, Calle-Vallejo et al. proposed a method for the determination of the thermodynamic stability based on density functional theory (DFT) calculation with exchange-correlation functional [155]. They correlated the Gibbs free energy of formation to the atomic number of metals. Depending on the oxidation state of A- and B-site metal two groups of compound can be distinguished, perovskites with the same oxidation state (+III) and perovskites in which the cationic oxidation states differ (+II and +IV). Whithin the groups the formation energies for materials with the same B-site cation are approximatly constant and independent of A-site cation. Both groups exhibit a systematic linear scalling between the stability and the atomic number.

1.5.1 Chemical stability

Most high-flux oxygen-transporting materials are formed on the basis of alkaline-earth metals, mainly barium and strontium. Unfortunatly, this elements are not favoured in regards to the chemical stability and tolerance to carbon dioxide, because of the formation of carbonates following by material decomposition. A thermodynamic approach can help with the estimation of alternative elements for carbon dioxide tolerant membranes. Yokogawa et al. proposed a comparison of the perovskite stabilization energy $\Delta_R H$ (Equation 18) to the metal carbonate formation energy [150]. The carbonate formation reaction from ABO_3 perovskite and carbon dioxide is defined as followed and can be divided in two steps:

$$ABO_3 + CO_2 \rightleftharpoons ACO_3 + BO_2 \tag{19}$$

$$ABO_3 \rightleftharpoons AO + BO_2 \tag{20}$$

$$AO + CO_2 \rightleftharpoons ACO_3 \tag{21}$$

Consequently, the reaction enthalpy for the carbonate formating reaction (Equation 19) can be defined as:

$$\Delta_R H^0(Equation\ 19) = \Delta_R H^0(ABO_3) - \Delta_R H^0(ACO_3) \tag{22}$$

It becomes clear, that the trend of metal carbonate formation is strongly influenced by the perovskite stabilization energy.

The Ellingham diagram in Figure 13 illustrates the relationship of the carbon dioxide chemical potential of metal carbonates decomposition (reverse reaction Equation 21) reactions with increasing temperature and in dependence of the carbon dioxide partial pressure. The diagram facilitates the estimation of metal carbonate stability at given conditions, by comparing of CO_2 chemical potential of the decomposition reaction and the one of corresponding partial pressure (dashed lines). At the crossing point the carbonate decomposition and carbonate formation reactions are in equilibrium. The metal carbonate is stable until the carbon dioxide chemical potential of the decomposition reaction is lower than the carbon dioxide chemical potential of the atmosphere at the corresponding partial pressure.

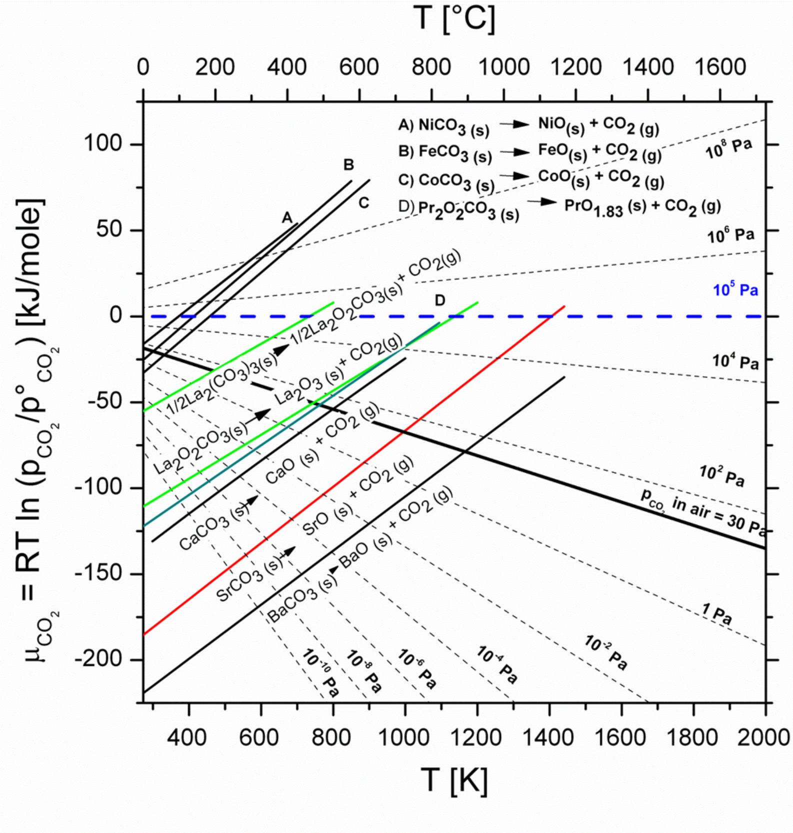

Figure 13: Ellingham diagram with decomposition temperature of carbonates under different carbon dioxide partial pressure. The dashed lines represent the carbon dioxide chemical potential in the atmosphere for different partial pressirus ($p^{O}_{CO_2} = 101.3$ kPa refers to standard conditions). Chemical potential of CO_2 above $NiCO_3$, $FeCO_3$, $CoCO_3$, $La_2O_2CO_3$, $Pr_2O_2CO_3$, $CaCO_3$, $SrCO_3$, $BaCO_3$ were calculated from thermodynamic data [156–158]. The chemical potential of $La_2(CO_3)_3$ was determined experimentally [139].

It should be noted, that the Ellingham diagram only considers the binary metal oxides and carbonates. There is a lack in thermodynamic data for more complex compounds. According to the Ellingham diagram the large metal cations like barium and strontium form very stable metal carbonates which decompose only over 1000 °C at a carbon dioxide partial pressure of 10^5 Pa. The smaller calcium or the 3d-metals form less stable carbonates.

The polarization of the carbonate anion (CO_3^{2-}) by the metal provides a qualitative explanation for these observations. The cation polarizing power *(PP)* for carbonates is defined as followed, where r is the ionic radius and Z is the ionic charge [157].

$$PP = \frac{\sqrt{r}}{Z} \tag{23}$$

The polarization of the carbonate anion structure leads to a distortion and weakening of the intra-ionic oxygen-carbon bonds. As a result carbon dioxide elimination from metal carbonate is alleviated. The thermal stability of the carbonate anion decreases with an increase of polarizing power of the cation due to the small cationic size and high charge. The smaller and more highly charged metal cations (3d-metals, lanthanum, praseodymium) form less stable carbonates when compared to larger and lower charged ones (barium, strontium). The same approach can also be transferred to the thermal stability of sulfur oxide compounds.

The presence of A and B cations in the perovskite structure with diverging charge to radius rations can promote acid/basic sites of markedly different strength [15]. Because carbon dioxide is a slightly acidic molecule, it adsorbs preferably on the basic sites. Tejuca et al. investigated the CO_2 adsorption-desorption reactions as well as the heats of adsorption on $LaBO_3$ (B = Cr, Fe, Co) over a wide temperature range [159–161]. The trend of adsorption extent was shown to follow the order $LaCrO_3 > LaFeO_3 > LaCoO_3$. In general, the amount of adsorbed CO_2 decreased continuously with increasing temperature. That phenomenon plays an important role during the oxygen permeation measurements in carbon dioxide containing athmospheres. Even the carbon dioxide tolerant materials demonstrate a slight decrease of oxygen-transport functionality in a broad temperature range, which is caused by blocking of the membrane surface by adsorbed carbon dioxide molecules [61].

1.5.2 Phase stability

The phase stability of oxide materials is mostly controlled by kinetic processes. Caused by the gradient of oxygen chemical potential ($\nabla\mu_{O_2}$) the diffusion of cations can occur [162–164]. The cation diffusion results from a gradient of the cation chemical potential ($\nabla\mu_A$, $\nabla\mu_B$) to the opposite site of the membrane, which arise according to the Gibbs-Duhem relation (at constant pressure and temperature).

$$x_A d\mu_A + x_B d\mu_B + +x_O d\mu_O = 0 \tag{24}$$

The cationic mobility can not be neglected, although it is much smaller than the oxygen mobility. The cation diffusion across the gradient of the cation´s chemical potential can lead to the degradation of a homogeneous material and the formation of different phases. Moreover, the material morphology can be changed, so a dense membrane can transform to a more porous structure.

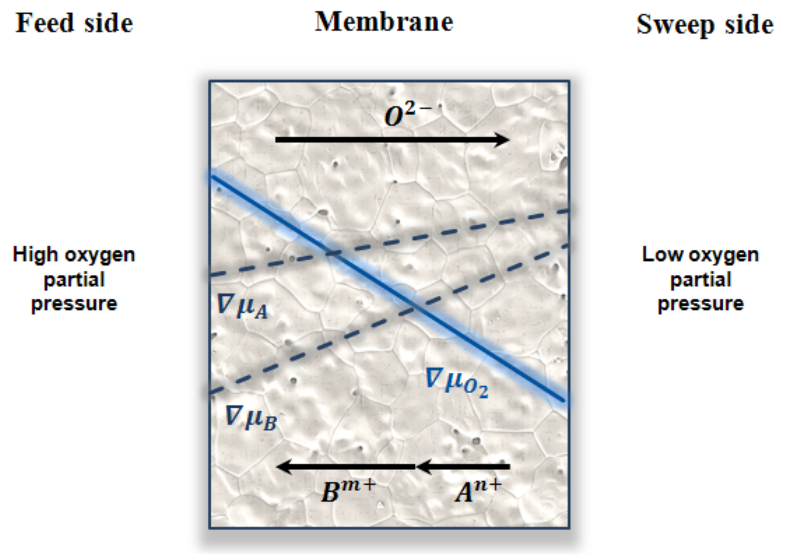

Figure 14: Gradient of the chemical potential of different material constituents with corresponding diffusion direction (According to [162, 163]).

In the IT range the cubic perovskite $(Ba_{0.5}Sr_{0.5})(Co_{0.8}Fe_{0.2})O_{3-\delta}$ (BSCF) tends to decompose into a hexagonal and a rhombohedral phase [38–44]. Both newly formed phases are reported to be cobalt and ion rich, and the phase transition occurs with greater extent on the membrane side with high oxygen partial pressure (feed side). At the one hand, the high oxygen partial pressure and moderate temperatures promote the oxidation of Co^{2+} (HS) ions to Co^{3+} (LS). At the other hand, the ionic radius of the oxidized cobalt cation is decreased, which causes the higher ion mobility through the bulk material and enhances the degradation and cobalt enrichment on the feed side.

From a thermodynamic point of view, the phase stability reflects the Gibbs free energy of the corresponding phase [152]. For example, the enthalpy of formation between the cubic and hexagonal modification of $SrMnO_3$ is only 6 kJ mol^{-1} [165]. As long as the crystal structure allows the transformation and the metal has accessible oxidation state, the phase transition occurs easily. The redox properties of the perovskites largely depend on the stability of the oxidation state involved. And the oxidation state of cation is strongly influenced by the non-stoichiometry of the compound, oxygen partial pressure and temperature. The effect of a high oxygen partial pressure at intermediate temperature on the phase stability of BSCF is discussed in Section 3.4. The difference in the relative Gibbs free energy of the possible phases can be the limiting factor to the phase stability. Thus, several different structural modifications of the given oxide compound can be close in their energy. The formation of domains or intergrowth in oxide materials reflect simultaneous realization of different ordering patterns due to the existence of different crystal structures being close in energy [152]. For example, the formation of different hexagonal polytypes of the perovskite structure, described in Section 1.2, is a sign of energetic equality.

Bibliography

[1] J. Kunze and U. Stimming. Energietechnologie: Elektrochemie gegen Wärmekraftmaschinen - ein Tribut an Wilhelm Ostwalds visionäre Aussagen. *Angew. Chem.*, 121:9394–9401, **2009**.

[2] U. Lehr, J. Nitsch, M. Kratzat, C. Lutz, and D. Edler. Renewable energy and employment in Germany. *Energy Policy*, 36:108–117, **2008**.

[3] R. Wüstenhagen and M. Bilharz. Green energy market development in Germany: effective public policy and emerging customer demand. *Energy Policy*, 34:1681–1696, **2006**.

[4] U. Büsgen and W. Dürrschmidt. The expansion of electricity generation from renewable energies in Germany a review based on the renewable energy sources act progress report 2007 and the new german feed-in legislation. *Energy Policy*, 37:2536–2545, **2009**.

[5] R. Hinrichs-Rahlwes. Renewable energy: Paving the way towards sustainable energy security lessons learnt from Germany. *Renewable Energy*, 49:10–14, **2013**.

[6] International Energy Agency. World energy outlook 2014. *OECD/IEA*, **2014**.

[7] BP p.l.c. BP statistical review of world energy 2014. **2014**.

[8] International Energy Agency. Tracking clean energy progress 2014. *OECD/IEA*, **2014**.

[9] Statistisches Bundesamt. *https://www.destatis.de/EN/FactsFigures/Economic Sectors/Energy/Energy.html* (28.04.2015). Economics sector - Energy, **2015**.

[10] B.V. Mathiesen, H. Lund, and K. Karlsson. 100 % renewable energy systems, climate mitigation and economic growth. *Applied Energy*, 88:488–501, **2011**.

[11] International Energy Agency. Tracking progress in carbon capture and storage. *OECD/IEA*, **2012**.

[12] International Energy Agency. Energy efficiency indicators: Fundamentals on statistics. *OECD/IEA*, **2014**.

[13] K. Ohlrogge and K. Ebert. *Membranen - Grundlagen, Verfahren und industrielle Anwendungen.* Wiley, New York, 1 edition, **2006**.

[14] A.S. Bhalla, R. Guo, and R. Roy. The perovskite structure - a review of its role in ceramic science and technology. *Mater. Res. Innovat.*, 4:3–26, **2000**.

[15] M.A. Pẽna and J.L. Fierro. Chemical structures and performance of perovskite oxides. *Chem. Rev.*, 101:1981–2017, **2001**.

[16] A. Manthiram, J.-H. Kim, Y.N. Kim, and K.-T. Lee. Crystal chemistry and properties of mixed ionic-electronic conductors. *J. Electroceram.*, 27:93–107, **2001**.

[17] P.J. Gelling and H.J.M. Bouwmeester. Solid state aspects of oxidation catalysis. *Catalysis Today*, 58:1–53, **2000**.

[18] V.V. Kharton. *Solid State Chemistry I: Fundamentals, Materials and their Applications.* Wiley-VCH, Weinheim, 1 edition, **2009**.

[19] X. Meng, B. Meng, X. Tan, N. Yang, and Z.-F. Ma. Synthesis and properties of $Ba_{0.5}Sr_{0.5}(Co_{0.6}Zr_{0,2})Fe_{0.2}O_{3-\delta}$ perovskite cathode material for intermediate temperature solid-oxide fuel cells. *Mater. Res. Bull.*, 44:1293–1297, **2009**.

[20] S. B. Adler. Factors govering oxygen reduction in solid oxide fuel cell cathodes. *Chem. Rev.*, 104:4791–4843, **2004**.

[21] E. Magnone. A systematic literature review in BSCF-based cathodes for solid oxide fuel cell application. *J. Fuel Cell Sci. Technol.*, 7:064001, **2010**.

[22] J. Richter, P. Holtappels, T. Graule, T. Nakamura, and L.J. Gauckler. Materials design for perovskite SOFC cathodes. *Monatsh. Chem.*, 140:985–999, **2009**.

[23] Y. Liu, X. Tan, and K. Li. Mixed conducting ceramics for catalytic membrane processing. *Catal. Rev.*, 48:145–198, **2006**.

[24] A. Thursfield and I.S. Metcalfe. The use of dence mixed ionic and electronic conducting membranes for chemical production. *J. Mater. Chem.*, 14:2475–2485, **2004**.

[25] J. Sunarso, S. Baumann, J.M. Serra, W.A. Meulenberg, S. Liu, Y.S. Lin, and J.C. Diniz da Costa. Mixed ionic-electronic conducting (MIEC) ceramic-based membranes for oxygen separation. *J. Membr. Sci.*, 320:113–41, **2008**.

[26] S.M. Hashim, A.R. Mohamed, and S. Bhatia. Current status of ceramic-based membranes for oxygen separation from air. *Adv. Colloid Interface Sci.*, 160:88–100, **2010**.

[27] K. Huang and J.B. Goodenough. *Solid oxide fuel cell technology.* Woodhead Publishing Limited, Cambridge, 1 edition, **2009**.

[28] J. Caro, H.H. Wang, C. Tablet, A. Kleinert, A. Feldhoff, T. Schiestel, M. Kilgus, P. Koelsch, and S. Werth. Evaluation of perovskites in hollow fibre and disk geometry in catalytic membrane reactors and in oxygen separators. *Catalysis Today*, 118:128–135, **2006**.

[29] M. Pavone, A.M. Ritzmann, and E.A. Carter. Quantum-mechanics-based design principle for solid oxide fuel cell cathode material. *Energy Environ. Sci.*, 4:4933–4937, **2011**.

[30] W. Zhou, R. Ran, and Z. Shao. Progress in understanding and development of $Ba_{0.5}Sr_{0.5}Co_{0.8}Fe_{0.2}O_{3-\delta}$-based cathodes for intermediate-temperature solid-oxide fuel cell: a review. *J. Power Sources*, 192:231–246, **2009**.

[31] L. Carret, K.A. Friedrich, and U. Stimmig. Fuel cells, fundamentals and applications. *Fuel Cells*, 1:5–39, **2005**.

[32] W. Zhou and Z. Zhu. The instability of solid oxide fuel cells in an intermediate temperature region. *APCChE*, 6:199–203, **2011**.

[33] Z. Shao, G. Xiong, H. Dong, W. Yang, and L. Lin. Synthesis, oxygen permeation study and membrane performance of a $Ba_{0.5}Sr_{0.5}Co_{0.8}Fe_{0.2}O_{3-\delta}$ oxygen-permeable dense ceramic reactor for partial oxiation of methane to syngas. *Sep. Purif. Technol.*, 25:97–116, **2001**.

[34] Z. Shao, W. Yang, Y. Cong, H. Dong, K. Tong, and G. Xiong. Investigation of the permeation behavior and stability of a $Ba_{0.5}Sr_{0.5}Co_{0.8}Fe_{0.2}O_{3-\delta}$ oxygen membrane. *J. Membr. Sci.*, 172:177–188, **2000**.

[35] Z. Shao and S.M. Haile. A high-performance cathode for the next generation of solid-oxide fuel cells. *Nature*, 431:170–173, **2004**.

[36] Z. Shao, S.M. Haile, J. Ahn, P.D. Ronney, Z. Zhan, and S.A. Barnett. A thermally self-sustained micro solid-oxide fuel-cell stack with high power density. *Nature*, 435:795–798, **2005**.

[37] J.-I. Jung and D.D. Edwards. X-ray photoelectron study on $Ba_{0.5}Sr_{0.5}Co_{0.8}Fe_{0.2}O_{3-\delta}$ (BSCF: x=0.2 and 0.8) ceramics annealed at different temperature and po_2. *J. Mater. Sci.*, 46:7415–7422, **2012**.

[38] P. Müller, H. Störmer, L. Dieterle, C. Niedrig, E. Ivers-Tiffée, and D. Gerthsen. Decomposition pathway of cubic $Ba_{0.5}Sr_{0.5}Co_{0.8}Fe_{0.2}O_{3-\delta}$ between 700 $°C$ and 1000 $°C$ analyzed by electron microscopic techniques. *Solid State Ionics*, 206:57–66, **2012**.

[39] F. Liang, H. Jiang, H. Luo, J. Caro, and A. Feldhoff. Phase stability and permeation behavior of a dead-end $Ba_{0.5}Sr_{0.5}Co_{0.8}Fe_{0.2}O_{3-\delta}$ tube membrane in high-purity oxygen production. *Chem. Mater.*, 23:4765–4772, **2011**.

[40] K. Efimov, Q. Xu, and A. Feldhoff. Transmission electron microscopy study of $Ba_{0.5}Sr_{0.5}Co_{0.8}Fe_{0.2}O_{3-\delta}$ perovskite decomposition at intermediate temperatures. *Chem. Mater.*, 22:5866–5875, **2010**.

[41] Z. Yang, J. Martynczuk, K. Efimov, A.S. Harvey, A. Infortuna, P. Kocher, and L.J. Gauckler. Oxygen-vacancy-related structural phase transition of $Ba_{0.8}Sr_{0.2}Co_{0.8}Fe_{0.2}O_{3-\delta}$. *Chem. Mater.*, 23:3169–3175, **2011**.

[42] D.N. Mueller, R.A. De Souza, T.E. Weirich, D. Roehrens, J. Mayer, and M. Martin. A kinetic study of the decomposition of the cubic perovskite-type oxide $Ba_xSr_{1-x}Co_{0.8}Fe_{0.2}O_{3-\delta}$ (BSCF) (x=0.1 and 0.5). *Phys. Chem. Chem. Phys.*, 12:10320–10328, **2010**.

[43] C. Niedrig, S. Taufall, M. Burriel, W. Menesklou, S.F. Wagner, S. Baumann, and E. Ivers-Tiffée. Thermal stability of the cubic phase in $Ba_{0.5}Sr_{0.5}Co_{0.8}Fe_{0.2}O_{3-\delta}$ (BSCF) 1. *Solid State Ionics*, 197:25–31, **2011**.

[44] M.M. Kuklja, Yu.A. Mastrikov, S.N. Rashkeev, and E.A. Kotomin. The structural disorder and lattice stability of (BaSr)(CoFe)O_3 complex perovskites. *ECS Transactions*, 35(1):2077–2084, **2011**.

[45] S. Yakovlev, C.-Y. Yoo, S. Fang, and H.J.M. Bouwmeester. Phase transformation and oxygen equilibration kinetics of pure and Zr-doped

$Ba_{0.5}Sr_{0.5}Co_{0.8}Fe_{0.2}O_{3-\delta}$ perovskite oxide probed by electrical conductivity relaxation. *Appl. Phys. Letters*, 96:254101, **2010**.

[46] X. Meng, N. Yang, B. Meng, X. Tan, Z.-F. Ma, and S. Liu. Zirconium stabilized $Ba_{0.5}Sr_{0.5}(Co_{0.8-x}Zr_x)Fe_{0.2}O_{3-\delta}$ perovskite hollow fiber membranes for oxygen separation. *Ceram. Int.*, 37:2701–2709, **2011**.

[47] J. Ton, W. Yang, B. Zhu, and R. Cai. Investigation of ideal zirconium-doped perovskite-type ceramic membrane materials for oxygen separation. *J. Membr. Sci.*, 203:175–189, **2002**.

[48] J. Martynczuk, F. Liang, M. Arnold, V. Sepelak, and A. Feldhoff. Aluminum-doped perovskites as high-performance oxygen permeation materials. *Chem. Mater.*, 21:1586–1594, **2009**.

[49] A. Demont, R. Sayers, M.A. Tsiamtsouri, S. Romani, P.A. Chater, H. Niu, C. Martí-Gastaldo, Z. Xu, Z. Deng, Y. Bréard, M.F. Thomas, J.B. Claridge, and M.J. Rosseinsky. Single sublattice endotaxial phase separation driven by charge frustration in a complex oxide. *J. Am. Chem. Soc.*, 135:10114–10123, **2013**.

[50] Z. Shao, G. Xiong, J. Tong, H. Dong, and W. Yang. Ba effect in doped $Sr(Co_{0.8}Fe_{0.2})O_{3-\delta}$ on the phase structure and oxygen permeation properties of the dense ceramic membranes. *Sep. Purif. Technol.*, 25:419–429, **2001**.

[51] D. Cebrucean, V. Cebrucean, and I. Ionel. CO_2 capture and storage from fossil fuel power plants. *Energy Procedia*, 63:18–26, **2014**.

[52] M.T. Ho, G.W. Allinson, and D.E. Wiley. Reducing the cost of CO_2 capture from flue gases using membrane technology. *Ind. Eng. Chem. Res.*, 47:1562–1568, **2008**.

[53] M.M. Faruque Hasan, F. Boukouvala, E.L. First, and C.A. Floudas. Nationwide, regional, and statewide CO_2 capture, utilization, and sequestration supply chain network optimization. *Ind. Eng. Chem. Res.*, 53:7489–7506, **2014**.

[54] M.K. Mondal, H.K. Balsora, and P. Varshney. Progress and trends in CO_2 capture/separation technologies: A review. *Energy*, 46:431–441, **2012**.

[55] D.M. D´Alessandro, B. Smit, and J.R. Long. Carbon dioxide capture: prospects for new materials. *Angew. Chem. Int. Ed.*, 49:6058–6082, **2010**.

[56] J.D. Figueroa, T. Fout, S. Plasynski, H. McIlvried, and R.D. Srivastava. Advances in CO_2 capture technology - the U.S. department of energy´s carbon sequestration program. *International Journal of Greenhouse Gas Control*, 2:9–20, **2008**.

[57] H. Stadler, F. Beggel, M. Habermehl, B. Persigehl, R. Kneer, M. Modigell, and P. Jeschke. Oxyfuel coal combustion by efficient integration of oxygen transport membranes. *International Journal of Greenhouse Gas Control*, 5:7–15, **2011**.

[58] M. Arnold, H. Wang, and A. Feldhoff. Influence of CO_2 on the oxygen permeation performance and the microstructure of perovskite-type $(Ba_{0.5}Sr_{0.5})(Co_{0.8}Fe_{0.2})O_{3-\delta}$ membranes. *J. Membr. Sci.*, 293:44–52, **2007**.

[59] K.E. Colombo, V.V. Kharton, A.P. Viskup, A.V. Kovalevsky, A.L. Shaula, and O. Bolland. Simulation of a mixed-conducting membrane-based gas turbine power plant for CO_2 capture: system level analysis of operation stability and individual process unit degradation. *J. Solid State Electrochem.*, 15:329–347, **2011**.

[60] G. S. Gallego, F. Mondragón, J.-M. Tatibouët, J. Barrault, and C. Batiot-Dupeyrat. Carbon dioxide reforming of methane over La_2NiO_4 as catalyst percursor - characterization of carbon deposition. *Catalysis Today*, 133-135:200–209, **2008**.

[61] T. Klande, K. Efimov, S. Cusenza, K.-D. Becker, and A. Feldhoff. Effect of doping, microstructure, and CO_2 on La_2NiO_4-based oxygen-transporting materials. *J. Solid State Chem.*, 184:3310–3318, **2012**.

[62] Y.Y. Wei, J. Tang, L.Y. Zhou, J. Xue, Z. Li, and H.H. Wang. Oxygen separation through U-shaped hollow fiber membrane using pure CO_2 as sweep gas. *AIChE J.*, 58:2856–2864, **2012**.

[63] J. Tang, Y.Y. Wei, L.Y. Zhou, Z. Li, and H.H. Wang. Oxygen permeation through a CO_2-tolerant mixed conducting oxide $(Pr_{0.9}La_{0.1})_2(Ni_{0.74}Cu_{0.21}Ga_{0.05})O_{4+\delta}$. *AIChE J.*, 58:2473–2478, **2012**.

[64] H. Luo, K. Efimov, H. Jiang, A. Feldhoff, and H. Wang. CO_2-stable and cobalt-free dual-phase membrane for oxygen separation. *Angew. Chem. Int. Ed.*, 50:759–763, **2012**.

[65] M. Balaguer, J. García-Fayos, C. Solís, and J.M. Serra. Fast oxygen separation through SO_2- and CO_2-stable dual-phase membrane based on $NiFe_2O_4$-$Ce_{0.8}Tb_{0.2}O_{2-\delta}$. *Chem. Mater.*, 25:4986–4993, **2013**.

[66] G. Rose. *Beschreibung einiger neuen Minerale des Urals, Poggendorff´s Annalen (Annalen der Physik und Chemie).* Verlag Johann Ambrosius Barth, Leipzig, Band 48, **1839**.

[67] G. Rose. *Reise nach dem Ural, dem Altei und dem Kaspischen Meere (Mineralogisch-geognostischer Teil und historischer Bericht der Reise).* Verlag der Sanderschen Buchhandlung (G.E. Reimer), Berlin, **1842**.

[68] R.H. Mitchell. *Perovskites: modern and ancient.* Almaz Press Inc., Ontario, 1 edition, **2002**.

[69] R. Merkle and J. Maier. Wie wird Sauerstoff in Oxid eingebaut? Kinetische Studie einer "simplen" Feststoffreaktion am Modellmaterial $SrTiO_3$. *Angew. Chem.*, 120:3936–3958, **2008**.

[70] P.M. Woodward. Octahedral tilting in perovskites I. Geometrical considerations. *Acta. Cryst. B*, 53:32–43, **1997**.

[71] P.M. Woodward. Octahedral tilting in perovskites II. Structure stabilizing forces. *Acta. Cryst. B*, 53:44–66, **1997**.

[72] F.S. Galasso. *Perovskites and high T_c superconuctors.* Gordon and Beach Sience Pubs., New York, **1990**.

[73] V.M. Goldschmidt. Die Gesetze der Kristallochemie. *Naturwissenschaften*, 14:477–485, **1926**.

[74] R.D. Shannon. Revised effective ionic radii and systematic studies of interatomix distances in halides and chalcogenides. *Acta Cryst.*, A32:751–767, **1976**.

[75] R.I. Hines. Atomistic simulation and ab-initio studies of polar solids. *Dissertation*, Bristol, **1997**.

[76] M. Levy. Crystal structure and defect properties in ceramic materials. *Dissertation*, Imperial College London, **2005**.

[77] C.P. Khattak and F.F.Y. Wang. *Handbook of the physics and chemistry of rare earths*. North-Holland Publisher, Amsterdam, **1979**.

[78] K. Efimov, T. Klande, N. Juditzki, and A. Feldhoff. Ca-containing CO_2-tolerant perovskite materials for oxygen separation. *J. Membr. Sci.*, 389:205–215, **2012**.

[79] M. O´Keefe and B.G. Hyde. Some structures typologically related to cubic perovskite ($E2_1$), $ReO_3(DO_9)$ and $Cu_3Au(L1_2)$. *Acta. Cryst.*, B33:3802–3813, **1977**.

[80] C. Michel, J.M. Moreau, and W.J. James. Structural relationship in compounds with R3c symmetry. *Acta. Cryst.*, B27:501, **1971**.

[81] L. Pauling. The principles determining the structure of complex ionic crystals. *J. Am. Chem. Soc.*, 51:1010–1026, **1929**.

[82] K. Yvon and E. Parthé. On the crystal chemistry of the closed packed transition metal carbides. I. the crystal structure of ζ-V, Nb and Ta carbids. *Acta Cryst.*, B26:149–153, **1970**.

[83] E. Parthé and K. Yvon. On the crystal chemistry of the closed packed transition metal carbides. II. a proposal for the natation of the different crystal structures. *Acta Cryst.*, B26:153–163, **1970**.

[84] P. Müller, H. Störmer, M. Meffert, L. Dieterle, C. Niedrig, S.F. Wagner, E. Ivers-Tiffée, and D. Gerthsen. Secondary phase formation in $Ba_{0.5}Sr_{0.5}Co_{0.8}Fe_{0.2}O_{3-\delta}$ studied by electron microscopy. *Chem. Mater.*, 25:564–573, **2013**.

[85] J. Sun, M. Yang, G. F, T. Yang, F. Liao, Y. Wang, M. Xiong, and J. Lin. New barium conaltite series $Ba_{n+1}Co_nO_{3n+3}(Co_8O_8)$: intergrowth structure containing perovskite and CdI_2-type layers. *Inorg. Chem.*, 45:9151–9153, **2006**.

[86] Rénald David, Alain Pautrat, Houria Kabbour, Mihai Sturza, Sergiu Curelea, Gilles André, Denis Pelloquin, and Oliver Mentré. Thermodynamic data on oxides at elevated temperatures. *Chem. Mater.*, 23:5191–5199, **2011**.

[87] D. Balz and K. Plieth. Die Struktur des Kaliumnickelfluorids, K_2NiF. *Z. Elektrochem.*, 59:545–551, **1955**.

[88] S.N. Ruddlesden and P. Popper. New compounds of the K_2NiF_4 type. *Acta. Cryst.*, 10:538–539, **1957**.

[89] S.N. Ruddlesden and P. Popper. The compound $Sr_3Ti_2O_7$ and its structure. *Acta. Cryst.*, 11:54–55, **1958**.

[90] C.N.R. Rao. Intergrowth structures in inorganic solids: A new class of materials. *Bull. Mater. Sci.*, 7:155–178, **1985**.

[91] A.N. Petrov, V.A. Cherepanov, A.Yu. Zuyev, and V.M. Zhukovsky. Intergrowth structures in inorganic solids: A new class of materials. *J. Solid State Chem.*, 77:1–14, **1988**.

[92] M. Zinkevich and A. Aldinger. Thermodynamic analysis of the ternary La-Ni-O system. *J. Alloy Compounds*, 375:147–161, **2004**.

[93] M. Zinkevich, N. Solak, H. Nitsche, and M. Ahrens andA. Aldinger. Stability and thermodynamic functions of lanthanum nickelates. *J. Alloy Compounds*, 438:92–99, **2007**.

[94] Z. Zhang and M. Greenblatt. Synthesis structure and properties of $Ln_4Ni_3O_{10-\delta}$ (Ln=La, Pr, Nd). *J. Solid State Chem.*, 177:236–246, **1995**.

[95] D.E. Rice and F.J. Buttrey. An X-ray diffraction study on the oxygen content phase diagram of $La_2NiO_{4+\delta}$. *J. Solid State Chem.*, 105:197–210, **1993**.

[96] D.J. Buttrey, P. Ganguly, J.M. Honig, C.N.R. Rao, and R.R. Schartman. Oxygen excess in layered lanthanide nickelates. *J. Solid State Chem.*, 74:233–238, **1988**.

[97] N. Nguyen, J. Choisnet, M. Hervieu, and B. Raveau. Oxygen defect K_2NiF_4-type oxides: the compounds $La_{2-x}Sr_xCuO_{4-x/2+\delta}$. *J. Solid State Chem.*, 39:120–127, **1981**.

[98] J.D. Jorgensen, B. Dabrowski, Shiyou Pei, D.R. Richards, and D.G. Hinks. Structure of the interstitial defects in $La_2NiO_{4+\delta}$. *Phys. Rev. B*, 40:2187–2199, **1989**.

[99] M.T. Fernández-Díaz, J.L. Martínez, and J. Rodríguez-Carvajal. High-temperature phase transformation of oxidized $R_2NiO_{4+\delta}$ (R=La, Pr and Nd) under vacuum. *J. Solid State Ionics*, 63-65:902–906, **1993**.

[100] J. Rodríguez-Carvajal, M.T. Fernández-Díaz, and J.L. Martínez. Neutron diffraction study on structural and magnetic properties of $La_2NiO_{4+\delta}$. *J. Phys. Condens. Mater.*, 3:3205–3234, **1991**.

[101] V. Faucheux, S. Pignard, and M. Audier. Structural study of lanthanum nickelate thin films deposited on different single crystal substrates. *J. Solid State Chem.*, 177:4616–4625, **2004**.

[102] M. Hücker, K. Chung, M. Chand, T. Vogt, J.M. Traquada, and F.J. Buttrey. Oxygen and strontium codoping of La_2NiO_4 : room-temperature phase diagrams. *Phys. Rev. B*, 70:0641051–0641069, **2004**.

[103] Z. Hiroi, T. Obata, M. Takano, and Y. Bando. Ordering of interstitial oxygen atoms in $La_2NiO_{4+\delta}$ observed by transmission electron microscopy. *Phys. Rev. B*, 41:11665–11668, **1990**.

[104] J.M. Tranquada, Y. Kong, J.E. Lorenzo, D.J. Butterey, D.E. Rice, and V. Sachan. Oxygen intercalation, stage ordering, and phase separation in $La_2NiO_{4+\delta}$ with $0.05 \leq \delta \leq 0.11$. *Phys. Rev. B*, 50:6340–6351, **1994**.

[105] S.J. Skinner. Characterisation of $La_2NiO_{4+\delta}$ using in-situ high temperature neutron powder diffraction. *J. Solid State Ionics*, 5:419–426, **2003**.

[106] P. Odier, Y. Nigara, and J. Coutures. Phase relations in in the La-Ni-O system: Influence of temperature and stoichiometry on the structure of $La_2NiO_{4+\delta}$. *J. Solid state Chem.*, 56:32–40, **1985**.

[107] P. Kofstad. Defects and transport properties of metal oxides. *Oxidation of Metals*, 44:3–27, **1995**.

[108] L. Smart and E. Moore. *Einführung in die Festkörperchemie.* Vieweg, Braunschweig, 1 edition, **1997**.

[109] J. Maier. *Festkörper - Fehler und Funktionen.* B.G. Teubner, Stuttgart - Leipzig, 1 edition, **2000**.

[110] J.F. McIntosh, W.G. Haje, D.H.A. Blank, and H.J.M Bouwmeester. Oxygen stoichiometry and chemical expansion of $Ba_{0.5}Sr_{0.5}Co_{0.8}Fe_{0.2}O_{3-\delta}$ measured by in situ neutron diffraction. *Chem. Mater.*, 18:2187, **2006**.

[111] F.A. Kröger and H.J. Vink. Relations between the concentrations of imperfections in crystalline solids. *Adv. Res. Appl.*, 3:307–435, **1956**.

[112] S. Hebert, D. Flahaut, C. Martin, S. Lemonnier, J. Noudem, C. Goupil, A. Maignan, and J. Hejtmanek. Thermoelectric properties of perovskites: Sign change of the Seebeck coefficient and high temperature properties. *Progress in Solid State Chem.*, 35:457–467, **2007**.

[113] R.L. Cook and A.F. Sammells. On the systematic selection of perovskite solid electrolytes for intermediate temperature fuel cells. *Solid State Ionics*, 45:311–321, **1991**.

[114] Z. Shao, G. Xiong, Y. Cong, and W. Yang. Synthesis and oxygen permeation study of novel perovskite-type $BaBi_xCo_{0.2}Fe_{0.8-x}O_{3-\delta}$. *J. Membr. Sci.*, 164:167–176, **2000**.

[115] D.P. Karim and A.T. Aldred. Localized level hoping transport in $La(Sr)CrO_3$. *Phys. Rev. B*, 20:2255–2263, **1979**.

[116] M.S. Islam. Computer modeling of defects and transport in perovskite oxides. *J. Solid State Ionics*, 154-155:75–85, **2002**.

[117] A.F. Sammells, R.L. Cook, J.H.White, J.J. Osborne, and R.C. MacDuff. Rational selection of advanced solid electrolytes for intermediate temperature cells. *Solid State Ionics*, 45:311–321, **1992**.

[118] M. Cherry, M.S. Islam, and C.R.A. Catlow. Oxygen ion migration in perovksite-type oxides. *J. Solid State Chem.*, 118:125–132, **1995**.

[119] M.S. Islam, M. Cherry, and C.R.A. Catlow. Oxygen diffusion in $LaMnO_3$ and $LaCoO_3$ perovskite-type oxides: a molecular dynamics study. *J. Solid State Chem.*, 124:230–237, **1996**.

[120] M. Yashima and T. Tsuji. Structural investigation of the cubic perovskite-type doped lanthanum cobaltite $La_{0.6}Sr_{0.4}CoO_{3-\delta}$ at 1531K: possible diffusion path of oxygen ions an an electrode material. *J. Appl. Cryst.*, 40:1166–1168, **2007**.

[121] R. Ali, M. Yashima, and F. Izumi. Diffusion path of oxide ions in an oxide ion conductor $La_{0.64}Sr_{0.4}Ti_{0.92}Nb_{0.08}O_{2.99}$ with a double perovskite-type structure. *Chem. Mater.*, 19:3260–3264, **2007**.

[122] A.R. Cleave, J.A. Kilner, S.J. Skinner, S.T. Murphy, and R.W. Grimes. Atomistic computer simulation of oxygen ion conduction mechanisms in $La_2NiO_{4+\delta}$. *J. Solid State Ionics*, 179:823–826, **2008**.

[123] L. Minervini, R.W. Grimes, J.A. Killner, and K. E. Sickafus. Oxygen migration in $La_2NiO_{4+\delta}$. *J. Mater. Chem.*, 10:2349–2354, **2000**.

[124] V.V. Kharton, A.P. Viskup, A.V. Kovalevsky, E.N. Naumovich, and F.M.B. Marques. Ionic transport in oxygen-hyperstiochiometric phase with K_2NiF_4-type structure. *Solid State Ionics*, 143:337–353, **2001**.

[125] C. Frayret, A. Villesuzanne, and M. Pouchard. Application of density functional theory to the modeling of the mixed ionic and electronic conductor $La_2NiO_{4+\delta}$: Lattice relaxation, oxygen mobility, and energetics of Frenkel defects. *J. Chem. Mater.*, 17:6538–6544, **2005**.

[126] A. Chroneos, D. Parfitt, J.A. Kilner, and R.W. Grimes. Anisotropic oxygen diffusion in tetragonal $La_2NiO_{4+\delta}$: molecular dynamics calculations. *J. Mater. Sci.*, 20:266–270, **2010**.

[127] E.N. Naumovich and V.V. Kharton. Atomic-scale insight into the oxygen ionic transport mechanism in La_2NiO_4-based materials. *J. Molecular Structure: THEOCHEM*, 946:57–64, **2010**.

[128] A. Kushima, D. Parfitt adn A. Chroneos, B. Yildiz, J.A. Kilner, and R.W. Grimes. Interstialcy diffusion of oxygen in tetragonal $La_2CoO_{4+\delta}$. *Phys. Chem. Chem. Phys.*, 13:2242–2249, **2011**.

[129] C. Tealdi, C. Ferrara, P. Mustarelli, and M.S. Islam. Vacancy and interstitial oxide ion migration in heavily doped $La_{2-x}Sr_xNiO_{4\pm\delta}$. *J. Mater. Chem.*, 22:8969–8975, **2012**.

[130] M. Lankhorst, H.J.M. Bouwmeester, and H. Verweij. Thermodynamics and transport of ionic and electronic defects in crystalline oxides. *J. Am. Ceram. Soc.*, 80:2175–2198, **1997**.

[131] Q.L. Liu, K.A. Khor, and S.H. Chan. High-performance low-temperature solid oxide fuel cell with novel BSCF cathode. *J. Power Sources*, 162:123–128, **2006**.

[132] C. Wagner. Beitrag zur Theorie des Anlaufvorgangs. *Z. Phys. Chem.*, B21:35, **1933**.

[133] C. Wagner. Beitrag zur Theorie des Anlaufvorgangs 2. *Z. Phys. Chem.*, B32:447, **1936**.

[134] C. Wagner. Equations for transport in solid oxides and sulfides of transition metals. *Prog. Solid State Chem.*, 10:3–16, **1975**.

[135] H.J.M. Bouwmeester, H. Kruidhof, and A.J. Burggraf. Importance of the surface exchange kinetics as rate limiting step in oxygen permeation through mixed-conducting oxides. *Solid State Ionics*, 72:185–194, **1994**.

[136] P. Cousin and R.A. Ross. Preparation of mixed oxides: a review. *Mater. Sci. Eng. A*, 130:119–1125, **1990**.

[137] Y.Y. Wei, H.F. Liu, J. Xue, Z. Li, and H.H. Wang. Preparation and oxygen permeation of U-shaped perovskite hollow fiber membranes. *J. AIChE*, 57:975–984, **2011**.

[138] J. Martynczuk, M. Arnold, J. Caro, H.H. Wang, and A. Feldhoff. How $(Ba_{0.5}Sr_{0.5})(Fe_{0.8}Zn_{0.2}O_{3-\delta})$ and $(Ba_{0.5}Sr_{0.5})(Co_{0.8}Fe_{0.2}O_{3-\delta})$ perovksites form via an EDTA/citric acid complexing method. *Adv. Mater.*, 19:2134–2140, **2007**.

[139] K. Efimov, M. Arnold, J. Martynczuk, and A. Feldhoff. Crystalline intermediate phase in the sol-gel-based synthesis of $La_2NiO_{4+\delta}$. *J. Am. Ceram. Soc.*, 92:876–880, **2009**.

[140] A. Feldhoff, J. Martynczuk, and H.H. Wang. Advanced $Ba_{0.5}Sr_{0.5}Fe_{0.8}Zn_{0.2}O_{3-\delta}$ perovskite-type ceramics as oxygen selective membrane: Evaluation of the synthetic process. *Progress Solid State Chem.*, 35:339–353, **2007**.

[141] A. Feldhoff, M. Arnold, J. Martynczuk, T.M. Gesing, and H.H. Wang. The sol-gel synthesis of perovskites by EDTA/citrate complesing method involves nanoscale solid state reactions. *Solid State Sci.*, 10:689–701, **2008**.

[142] B.L. Cushing, V.L. Kolesnichenko, and C.J. O´Connor. Resent advences in the liquid-phase syntheses of inorganic nanoparticles. *Chem. Rev.*, 104:2893–3946, **2004**.

[143] L.G. Tejuca, J.L. Fierro, and M.D. Tascon. Structure and reactivity of perovskite-type oxides. *Advances Catal.*, 36:237–328, **1989**.

[144] Y.G. Metlin and Y.D. Tretyakiv. Chemical routes for preparation of oxide high-temperature superconducting powders and precursors for superconductive ceramics, coating and composites. *J. Mater. Chem.*, 4:1659–1665, **1994**.

[145] M.N. Rahaman. *Ceramic processing and sintering.* CRC-Press Taylor and Francis Group, Boca Raton, 2 edition, **2003**.

[146] S. Scholze. *Keramik.* Springer, Berlin/Heidelberg, 7 edition, **2007**.

[147] O. Guillon, J. Gonzalez-Julian, B. Dargatz, T. Kessel, G. Schierning, J. Räthel, and M. Herrmann. Field-assisted sintering technology/spark plasma sintering: mechnism, materials, and technology developments. *Adv. Eng. Mater.*, 16:830–849, **2014**.

[148] R. Raj, M. Cologne, and J.S. Francis. Influence of externally imposed and internally generated electrical fields on grain growth, diffusion creep, sintering and related phenomena in ceramics. *J. Am. Ceram. Soc.*, 94:1941–1965, **2011**.

[149] S. Gosh, A.H. Chokshi, P. Lee, and R. Raj. A high effect of weak dc electrical fields on grain growth in zirconia. *J. Am. Ceram. Soc.*, 92:1856–1859, **2009**.

[150] H. Yokokawa, N. Sakai, T. Kawada, and M. Dokiya. Thermodynamic stabilities of perovskite oxides for electrodes and other electrochemical materials. *Solid State Ionics*, 52:43–56, **1992**.

[151] T. Katsura, T. Sekine, K. Kitayama, T. Sugihara, and T. Kimizuka. Thermodynamic properties of Fe-Lanthanoid-O compounds at high temperatures. *J. Solid State Chem.*, 23:43–57, **1978**.

[152] S. Stølen, E. Bakken, and C.E. Mohn. Oxygen-deficient perovskites: linking structure, energetics and ion transport. *Phys. Chem. Chem. Phys.*, 8:429–447, **2006**.

[153] S. Stølen and T. Grande. *Chemical Thermodynamics of materials: macroscopic and microscopic aspects.* John Wiley and Sons, Chichester, **2003**.

[154] A.F. Holleman and N. Wiberg. *Lehrbuch der anorganischen Chemie.* Walter de Gruyter, Berlin, New York, 102 edition, **2007**.

[155] F. Calle-Vallejo, J.I. Martínez, J.M. García-Lastra, M. Morgensen, and J. Rossmeisl. Trends in stability of perovskite oxides. *Angew. Chem.*, 122:7865–7867, **2010**.

[156] I. Barin, F. Sauert, and G. Platzki. *Thermochemical Data of Pure Substances.* Wiley-VCH, Weinheim, 3 edition, **1995**.

[157] K.H. Stern. *High temperature properties and thermal decomposition of inorganic salts with oxyanions.* CRC Press, Boca Raton, **2001**.

[158] R. Sharma, H. Hinode, and L. Eyring. A study of praseodymium hydroxycarbonate and praseodymium carbonatehydrate. *J. Solid State Chem.*, 92:401–419, **1991**.

[159] L.G. Tejuca, A.T. Bell, J.L.G. Fierro, and M.A. Pẽna. Surface behaviour of reduced $LaCoO_3$ as studied by TPD of CO, CO_2 and H_2 probes and by XPS. *Appl. Surface Sci.*, 31:301–316, **1988**.

[160] L.G. Tejuca and J.L.G. Fierro. XPS and TPD probe techniques for study of $LaNiO_3$ perovksite oxide. *Thermochimica Acta*, 147:361–375, **1989**.

[161] L.G. Tejuca, A.T. Bel, and V.C. Corberan. TPD and IR spectroscopy of probe techniques for study of CO, CO_2 and H_2 adsorption on $LaCrO_3$ perovksite oxide. *Appl. Surface Sci.*, 37:353–366, **1989**.

[162] H. Schmalzried. Demixing, decomposition and degradation of oxides in chemical potential gradient. *J. Chem. Soc. Faraday Trans.*, 86:1273–1280, **1990**.

[163] M. Martin. Materials in thermodynamic potential gradients. *J. Chem. Thermodynamic*, 35:1291–1308, **2003**.

[164] M. Martin. Electrotransport and demixing in oxides. *Solid State Ionics*, 136-137:331–337, **2000**.

[165] L. Rørmark, S. Stølen, K. Wiik, and T. Grande. Enthalpies of formation of $La_{1-x}A_xMnO_{3\pm\delta}$ (A=Ca and Sr) measured by high-temperature solution calorimetry. *J. Solid State Chem.*, 163:186–193, **2002**.

List of Figures

2 Chemical stability of oxide ceramics

2.1 Summary

This chapter approaches the chemical stability of perovskites and perovskite-related compounds, in particular the structure and phase stability in carbon dioxide environment. Based on thermodynamic considerations and referred to perovskite stabilization energies and the polarization power of a metal cation, the stability range of the tolerance to carbon dioxide is investigated.

The microstructure investigation and the way of carbonate formation in LSCF perovskites is promoted in section 2.2. The SEM and TEM analysis confirm the strong tendency of materials with high strontium content to form metal carbonates at the experimental conditions. Nevertheless, LSCF6482 is found to be a carbon dioxide stable material. Even after 200 h exposure to carbon dioxide at 1173 K no phase degradation and no metal carbonates are observed.

Section 2.3 describes the effect of partial subsitution of strontium by lanthanum in perovskite series $La_{1-x}Sr_xCo_{0.8}Fe_{0.2}O_{3-\delta}$ with x=1, 0.8, 0.6, 0.4 (LSCF). At room temperature all materials, despite the rhombohedral LSCF6482, exhibit cubic perovskite strucure. However, phase transition to cubic perovskite at elevated temperatures is observed for LSCF6482 by in-situ XRD. Although the carbon dioxide stability increases with increasing lanthanum content, the oxygen permeation flux decreases considerably.

Section 2.4 deals with the chemical stability of alkaline-earth free Ruddlesden-Popper phase $(Pr_{0.9}La_{0.1})_2(Ni_{0.74}Cu_{0.21}Ga_{0.05})O_{4+\delta}$ in presence of CO_2 and SO_2. In situ XRD experiments in oxidizing and reducing atmospheres show excellent chemical stability of material, as well as very high carbon dioxide tolerance. The chemical stability in sulfur dioxideis atmosphere is whereas not sufficiently. $Pr_2O_2SO_4$, $La_2O_2SO_4$ and NiO_2 are formed after SO_2 treatment and the material developed some porosity on the side exposed to SO_2.

2.2 Investigation of carbonates in oxygen-transporting membrane ceramics

---

Reprinted with kind permission from Elsevier:
Olga Ravkina, Tobias Klande and Armin Feldhoff
Journal of Membrane Science **480** (2015) 31-38.
doi:10.1016/j.memsci.2015.01.042

Journal of Membrane Science 480 (2015) 31–38

Contents lists available at ScienceDirect

Journal of Membrane Science

journal homepage: www.elsevier.com/locate/memsci

Investigation of carbonates in oxygen-transporting membrane ceramics

Olga Ravkina*, Tobias Klande, Armin Feldhoff

Institute of Physical Chemistry and Electrochemistry, Leibniz Universität Hannover, Callinstraße 3A, D-30167 Hannover, Germany

ARTICLE INFO

Article history:
Received 14 September 2014
Received in revised form
13 January 2015
Accepted 22 January 2015
Available online 2 February 2015

Keywords:
Oxygen-transporting membrane
Carbonate formation
Long-term oxygen permeation
Transmission electron microscopy
Electron-energy loss spectroscopy

ABSTRACT

The performance of perovskite-type oxygen-transporting membranes during CO_2 sweeping has been investigated. The series of $La_{1-x}Sr_xCo_{0.8}Fe_{0.2}O_{3-\delta}$ (LSCF) materials with $x=1$, 0.8, 0.6 and 0.4 (SCF, LSCF2882, LSCF4682, LSCF6482) were synthesized by the sol–gel method and characterized by X-ray diffraction (XRD). To investigate the poisoning effect of CO_2 on the phase composition and microstructure of the membranes after long-term oxygen permeation experiments (more than 200 h) at 1173 K under a CO_2 atmosphere, transmission electron microscopy (TEM) investigations were carried out. Electron-energy loss spectroscopy (EELS) and energy-dispersive X-ray spectroscopy (EDXS) revealed the formation of carbonate at the outer surface of the LSCF materials with low lanthanum content, which correlates with a decrease in oxygen permeation flux. Nevertheless, the LSCF 6482 material is tolerant to CO_2 gas. No carbonate layer was found after 200 h of operation, and the oxygen flux remained stable.

1. Introduction

Dense ceramic membranes made of mixed oxygen–ionic and electronic conducting (MIEC) materials can pave the way for energy conversion technologies such as solid oxide fuel cells and “clean-coal” oxy-fuel combustion with less environmental pollution than alternative approaches [1–3]. Using an oxygen-transporting membrane with absolute selectivity for oxygen enables not only lower costs, but also reduced production of climate-damaging carbon dioxide [4–6].

These applications require membrane materials, that are chemically and thermally stable against atmospheric carbon dioxide at working conditions. The formation of low amounts of carbonates or layers on membrane surfaces may be avoided by properly selecting the materials. High-performance materials with respect to total oxygen flux are based on ABO_3 cubic perovskite-type oxides containing the alkaline-earth elements barium and strontium on the A-site, such as $Ba_{0.5}Sr_{0.5}Co_{0.8}Fe_{0.2}O_{3-\delta}$ [7]. However, these elements tend to form carbonates under carbon dioxide atmosphere [8–10]. Alternative materials without barium and strontium offer better stability at the cost of lower oxygen flux. Nevertheless, alkaline-earth free membranes, such as dual-phase materials or Ruddlesden Popper materials, have been reported to be tolerant to CO_2 [11–17].

There are several factors that can influence carbonate formation. From the thermodynamic point of view, alkaline-earth metals tend to form stable carbonates with decomposition temperatures below 1373 K at 1 bar of ambient pressure. The Ellingham diagram clearly demonstrates the stability of carbonates as a function of the chemical potential of carbon dioxide [13,17]. Therefore, it is favorable to use metals that form unstable carbonates at a given pressure and temperature, because the CO_2 chemical potential of the decomposition reaction exceeds that at the corresponding partial pressure. Lanthanum oxycarbonate decomposes at 1173 K and 1 bar $p(CO_2)$ and is a good alternative to alkaline-earth metals [18]. Another important factor is the polarizing power of the metal cation [18–20]. The cation polarizing power (PP) for carbonates is defined as $PP=r^{0.5}/Z$, where r is the root of the ionic radius and Z is the ionic charge [18]. The polarization of the carbonate anion structure leads to the distortion and weakening of the intra-ionic oxygen–carbon bonds. The thermal stability of the carbonate anion decreases with increasing polarizing power of the cation due to the small cationic size and high charge. As a result, the smaller and more highly charged La^{3+} ($r=136$ pm) forms less stable carbonates as compared to Sr^{2+} ($r=144$ pm) [21]. Considering these aspects, one approach might be to dope lanthanum, a less reactive element, at the alkaline-earth A crystal site of perovskite.

LSCF was reported to be a CO_2 tolerant material. Tan et al. [22] demonstrated a LSCF hollow fiber membrane that showed stable flux for over 100 h using pure CO_2 as a sweep gas. Although they found some 1.4 μm of erosion on the sweep side of the fiber, the structure of the material remained in a good condition. Moreover, LSCF was tested in an oxide-carbonate dual-phase membrane for carbon dioxide separation by Norton et al. [23]. In the presence of

---

* Corresponding author: Tel.: +49 511 763 4896; fax: +49 511 763 19121.
E-mail address: olga.ravkina@pci.uni-hannover.de (O. Ravkina).

http://dx.doi.org/10.1016/j.memsci.2015.01.042
0376-7388/

oxygen, the carbonate reaction with the LSCF was inhibited and stable CO_2 flux at temperatures of 1123–1223 K was achieved.

As we have recently reported, in the perovskite $SrCo_{0.8}Fe_{0.2}O_{3-\delta}$ (SCF), strontium was partially substituted by lanthanum to yield $La_{1-x}Sr_xCo0_{.8}Fe_{0.2}O_{3-\delta}$ (LSCF) with x down to 0.4. The effect of A-site doping on the CO_2 tolerance of the materials was investigated [24]. It has been shown that using pure CO_2 as the sweep gas causes a halt in oxygen permeation flux after 30 h of operation for SCF, after 200 h for LSCF 2882 and after 60 h for LSCF 4682. The lanthanum-rich LSCF 6482 membrane achieved a stable oxygen flux for the investigated period of over 200 h. Furthermore, a decrease in oxygen permeation flux with increasing lanthanum content was established. Nevertheless, a more detailed investigation of the CO_2 poisoning mechanism and microstructure changes for the LSCF series is required. In this study, we extend our previous work [24] and report a more detailed study of these compositions with respect to long-term oxygen permeation under carbon dioxide atmospheres. The results were correlated with the microstructure using transmission and scanning electron microscopy techniques.

2. Experimental

2.1. Sample preparation

Powders were synthesized via a combined citrate and EDTA complexing method using stoichiometric amounts of $La(NO_3)_3$, $Sr(NO_3)_2$, $Co(NO_3)_2$ and $Fe(NO_3)_3$. The reaction mixture was then heated under constant stirring to obtain a purple-colored gel. The resulting gel was subsequently pre-calcined in ambient air at 773 K. After thorough grinding, the pre-calcined powder was finally calcined for 10 h at 1273 K in ambient air to obtain the pure perovskite phase. Green bodies of the membranes were obtained by uniaxial compression of the powders at 150 MPa for 30 min. After sintering at 1473 K for SCF, 1523 K for LSCF 2882 and 1573 K for LSCF 4682 and LSCF 6482 in ambient air for 10 h, 1 mm thick perovskite ceramic membranes were obtained. Heating and cooling rates of 2 K min^{-1} were used.

The crystal structure of each powder and membrane was analyzed by X-ray diffraction (XRD) using a Bruker-AXS D8 Advance diffractometer with Cu K_α radiation as shown by Klande et al. [24].

2.2. Oxygen permeation

The oxygen permeation experiments were carried out on a home-made high-temperature permeation cell, which has been described elsewhere [25,26]. Before measurement, both sides of the membranes were carefully polished with 800 mesh emery paper to obtain a uniform surface. Discs were then sealed into a ceramic tube with gold paste (conducting paste, Heraeus) at 1223 K for 10 h. After sealing, gas flow rates were delivered to the reactor by mass flow controllers (Bronckhorst). The feed side of the membrane was fed with synthetic air (20 vol% O_2/80 vol% N_2) at a rate of 150 mL min^{-1}. The sweep side was flushed with He (29 mL min^{-1}, 99.995%) or with CO_2 (29 mL min^{-1}, 99.995%). An online-coupled Agilent 7890 gas chromatograph with a Carboxen 1000 column was employed to analyze the gas mixture. The absolute flow rates of the effluents were calculated using neon (1 mL min^{-1}, 99.995%) as an internal standardization. By measuring the N_2 concentration, the total O_2 leakage was calculated and subtracted from the total oxygen flux.

2.3. Scanning electron microscopy

Scanning electron microscopy (SEM) studies were carried out on a JEOL JSM-6700F field-emission scanning electron microscope using a secondary electron detector at an accelerating voltage of 2 kV. For backscattered-electron channeling contrast imaging at a higher excitation voltage (15 kV), the membrane was vibration-polished using a Buehler VibroMet 2 vibratory polisher to preserve the crystallinity to the very surface.

2.4. Transmission electron microscopy

To analyze the microstructure of the membrane after the oxygen permeation experiments, transmission electron microscopy (TEM) was conducted at 200 kV with a JEOL JEM-2100F-UHR field-emission instrument, which was equipped with a Gatan GIF 2001 energy filter and a charge-coupled device (CCD) camera in order to obtain energy energy-loss (EEL) spectra. The microscope was operated in bright-field mode, and a scanning TEM (STEM) was used in a high-angle annular dark-field (HAADF). An energy-dispersive X-ray spectrometer (EDXS), Oxford Instruments INCA-300, with an ultra-thin window was used for elemental analysis at an excitation voltage of 200 kV.

Specimens for TEM investigations were prepared by covering the sweep side with a silicon single crystal using epoxy. The protected membrane pieces were than polished with polymer-embedded diamond lapping films down to 0.015 mm thickness. After the specimens were supported on a copper slot grid the electron transparency was achieved by argon ion sputtering at 3 kV with incident angles of 6° (Gatan, model 691 PIPS).

3. Results and discussion

3.1. Surface state after oxygen permeation with CO_2 sweep gas

Fig. 1 shows the polished SCF, LSCF 2882 and LSCF 4682 membrane cross-sections after the long-term oxygen permeation experiment with CO_2 as a sweep gas. As reported by Klande et al. [24], the oxygen flux of the SCF membrane declines after 30 h in carbon dioxide atmosphere. The reason for this observation is demonstrated in

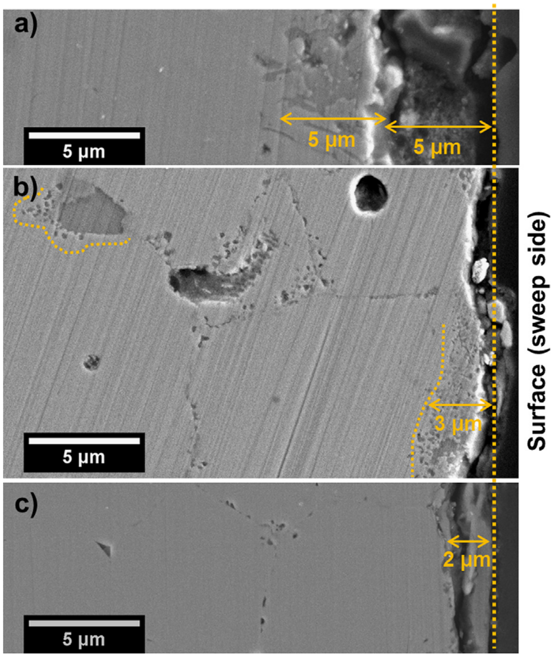

Fig. 1. SEM of the polished cross-section after long-term oxygen permeation measurement. The CO_2 sweep side is marked with a straight dotted line. (a) SCF membrane after 30 h. (b) LSCF 2882 after 200 h. (c) LSCF 4682 after 60 h.

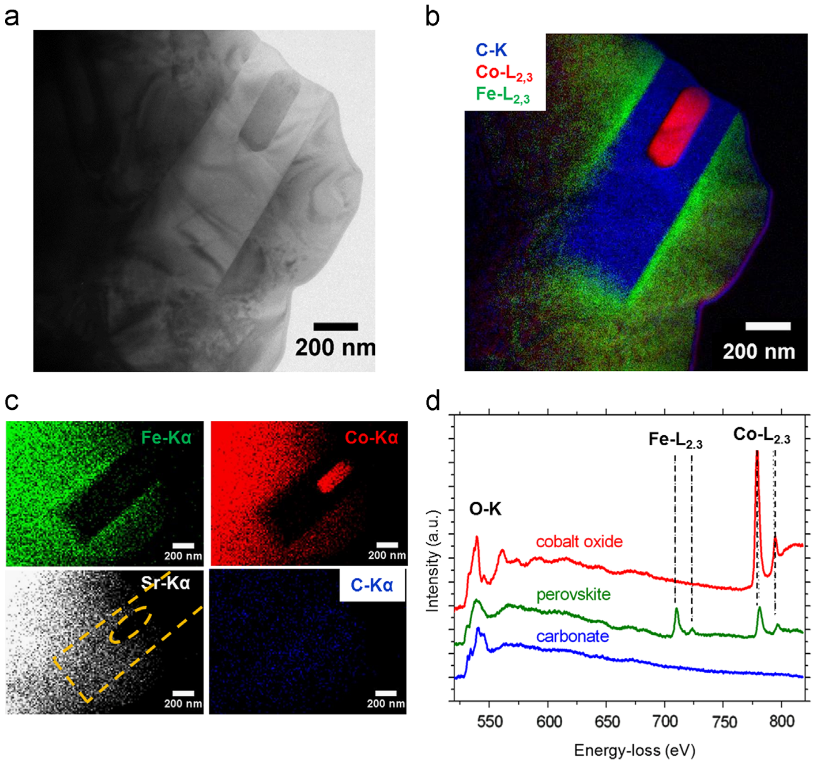

Fig. 2. CO_2-exposed sweep side of the SCF membrane after 30 h experiment. (a) STEM and (b) EFTEM of a sweep side surface. (c) EDXS mapping of the specimen. The border of $SrCO_3$ is labeled with an orange dashed line. (d) EELS spectrum in the energy-loss range from 450 to 850 eV of the perovskite, cobalt oxide and strontium carbonate. (For interpretation of references to color in this figure, the reader is referred to the web version of this article.)

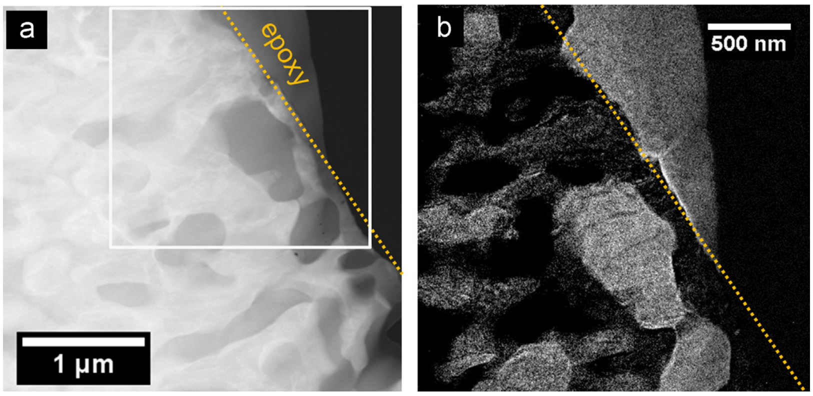

Fig. 3. CO_2-exposed sweep side of the LSCF 2882 membrane after 200 h experiment. The border of the epoxy adhesive is labeled with an orange line. (a) STEM high-angle annular dark-field and (b) carbon distribution by EFTEM.

Fig. 1a. Some changes in the material microstructure and composition on the sweep side surface can be observed. This transformation imparts 10 μm thick layer of which a 5 μm thick layer below the membrane surface appears to have a porous structure, suggesting the complete decomposition of the SCF material in this region. Below this porous structure, a 5 μm dense layer is formed. These results are in agreement with the SEM/EDXS results published by Klande et al. [24] concerning the SCF membrane surface after using CO_2 as a sweeping gas for 24 h. It was shown that a change in composition of the surface material compared to the bulk took place, and that the top layer was depleted of cobalt and iron. Analysis of the fractured surface revealed a 25 μm carbon-rich layer close to the sweep side [24]. Investigation of the polished SCF membrane cross-section enables an accurate estimation of the decomposition layer thickness, which explains the deviation in the carbonate layer thickness. The detailed TEM examination of the formed layer is given in Section 3.2.

The depth profiles of LSCF 2882 and LSCF 4682 are shown in Fig. 1b and c. In comparison to SCF the sweep side surface changes are less pronounced. However, 3 μm and 2 μm thick surface layers formed for LSCF 2882 and LSCF 6482, respectively. Additionally, a new phase formed at the grain boundaries, and inclusions are present at 20–25 μm of depth. The decrease in the dense outer layer correlates with the increasing oxygen permeation flux in carbonate atmosphere for La-doped SCF as reported by Klande et al. [24].

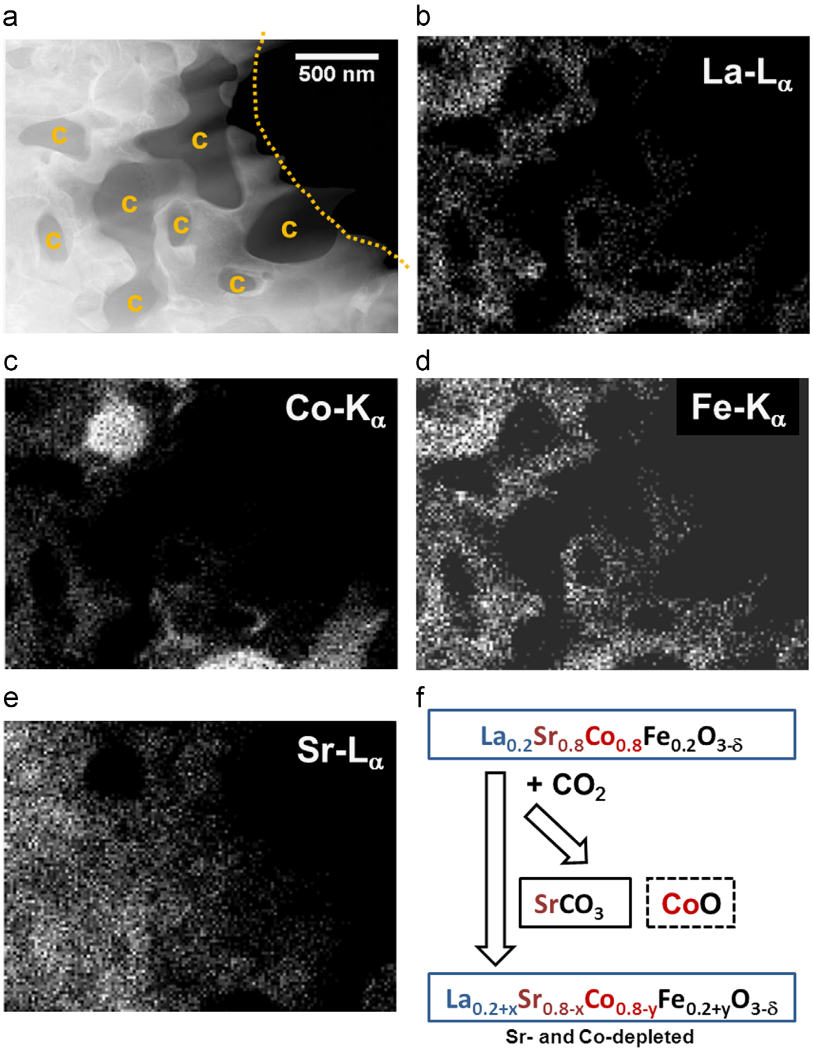

Fig. 4. CO_2-exposed sweep side of the LSCF 2882 membrane after 200 h of the oxygen-permeation experiment. The border of epoxy adhesive is labeled with an orange line and carbonate is marked by orange letter "c". (a) STEM high-angle annular dark-field and EDXS elemental maps. (b) Scheme of LSCF 2882 decomposition after exposure to CO_2 atmosphere. (For interpretation of references to color in this figure legend, the reader is referred to the web version of this article.)

Furthermore, the decrease in the grain size with increasing La content confers an enlargement of the surface and could promote the formation of the grain boundary-phase. Similar observations have been made by Arnold et al. [8], who investigated BSCF membranes after CO_2 exposure. They also detected a dense carbonate layer on the membrane surface, when carbon dioxide was used. However, the layer thickness for BSCF was 40–50 μm after 72 h of oxygen permeation experiment. By avoiding the large Ba^{2+} ion (161 pm [21]), which tends to form stable carbonates and has high carbonate decomposition enthalpy in the LSCF-system, more CO_2 tolerant materials can be compounded [18,21]. The polished LSCF 6482 specimen displayed no dense layer on the surface. Therefore, the cross-section of the LSCF 6482 was vibration-polished to achieve a better resolution. The investigation of LSCF 6482 is described in Section 3.3.

3.2. *TEM investigation after operation in CO_2*

For the detailed TEM investigation, the SCF and LSCF 2882 materials were chosen after the oxygen permeation experiments with CO_2 as the sweep gas. The oxygen permeation flux of SCF stopped after 30 h of CO_2 exposure. Fig. 2a shows the STEM annular dark-field micrograph of the cross-section near the sweep side. Regions with different phase composition can be seen in the presented grain. To obtain more information about the phase composition, EELS and energy-filtered TEM (EFTEM) were conducted. These methods are suitable for the analysis of carbon, because there is no dependence on the fluorescence yield as there is in EDXS. In addition, different phases can be distinguished by the specific fine structure. The results are shown in Fig. 2b and d. The EELS spectrum in Fig. 2d is shown in the energy-loss range of 480–850 eV. The perovskite phase (green) exhibits edge of Fe-$L_{2,3}$ (710 and 723 eV [25]), Co-$L_{2,3}$ (782 and 796 eV) and O-K. Moreover, CoO (red) is also present and shows Co-$L_{2,3}$ fine structures. The last identifiable phase is the strontium carbonate phase (blue), which exhibits only the O-K edge in the shown energy-loss range. The fine structure of O-K ELNES is in accordance with the literature about $SrCO_3$ [24,28]. Fig. 2b represents the corresponding EFTEM map of CoO (red) inclusion, surrounded with carbon-rich phase (blue) and perovskite phase (green).

The EDXS analysis completes the phase investigation. Fig. 2c shows the elemental distribution in the material. In the perovskite phase, no segregation can be seen, and all the elements (Co, Fe and Sr)

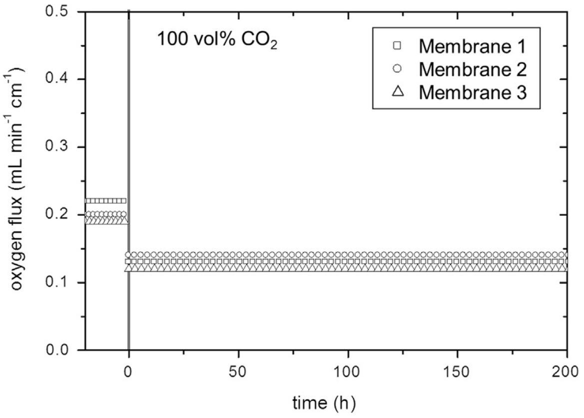

Fig. 5. Long-term oxygen permeation measurements at 1173 K of the 1 mm thick LSCF 6482 membrane. Membranes 1, 2 and 3 denote three different membranes that were measured under same conditions. After 20 h of sweeping with He, the sweep gas was changed to CO_2, and the operating time was set to zero. The conditions were follows: feed flow rates 150 mL min^{-1} synthetic air (80% N_2, 20% O_2); sweep flow rates CO_2=29 mL min^{-1}, Ne=1 mL min^{-1}.

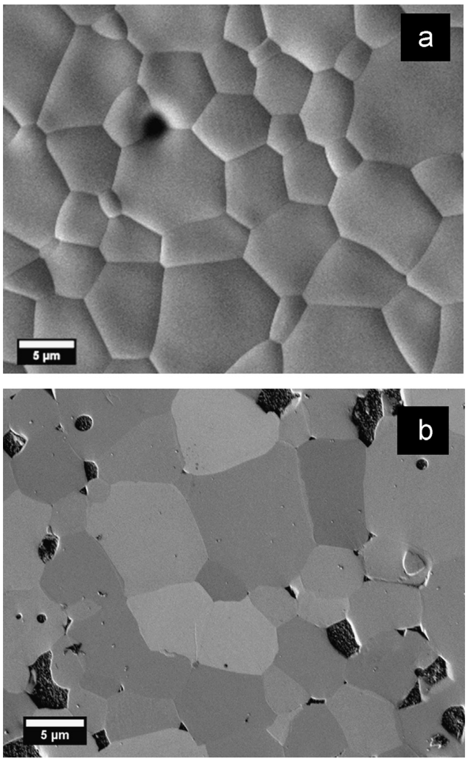

Fig. 6. Secondary electron micrograph of LSCF 6482 ceramic: (a) the membrane surface as sintered at 1523 K for 10 h in air and (b) backscattered-electron channeling micrograph of the vibration-polished LSCF 6482 membrane cross-section after the 200 h of long-term oxygen permeation experiment with CO_2 sweep gas at 1173 K.

are homogeneously distributed. However, there is a region that shows the complete absence of iron and cobalt, but the presence of strontium. This result agree with the EFTEM results for the strontium carbonate phase. The CoO inclusion can clearly be observed by EDXS as only Co is evident in this area.

Fig. 3a shows a STEM high-angle annular dark-field micrograph of the LSCF 2882 membrane cross-section after 200 h of operation with CO_2 sweeping. Again, an area with different phase compositions is seen, which appears in different contrast. The surface of the membrane was not damaged or changed during TEM sample preparation. The rest of the epoxy still covers the surface and leaves it in the original state. The carbon distribution is seen in the EFTEM images in Fig. 3b. Interestingly, although a monolithic dense carbonate layer does not truly form, the carbonate particles densely coalesce. The EELS spectrum of the LSCF 2882 has been reported by Klande et al. [24]. Additionally, EDXS analysis was carried out. Fig. 4a–e shows the STEM high-angle annular dark-field micrograph and the corresponding elemental maps. The carbonate phase is marked with an orange letter “c”. The distribution of lanthanum and iron (La-L$_\alpha$ and Fe-K$_{\alpha,}$ Fig. 4b and c) is homogenous in the perovskite phase, but neither of these elements can be found in the carbonate regions. Furthermore, a cobalt-rich phase (Co-K$_\alpha$) is shown in Fig. 4c, which shows the formation of CoO inclusion. Strontium distribution is shown in Fig. 4e. It is obvious that the cobalt-rich phase is strontium depleted, but the carbonate phase exhibits the appropriate amount of strontium (Sr-L$_\alpha$).

In summary, both materials SCF and LSCF 2882 form carbonate layers, which consist of carbonate particles on the outer surface that coalesce into a dense layer. Furthermore, the carbonate is intermixed not only with perovskite, but also with cobalt oxide, which is incorporates directly into the grains. The scheme, shown in Fig. 4f, demonstrates a possible decomposition route for LSCF materials during carbon dioxide exposure. The original perovskite, LSCF 2882 in this case, forms strontium carbonate in contact with CO_2, and as a result of the Sr-non-stoichiometry, cobalt oxide segregates. A Sr- and Co-depleted perovskite remains after decomposition. This perovskite might still have oxygen exchange and oxygen transport capabilities, which is in agreement with oxygen permeation experiments conducted by Klande et al. [24]. The oxygen permeation flux decreases as the carbonate forms a compact, dense and thick layer, which enabled the oxygen ion transport and oxygen removal on the sweep side in our experiments. Because of the high strontium content in SCF, the oxygen flux declines after only 30 h. It is likely that the carbonate particles in SCF form a more compact layer compared to LSCF 2882, where the oxygen flux decreases after 200 h of sweeping with CO_2. As seen in Fig. 1a, the top of the SCF membrane surface is covered with a 5 μm porous layer and 5 μm dense layers. As reported by Partovi et al., the carbonate layer does not have good thermo-mechanical stability [29]. It is possible, that the porous layer is formed by the exfoliation of some carbonate particles during cooling.

3.3. Investigation of LSCF 6482 membrane

3.3.1. Oxygen permeation fluxes

Oxygen permeation of LSCF 6482 was measured under the same conditions as described by Klande et al. As reported, the LSCF 6482 demonstrated a high stability over more than 200 h at 1173 K of sweeping with CO_2, even though the value of the oxygen flux was lowest one compared to the Sr-rich materials of the LSCF-series [24]. To confirm these results, long-term oxygen permeation measurements were repeated three times at the given conditions. Fig. 5 shows the result of the permeation experiment. The membrane reactor was first operated 20 h at 1173 K using He as the sweep gas. Then, the reactor was switched to 100 vol% CO_2 as the sweep gas at the same temperature. As evident from Fig. 5, the oxygen flux decreased from 0.2 mL min^{-1} cm^{-2} to 0.14 mL min^{-1} cm^{-2}. That effect can be explained by the inhibitory effect of CO_2 molecules on the surface exchange reaction, which has been discussed in the literature [22,30–32]. CO_2 molecules can be chemically adsorbed at the membrane surface resulting in a decline in the oxygen partial

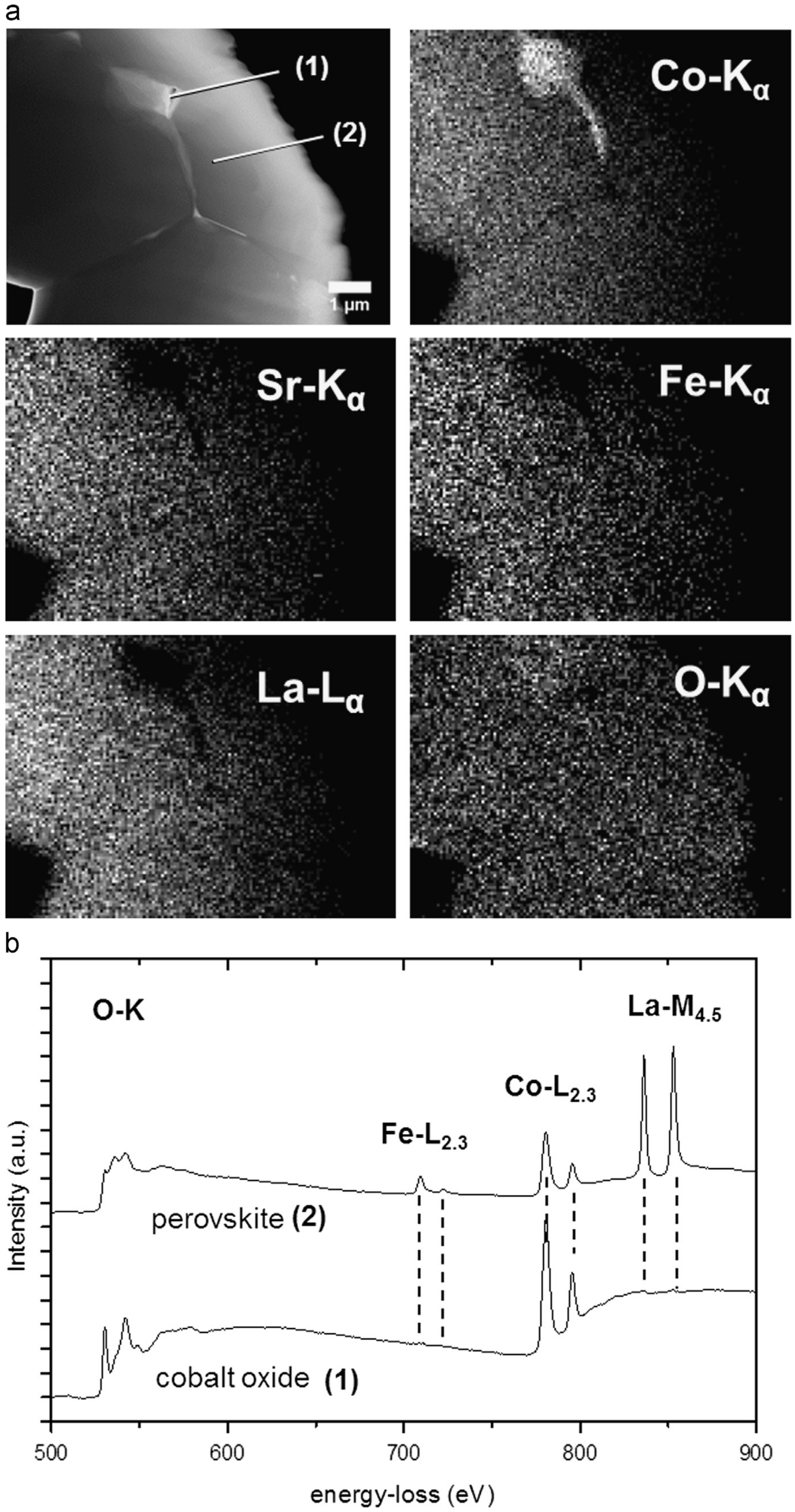

Fig. 7. CO_2-exposed sweep side of the LSCF 6482 membrane after 200 h of the oxygen permeation experiment: (a) STEM high-angle annular dark-field image and EDXS elemental distribution. (b) EELS spectrum in the energy-loss range from 500 to 900 eV of the perovskite and cobalt oxide inclusion.

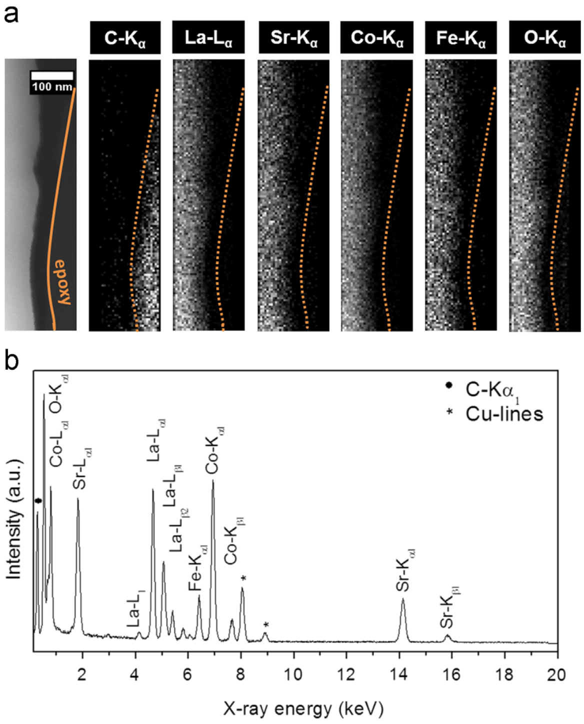

Fig. 8. Cross-section of the CO_2-exposed LSCF 6482 membrane after 200 h experiment. (a) STEM and EDXS elemental distribution of the surface. The border of the epoxy adhesive is marked with an orange line. (b) EDX spectrum of the displayed specimen area. Cu appears due to a narrow TEM pole and does not belong to the specimen. The carbon $K_{\alpha 1}$ line results from the epoxy. (For interpretation of references to color in this figure, the reader is referred to the web version of this article.)

pressure gradient. In all measurements, the LSCF 6482 membrane displayed a stable oxygen permeation flux over 200 h. A small error of ± 0.01 mL min^{-1} cm^{-2} is within the measurement error.

3.3.2. LSCF 6482 membrane after operation in CO_2

As the depth profile of the LSCF 6482 cross-section after the exposure to CO_2 at 1173 K does not show any concrete results, the specimen after oxygen permeation experiment was vibration-polished to preserve the crystallinity of the surface. The results are shown in Fig. 6. The LSCF 6482 membrane surface as sintered at 1523 K is shown in Fig. 6a. The vibration-polished cross-section near the sweep side surface is shown in Fig. 6b. The LSCF shows no phase segregation, which explains the stable oxygen flux after 200 h. The elemental content could be identified by EDXS and EELS as shown in Fig. 7. The STEM high-angular annular dark-field image in Fig. 7a shows a grain boundary triple junction at the sweep side surface. The EDXS elemental distribution provides evidence of the formation of cobalt-rich (Co-K_α), phase at the boundaries. Compared to SCF and LSCF 2882, the cobalt-rich phase CoO was formed directly in the grain.

The EELS spectra were collected in the energy-loss range from 500 to 900 eV from the cobalt-rich phase (1) and perovskite grain (2). The EELS spectrum of the perovskite exhibits peaks attributed to Fe-$L_{2,3}$ (710 and 723 eV [27]), Co-$L_{2,3}$ (782 and 796 eV) and La-$M_{4,5}$ (837 and 854 eV). The O-K electron-loss near edge structure (ELNES) for the LSCF 6482 perovskite is slightly different from the O-K ELNES of SCF (Fig. 2d) and LSCF 2882 [23]. The reason for this difference is that the O-K ELNES is extremely sensitive to the local environment of the oxygen atoms. As the perovskite composition is varied and the lanthanum content is different in every composition of the LSCF series, there might be influence on the fine structure of the O-K ELNES. The CoO EELS spectrum (2) shows only Co-$L_{2,3}$ and O-K signals.

No carbonate particles on the outer surface could be detected. Carbonate is very sensitive to the high-energy electron beam, which can cause decomposition into CO_2 and oxide [27]. To ensure that no carbonate was formed, the cross-section of the sweep side was protected by epoxy due to the sample preparation and is shown in Fig. 8a. Furthermore, the magnification is higher than in Fig. 8. The border of the epoxy is labeled with an orange line. No carbonate could be detected as seen from the EDXS elemental distribution, even at the nano-scale. Lanthanum, strontium, cobalt, iron and oxygen show homogenous distribution over the specimen. No Sr enrichment is observed, which would indicate $SrCO_3$ formation. The carbon elemental map (C-K_α) demonstrates carbon enrichment only in the epoxy. Fig. 8b shows the corresponding EDX spectrum of the specimen. There are no impurities in the material, and only the expected elements are observed in the sample. The C-K_α belongs to the epoxy, and Cu-lines appear due to a narrow TEM pole. In contrast to the investigation by Tan et al., no surface erosion or segregation was observed [22].

It can be concluded, that LSCF 6482 is a CO_2 tolerant material at 1173 K. Considering the thermodynamic aspect of perovskite formation reported by Yokokawa et al. [33], the increasing La content can stabilize the perovskite structure and thermodynamically disfavor the formation of carbonate. These considerations are appropriate at 1173 K. Additionally, according to the Ellingham diagram, a lowering of the operation temperature can change the thermodynamic equilibrium and the formation of lanthanum oxycarbonate and lanthanum carbonate can be promoted [17–19]. In our investigation the thermodynamic forces prevail the kinetics. As reported by Yang et al. [34], for a dense perovskite-type metal oxide, the carbon reaction can only occur on the external surface of particles with a slow reaction rate. For dense ceramic, the carbonation rate decreases with increasing grain size. Therefore, according to the particle size, for the LSCF6482 membrane with the smallest grains, the carbonation rate should increase and lead to poisoning of the material. In our investigations, we observed mutual effect. This gives clear indication that thermodynamics prevails in our investigations.

4. Conclusions

The series of $La_{1-x}Sr_{x}Co0_{.8}Fe_{0.2}O_{3-\delta}$ (LSCF) membranes with $x=1$, 0.8, 0.6 and 0.4 (SCF, LSCF2882, LSCF4682, LSCF6482) was synthetized by the sol–gel method. Microstructural analysis after long-term oxygen permeation experiments using CO_2 as the sweeping gas showed that carbonates formed a dense layer consisting of compact carbonate particles in the materials with low La content on the CO_2 exposed side. That layer prevents oxygen permeation, which leads to a decrease in the oxygen flux. The decomposition route after treatment with CO_2 was proposed. EELS were obtained for the SCF and LSCF 6482 compounds. The high tolerance of the LSCF 6482 material was observed in several long-term oxygen permeation measurements. Furthermore, the TEM investigations of the LSCF 6482 membrane provide evidence of the stability of the perovskite structure. No carbonate layer on the sweep side was found in this material.

Acknowledgments

The authors sincerely acknowledge financial support from the Chinese-German Center for Science (GZ676) and the Deutsche

Forschungsgemeinschaft (FE 928/4-1) as well as fruitful discussions with Prof. Jürgen Caro.

References

[1] R. Bredesen, K. Jordal, O. Bolland, High-temperature membranes in power generation with CO_2 capture, Chem. Eng. Process 43 (2004) 1129–1158.

[2] H. Stadler, F. Beggel, M. Habermehl, P. Persigehl, R. Kneer, M. Modigell, P. Jeschke, Oxyfuel coal combustion by efficient intergration of oxygen transport membranes, Int. J. Greenh. Gas Control 5 (2011) 7–15.

[3] D. Grielen, J. Podkanski, Prospect for CO_2 Capture and Storage, OECD/IEA, Paris, France, 2004.

[4] X.Y. Tan, K. Li, A. Thursfield, I.S. Metcalfe, Oxyfuel combustion using a catalytic ceramic membrane reactor, Catal. Today 131 (2008) 292–304.

[5] A. Smith, J. Klosek, A review of air separation technologies and their integration with energy conversion process, Fuel Process. Technol. 70 (2001) 115–134.

[6] International Energy Agency, World Energy Outlook 2011, OECD, Paris, 2011.

[7] Z. Shao, S. Haile, A high-performance cathode for the next generation of solid-oxide fuel cells, Nature 431 (2004) 170.

[8] M. Arnold, H. Wang, A. Feldhoff, Influence of CO_2 on the oxygen permeation performance and the microstructure of perovskite-type $(Ba_{0.5}Sr_{0.5})(Co_{0.8}Fe_{0.2})O_{3-\delta}$ membranes, J. Membr. Sci. 293 (2007) 44–52.

[9] O. Czuprat, M. Arnold, S. Schirrmeister, T. Schiestel, J. Caro, Influence of CO_2 on the oxygen permeation performance of perovskite-type $BaCo_xFe_yZr_zO_{3-\delta}$ hollow fiber membranes, J. Membr. Sci. 364 (2010) 132–137.

[10] J.X. Yi, M. Schroeder, T. Weirich, J. Mayer, Behavior of $Ba(Co,Fe,Nb)O_{3-\delta}$ perovskite in CO_2-containing atmospheres: degradation mechanism and materials design, Chem. Mater. 22 (2010) 132–137.

[11] T. Klande, K. Efimov, S. Cusenza, K.D. Becker, A. Feldhoff, Effect of doping, microstructure, and CO_2 on $La_2NiO_{4+\delta}$ based oxygen-transporting materials, J. Solid State Chem. 184 (2011) 3310–3318.

[12] Q. Zeng, Y. Zuo, C. Fan, C. Chen, CO_2-tolerant oxygen separation membranes targeting CO_2 capture application, J. Membr. Sci. 335 (2009) 140–144.

[13] K. Efimov, T. Klande, N. Juditzki, A. Feldhoff, Ca-containing CO_2-tolerant perovskites materials for oxygen separation, J. Membr. Sci. 389 (2012) 205–215.

[14] H. Luo, K. Efimov, H. Jiang, A. Feldhoff, H. Wang, J. Caro, CO_2 stable and cobalt-free dual-phase membrane for oxygen separation, Angew. Chem. Int. Ed. 50 (2011) 759–763.

[15] X.F. Zhu, H.Y. Liu, Y. Cong, W.S. Yang, Novel dual-phase membranes for CO_2 capture via an oxyfuel route, Chem. Commun. 48 (2012) 251–253.

[16] J. Tang, Y.Y. Wei, L.Y. Zhou, Z. Li, H.H. Wang, Oxygen permeation through a CO_2 tolerant mixed conducting oxide $(Pr_{0.9}La_{0.1})_2(Ni_{0.74}Cu_{0.21}Ga_{0.05})O_{4+\delta}$, AIChE J. 58 (2012) 2473–2478.

[17] Y. Wei, O. Ravkina, T. Klande, H. Wang, A. Feldhoff, Effect of SO_2 and CO_2 on oxygen permeation and microstructure of $(Pr_{0.9}La_{0.1})_2(Ni_{0.74}Cu_{0.21}Ga_{0.05})O_{4+\delta}$ membranes, J. Membr. Sci. 429 (2013) 147–154.

[18] K.H. Stern, High Temperature Properties and Thermal Decomposition of Inorganic Salts with Oxyanions, CRC Press, Boca Raton, London, New York, Washington D.C., 2011.

[19] K. Efimov, M. Arnold, J Martynczuk, A. Feldhoff, Crystalline intermediate phases in the sol–gel-based synthesis of $La_2NiO_{4+\delta}$, J. Am. Ceram. Soc. 92 (2008) 876–880.

[20] V.M. Goldschmidt, T. Barth, G. Lunde, W. Zachariasen, Geochemische Verteilungsgesetze der Elemente: 7, Die Gesetze der Kristallchemie, I Kommission Hos Jacob Dybwad, Oslo (1926) 58–74.

[21] R.D. Shannon, Revised effective ionic radii and systeatic studies of interatomic distances in halids and chalcogenides, Acta Crystallogr. Sect. A 32 (1976) 751–767.

[22] X. Tan, N. Liu, B. Meng, J. Sunarso, K. Zhang, S. Liu, Oxygen permeation behavior of $La_{0.6}Sr_{0.4}Co_{0.8}Fe_{0.2}O_3$ hollow fibre membranes with highly concentrated CO_2 exposure, J. Membr. Sci. 389 (2012) 216–222.

[23] T.T. Norton, J. Ortiz-Landeros, Y.S. Lin, Stability of La–Sr–Co–Fe oxide–carbonate dual-phase membranes for carbon dioxide separation at high temperatures, Ind. Eng. Chem. Res. 53 (2014) 2432–2440.

[24] T. Klande, O. Ravkina, A. Feldhoff, Effect of A-site lanthanum doping on the CO_2 tolerance of $SrCo_{0.8}Fe_{0.2}O_{3-\delta}$ oxygen-transporting membranes, J. Membr. Sci. 437 (2013) 122–130.

[25] J. Martynczuk, M. Arnold, A. Feldhoff, Influence of grain size on the oxygen permeation performance of perovskite-type $(Ba_{0.5}Sr_{0.5})(Co_{0.8}Zn_{0.2})O_{3-\delta}$ membranes, J. Membr. Sci. 322 (2008) 375–382.

[26] H. Wang, C. Tablet, A. Feldhoff, J. Caro, Investigation of phase structure, sintering, and permeability of perovskite-type $Ba_{0.5}Sr_{0.5}Co_{0.8}Fe_{0.2}O_{3-\delta}$ membranes, J. Membr. Sci. 262 (2005) 20–26.

[27] A. Feldhoff, J. Martynczuk, M. Arnold, M. Myndyk, I. Bergmann, V. Sepelak, W. Gruner, U. Vogt, A Hähnel, J. Woltersdorf, Spin-state transition of iron in $(Ba_{0.5}Sr_{0.5})(Co_{0.8}Zn_{0.2})O_{3-\delta}$ perovskite, J. Solid State Chem. 182 (2009) 2961–2971.

[28] J.L. Mansot, V. Golabkan, L. Romana, T. Cesaire, Chemical and physical characterization by EELS of strontium hexanoat reverse micelles and strontium carbonate nanophase produced during tribological experiments, J. Microsc. 210 (2003) 110–118.

[29] K. Partovi, F. Liang, O. Ravkina, J. Caro, High-flux oxygen-transporting membrane $Pr_{0.6}Sr_{0.4})(Co_{0.5}Fe_{0.5})O_{3-\delta}$: CO_2 stability and microstructure, Mater. Interfaces 6 (2014) 10274–10282.

[30] J.A. Lane, J.A. Kilner, Oxygen surface exchange on gadolinia doped ceria, Solid State Ion. 136–137 (2000) 927–932.

[31] K. Yashiro, S. Onuma, A. Kaimai, Y. Nigara, T. Kawada, J. Mizusaki, K. Kawamura, T. Horita, H. Yokokawa, Mass transport properties of $Ce_{0.9}Gd_{0.1}O_{2-\delta}$ at the surface and in the bulk, Solid State Ion. 152–153 (2002) 469–476.

[32] I.V. Khromushin, T.I. Aksenova, Z.R. Zhotabaev, Mechanism of gas-solid exchange process for some perovskites, Solid State Ion. 162–163 (2003) 37–40.

[33] H. Yokokawa, N. Sakai, T. Kawada, M. Dokiya, Thermodynamic stabilities of perovskite oxides for electrodes and other electrochemical materials, Solid State Ion. 52 (1992) 43–56.

[34] Q. Yang, Y.S. Lin, Kinetics of carbon dioxide sorption on perovskite-type metal oxides, Ind. Eng. Chem. Res. 45 (2006) 6302–6310.

2.3 Effect of A-site lanthanum doping on the CO_2 tolerance of $SrCo_{0.8}Fe_{0.2}O_{3-\delta}$ oxygen-transporting membranes

---

Reprinted with kind permission from Elsevier:
Tobias Klande, Olga Ravkina and Armin Feldhoff
Journal of Membrane Science **437** (2013) 122-130.
doi:10.1016/j.memsci.2013.02.051

Journal of Membrane Science 437 (2013) 122–130

Contents lists available at SciVerse ScienceDirect

Journal of Membrane Science

journal homepage: www.elsevier.com/locate/memsci

Effect of A-site lanthanum doping on the CO_2 tolerance of $SrCo_{0.8}Fe_{0.2}O_{3--\delta}$ oxygen-transporting membranes

Tobias Klande*, Olga Ravkina, Armin Feldhoff

Institute of Physical Chemistry and Electrochemistry, Leibniz Universität Hannover, Callinstraße 3a, D-30179 Hannover, Germany

ARTICLE INFO

Article history:
Received 19 November 2012
Received in revised form
12 February 2013
Accepted 24 February 2013
Available online 5 March 2013

Keywords:
Oxygen-transporting membrane
Carbon dioxide
In-situ X-ray diffraction
Long-term oxygen permeation
Transmission electron microscopy

ABSTRACT

The $SrCo_{0.8}Fe_{0.2}O_{3-\delta}$ (SCF) perovskite was systematically doped with increasing lanthanum content up to 60 wt% on the A-site to investigate the effect on CO_2 tolerance. Different powders were prepared by a sol-gel method and the materials were characterized by *in-situ* X-ray diffraction (XRD) and long-term oxygen permeation measurements in CO_2-containing atmospheres. The microstructure was investigated using scanning electron microscopy (SEM) and transmission electron microscopy (TEM). All powders exhibit cubic perovskite structure except the rhombohedral $La_{0.6}Sr_{0.4}Co_{0.8}Fe_{0.2}O_{3-\delta}$ (LSCF 6482), which however, shows a phase transition into cubic perovskite structure at higher temperature. By doping 20 wt% lanthanum, the tolerance against CO_2 is considerably increased and doping with 60 wt% lanthanum resulted in a stable oxygen permeation performance in CO_2 atmosphere for at least 200 h. Oxygen permeation experiments in an air/helium gradient showed that with increasing lanthanum content the oxygen permeation flux decreases. Microstructure analysis of the membranes after CO_2 operation showed that the carbonate preferentially forms a dense layer at the carbon dioxide exposed sweep side of the membranes.

1. Introduction

The increasing demand of electricity, which is mainly produced by combustion of fossil fuels, leads to global warming by emission of green-house gases [1]. To reduce the climate-damaging carbon dioxide, new processes such as oxy-fuel combustion [2], in which pure oxygen is directly combusted with fossil fuels, are needed. The formed products are mainly carbon dioxide and water vapor, which can be easily separated by condensation. However, the production of oxygen by means of cryogenic processes or pressure swing adsorption (PSA) are expensive and energy intensive [3]. Using ceramic oxygen-transporting membranes, which supply an unrivalled selectivity for O_2, these costs can be lowered, resulting in better overall efficiency and lower electricity costs. Because the flame temperature would be too high, the oxygen has to be diluted before combustion. This can be done by the formed carbon dioxide flue gas in order to achieve an economically reasonable process. Another advantage would be that the generated process heat can be used to hold the membrane at operation temperature. By operating the membrane in sweep-gas mode at ambient pressure even more energy can be saved compared to highly pressurized operation or operation under vacuum conditions [4,5].

The prominent mixed-ionic electronic conducting (MIEC) materials contain alkaline-earth cations, mainly barium and strontium, on the A-site of the ABO_3 perovskite structure, which on the one hand supply high oxygen fluxes, but on the other hand lead to membrane degradation in the presence of CO_2, which was shown for $Ba_{0.5}Sr_{0.5}Co_{0.8}Fe_{0.2}O_{3-\delta}$ for example [6]. A way to handle this problem is to avoid alkaline-earth elements leading to CO_2 tolerant materials such as $La_2NiO_{4+\delta}$ [7] or dual-phase materials such as 40 wt% $NiFe_2O_4-$60 wt% $Ce_{0.9}Gd_{0.1}O_{2-\delta}$ [8]. A further approach is to stabilize the structure of known, but CO_2-intolerant materials by doping less reactive elements on the A- and/or B-site. For example Chen et al. and Zeng et al. doped SCF with 10% tantalum [9] or 10% titanium [10], which greatly improves tolerance towards CO_2. The A site is predestinated to be substituted by rare-earth cations or smaller alkaline-earth cations such as calcium. By a thermodynamic approach using an Elligham diagram, which was provided by Efimov et al. [11], it can be seen that the smaller La^{3+} ion ($r=136$ pm) shows improved tolerance against CO_2 as compared to the bigger Sr^{2+} ion ($r=144$ pm). However, the substitution of elements may lead to structural changes, reduced lattice parameters and therefore to significantly lower oxygen fluxes. Although, Tan et al. investigated the stability of $La_{0.6}Sr_{0.4}Co_{0.8}Fe_{0.2}O_{3-\delta}$ hollow-fiber membranes in CO_2 atmospheres [12] a systematic study of the influence of the lanthanum concentration on the A-side of SCF is apparently missing.

---

* Corresponding author. Tel.: +49 511 762 2943; fax: +49 511 762 19121.
E-mail address: tobias.klande@pci.uni-hannover.de (T. Klande).

0376-7388/$ - see front matter © 2013 Elsevier B.V. All rights reserved.
http://dx.doi.org/10.1016/j.memsci.2013.02.051

In the present work the effect of the lanthanum concentration in $La_{1-x}Sr_xCo_{0.8}Fe_{0.2}O_{3-\delta}$ ($x=1$, 0.8, 0.6, 0.4) on CO_2 tolerance was systematically examined by XRD, *in-situ* XRD in CO_2 atmospheres and long-term oxygen permeation experiments in an air/helium or air/CO_2 gradient. Furthermore the membranes were investigated by SEM before and after the CO_2 exposure. The results of TEM investigations are also reported.

2. Experimental

2.1. Sample preparation

The powders were synthesized by sol–gel-route using stoichiometric amounts of $La(NO)_3$, $Sr(NO)_2$, $Co(NO)_2$, $Fe(NO)_3$, ethylenediaminetetraacetic acid (EDTA) and citric acid. The resulting gel was heated and stirred over night and then precalcined in ambient air at 773 K. After thoroughly grinding, the product was calcined for 10 h at 1273 K in ambient air. Green bodies of membranes were obtained by uniaxially pressing the powders at 150 MPa for 30 min, followed by sintering at 1473 K for SCF ($SrCo_{0.8}Fe_{0.2}O_{3-\delta}$), 1523 K for LSCF 2882 ($La_{0.2}Sr_{0.8}Co_{0.8}Fe_{0.2}O_{3-\delta}$), and 1573 K for LSCF 4682 ($La_{0.4}Sr_{0.6}Co_{0.8}Fe_{0.2}O_{3-\delta}$) and LSCF 6482 ($La_{0.6}Sr_{0.8}Co_{0.8}Fe_{0.2}O_{3-\delta}$) in ambient air for 10 h. At all times heating and cooling rates of 3 K min^{-1} were used.

2.2. X-ray diffraction

X-ray diffraction (XRD) analysis was performed at room temperature using a Bruker-AXS D8 Advance diffractometer with Cu K_α radiation. Data sets were recorded in a step-scan mode in the 2Θ range of 20–100° with intervals of 0.02°. High-temperature measurements were conducted in an *in-situ* cell HTK-1200 N (Anton-Paar) between room temperature and 1273 K in an atmosphere consisting of 50 vol% CO_2/50 vol% N_2. The heating rate was 12 K min^{-1} with an equilibrium time of 30 min before each measurement. The XRD data were analyzed using TOPAS 4.0 software (Bruker AXS). The displacement of oxygen at different temperatures was determined by the Rietveld method.

2.3. Oxygen permeation

Oxygen permeation was measured in a house-made high-temperature permeation cell as described elsewhere [13,14]. Before the measurements both sides of the membranes were carefully polished

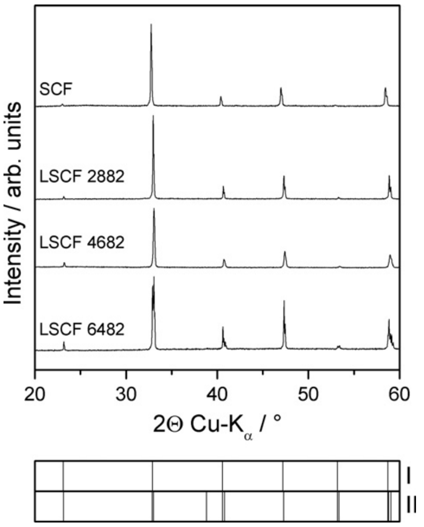

Fig. 1. Room-temperature XRD pattern of $(La_{1-x}Sr_x)(Co_{0.8}Fe_{0.2})O_3$ ($x=1$, 0.8, 0.6, 0.4) powders. The calculated Bragg positions for (I) cubic perovskite (s.g. $Pm\overline{3}m$, $a=3.875$ Å) and (II) rhombohedral perovskite (s. g. $R\overline{3}c$, a $=5.444$ Å, $c=13.241$ Å) are indicated at the bottom of the figure.

Table 1
Room-temperature unit cell parameters of $(La_{1-x}Sr_x)(Co_{0.8}Fe_{0.2})O_3$ ($x=1$, 0.8, 0.6, 0.4) after sintering for 10 h at the given temperature in air.

Sample	Lattice parameters [Å]			Unit cell volume [Å^3]	Space group
	a	*b*	*c*		
SCF ($T=1473$ K)	3.8651	–	–	57.74	$Pm\overline{3}m$
LSCF 2882 ($T=1523$ K)	3.8404	–	–	56.64	$Pm\overline{3}m$
LSCF 4682 ($T=1573$ K)	3.8380	–	–	56.54	$Pm\overline{3}m$
LSCF 6482 ($T=1573$ K)	5.4429	–	13.2406	339.70	$R\overline{3}c$

Table 2
Temperature-dependent lattice parameters of LSCF 6482. The rhombohedral distortion was calculated using the relationship:$\tan\omega=2\sqrt{3}(0.5-x)$ [20]. Z=number of formula units per unit cell, R_{exp}=expected R-factor, R_{wp}=weighted profile R-factor.

	T/K	a/Å^3	c/Å	V/Å^3	VZ^{-1}/Å^3	x (O)	ω/°	R_{exp}/%	R_{wp}/%
Rhombohedral phase R3c $Z=6$	303	5.443	13.241	339.70	56.62	0.533	−6.6	3.34	4.13
	373	5.448	13.264	340.90	56.82	0.531	−6.1	3.29	4.03
	473	5.455	13.300	342.73	57.12	0.527	−5.3	3.24	4.02
	573	5.462	13.337	344.59	57.43	0.525	−4.9	3.22	3.91
	673	5.470	13.378	346.70	57.78	0.515	−2.9	3.19	4
Cubic phase $Pm\overline{3}m$ $Z=1$	773	3.875		58.17		0.5		3.17	4.07
	873	3.886		58.68		0.5		3.15	3.99
	973	3.899		59.26		0.5		3.13	3.88
	1073	3.912		59.88		0.5		3.12	3.83
	1173	3.926		60.53		0.5		3.1	3.78
	1273	3.941		61.21		0.5		3.09	3.68

with 800 mesh emery paper to obtain a uniform surface area. The membranes were sealed on an alumina tube using a gold cermet (Heraeus). The feed side was fed with synthetic air (20 vol% O_2/80 vol% N_2) at a rate of 150 mL min^{-1}, whilst Ne (1.0 mL min^{-1}, 99.995%) and He (29.0 mL min^{-1}, 99.995%) or CO_2 (29.0 mL min^{-1}, 99.995%) were applied to the sweep side. An online-coupled Agilent 7890 gas chromatograph with a Carboxen 1000 column was employed to analyze the gas mixture. Using neon as an internal standard, the absolute flux rate was calculated. By measuring the N_2 concentration, the total O_2 leakage was calculated and subtracted from the total O_2 flux.

2.4. Scanning electron microscopy

Field-emission scanning electron microscopy (FE-SEM) imaging was performed on a JEOL JSM-6700F field-emission instrument at low excitation voltage of 2 kV. For backscattered-electron channeling contrast imaging at higher excitation voltages, the samples were vibrational-polished to preserve crystallinity up to the very surface. An energy-dispersive X-ray spectrometer (EDXS), Oxford Instruments INCA-300, with an ultra-thin window was used for the elemental analysis at excitation voltage of 20 kV.

2.5. Transmission electron micoscopy

Transmission electron microscopy (TEM) investigations were made at 200 kV on a JEOL JEM-2100F-UHR field-emission instrument (C_S=0.5 mm, C_C=1.2 mm). The microscope was operated in bright-field mode and as well as a scanning TEM (STEM) in high-angle annular dark-field (HAADF) mode including electron energy-loss spectroscopy (EELS) and electron-loss near-edge structures (ELNES) and in selected area electron diffraction (SAED) mode. An energy-dispersive X-ray spectrometer (EDXS), Oxford Instruments INCA-200, was used for the elemental analysis at excitation voltage of 200 kV. The preparation method of the TEM specimen is described in detail elsewhere [6].

3. Results and discussion

3.1. Characterization of powders

As seen in Fig. 1 all samples are single-phase materials. The $La_{1-x}Sr_xCo_{0.8}Fe_{0.2}O_3$ (x=1, 0.8, 0.6) powders exhibit the cubic perovskite structure (s.g.$Pm\overline{3}m$ 221), whereas LSCF 6482 exhibits rhombohedral structure at room temperature (s.g. $R\overline{3}c$ 167). The obtained unit cell parameters, presented in Table 1, are in good accordance with literature data on SCF [15], LSCF 4682 [16], and LSCF 6482 [17]. The decrease of the cell parameters with increasing lanthanum content is consistent with the decrease of the average A-site cation radius (Sr^{2+} (144 pm) is partly replaced by La^{3+} (136 pm)) [18]. The Goldschmidt tolerance factor of SCF is close to unity, which proposes cubic perovskite structure [19]. With increasing lanthanum content, the Goldschmidt tolerance factor decreases which may explain the shift to rhombohedral structure for the end member of our study LSCF 6482. The rhombohedral distortion was estimated to be $\omega = -6.6^\circ$ at room temperature (Table 2). It was calculated from the x coordinate of the displaced oxygen atom as obtained by XRD data calculated by the Rietveld method using the following relationship:$\tan\omega = 2\sqrt{3}(0.5-x)$ [20]. The tilt around the c-axis could be positive (clockwise) or negative (anti-clockwise) whether the displacement of the oxygen is below 0.5 or above. The oxygen in the ideal cubic non-distored perovskite structure is located at the highly symmetric crystallographic Wyckoff position 3d (0.5, 0, 0).

3.2. Membrane microstructure

The optimum sintering temperature for each membrane composition was found by several experiments at different temperatures. The effect of even small deviations from the optimum sintering temperature can have a huge impact on the microstructure. As an example, the surface of the LSCF 2882 membrane sintered at 1373 K for 10 h is shown in Fig. 2a. Because the sintering temperature was too low, no densification was observed, which leads to a large amount of porosity. However, sintering the membrane at 1573 K, which is only 50 K over the found optimum sintering temperature, leads to precipitation of cobalt-enriched perovskite in the grain boundaries as was proven by EDXS analysis (Fig. 2b). The relative elemental distribution of all cations is given in Table 3. The bulk composition of the material changes, which may have a significant influence on the materials properties. The optimum sintering temperatures were

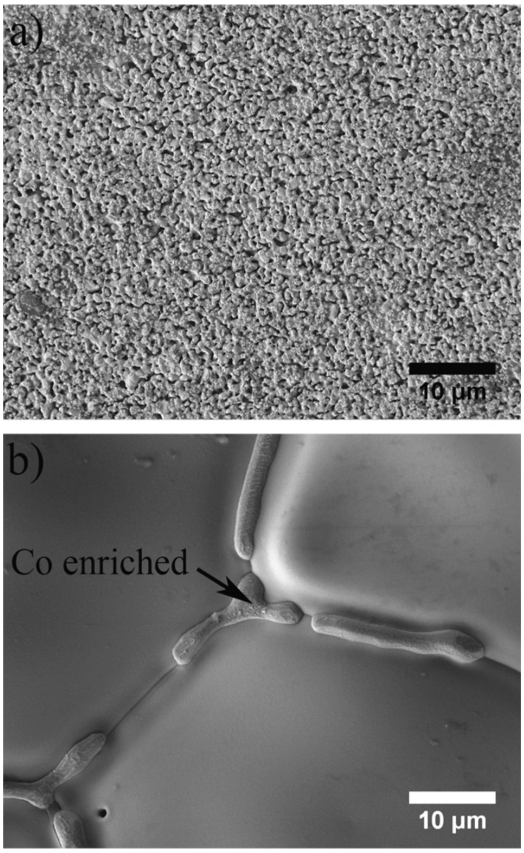

Fig. 2. LSCF 2882 sintered at (a) 1373 K and (b) 1573 K for 10 h in air.

Table 3
Summary of the elemental distribution of La, Sr, Co, and Fe ($\sum$metal cations=100 at%) obtained by EDXS of the LSCF 2882 membrane at the bulk and the segregated phase at the grain boundary (associated to Fig. 2b).

	Bulk membrane	Grain boundary
La/at%	10	7
Sr/at%	44	29
Co/at%	36	57
Fe/at%	10	7

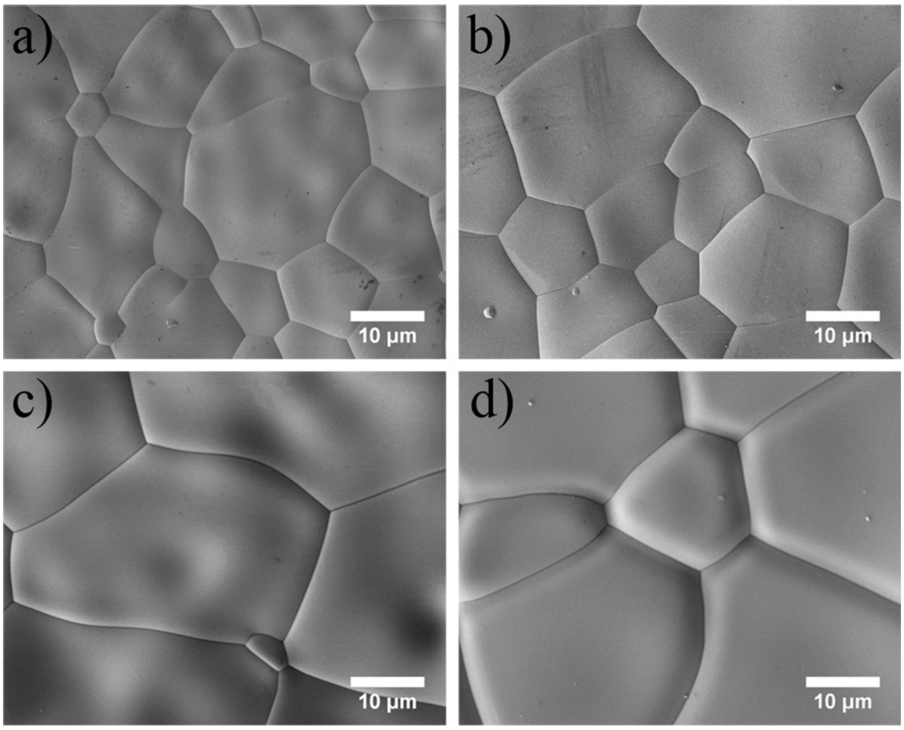

Fig. 3. SE surface view micrographs of the grain structure of (a) SCF (b) LSCF 2882 (c) LSCF 4682 and (d) LSCF 6482. For sintering times refer to Table 1.

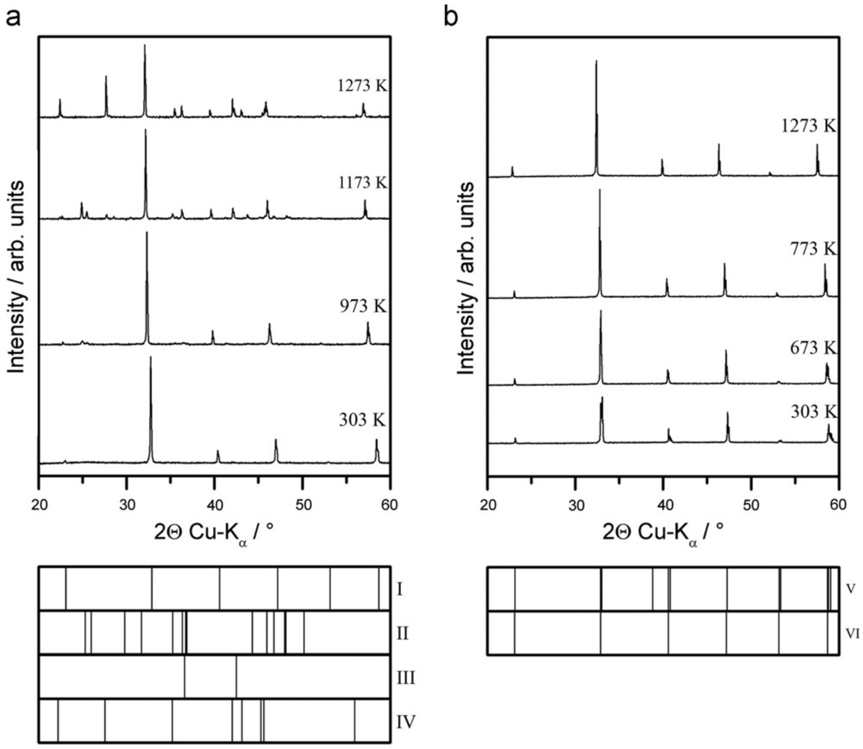

Fig.4. *In-situ* XRD at given temperatures in an atmosphere of 50 vol% CO_2/50 vol% N_2 of (a) SCF and (b) LSCF 6482. The calculated Bragg positions for (I) cubic SCF (ICSD 79022), (II) orthorhombic $SrCO_3$ (ICSD 15195), (III) cubic CoO (ICSD 28505), (IV) rhombohedral $SrCO_3$ (ICSD 27446), (V) rhombohedral LSCF 6482 (s. g. $R\overline{3}c$, a=5.444 Å, c=13.241 Å) and (VI) cubic LSCF 6482 (s.g. $Pm\overline{3}m$, a=3.875 Å) are given at the bottom of the figures. The total period including equilibration and measurement times was 60 min at a given temperature interval.

found to be 1473 K for SCF, 1523 K for LSCF 2882, and 1573 K for LSCF 4682 and LSCF 6482. The obtained surface micrographs show neither porosity nor any segregation of secondary phases inside the grain boundaries (Fig. 3). The average grain size was determined using the Image J [21] particle analyzer by measuring the grain area in μm^2 for a series of micrographs for each membrane, and then the grain diameter was estimated by assuming circle-shaped grains. The SCF membrane exhibits the smallest grains with an average grain size of 6.5 μm. With increasing lanthanum content and higher sintering temperature the grain size increases to 11.2 μm for LSCF 2882, 14.9 μm for LSCF 4682 and 22.5 μm for LSCF 6482. With higher sintering temperatures an increase of the average grain size was expected. Comparing the LSCF 4682 and LSCF 6482 membranes which were sintered at the same temperature a significant dependence of the lanthanum concentration on grain growth was found.

3.3. *In-situ* X-ray diffraction

To get an overview of the stability of the SCF and LSCF systems a series of high-temperature *in-situ* XRD measurements were conducted for each composition in an atmosphere consisting of 50 vol% CO_2 and 50 vol% N_2. Due to thermodynamic considerations presented in an Elligham diagram it was shown that the $SrCO_3$ phase is stable until 1357 K at a CO_2 pressure of 5×10^4 Pa before it decomposes into SrO and CO_2 [11]. By doping with lanthanum, which exhibits a much higher resistance towards CO_2 and carbonate formation, it is therefore expected to improve the stability of the solid solutions against CO_2. The challenge is to find the optimum amount of strontium that has to be replaced to greatly enhance tolerance against CO_2 and simultaneously keep the oxygen permeation flux as high as possible.

In Fig. 4a a selection of high temperature *in-situ* XRD of SCF in an atmosphere of 50 vol% CO_2/50 vol% N_2 are shown. The cubic $SrCo_{0.8}Fe_{0.2}O_{3-\delta}$ system is stable from room temperature up to 873 K. At 973 K slow decomposition is initialized resulting in a phase mixture of cubic SCF perovskite and orthorhombic strontium carbonate phase. The dwelling time of 60 min was sufficient to facilitate the reaction. At 1073 K cubic cobalt oxide could be detected by XRD data. At 1173 K the orthorhombic $SrCO_3$ transforms into a rhombohedral modification. This behaviour has been already observed for barium and strontium carbonates. According to Strømme et al. this modification is stable at 1193 K [22], which is in good agreement with our high-temperature data. After quenching in CO_2 atmosphere, the formerly single-phase perovskite was decomposed into cubic SCF perovskite, orthorhombic strontium carbonate and cubic cobalt oxide.

The LSCF 2882 and LSCF 4682 solid solutions showed similar behavior as reported for SCF above. The formation of orthorhombic strontium carbonate begun at 973 K. The latter change into the rhombohedral carbonate modification was also observed. After cooling in 50 vol% CO_2/50 vol% N_2 containing atmosphere the perovskites were decomposed into cubic LSCF perovkite, orthorhombic strontium carbonate and cubic cobalt oxide, which was observed for the related $BaCo_{0.4}Fe_{0.4}Zr_{0.2}O_{3-\delta}$ by Efimov et al. [23].

The LSCF 6482 system showed tolerance against CO_2 (Fig. 4b). The perovskite structure is stable at all times on the time scale of the experiment (60 min at each temperature interval of 100 K). At room temperature the perovskite is in a rhombohedral modification. A phase transition from rhombohedral to cubic symmetry could be observed at 673–773 K, which is in agreement with previously reported transition temperatures by Wang et al. [24]. This behaviour was reported for the comparable perovskite system $La_{0.6}Ca_{0.4}Co_{0.8}Fe_{0.2}O_{3-\delta}$ (LCCF 6482) as well, but at

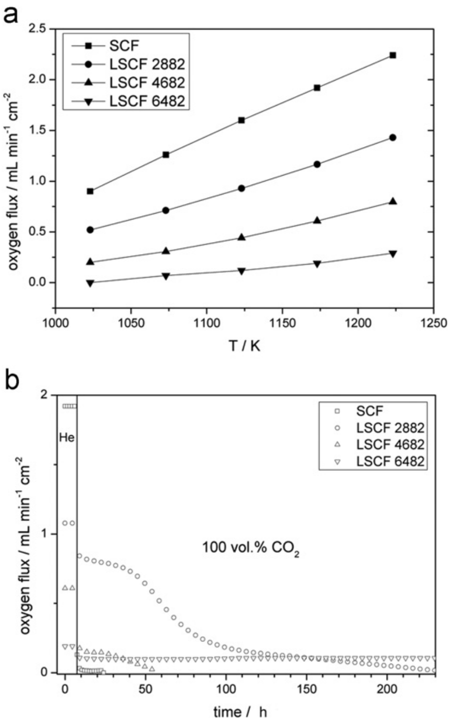

Fig. 5. (a) Oxygen permeation flux of 1 mm thick membranes. Conditions: feed flow rate: 150 mL min^{-1} synthetic air (80 vol% N_2, 20 vol% O_2). Sweep flow rates He=29 mL min^{-1}, Ne=1 mL min^{-1} (b) Long-term measurement at 1173 K. Sweep flow rates: CO_2=29 mL min^{-1}, Ne=1 mL min^{-1}.

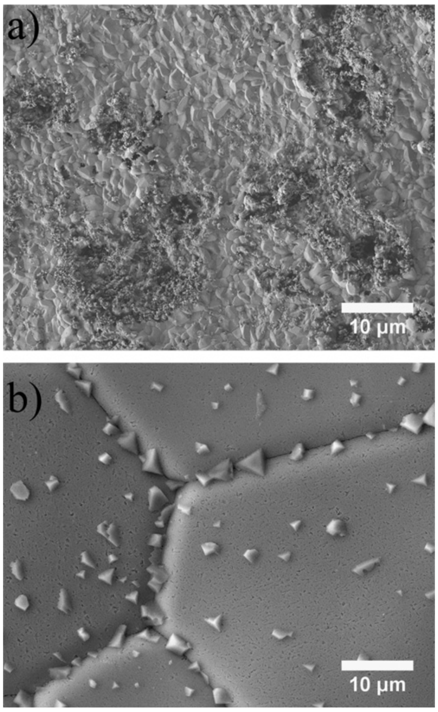

Fig. 6. (a) SCF membrane surface of the sweep side after operation for 24 h in 100 vol% CO_2 and (b) LSCF 6482 membrane surface after operation for over 100 h in 100 vol% CO_2.

slightly higher temperatures by Efimov et al. [11]. At room temperature, the rhombohedral tilt ω was determined to be around -6.6°. With increasing temperature this tilt decreases and turns over into cubic perovskite structure at around 773 K. The transformation took place without a significant change in the cell volume per each formula unit (Table 2). After quenching in 50 vol% CO_2 and 50 vol% N_2 the perovskite conserves the cubic symmetry. This is most probably related to the absence of oxygen during quenching from high temperatures.

3.4. *Permeation*

Oxygen permeation of all membranes was measured under the same conditions. Fig. 5a shows the oxygen permeation flux in an air helium gradient in the temperature range between 1023 and 1223 K. Before the measurements both sides of each membrane were carefully polished with 800 mesh emery paper to obtain a uniform surface area. It is obvious that the SCF solid solution exhibits the highest oxygen permeation flux with a value of 2.2 mL $min^{-1}cm^{-2}$ at 1223 K. By increasing the lanthanum content to 0.2, 0.4 and 0.6 mol% the oxygen permeation flux decreases significantly to 1.4 mL $min^{-1}cm^{-2}$ for LSCF 2882, 0.8 mL $min^{-1}cm^{-2}$ for LSCF 4682 and 0.3 mL $min^{-1}cm^{-2}$ for LSCF 6482. This observation is explained by point defect behavior. By introduction of trivalent lanthanum atoms in the SCF perovskite structure, the amount of oxygen vacancies is reduced to compensate the higher positive charge. Consequentially, this leads to lower oxygen transport. To analyze the materials as possible CO_2-tolerant materials, the membrane reactor was then switched to 100 vol% CO_2 as sweep gas at constant temperature of 1173 K. As is evident from Fig. 4b the oxygen flux of undoped SCF was strongly decreased and almost stopped after 3 h of operation. This is explained by formation of a dense layer of $SrCO_3$ and CoO at the sweep side of the membrane and was proven by *in-situ* XRD and SEM (see Fig. 7 and Section 3.5). The oxygen flux of LSCF 2882 and LSCF 4682 shows a slow decrease with regions of different slopes. After switching to pure CO_2 the oxygen flux decreases slowly and after 40 h of operation for LSCF 2882 and 26 h of operation for LSCF 4682 the flux decreases faster. This is in contrast to SCF membrane. It was expected that the membranes with higher strontium content will lead to a quicker membrane degradation and failure. However, at the first glance contradicting results were obtained because the LSCF 2882 membrane exhibited a longer operation time in CO_2 than the LSCF 4682 membrane. With the addition of small amounts of lanthanum (starting at 0.2 mol%) the oxygen flux is not stopped immediately after switching to CO_2 gas (as observed for SCF) but decreases slowly with time. Since LSCF 2882 exhibited a higher initial oxygen flux (Fig. 5a) due to a higher amount of oxygen vacancies it took a longer time until oxygen permeation broke down completely. Yokokawa et al. described the thermodynamic aspect of the perovskite formation [25]. With increasing lanthanum content the perovskite stabilization energies are increased, which led to relative stabilization of LSCF 2882 and LSCF 4682 compared to the SCF membrane. For the LSCF 6482 composition the perovskite phase may be thermodynamically favored over the carbonate formation, which may explain the good CO_2 tolerance of the material. Furthermore, the process of oxygen transport through a dense membrane is controlled (i) by surface exchange with the gas phase on the sweep side, (ii) by bulk diffusion, and (iii) by surface exchange with the gas phase on the feed side of the membrane [26]. The CO_2 interacts with the membrane by forming carbonates and by adsorption on the surface, which hinders the release of O_2 molecules [27]. Tan et al. observed a correlation between the decreasing overall oxygen permeation flux and the increasing content of CO_2 (0, 20, 50, 70 and 100 vol% CO_2) in the

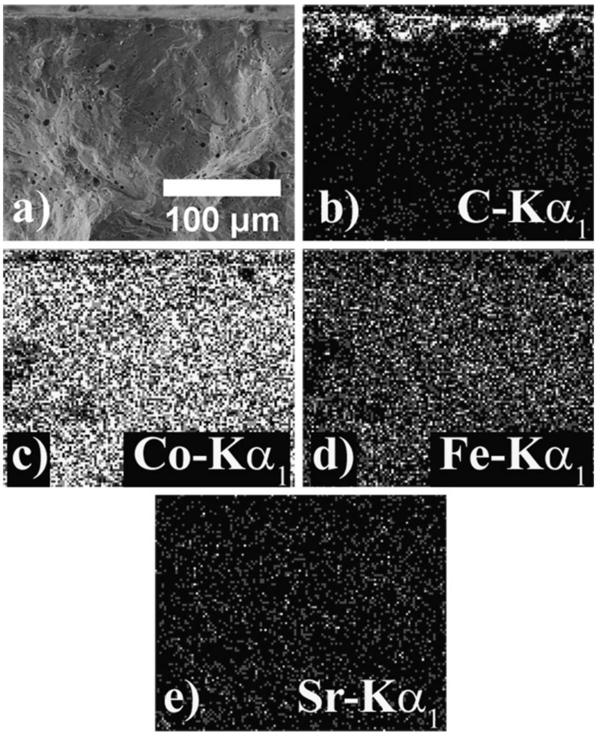

Fig. 7. (a) Fracture surface close to the sweep side of the SCF membrane after operation for 24 h in 100 vol%. CO_2 sweep gas. (b–f) Elemental distribution by EDXS of the area shown in (a).

sweep gas for LSCF 6482 hollow-fiber membranes [12]. They proposed that CO_2 molecules are chemically adsorbed at the membrane surface, thus reducing oxygen partial pressure gradient and surface exchange rates. This was discussed by several groups elsewhere [28–30]. By increasing the lanthanum content the stabilization energy of the perovskite is raised, as expected from the thermodynamic data from the Ellingham diagram [11], which accounts for a higher CO_2 tolerance of the materials. The 1 mm thick LSCF 6482 membrane achieved an oxygen permeation flux of 0.1 mL $min^{-1}cm^{-2}$ and was stable in 100 vol% CO_2 atmosphere for the investigated period of over 200 h continuous operation.

3.5. Membranes after operation in CO_2

Fig. 6 shows the SCF and LSCF 6482 membranes after operation in CO_2-containing atmospheres. For these experiments the membranes were not polished to provide a better comparability before and after exposure to CO_2. However, same conditions as in the oxygen permeation measurements were used. It is obvious that the surface of the SCF membrane (Fig. 6a) was changed as compared to the well defined grain structure as obtained before the CO_2 experiment (Fig. 3a). The segregated blooming phase on the surface was found to be cobalt and iron enriched, thus we expect that it is cobalt oxide as proven by XRD analysis in Section 3.3 and small amounts of iron oxide. The dense surface layer was depleted of iron and cobalt. From the presence carbon it could be concluded that it is strontium carbonate, as expected by *in-situ* XRD (Section 3.3). The operation in CO_2 atmosphere led to a severe etching of the membrane surface. The LSCF 6482 membrane, which was operated for over 200 h in CO_2 atmosphere showed no formation of carbonates or etchings on the surface (Fig. 6b). Segregation of small particles at the surface was observed. The EDXS analysis showed no change of composition compared to the bulk membrane material.

The fracture surface close to the sweep side of the SCF membrane after operation for 24 in pure CO_2 showed an enrichment of carbon in an around 25 µm thick top layer (Fig. 7a and b). Cobalt, iron and strontium were homogenously distributed. This is in contrast to observation for BSCF from Arnold et al. who found a 40–50 µm thick mixed carbonate and perovskite layer [6]. The thicker layer may be related to higher carbonate decomposition enthalpies (ΔH) for the bigger barium ions [31].

The fracture surface of LSCF 2882 and LSCF 6482 were vibrational polished to preserve crystallinity to the very surface and then investigated using backscattered-electron channeling contrast imaging. The LSCF 6482 showed no phase segregation up to the surface of the membrane (Fig. 8b), which shows the good CO_2 tolerance of the material. In Fig. 8a the sweep side region of LSCF 2882 showed phase segregation as expected by *in-situ* XRD. The elemental content could not be identified by EDXS in the SEM. See below for TEM analysis.

TEM Fig. 9a shows two grains in close contact with an inclusion inside the grain boundary. The obtained SAED patterns for the upper and lower grain exhibited the cubic perovskite structure (Fig. 9b and c). The upper grain is orientated along zone axis [0 0 1] and the lower grain is oriented along zone axis [2 0 1].

Furthermore, the region close to the surface was analyzed by different TEM techniques. The STEM annular dark-field micrograph shows regions with different phase composition, which show up with different contrasts (Fig. 10a). The inset shows a SAED pattern of the considered orthorhombic carbonate phase oriented along zone axis [2 1 1]. Following the *in-situ* XRD analysis it was expected to find different phases of cubic strontium-depleted perovskite, orthorhombic strontium carbonate and cubic cobalt oxide. The analysis of the phase composition was performed in STEM mode by EELS. The

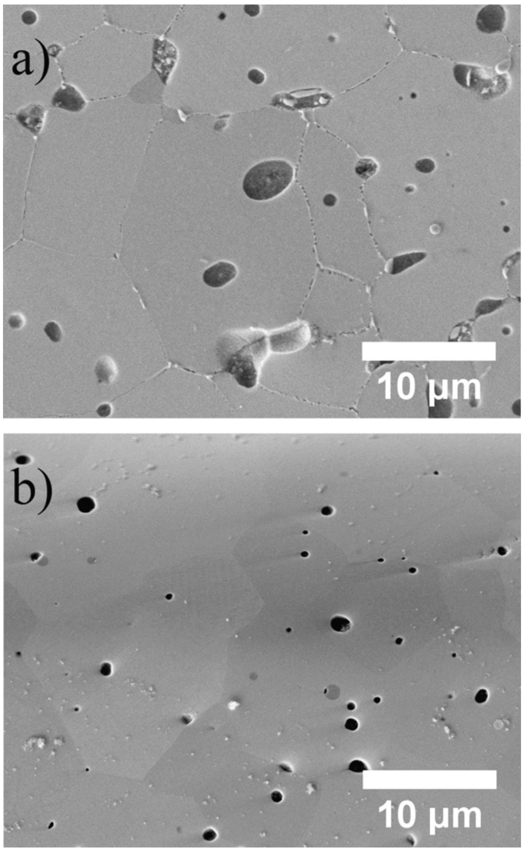

Fig. 8. Channeling contrast images of the membrane cross-section close to sweep side of (a) LSCF 2882 and (b) LSCF 6482 membranes (white residues are Al_2O_3 particles from polishing process, black pinholes are due to closed porosity).

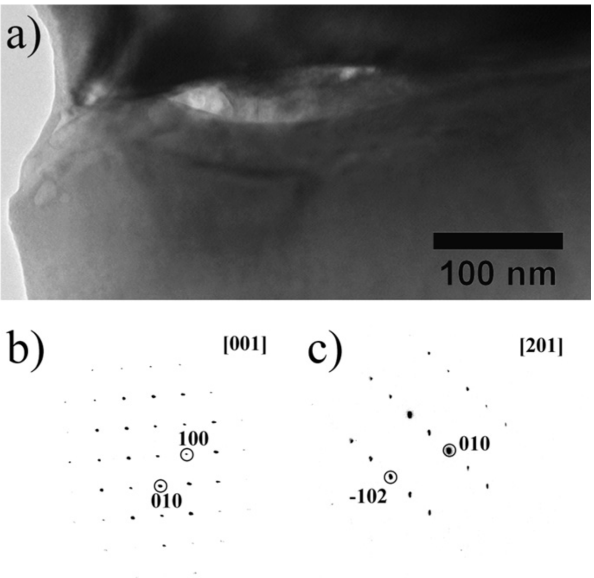

Fig. 9. CO_2-exposed sweep side of LSCF 2882 membrane after 200 h of operation. (a) Bright-field TEM of two grains in close contact. (b) SAED pattern of the upper grain. (c) SAED pattern of the lower grain.

EEL spectrum in Fig. 10b in the energy-loss range of 260–340 eV was obtained from carbonate areas in Fig. 10a. The energies of 272 and 282 eV correspond to the Sr–$M_{2,3}$ edges and the energies of 290 and 300 eV correspond to C–K edges, which are typical for carbonates [32,33], indicating the transition of carbon 1 s electrons into higher unoccupied levels, which correspond to the carbonate C=O double and C–O single bonds [34,35]. In the energy-loss range of 500–900 eV the EEL spectrum of the perovskite exhibits peaks of Fe–$L_{2,3}$ (710 and 723 eV [36]), Co–$L_{2,3}$ (782 and 796 eV) and La–$M_{4,5}$ (837 and 854 eV). These elements were absent in the spectra of the carbonate phase (Fig. 10c). The O–K ELNES shown in Fig. 10d is very sensitive to the local environment of the oxygen atoms. The carbonate spectrum exhibits a narrow peak at 533 eV followed by the most intense peak at 539 and a smaller peak at 544 eV. This is in accordance with literature about $SrCO_3$ [34]. The O–K ELNES for the perovskite is slightly different. The leading peak at 530 eV corresponds to hybridization of the cobalt and iron d_{xy},d_{xz} and d_{yz} orbitals with unoccupied oxygen 2p states via 2p–3d interactions, as observed for complex oxides [37]. The following peaks at 532 and 538 eV may be attributed to additional interactions with the ns and np states of lanthanum and strontium. The small peak at 541 eV is related to excitations of O 2p electrons into unoccupied Co, Fe d_z^2 and d_{x-y}^2 orbitals [6]. Furthermore, cobalt oxide was detected in the near-surface region (spectra not shown). The carbonate areas are very sensitive to the high-energetic electron beam and holes were drilled easily into them. Beam irradiation causes the decomposition of $SrCO_3$ into SrO and CO_2, which lead to a change of the O–K edges [34]. The perovskite grains were not damaged by the electron beam in the typical time scale of an EELS experiment (several minutes).

4. Conclusions

The series of $La_{1-x}Sr_xCo_{0.8}Fe_{0.2}O_{3-\delta}$ (x=1, 0.8, 0.6, 0.4) was successfully synthesised by a sol–gel method. All powders and membranes exhibit cubic perovskite structure, except the rhombohedral LSCF 6482, which adopts cubic perovskite structure at temperatures above 673 K. *In-situ* XRD measurements and long-term oxygen permeation measurements in CO_2-containing atmosphere reveal the high tolerance of LSCF 6482 towards CO_2. Oxygen permeation experiments in an air/helium gradient showed that with increasing lanthanum content the oxygen permeation flux decreases. Microstructure analysis of the membranes after CO_2 operation showed that the carbonate preferentially forms a dense layer at the carbon dioxide exposed sweep side of the membranes.

Acknowledgements

The authors greatly acknowledge financial support from the Chinese-German Centre for Science (GZ676) and the Deutsche Forschungsgemeinschaft (FE 928/4-1) and fruitful discussions with Prof. Jürgen Caro.

References

[1] International Energy Agency, World energy outlook 2011, OECD, Paris, 2011.
[2] R. Bredesen, K. Jordal, O. Bolland, High-temperature membranes in power generation with CO_2 capture, Chem. Eng. Process 43 (2004) 1129–1158.

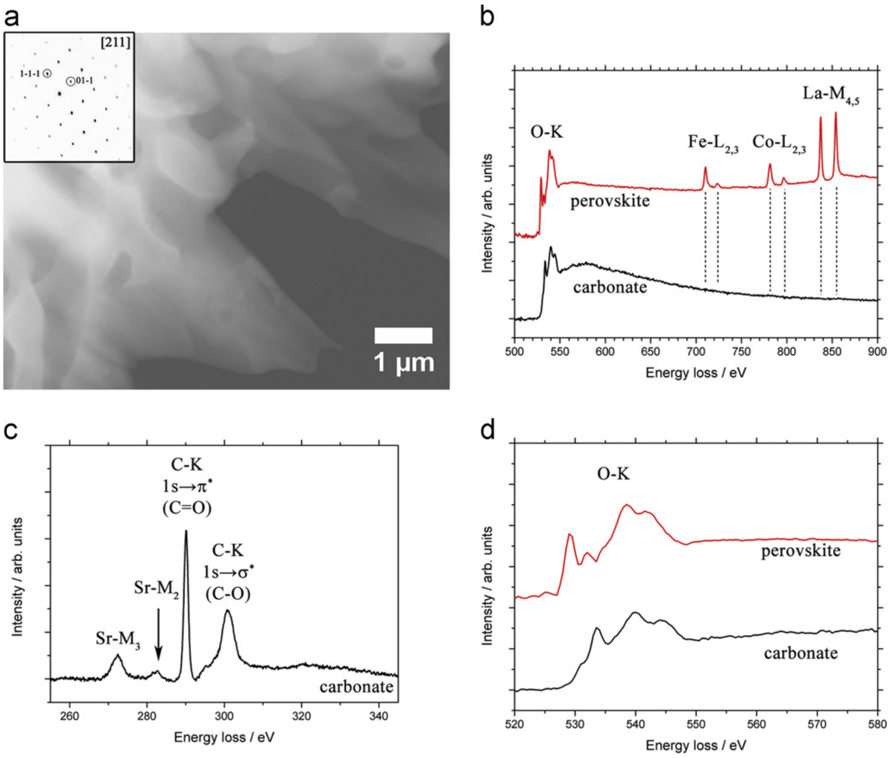

Fig. 10. (a) STEM-HAADF micrograph of the sweep-side surface of a LSCF 2882 membrane after 200 h of operation in 100 vol% CO_2. Inset shows the SAED pattern of the carbonate phase (b) EEL spectrum in the energy-loss range from 500 to 900 eV of the perovskite and carbonate phase with O–K, Fe–L, Co–L and La–M ionization edges. (c) EEL spectrum in the energy-loss range from 260 to 340 eV of the carbonate phase with Sr–M and C–K ionization edges. (d) Characteristic O–K ELNES of the perovskite and carbonate phase.

[3] A.R. Smith, J. Klosek, A review of air separation technologies and their integration with energy conversion processes, Fuel Process Technol. 70 (2001) 115–134.

[4] H. Stadler, F. Beggel, M. Habermehl, B. Persigehl, R. Kneer, M. Modigell, P. Jeschke, Oxyfuel coal combustion by efficient integration of oxygen transport membranes, Int. J. Greenhouse Gas Control 5 (2011) 7–15.

[5] X. Tan, K. Li, Oxygen production using dense ceramic hollow fiber membrane modules with different operating modes, AIChE J. 53 (2007) 838–845.

[6] M. Arnold, H. Wang, A. Feldhoff, Influence of CO_2 on the oxygen permeation performance and the microstructure of perovskite-type $(Ba_{0.5}Sr_{0.5})(Co_{0.8}Fe_{0.2})O_{3-\delta}$ membranes, J. Membr. Sci. 293 (2007) 44–52.

[7] T. Klande, K. Efimov, S. Cusenza, K.D. Becker, A. Feldhoff, Effect of doping, microstructure, and CO_2 on $La_2NiO_{4+\delta}$-based oxygen-transporting materials, J. Solid State Chem. 184 (2011) 3310–3318.

[8] H. Luo, K. Efimov, H. Jiang, A. Feldhoff, H. Wang, J. Caro, CO_2-stable and cobalt-free dual phase membrane for oxygen separation, Angew. Chem. Int. Ed. 50 (2011) 759–763.

[9] W. Chen, C. Chen, L. Winnubst, Ta-doped $SrCo_{0.8}Fe_{0.2}O_{3-\delta}$ membranes: phase stability and oxygen permeation in CO_2 atmosphere, Solid State Ionics 196 (2011) 30–33.

[10] Q. Zeng, Y. Zuo, C. Fan, C. Chen, CO_2-tolerant oxygen separation membranes targeting CO_2 capture application, J. Membr. Sci. 335 (2009) 140–144.

[11] K. Efimov, T. Klande, N. Juditzki, A. Feldhoff, Ca-containing CO_2-tolerant perovskite materials for oxygen separation, J. Membr. Sci 389 (2012) 205–215.

[12] X. Tan, N. Liu, B. Meng, J. Sunarso, K. Zhang, S. Liu, Oxygen permeation of $La_{0.6}Sr_{0.4}Co_{0.8}Fe_{0.2}O_3$ hollow fiber membranes with highly concentrated CO_2 exposure, J. Membr. Sci 389 (2012) 216–222.

[13] J. Martynczuk, M. Arnold, A. Feldhoff, Influence of grain size on the oxygen permeation performace of perovskite-type $(Ba_{0.5}Sr_{0.5})(Co_{0.8}Zn_{0.2})O_{3-\delta}$ membranes, J. Membr. Sci. 322 (2008) 375–382.

[14] H. Wang, C. Tablet, A. Feldhoff, J. Caro, Investigation of phase structure, sintering, and permeability of perovskite-type $Ba_{0.5}Sr_{0.5}Co_{0.8}Fe_{0.2}O_{3-\delta}$ membranes, J. Membr. Sci. 262 (2005) 20–26.

[15] W.T.A. Harrison, T.H. Lee, Y.L. Yang, D.P. Scarfe, L.M. Liu, A.J. Jacobson, A neutron diffraction study of two strontium cobalt iron oxides, Mater. Res. Bull. 30 (1995) 621–630.

[16] T.V. Aksenova, M.V. Anan'ev, L.Y. Gavrilova, V.A. Cherepanov, Phase equilibria and crystal structures of solid solutions in the system $LaCoO_3$–$SrCoO_{2.5}$–$SrFeO_3$–$LaFeO_3$, Inorg. Mater. 43 (2007) 296–300.

[17] J.E. ten Elshof, J. Boeijsma, Powder diffraction of $La_1A_xCo_{0.8}Fe_{0.2}O_3$ (A=Sr, Ba), Powder Diffr. 11 (1996) 28–30.

[18] R.D. Shannon, Revised effective ionic radii and systematic studies of interatomic distances in halides and chalcogenides, Acta Crystallogr., Sect. A: Found. Crystallogr. 32 (1976) 751–767.

[19] V.M. Goldschmidt, Die Gesetze der Kristallchemie, Naturwiss 14 (1926) 477–485.

[20] R.H. Mitchell, Perovskites: Modern and Ancient, Almaz Press Inc, Ontario, Canada, 2002.

[21] M.D. Abramoff, P.J. Magelhaes, S.J. Ram, Image processing with image J, Biophotonics Int. 11 (2004) 36–42.

[22] K.O. Strømme, On the crystal structures of the high-temperature forms of strontium and barium carbonate and structurally related compounds, Acta Chem. Scand. A 29 (1975) 105–110.

[23] K. Efimov, O. Czuprat, A. Feldhoff, *In-situ* X-ray diffraction study of carbonate formation and decomposition in perovskite-type BCFZ, J. Solid State Chem. 184 (2011) 1085–1089.

[24] S. Wang, M. Katsuki, M. Dokiya, T. Hashimoto, High temperature properties of $La_{0.6}Sr_{0.4}Co_{0.8}Fe_{0.2}O_{3-\delta}$ phase structure and electrical conductivity, Solid State Ionics 159 (2003) 71–78.

[25] H. Yokokawa, N. Sakai, T. Kawada, M. Dokiya, Thermodynamic stabilities of perovskite oxides for electrodes and other electrochemical materials, Solid State Ionics 52 (1992) 43–56.

[26] H.J.M. Bouwmeester, H. Kruidhof, A.J. Burggraf, Importance of the surface exchange kinetics as rate limiting step in oxygen permeation through mixed-conducting oxides, Solid State Ionics 72 (1994) 185–194.

[27] J.E. ten Elshof, H.J.M. Bouwmeester, H. Verweij, Oxygen transport through $La_{1-x}Sr_xFeO_{3-\delta}$ membranes. II. Permeation in air/CO, CO_2 gradients, Solid State Ionics 89 (1996) 81–92.

[28] J.A. Lane, J.A. Kilner, Oxygen surface exchange on gadolinia doped ceria, Solid State Ionics 136-137 (2000) 927–932.

[29] K. Yashiro, S. Onuma, A. Kaimai, Y. Nigara, T. Kawada, J. Mizusaki, K. Kawamura, T. Horita, H. Yokokawa, Mass transport properties of $Ce_{0.9}Gd_{0.1}O_{2-\delta}$ at the surface and in the bulk, Solid State Ionics 152–153 (2002) 469–476.

[30] I.V. Khromushin, T.I. Aksenova, Z.R. Zhotabaev, Mechanism of gas–solid exchange processes for some perovskites, Solid State Ionics 162–163 (2003) 37–40.

[31] K.H. Stern, E.L. Weise, High temperature properties and decomposition of inorganic salts, Part 2: Carbonates, NSRDS-NBS 30 (1969) 1–27.

[32] F. Hofer, P. Golob, New examples for near-edge fine structures in electron energy loss spectroscopy, Ultramicroscopy 21 (1987) 379–384.

[33] M. Cai, S. Liu, K. Efimov, J. Caro, A. Feldhoff, H. Wang, Preparation and hydrogen permeation of $BaCe_{0.95}Nd_{0.05}O_{3-\delta}$ membranes, J. Membr. Sci. 343 (2009) 90–96.

[34] J.L. Mansot, V. Golabkan, L. Romana, T. Césaire, Chemical and physical characterization by EELS of strontium hexanoate reverse micelles and strontium carbonate nanophase produced during tribological experiments, J. Microsc. 210 (2003) 110–118.

[35] J. Martynczuk, M. Arnold, H. Wang, J. Caro, A. Feldhoff, How $(Ba_{0.5}Sr_{0.5})(Fe_{0.8}Zn_{0.2})O_{3-\delta}$ and $(Ba_{0.5}Sr_{0.5})(Co_{0.8}Fe_{0.2})O_{3-\delta}$ perovskites form via an EDTA/citric acid complexing method, Adv. Mater. 19 (2007) 2134–2140.

[36] A. Feldhoff, J. Martynczuk, M. Arnold, M. Myndyk, I. Bergmann, V. Šepelák, W. Gruner, U. Vogt, A. Hähnel, J. Woltersdorf, Spin-state transition of iron in $(Ba_{0.5}Sr_{0.5})(Fe_{0.8}Zn_{0.2})O_{3-\delta}$ perovskite, J. Solid State Chem. 182 (2009) 2961–2971.

[37] A.S. Sefat, G. Amow, M. Wu, G.A. Botton, J.E. Greedan, High-resolution EELS study of the vacancy-doped metal/insulator system, $Nd_{1-x}TiO_3$, $x=0$ to 0.33, J. Solid State Chem. 178 (2005) 1008–1016.

2.4 Effect of CO_2 and SO_2 on oxygen permeation and microstructure of $(Pr_{0.9}La_{0.1})_2(Ni_{0.74}Cu_{0.21}Ga_{0.05})O_{4+\delta}$ membranes

Reprinted with kind permission from Elsevier:
Yanying Wei, Olga Ravkina, Tobias Klande and Armin Feldhoff
Journal of Membrane Science **429** (2013) 147-154.
doi:10.1016/j.memsci.2012.11.075

Journal of Membrane Science 429 (2013) 147–154

Contents lists available at SciVerse ScienceDirect

Journal of Membrane Science

journal homepage: www.elsevier.com/locate/memsci

Effect of CO_2 and SO_2 on oxygen permeation and microstructure of $(Pr_{0.9}La_{0.1})_2(Ni_{0.74}Cu_{0.21}Ga_{0.05})O_{4+\delta}$ membranes

Yanying Wei [a], Olga Ravkina [b], Tobias Klande [b], Haihui Wang [a,*], Armin Feldhoff [b,**]

[a] School of Chemistry & Chemical Engineering, South China University of Technology, 381 Wushan Road, Guangzhou 510640, China
[b] Institute of Physical Chemistry and Electrochemistry, Leibniz University Hannover, Callinstrasse3-3A, Hannover D-30179, Germany

ARTICLE INFO

Article history:
Received 12 September 2012
Received in revised form
28 November 2012
Accepted 29 November 2012
Available online 5 December 2012

Keywords:
Membrane
Oxygen permeation
CO_2
SO_2
Chemical stability

ABSTRACT

U-shaped K_2NiF_4-type oxide hollow-fiber membranes based on $(Pr_{0.9}La_{0.1})_2(Ni_{0.74}Cu_{0.21}Ga_{0.05})O_{4+\delta}$ (PLNCG) were successfully prepared through a phase-inversion spinning process. The effect of CO_2 and SO_2 on the oxygen permeation, phase structure and the microstructure of the material were investigated. In situ XRD patterns of PLNCG under air, Ar and CO_2 atmosphere in the range from room temperature to 1000 °C were performed and indicate a good phase stability under oxidizing and reducing conditions as well as chemical stability against CO_2. Effects of SO_2 concentration in the sweep gas and the feed gas on the oxygen permeation flux through the PLNCG hollow-fiber membrane, as well as on membrane's microstructure were also investigated. $Pr_2O_2SO_4$, $La_2O_2SO_4$ and NiO formed after SO_2 treatment and the material developed some porosity on the side exposed to SO_2. The observations indicate that the PLNCG membrane is highly stable against CO_2 but sensitive to SO_2.

1. Introduction

Carbon dioxide is generally held to be one of the most significant contributors to global warming. Fossil-fuel fired power plants are responsible for more than one third of the total global CO_2 emissions [1]. Therefore, reducing the CO_2 emission from fossil fuel-fired power plants becomes a key issue. One solution might be provided by the oxyfuel process, which involves a denitrogenation of the combustion gas and consists in the burning of fossil fuel in an oxygen-enriched atmosphere to produce a flue gas highly concentrated in CO_2. Recently, ceramic membranes with mixed oxygen-ionic and electronic conductivity (MIEC membranes) have attracted increasing attention due to their potential applications in oxygen supply for power stations with CO_2 sequestration according to the oxyfuel concept [2]. In the natural gas-based oxyfuel power plant process, the membrane is integrated in a recirculated flue gas stream, which consists of 25–30 vol% water vapor, 70–75 vol% CO_2, 1–3 vol% O_2 and a SO_2 content of about 400 ppm [3]. For this reason, the MIEC membranes used in the oxyfuel process should not only have good oxygen permeability, but also good chemical stability especially at least against these major components.

So far, most studies of the MIEC membranes have been focused on the perovskite-type oxides which have unrivalled oxygen permeation fluxes [4–15]. However, the perovskite material containing alkaline-earth elements such as Ba and Sr are quite sensitive to CO_2 due to the formation of carbonates [16–21]. Yi et al. [17] found that the perovskite-type $BaCo_{0.4}Fe_{0.4}Nb_{0.2}O_{3-\delta}$ membrane material decomposes to form a compact $BaCO_3$ surface layer and a subjacent porous decomposed zone which consists of CoO and a Co-depleted phase after being exposed to CO_2 atmosphere. Czuprat et al. [18] and Yang et al. [20] also found the formation of $BaCO_3$ and $SrCO_3$ in the XRD patterns of $BaCo_xFe_yZr_zO_{3-\delta}$ $(x+y+z=1)$ and $La_{0.1}Sr_{0.9}Co_{0.5}Fe_{0.5}O_{3-\delta}$, respectively, after the treatment in CO_2-containing atmosphere. The oxygen permeation flux through these alkaline-earth elements-containing perovskite membranes decreases sharply once CO_2 is introduced in the sweep gas or the feed air [16–21].

Recently, intensive efforts have been made to develop CO_2-tolerant mixed conducting oxides. The dual-phase membranes made of ionic conductor and electronic conductor, are proposed as alternatives to mono-phase perovskites, because these oxides inherently possess high chemical stability against acidic or reducing gases. Zhu et al. [22] reported dual-phase membrane for CO_2 capture with higher oxygen permeation flux, while this dual-phase membrane still contains 3% alkaline-earth metal which could has a negative influence on the long-term stability in the practical application of high CO_2 concentration. Luo et al. [23] developed two kinds of alkaline-earth metal-free dual-phase oxygen permeable membrane materials, 60 wt% $Ce_{0.9}Gd_{0.1}O_{2-\delta}$–

---

[*] Corresponding author. Tel./fax: +86 20 8711 0131.
[**] Corresponding author. Tel.: +49 511 762 2940; fax: +49 511 7621 9121.
E-mail addresses: hhwang@scut.edu.cn (H. Wang), armin.feldhoff@pci.uni-hannover.de (A. Feldhoff).

0376-7388/$ - see front matter © 2012 Elsevier B.V. All rights reserved.
http://dx.doi.org/10.1016/j.memsci.2012.11.075

40 wt% $NiFe_2O_4$ and 40 wt% Fe_2O_3–60 wt% $Ce_{0.9}Gd_{0.1}O_{2-\delta}$, which exhibit good stability under CO_2-containing atmosphere, but the oxygen permeation fluxesare relatively low. Liu's group [24] designed a new CO_2-tolerant ion-transporting ceramic membrane system with an external short circuit for oxygen separation. This membrane system showed an appreciated oxygen permeation flux at intermediate temperatures, however, an expensive noble metal layer was used, which turns out as a drawback. In recent years, alkaline-earth metal-free K_2NiF_4-type MIEC membrane materials have been found to be CO_2-tolerant, such as $La_2NiO_{4+\delta}$ [25,26]. In our previous work [27,28], we investigated previously characterized material $(Pr_{0.9}La_{0.1})_2(Ni_{0.74}Cu_{0.21}Ga_{0.05})O_{4+\delta}$ (PLNCG) [29], which is also proved to be a CO_2-stable material with an oxygen permeation flux of 0.9 ml/min/cm^2 with a hollow-fiber architecture.

However, the chemical stability against SO_2 is also important for some applications. There are much less publications available concerning the impact of SO_2. So far, only Engels et al. [26] reported the effect of SO_2 on the stability and the oxygen permeation of the oxygen permeable membrane. However, publications about the detailed effect of SO_2 on the oxygen permeation of the MIEC membranes, as well as the chemical stability are not available from the literature. In this paper, the effect of CO_2 and especially SO_2 on the oxygen permeation and microstucture of PLNCG hollow-fiber membrane are investigated in detail.

2. Experimental

2.1. Sample preparation

The sol–gel route based on citric acid and EDTA as complexing and gelation agents has been adapted to prepare the PLNCG powder [27]. For spinning hollow-fiber membranes, the powder was ball-milled for 24 h and then it was dried using a spray dryer (Büchi Mini Spray Dryer, B-290) with a nozzle of 1 μm. The obtained fine powder was used for the preparation of the U-shaped hollow-fiber membrane. The U-shaped PLNCG hollow fibers were fabricated using a wet spinning/sintering technology [30]. The spinning solution was composed of 9.29 wt% polyethersulfone (PESf, A-300, BASF), 37.18 wt% 1-methyl-2-pyrrolidinone (NMP, AR Grade, purity $>99.8\%$, Kermel Chem Inc, Tianjin, China), 0.93 wt% polyvinyl pyrrolidone (PVP, K30, Boao biotech co, Shanghai, China) and 52.60 wt% PLNCG powder. A spinneret with an orifice diameter of 1.5 mm and an inner diameter of 1.0 mm was used to obtain the hollow-fiber precursors. Deionized water and tap water were used as the internal and external coagulants, respectively. Afterwards, the PLNCG hollow-fiber precursors were sintered at 1300 °C for 3 h with the air flow rate of 60 ml/min to remove the polymer and get gas-tight membranes.

2.2. X-ray diffraction analysis and thermal expansion measurement

Crystal structure and lattice parameters of PLNCG powder were characterized by in-situ high-temperature X-ray diffraction (in situ XRD) under different atmospheres, including air, Ar and CO_2 using D8 Advance, Bruker-AXS, with Cu $K_{\alpha1,2}$ radiation. The measurements were conducted in a high-temperature cell HTK 1200N (Anton-Paar) between room temperature and 1273 K. The heating rate was 12 K/min with an equilibration time of 30 min before each measurement. Data sets were recorded in step-scan mode in the angular range of $10^\circ \leq 2\theta \leq 90^\circ$ at an interval of 0.02°. The coefficient of thermal expansion (CTE) of the sintered PLNCG hollow fiber membrane was determined with a high-temperature dilatometer (Model Netzsch DIL 402C, Germany) in the range from room temperature to 1000 °C in Ar atmosphere and the heating rate was 10 K/min.

2.3. Scanning electron microscopy and EDXS analysis

Field-emission scanning electron microscopy (FE-SEM) imaging was performed using a JEOL JSM-6700 Field-emission instrument at a low excitation voltage of 2 kV. An energy-dispersive X-ray spectrometer (EDXS), Oxford Instruments INCA-300, with an ultrathin window was used for the elemental analysis at an excitation voltage of 15 kV.

2.4. Oxygen permeation measurements

The effect of different SO_2 concentrations in the sweep gas and feed gas side on the oxygen permeation fluxes through the U-shaped PLNCG hollow-fiber membranes were investigated in a high-temperature permeation cell, as shown in our previous work [28]. The U-shaped PLNCG-hollow fiber membrane was sealed in a corundum tube with two channels by a commercial ceramic sealant (HT767, Hutian, China). Air or He mixed with some ppm-concentration SO_2 went through the shell (feed) and core (sweep) side of the hollow-fiber membrane, respectively. To compare the switching behavior under He/CO_2, air was fed in the shell side while He or CO_2 was swept in the core side. The gas-flow rates were controlled by mass-flow controllers (MFC, Seven Star D08-4F/ZM) calibrated using a soap-bubble flow meter. The composition of the permeated gases were measured using an online gas chromatograph (GC, Agilent 7890) with a thermal conductivity detector (TCD) detector. The leakage of the oxygen due to the imperfect sealing at high temperatures was less than 0.5% during all the experiments. The details for calculation of the oxygen permeation flux are given elsewhere [28,30].

3. Results and discussion

3.1. CO_2 effect on PLNCG material

The stability of metal oxides in the CO_2-containing atmospheres can be estimated using the Ellingham diagram shown in Fig. 1. This type of graphical representation allows the prediction of thermodynamic stability of carbonates at given temperature and CO_2 partial pressure. The dashed lines give the chemical potential of CO_2 at various partial pressures. Additionally, the solid lines represent the chemical potential of CO_2 during the decomposition of corresponding carbonates. These values are conforming to the negative values of standard free enthalpy of decomposition reaction and were calculated elsewhere [31–33]. The chemical potential of CO_2 for decomposition reaction of $Pr_2O_2CO_3$ was calculated from thermodynamic data given elsewhere [34]. The relative stability of carbonates can be evaluated through the comparison of the CO_2 chemical potential at given temperature. From thermodynamic point of view, the carbonate is stable until the CO_2 chemical potential of the decomposition reaction is lower than at the corresponding partial pressure. For example, $La_2(CO_3)_3$ is stable up to 450 °C and 10^5 Pa CO_2 partial pressure (Fig. 1, bold dashed line). With increasing temperature, above 450 °C, it decomposes into $La_2O_2CO_3$. Accordingly, the PLNCG material should be stable in a CO_2 containing atmosphere at 10^5 Pa above 900 °C.

As can be seen from the Ellingham diagram in Fig. 1, $NiCO_3$ is less stable than $La_2(CO_3)_3$, $La_2O_2CO_3$ and $Pr_2(CO_3)_3$. The decomposition of $CuCO_3$ is spontaneous from ambient temperature upward and there are no known gallium carbonate compounds [35]. The thermal stability of carbonate anion decreases with

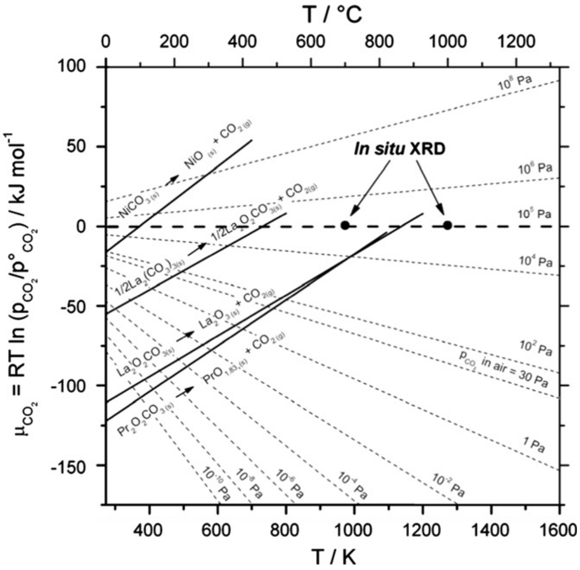

Fig. 1. Ellingham diagram with decomposition temperatures of carbonates under different CO_2 partial pressures. The dashed lines represent the chemical potential of CO_2 in the surrounding atmosphere for different partial pressures. $p(CO_2)=101.3$ kPa refers to standard conditions. The black dots represent conditions for the in situ XRD experiments shown in Figs. 2 and 3.

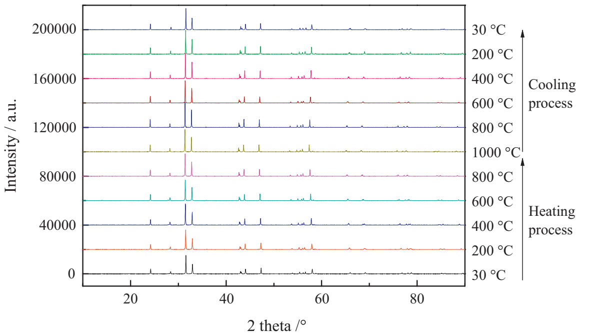

Fig. 2. In situ XRD patterns of PLNCG under CO_2 atmosphere ($p(CO_2)=10^5$ Pa) in the range from room temperature to 1000 °C.

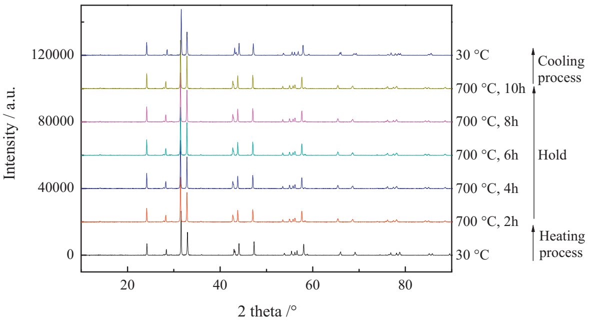

Fig. 3. In situ XRD patterns of PLNCG under CO_2 atmosphere ($p(CO_2)=10^5$ Pa) during holding at 700 °C for 10 h.

increasing polarising power of the associated cation [36]. Summarizing, the small cationic size and high charge promote the carbonate decomposition. The polarization of the CO_3^{2-}-anion induces distortion and weakening of the C–O–bonds, which alleviates the CO_2 elimination from the carbonate. The relativly big ionic radius of La^{3+} ($r=136$ pm) and Pr^{3+} ($r=118$ pm) cations, as compared with Ni^{2+} ($r=69$ pm), Cu^{2+} ($r=73$ pm) and Ga^{3+} ($r=62$ pm) [37] causes higher stability of $La_2(CO_3)_3$, $La_2O_2CO_3$ and $Pr_2(CO_3)_3$. Based on the given information about the ionic radius and charge of copper and gallium ions, it is possible to make a qualitative estimation for CO_2 chemical potential of carbonate decomposition reaction according to Fig. 1. The Cu^{2+} ion has the same charge, but a bigger ionic radius as compared to Ni^{2+} ion. As a result, similar, but more negative values for CO_2 chemical potential can be expected. Ga^{3+} with the smallest ionic size and highest charge forms the thermally less stable carbonate, so that the values of the CO_2 chemical potential should be positive even at temperatures lower than 273 K (i.e., the respective line for Ga carbonate is expected to lie higher in Fig. 1 than the one for Ni carbonate). However, it should be noted that the Ellingham diagram gives only a rough outline of the thermodynamic stability of the binary oxides or carbonates. The stabilization energy of the PLNCG structure may also play an important role on the tolerance of the material against CO_2, just as well as the kinetic of the decomposition reaction, which are not considered in the Ellingham diagram [38].

Nevertheless, according to the thermodynamic considerations, a high chemical stability of the PLNCG material in a CO_2-containing environment can be expected and is in agreement with our previous findings [27,28]. Furthermore, the in situ XRD measurements were performed on PLNCG under CO_2 atmosphere ($p(CO_2)=10^5$ Pa) in the range from room temperature to 1000 °C. As shown in Fig. 2, no additional reflections that would indicate the presence of other phases, e.g., carbonates or phase transitions during heating or cooling processes. These results are in agreement with the Ellingham diagram. At given pressure and temperature (10^5 Pa, 1000 °C) the carbonates are not stable, because the CO_2 chemical potential of the decomposition reaction is higher than the one of corresponding partial pressure (Fig. 1, right black dot). It can be easily deduced from Fig. 1 that the carbonate tends to form when PLNCG is exposed to CO_2 atmosphere at lower temperature. For a deeper study on the CO_2-tolerance of PLNCG, the in situ XRD patterns of PLNCG under CO_2 atmosphere ($p(CO_2)=10^5$ Pa) was acquired not only in the heating and cooling process, but also when the temperature was hold at 700 °C for up to 10 h. According to the Ellingham diagram, LaO_2CO_3 and PrO_2CO_3 should be stable under these conditions (Fig. 1, left dot). Accordingly, as shown in Fig. 3, all the in situ diffractograms of PLNCG powder after different stages of CO_2 treatment at 700 °C show the pure K_2NiF_4 structure and no carbonate reflections are observed. This is in accordance with the findings of Efimov et al. [32] After the holding, the PLNCG powder sample still maintains the original phase structure when the temperature decreases down to 30 °C which indicates the PLNCG has a good chemical stability against CO_2 atmosphere.

Fig. 4 compares the in situ XRD patterns of PLNCG in air, Ar and CO_2 atmosphere at 1000 °C. There is no difference among the phase structures in different atmospheres, which are the same with the pure K_2NiF_4 structure (see Figs. 2 and 3). The result indicates that PLNCG possesses, at high temperatures, not only good phase stability in air (oxidizing) and argon (reducing) atmospheres but as well as good chemical stability under CO_2 atmosphere. Due to thermal expansion, the PLNCG unit cell volumes expand and the lattice parameters increase with increasing temperature. Therefore, the diffraction peaks in XRD patterns shown in Figs. 2 and 3 shift to low angle at high temperatures and they shift back to high angle during cooling process. Using the temperature-dependent shift of the cell volume during these

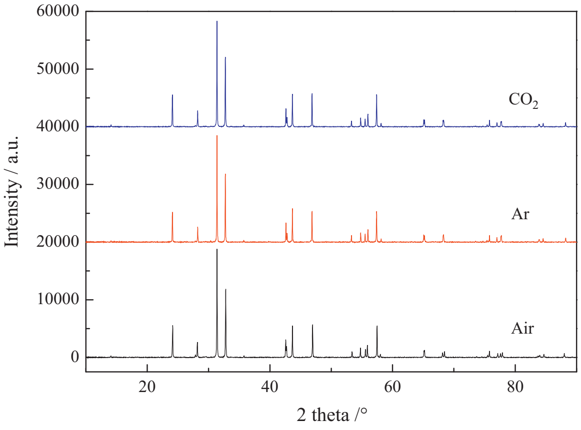

Fig. 4. Comparison of the in situ XRD patterns of PLNCG in air, Ar and CO_2 atmosphere at 1000 °C.

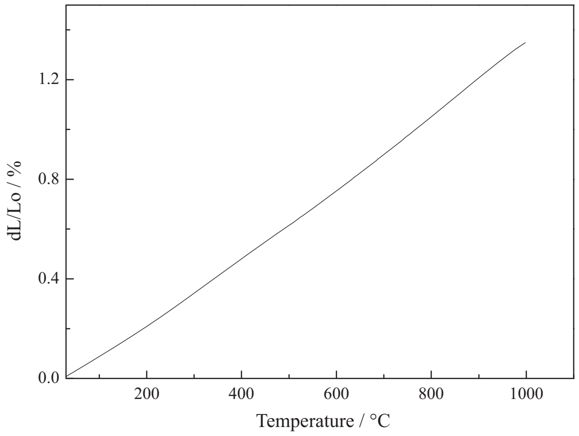

Fig. 5. Thermal expansion curve for the sintered PLNCG hollow fiber membrane in Ar atmosphere in the range of room temperature to 1000 °C.

measurements, the CTEs of PLNCG under different atmospheres are estimated to be $13.9 \times 10^{-6}\,K^{-1}$, $15.0 \times 10^{-6}\,K^{-1}$ and $15.1 \times 10^{-6}\,K^{-1}$ under the atmosphere of synthetic air, Ar and CO_2, respectively. Fig. 5 presents the actual measurement results of thermal expansion curve from the dilatometer and the actual CTE calculated based on these data. It can be seen that the CTE of PLNCG increases with the temperature increasing, which is attributed to the increasing atomic spacing at elevated temperature, i.e., the average distance between particles among the lattice increases with increasing temperature. The CTE value of PLNCG in Ar from 30 °C to 1000 °C is $13.9 \times 10^{-6}\,K^{-1}$, which is approximately the same as the value calculated from the diffraction peak shift of the in situ XRD results. Klande et al. [25] found the CTE of $La_2NiO_{4+\delta}$ was $15.1 \times 10^{-6}\,K^{-1}$ under an atmosphere containing 50 vol% CO_2 and 50 vol% air while it was also reported in the literature the CTE value of $11.9 \times 10^{-6}\,K^{-1}$ and $13.7 \times 10^{-6}\,K^{-1}$ measured in air [39,40]. The CTE of PLNCG calculated here is in a good agreement with the published results [39,40]. A relationship between the phase stability and CTE was proposed [41]: the lower the CTE, the higher is the thermomechanical stability of the materials, which is desirable for industrial applications to prevent the failure of the membranes. Compared to 3D perovskites (such as $Ba_{0.5}Sr_{0.5}Co_{0.8}Fe_{0.2}O_{3-\delta}$ or $Ba_{0.5}Sr_{0.5}Fe_{0.8}Zn_{0.2}O_{3-\delta}$) with CTE values between $20 \times 10^{-6}\,K^{-1}$ and $24 \times 10^{-6}\,K^{-1}$ [42–45], PLNCG possesses a better thermomechanical stability, which promotes the application in oxyfuel techniques for CO_2 capture and storage.

3.2. SO_2 effect on PLNCG material

Fig. 6 shows the effect of SO_2 with different concentrations in the sweep gas on the oxygen permeation flux through the U-shaped PLNCG hollow-fiber membrane. When helium is used as the sweep gas, a constant oxygen permeation flux of 0.9 ml/min/cm^2 is obtained. When the helium containing SO_2 is used as the sweep gas, the oxygen permeation flux deceases with time and SO_2 concentrations. Once the sweep gas containing 84 ppm SO_2 is used, the oxygen permeation flux decreases by 22% immediately and it keeps decreasing with time gradually. The decrease of the oxygen permeation flux is accelerated with a higher SO_2 concentration in the sweep gas. When the sweep gas contains 383 ppm SO_2, a drop of 88% oxygen permeation flux is observed within 60 min. It was also found by Engels et al. [26] that SO_2 in the sweep gas causes an immediate stagnation of the oxygen permeation through $Sr_{0.5}Ca_{0.5}Mn_{0.8}Fe_{0.2}O_{3-\delta}$ and $La_2NiO_{4+\delta}$ membranes. When the sweep gas is shifted back to pure helium, the initial oxygen permeation fluxes were reached again gradually. Zhang et al. [46] have investigated the SO_2 poisoning effect on the perovskite catalyst based on $LaFe_{0.8}Cu_{0.2}O_3$ and they found there were two distinct poisoning mechanisms depending on SO_2 concentration: (i) at low SO_2 concentration, a reversible poisoning was observed due to the competitive adsorption of SO_2 and reactants as well as the coverage of active sites by surface sulfite and sulfate species; (ii) at higher SO_2 concentration, a severe sulfatation with destruction of the perovskite structure and the generation of sulfate phases was observed, which leads to an irreversible loss of catalyst activity. Coming back to our work, PLNCG undergoes a sulfation reaction which leads to the formation of sulfate and resulting in the decrease of the oxygen permeation flux with the following equation:

$$\begin{aligned}&(Pr_{0.9}La_{0.1})_2(Ni_{0.74}Cu_{0.21}Ga_{0.05})O_{4+\delta}+SO_2+(1.025-\delta)/2O_2\\&\quad=0.1La_2O_2SO_4+0.9Pr_2O_2SO_4+0.74NiO+0.21CuO\\&\qquad+0.025Ga_2O_3 \qquad (1)\end{aligned}$$

Therefore, it takes a longer time for the oxygen permeation flux through the membrane to recover if it was exposed to a higher concentrated SO_2-containing atmosphere as it was observed in Fig. 6.

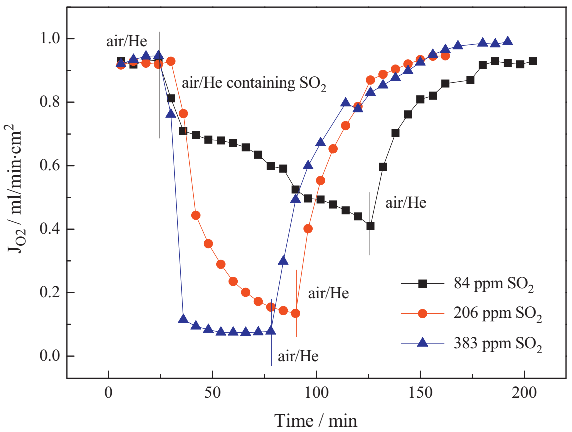

Fig. 6. Effect of SO_2 with different concentrations in sweep gas on the oxygen permeation flux through the U-shaped PLNCG hollow-fiber. Conditions: $T=975$ °C, $F_{air}=180$ ml/min, $F_{He+SO_2}=60$ ml/min.

Fig. 7 represents the effect of SO_2 with different concentrations in feed gas on the oxygen permeation flux through the U-shaped PLNCG hollow-fiber membrane. The SO_2 in the feed gas causes an immediate decrease of the oxygen permeation rate. Even when the sweep gas is shifted back to pure helium, it is difficult to regenerate within a few hours and reach the initial oxygen permeation flux for PLNCG hollow-fiber membrane. Compared to the effect of SO_2 in the sweep side, it seems that the errosion happens much more deeply and seriously in the feed side. The reaction between SO_2 and PLNCG can be identified by Eq. (1). SO_2 in the feed side elevates the sulfate formation due to the higher oxygen partial pressure.

Fig. 8 shows the comparison of the switching behavior under He/CO_2 between the membranes which has been exposed to SO_2 or not. The feed gas is air and the sweep gas changes between He and CO_2 here. The oxygen permeation experiment was performed on two PLNCG membranes. One of the PLNCG membrane has been exposed to SO_2-containing atmosphere while the other one has been not. At the beginning, the oxygen permeation fluxes through these two membranes are similar. When the sweep gas is changed from He to CO_2, the oxygen permeation flux through the fresh membrane is reduced to 0.90 ml/min/cm^2. Only a slight decrease of the oxygen permeation flux through the PLNCG hollow-fiber membrane is observed. When the sweep gas is shifted back to pure He, the oxygen permeation flux through the PLNCG hollow-fiber membrane can be recovered immediately. During this cycle of the sweep gas shifting between He and CO_2, the oxygen permeation flux through the fresh PLNCG hollow-fiber membrane exhibits good resistance to CO_2 and excellent reversibility. However, the oxygen permeation flux through the membrane exposed to SO_2 decreases sharply, it drops even lower than 0.6 ml/min/cm^2 once the sweep gas changes from He to CO_2. After about 20 min, the oxygen permeation flux hits the bottom and then begins to increase gradually with time. The oxygen permeation flux through the membrane can be recovered by sweeping with pure CO_2 for 2 h. Engels et al. [26] reported the oxygen permeability recovery lines of $Sr_{0.5}Ca_{0.5}Mn_{0.8}Fe_{0.2}O_{3-\delta}$ and $La_2NiO_{4+\delta}$ membranes swept by CO_2 after exposed to SO_2-containing atmosphere. Compared to that of the perovskite $Sr_{0.5}Ca_{0.5}Mn_{0.8}Fe_{0.2}O_{3-\delta}$ membrane, the oxygen permeation flux through the $La_2NiO_{4+\delta}$ membrane can be recovered by sweeping with pure CO_2 again, although the required recovery time is much longer at lower temperatures.The recovery trend of the oxygen permeation flux through the PLNCG membrane after exposure to SO_2 in Fig. 8 is similar to that of $La_2NiO_{4+\delta}$ membrane reported.

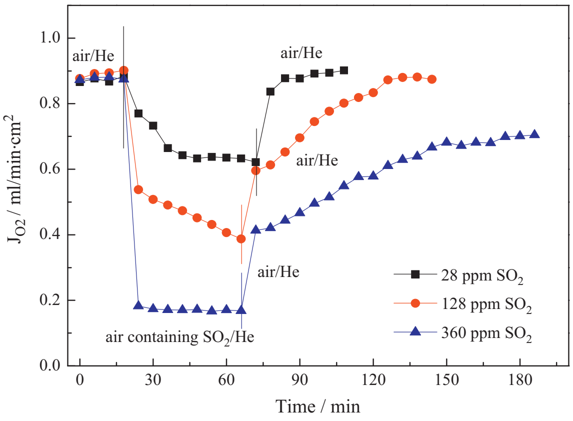

Fig. 7. Effect of SO_2 with different concentrations in feed gas on the oxygen permeation flux through the U-shaped PLNCG hollow-fiber. Conditions: $T = 975$ °C, $F_{air+SO_2} = 180$ ml/min, $F_{He} = 60$ ml/min.

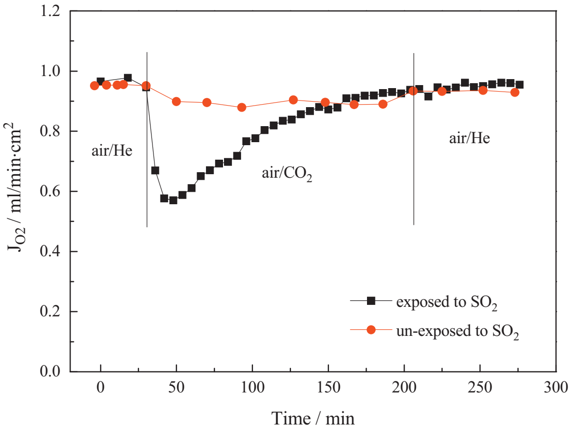

Fig. 8. Comparison of the switching behavior under He/CO_2 in the sweep gas between the membranes which has been exposed to SO_2 or not. Conditions: $T = 975$ °C, $F_{air} = 180$ ml/min, $F_{He} = F_{CO_2} = 60$ ml/min.

After the oxygen permeation test with SO_2, the U-shaped PLNCG hollow-fiber membrane sample was characterized by SEM and EDXS. The SEM micrographs of the fracture surface of a PLNCG hollow fiber after exposure to SO_2 on the sweep side at 975 °C are shown in Fig. 9a. A significant change of the morphology close to the sweep side can be clearly observed. The transformation affects a region in a distance of 150 μm from the sweep side surface, which is equal to a half thickness of the fiber wall. Fig. 9b shows the middle of the fracture surface, representing the feed-side region (I) and sweep-side region (II) in a higher magnification. As can been seen from the micrograph, the material developed high porosity on the side exposed to SO_2. The change of the morphology can be an evidence for the destruction of the PLNCG structure. That assumption is supported by the EDX spectra presented in Fig. 9c and Fig. 9d. The material on the sweep side (II) contains, among the PLNCG elements, sulfur, which is not existent in the feed-side region (I). Although the oxygen permeation flux through the membrane can be recovered, but the densified structure cannot be recovered unless the membrane was re-sintered at high temperatures.

The poisoning effect of SO_2 on perovskites or perovskite-type materials was already reported, but there is still a lack of investigation on detailed mechanism of poisoning and its influence on the oxygen permeation. Engels et al. [26] reported about a negative effect of 360 ppm SO_2 in the sweep gas on the oxygen permeation flux for $La_2NiO_{4+\delta}$ tubes. After 72 h operation at 850 °C, an up to 50 nm dense sulfur-containing layer on the surface was formed [26]. Unfortunately, the sulfur-containing phase was not identified.

In order to identify the formed sulfur-containing phases, the fiber exposed to SO_2 was crashed and analyzed using XRD technique. The corresponding XRD patterns of the fresh and spent PLNCG hollow fiber membranes are shown in Fig. 10. X-ray diffraction result of the fresh one indicated that the phase of the PLNCG hollow fiber membrane sintered at 1300 °C is the pure K_2NiF_4-structure without sulfate. The polyethersulfone has been decomposed and the sulfur has been run out during the high temperature sintering process. Therefore, it can be deduced that the amount of the residual sulfur from polyethersulfone can be ignored. It has to be pointed out that although polyethersulfone is used for the preparation of hollow fibers, the membrane can be operated for a long time with a steady oxygen permeation flux [47]. In other words, compared to the foreign sulfur from SO_2-

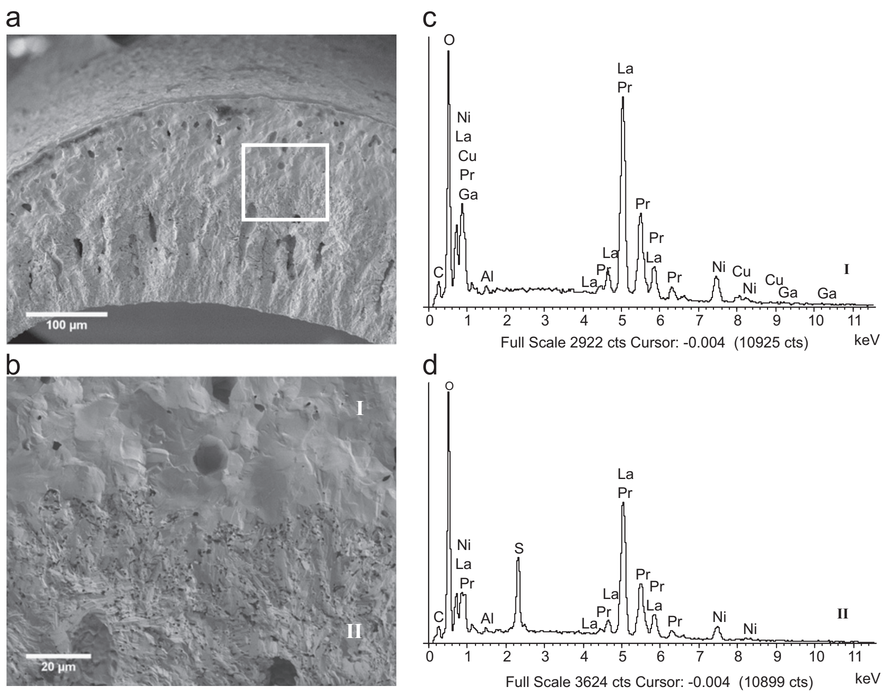

Fig. 9. (a) SEM micrograph of PLNCG's fractured fiber cross-section after exposing to SO_2 on the sweep (core) side. (b) SEM micrograph of the tagged region from (a) with labeling areas (I) and (II) for elemental analysis. (c) and (d) EDX spectra of the selected areas. The Al line appears due to ball milling of the powder.

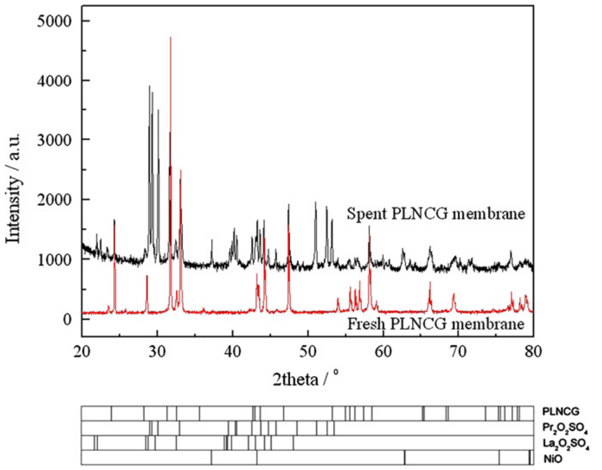

Fig. 10. XRD patterns of the fresh PLNCG hollow fiber membrane sintered at 1300 °C and the spent fiber after SO_2 measurement. The Bragg positions for PLNCG, sulfur containing phases $Pr_2O_2SO_4$, $La_2O_2SO_4$ and NiO are marked with ticks at the bottom of the figure.

containing atmosphere, the negative effect of the inherent sulfur from polyethersulfone can be omitted. The XRD pattern of the spent one demonstrates that the PLNCG structure is destroyed and new phases are formed during the permeation measurement with SO_2 in the sweep gas. The main products are identified as $Pr_2O_2SO_4$, $La_2O_2SO_4$ and NiO. The formation of $La_2O_2SO_4$ is earlier reported for $La_{0.9}Sr_{0.1}CoO_3$ perovskite exposed to SO_2 at 700 °C [48].

In general, the thermal stability of sulfates follows the same trend as the thermal stability of the carbonates. Again, the polarising power of the corresponding cation rules over the thermal sulfate decomposition. The distortion of the sulfate ion increases with increasing electronegativity and decreasing ionic radius. So the sulfates with big and lower charged cations are expected to be more stable [35,49]. It is known from the investigations of roasting processes that the copper sulfate decomposes from approximately 760 °C and nickel sulfate from 820 °C. The decomposition ratio of $CuSO_4$ and $NiSO_4$ is almost 100% at 950 °C [50]. The low stability of copper sulfate at 975 °C operating temperature could approve our XRD results.

As a consequence of their relative big ionic radii, lanthanum and praseodymium ions form more stable sulfate compounds as nickel and copper. Lanthanum and praseodymium sulfates decompose to corresponding oxides with intermediate oxysulfates, which are stable in the temperature range from 900 °C to 1200 °C [35,49,51]. Consequently, to avoid the poisoning of the PLNCG membrane with sulfur it might be helpful to operate at temperatures above 1200 °C, which then, however, will be close to the sintering temperature.

Our results demostrate that the U-shaped PLNCG hollow-fiber membrane exhibits good oxygen permeability and excellent chemical stability in CO_2-containing atomsphere. On the other hand, PLNCG is a SO_2-sensitive material due to the metals of Pr and La, which tend to form sulfate under SO_2-containing atmospheres.

4. Conclusions

Phase structure and stability of a K_2NiF_4-type material based on $(Pr_{0.9}La_{0.1})_2(Ni_{0.74}Cu_{0.21}Ga_{0.05})O_{4+\delta}$ (PLNCG) was studied by in situ X-ray diffraction (in situ XRD) in the temperature range of 30–1000 °C under different atmospheres (synthetic air, Ar and CO_2). The PLNCG powder sample maintains the original phase structure during the heating and cooling process in each atmosphere which indicates the PLNCG has a good phase stability under oxdidzing and reducing conditions as well as a good chemical stability against CO_2. By analyzing the lattice parameters, the thermal expansion coefficients (CTEs) of PLNCG under synthetic air, Ar and CO_2 are obtained to be $13.9 \times 10^{-6}\,K^{-1}$, $15.0 \times 10^{-6}\,K^{-1}$ and $15.1 \times 10^{-6}\,K^{-1}$, respectively. The effects of SO_2 on the oxygen permeation flux through the PLNCG hollow-fiber membrane are also investigated. The oxygen permeation flux decreases sharply once SO_2 is added in the sweep gas or feed gas. It needs a period of time for the oxygen permeation flux through the membrane recovery when SO_2 is added in the sweep side while it is more difficult if SO_2 is added in the feed side. The XRD, SEM and EDXS results represent that the sulfate forms after SO_2 treatment. The main products are identified as $Pr_2O_2SO_4$, $La_2O_2SO_4$ and NiO and the material develops high porosity on the side exposed to SO_2. To sum up, the U-shaped PLNCG hollow-fiber membrane exhibits good oxygen permeability and excellent chemical stability in CO_2-containing atomosphere, while it is sensitive against SO_2 due to the metals of Pr and La, which tend to form sulfate under SO_2-containing atmospheres.

Acknowledgements

The authors greatly acknowledge the financial support from the Chinese-German Centre for Science (GZ676), the Deutsche Forschungsgemeinschaft (FE 928/4-1), Natural Science Foundation of China (no. 21176087), the Specialized Research Fund for the Doctoral Program of Higher Education (no. 20110172110013), the International Cooperation Project supported by the Department of Science and Technology of Guangdong Province (no. 2009B050700017) and the National Science Fund for Distinguished Young Scholars of China (no. 21225625). The authors also acknowledge Prof. J. Caro in this cooperation. Y.Y. Wei also acknowledges H.X. Luo for the technical support.

References

[1] D. Grielen, J. Podkanski, Prospects for CO_2 Capture and Storage, OECD/IEA, Paris, France, 2004.

[2] X.Y. Tan, K. Li, A. Thursfield, I.S. Metcalfe, Oxyfuel combustion using a catalytic ceramic membrane reactor, Catal. Today 131 (2008) 292–304.

[3] C. Weber, M. Mueller,Thermodynamische Modellrechnungen zum OXYCOA-LAC-Prozess, VDI-Berichte 1988, 23. Deutscher Flammentag, Berlin, 2007, p. 503–508.

[4] Z. Liu, G. Zhang, X. Dong, W. Jiang, W. Jin, N. Xu, Fabrication of asymmetric tubular mixed-conducting dense membranes by a combined spin-spraying and co-sintering process, J. Membr. Sci. 415-416 (2012) 313–319.

[5] S. Song, P. Zhang, M. Han, S.C. Singhal, Oxygen permeation and partial oxidation of methane reaction in $Ba_{0.9}Co_{0.7}Fe_{0.2}Nb_{0.1}O_{3-\delta}$ oxygen permeation membrane, J. Membr. Sci. 415-416 (2012) 654–662.

[6] T. Nagai, W. Ito, T. Sakon, Relationship between cation substitution and stability of perovskite structure in $SrCoO_{3-\delta}$-based mixed conductors, Solid State Ionics 177 (2007) 3433–3444.

[7] G. Zhang, Z. Liu, N. Zhu, W. Jiang, X. Dong, W. Jin, A novel Nb_2O_5-doped $SrCo_{0.8}Fe_{0.2}O_{3-\delta}$ oxide with high permeability and stability for oxygen separation, J. Membr. Sci. 405-406 (2012) 300–309.

[8] R.V. Franca, A. Thursfield, I.S. Metcalfe, $La_{0.6}Sr_{0.4}Co_{0.2}Fe_{0.8}O_{3-\delta}$ microtubular membranes for hydrogen production from water splitting, J. Membr. Sci. 389 (2012) 173–181.

[9] C.Y. Tsai, A.G. Dixon, Y.H. Ma, W.R. Moser, M.R. Pascucci, Dense perovskite, $La_{(1-x)}A'_xFe_{1-y}Co_yO_{3-\delta}$ (A'=Ba, Sr, Ca), membrane synthesis, applications and characterization, J. Am. Ceram. Soc. 81 (1998) 1437–1444.

[10] S. Baumann, J.M. Serra, M.P. Lobera, S. Escolástico, F. Schulze-Kueppers, W.A. Meulenberg, Ultrahigh oxygen permeation flux through supported $Ba_{0.5}Sr_{0.5}Co_{0.8}Fe_{0.2}O_{3-\delta}$ membranes, J. Membr. Sci. 377 (2011) 198–205.

[11] Z.P. Shao, W.S. Yang, Y. Cong, H. Dong, J.H. Tong, G.X. Xiong, Investigation of the permeation behaviour and stability of a $Ba_{0.5}Sr_{0.5}Co_{0.8}Fe_{0.2}O_{3-\delta}$ oxygen membrane, J. Membr. Sci. 172 (2000) 177–188.

[12] A. Leo, S. Smart, S. Liu, J.C.D. da Costa, High performance perovskite hollow fibres for oxygen separation, J. Membr. Sci. 368 (2011) 64–68.

[13] J. Sunarso, J. Motuzas, S. Liu, J.C.D. da Costa, Bi-doping effects on the structure and oxygen permeation properties of $BaSc_{0.1}Co_{0.9}O_{3-\delta}$ perovskite membranes, J. Membr. Sci. 361 (2010) 120–125.

[14] Q.H. Yin, Z.H. Yang, Y.S. Lin, Effects of microstructure on oxygen transport in perovskite-type oxides, J. Mater. Sci. 41 (2006) 4865–4870.

[15] J. Sunarso, S. Liu, J.C.D. da Costa, Structure effect on the oxygen permeation properties of barium bismuth iron oxide membranes, J. Membr. Sci. 351 (2010) 44–49.

[16] M. Arnold, H.H. Wang, A. Feldhoff, Influence of CO_2 on the oxygen permeation performance and the microstructure of perovskite-type $(Ba_{0.5}Sr_{0.5})(Co_{0.8}Fe_{0.2})O_{3-\delta}$ membranes, J. Membr. Sci. 293 (2007) 44–52.

[17] J.X. Yi, M. Schroeder, T. Weirich, J. Mayer, Behavior of $Ba(Co, Fe, Nb)O_{3-\delta}$ perovskite in CO_2-containing atmospheres: degradation mechanism and materials design, Chem. Mater. 22 (2010) 6246–6253.

[18] O. Czuprata, M. Arnold, S. Schirrmeister, T. Schiestel, J. Caro, Influence of CO_2 on the oxygen permeation performance of perovskite-type $BaCo_xFe_yZr_zO_{3-\delta}$ hollow fiber membranes, J. Membr. Sci. 364 (2010) 132–137.

[19] J. Martynczuk, K. Efimov, L. Robben, A. Feldhoff, Performance of zinc-doped perovskite-type membranes at intermediate temperatures for long-term oxygen permeation and under a carbon dioxide atmosphere, J. Membr. Sci. 344 (2009) 62–70.

[20] Q. Yang, Y.S. Lin, M. Bulow, High temperature sorption separation of air for producing oxygen-enriched CO_2 stream, AIChE J. 52 (2006) 574–581.

[21] J.H. Tong, W.S. Yang, B.C. Zhu, R. Cai, Investigation of ideal zirconium-doped perovskite-type ceramic membrane materials for oxygen separation, J. Membr. Sci. 203 (2002) 175–189.

[22] X.F. Zhu, H.Y. Liu, Y. Cong, W.S. Yang, Novel dual-phase membranes for CO_2 capture via an oxyfuel route, Chem. Commun. 48 (2012) 251–253.

[23] H.X. Luo, K. Efimov, H.Q. Jiang, A. Feldhoff, H.H. Wang, J. Caro, CO_2-stable and cobalt-free dual-phase membrane for oxygen separation, Angew. Chem. Int. Ed. 50 (2011) 759–763.

[24] K. Zhang, Z.P. Shao, C.Z. Li, S.M. Liu, Novel CO_2-tolerant ion-transporting ceramic membranes with an external short circuit for oxygen separation at intermediate temperatures, Energy Environ. Sci. 5 (2012) 5257–5264.

[25] T. Klande, K. Efimov, S. Cusenza, K.D. Becker, A. Feldhoff, Effect of doping, microstructure, and CO_2 on $La_2NiO_{4+\delta}$-based oxygen-transporting materials, J. Solid State Chem. 184 (2011) 3310–3318.

[26] S. Engels, T. Markus, M. Modigell, L. Singheiser, Oxygen permeation and stability investigations on MIEC membrane materials under operating conditions for power plant processes, J. Membr. Sci. 370 (2011) 58–69.

[27] J. Tang, Y.Y. Wei, L.Y. Zhou, Z. Li, H.H. Wang, Oxygen permeation through a CO_2-tolerant mixed conducting oxide $(Pr_{0.9}La_{0.1})_2(Ni_{0.74}Cu_{0.21}Ga_{0.05})O_{4+\delta}$, AIChE J. 58 (2012) 2473–2478.

[28] Y.Y. Wei, J. Tang, L.Y. Zhou, J. Xue, Z. Li, H.H. Wang, Oxygen separation through U-shaped hollow fiber membrane using pure CO_2 as sweep gas, AIChE J. 58 (2012) 2856–2864.

[29] M. Yashima, M. Enoki, T. Wakita, R. Ali, Y. Matsushita, F. Izumi, T. Ishihara, Structural disorder and diffusional pathway of oxide ions in a doped Pr_2NiO_4-based mixed conductor, J. Am. Chem. Soc. 130 (2008) 2762–2763.

[30] Y.Y. Wei, H.F. Liu, J. Xue, Z. Li, H.H. Wang, Preparation and oxygen permeation of U-shaped perovskite hollow fiber membranes, AIChE J. 57 (2011) 975–984.

[31] I. Barin, F. Sauert, G. Platzki, Thermochemical Data of Pure Substances, third ed., Wiley-VCH, Weinheim, 1995.

[32] K. Efimov, M. Arnold, J. Martynczuk, A. Feldhoff, Crystalline intermediate phases in the sol gel-based synthesis of $La_2NiO_{4+\delta}$, J. Am. Ceram. Soc. 92 (2008) 876–880.

[33] K. Efimov, T. Klande, N. Juditzki, A. Feldhoff, Ca-containing CO_2-tolerant perovskite material for oxygen separation, J. Membr. Sci. 389 (2012) 205–215.

[34] R. Sharma, H. Hinode, L. Eyring, A study of praseodymium hydroxy carbonate and praseodymium carbonate hydrate, J. Solid State Chem. 92 (1991) 401–419.

[35] K.H. Stern, High Temperature Properties and Thermal Decomposition of Inorganic Salts with Oxyanions, CRC Press, Boca Raton, London, New York, Washington D.C, 2011.

[36] V.M. Goldschmidt, T. Barth, G. Lunde, W. Zachariasen, Geochemische Verteilungsgesetze der Elemente: 7, Die Gesetze der Krystallochemie, Oslo, I Kommission Hos Jacob Dybwad 1926 (1926) 58–74.

[37] R.D. Shannon, Revised effective ionic radii and systeatic studies of interatomic distances in halides and chalcogenides, Acta Crystakkogr. Sec. A 32 (1976) 751–767.

[38] H. Yokokawa, N. Sakay., M. Dokiya, Thermodynamic stabilities of perovskite oxides for electrodes and other electrochemical materials, Solid State Ionics 52 (1992) 43–56.

[39] M. Al Daroukh, V.V. Vashook, H. Ullmann, F. Tietz, I. Arual Raj, Oxides of the AMO_3 and A_2MO_4-type: structural stability, electrical conductivity and thermal expansion, Solid State Ionics 158 (2003) 141–150.

[40] G. Amow, S.J. Skinner, Recent developments in Ruddlesden-Popper nickelate systems for solid oxide fuel cell cathodes, J. Solid State Electrochem. 10 (2006) 538–546.

[41] H.H. Wang, C. Tablet, W.S. Yang, J. Caro, In situ high temperature X-ray diffraction studies of mixed ionic and electronic conducting perovskite-type membranes, Mater. Lett. 59 (2005) 3750–3755.

[42] S. McIntosh, J.F. Vente, W.G. Haije, D.H.A. Blank, H.J.M. Bouwmeester, Oxygen stoichiometry and chemical expansion of $Ba_{0.5}Sr_{0.5}Co_{0.8}Fe_{0.2}O_{3-\delta}$ measured by in-situ neutron diffraction, Chem. Mater. 18 (2006) 2187–2193.

[43] J.F. Vente, W.G. Haije, Z.S. Rak, Performance of functional perovskite membranes for oxygen production, J. Membr. Sci. 276 (2006) 178–184.

[44] K. Efimov, T. Halfer, A. Kuhn, P. Heitjans, J. Caro, A. Feldhoff, Novel cobalt-free oxygen-permeable perovskite type membrane, Chem. Mater. 22 (2010) 1540–1544.

[45] A. Feldhoff, J. Martynczuk, M. Arnold, M. Myndyk, I. Bergmann, V. Sepelak, W. Gruner, U. Vogt, A. Hahnel, J. Woltersdorf, Spin-state transition of iron in $Ba_{0.5}Sr_{0.5}Fe_{0.8}Zn_{0.2}O_{3-\delta}$ perovskite, J. Solid State Chem. 182 (2009) 2961–2971.

[46] R.D. Zhang, H.S. Alamdari, S. Kaliaguine, SO_2 poisoning of $LaFe_{0.8}Cu_{0.2}O_3$ perovskite prepared by reactive grinding during NO reduction by C_3H_6, Appl. Catal. A 340 (2008) 140–151.

[47] Y. Wei, J. Tang, L. Zhou, Z. Li, H. Wang, Oxygen permeation through U-shaped K_2NiF_4-type oxide hollow-fiber membranes, Ind. Eng. Chem. Res. 50 (2011) 12727–12734.

[48] H. Wang, Y. Zhu, R. Tan, W. Yao, Study on the poisoning mechanism of sulfur dioxid for perovskite $La_{0.9}Sr_{0.1}CoO_3$ model catalysts, Catal. Lett. 82 (2002) 199–204.

[49] K.H. Stern, E.L. Weise, High Temperature Properties and Decomposition of Inorganic Salts, Part 1. Sulfates, NSRDS, Washington, 1966.

[50] P. Pandher, S. Thomas, D. Yu, M. Barati, T. Utigard, Sulfate formation and decomposition of nickel concentrates, Metall. Mater. Trans. B. 42B (2011) 291–299.

[51] R.L. Wilfong, L.P. Domingues, L.R. Furlong, Thermogravimetric analysis of five salts of praseodymium, neodymium and samarium, J. Am. Ceram. Soc. 47 (1964) 240–241.

3 Phase stability of oxide ceramics

3.1 Summary

This chapter adresses the effect of membrane microstructure, phase composition and crystallographic structure on the functionality of oxide ceramics as oxygen-transporting materials. A way to design the material microstructure, is to vary the synthesis conditions on the one side and the synthesis techniques on the other side.

The influence of different sintering techniques on La_2NiO_4 ceramic is reported in Section 3.2. By applying field-assisted sintering technique / spark plasma sintering (FAST/SPS), a drastic reduction of ceramic grain size (0.015 μm^2 area in polished specimen) can be achieved, as compared to a common pressureless sintering (6.11 μm^2 area in polished specimen). The microstructure analysis of membranes is performed by transmission and scanning electron microscopy combined with energy-dispersive X-ray spectroscopy and electron energy-loss spectroscopy. Additionally, phase transition from orthorhombic to tetragonal crystallographic structure in the FAST/SPS material is observed and investigated by temperature-dependent X-ray powder diffraction.

Section 3.3 deals with investigations on BSCF and SCF membranes. Grain growth is controlled by varying the dwell time during sintering. TEM investigations reveal a phase transition at the oxygen-depleted sweep side of the membrane. At 1373 K the cubic perovskite phase decomposes to an ordered $SrCo_{0.8}Fe_{0.2}O_{2.5}$ brownmillerite by-phase.

The decomposition passway of the cubic BSCF perovskite into trigonal $Ba_3Co_{10}O_{17}$ lamellae and 2H-hexagonal perovskite under elevated oxygen pressure (1 to 50 bar) is reported in Section 3.4. Thermogravimetric results show a high-temperature and low-temperature separation processes. The structures are characterized by different electron microscopy techniques.

3.2 Influence of different sintering techniques on microstructure and phase composition of oxygen-transporting ceramic

Reprinted with kind permission from Elsevier:
Olga Ravkina, Jan Räthel and Armin Feldhoff
Journal of the European Ceramic Society **35** (2015) 2833-2843.
doi:10.1016/j.jeurceramsoc.2015.03.039

Available online at www.sciencedirect.com
ScienceDirect
Journal of the European Ceramic Society 35 (2015) 2833–2843
www.elsevier.com/locate/jeurceramsoc

Influence of different sintering techniques on microstructure and phase composition of oxygen-transporting ceramic

Olga Ravkina[a,*], Jan Räthel[b], Armin Feldhoff[a]

[a] *Institute of Physical Chemistry and Electrochemistry, Leibniz Universität Hannover, Callinstrasse 3A, D-30167 Hannover, Germany*
[b] *Fraunhofer Institute for Ceramic Technologies and Systems IKTS, Winterbergstraße 28, D-01277 Dresden, Germany*

Received 26 February 2015; received in revised form 27 March 2015; accepted 28 March 2015
Available online 15 April 2015

Abstract

The membrane microstructure and phase composition of Ruddlesden–Popper-type $La_2NiO_{4+\delta}$ ceramics, which were prepared by field-assisted sintering technique/spark plasma sintering (FAST/SPS) process or by conventional pressing and pressureless sintering were investigated. As starting material, a $La_2NiO_{4+\delta}$ powder, with an average particle size of 0.2 μm was used. The grain-size distribution of the resulting membranes varied from 0.015 μm² for FAST/SPS sintered ceramic to 6.11 μm² for pressureless sintered membrane. The microstructure analysis of membranes was performed by transmission and scanning electron microscopy combined with energy-dispersive X-ray spectroscopy and electron energy-loss spectroscopy. Phase transition from orthorhombic to tetragonal crystallographic structure in FAST/SPS material was investigated by temperature-dependent X-ray powder diffraction. The effect of sintering technique and grain size on the oxygen permeation performance of the membranes is discussed with respect to impurities in the material.

Keywords: Ruddlesden–Popper phase; Phase transition; FAST/SPS sintering; Microstructure; Electron microscopy

1. Introduction

Due to promising electrical properties, layered Ruddlesden–Popper oxide materials from the $La_2NiO_{4+\delta}$ system have attracted considerable attention in a broad field of interest. Ruddlesden–Popper phases show great promise for application as ferroelectric devices [1,2], gas sensors [3], and oxygen-transporting membranes [4–7] or in intermediate temperature solid oxide fuel cells [8]. The application in energy conversion technology such as solid oxide fuel cell and oxy-fuel combustion require chemically and thermally stable materials in carbon dioxide atmosphere at working conditions [9–14]. Lanthanum nickelate $La_2NiO_{4+\delta}$ is an alkaline-earth metals free auspicious alternative to the commonly used perovskites, such as $Ba_{0.5}Sr_{0.5}Co_{0.8}Fe_{0.2}O_{3-\delta}$ (BSCF), which tends to form carbonates during the exposure to CO_2 [15–18].

Lanthanum nickelates are layered compounds with general formula $La_{n+1}Ni_nO_{3n+1}$ ($n = 1, 2, 3$). The crystal structure is composed of n alternating perovskite-like $LaNiO_3$ blocks and rock-salt-like LaO layers, which are arranged along the c-axis [19,20]. These materials are mixed ionic-electronic conductors. The oxygen migration through $La_2NiO_{4+\delta}$ occurs primarily anisotropically at elevated temperatures via interstitialcy transport mechanism in the LaO layer. The oxygen-vacancy migration mechanism in the perovskite-like $LaNiO_3$ blocks is of less significance. Diffusion along the c-axis is assumed to be neglible [21,22].

Based on oxygen excess δ and temperature conditions, different crystallographic structures have been reported [23–30]. Lanthanum nickelate occurs in a variety of structural modifications with an orthorhombic distortion based on tetragonal *I4/mmm* space group. Hücker et al. have constructed a oxygen-content schematic phase diagram for temperatures between 0 K and 350 K [31]. They also have investigated the effect of Sr-doping on phase composition for $La_{2-x}Sr_xNiO_{4+\delta}$. Skinner reported only one phase transformation on heating, which

---

* Corresponding author. Tel.: +49 511 763 4896; fax: +49 511 763 19121.
E-mail address: olga.ravkina@pci.uni-hannover.de (O. Ravkina).

http://dx.doi.org/10.1016/j.jeurceramsoc.2015.03.039

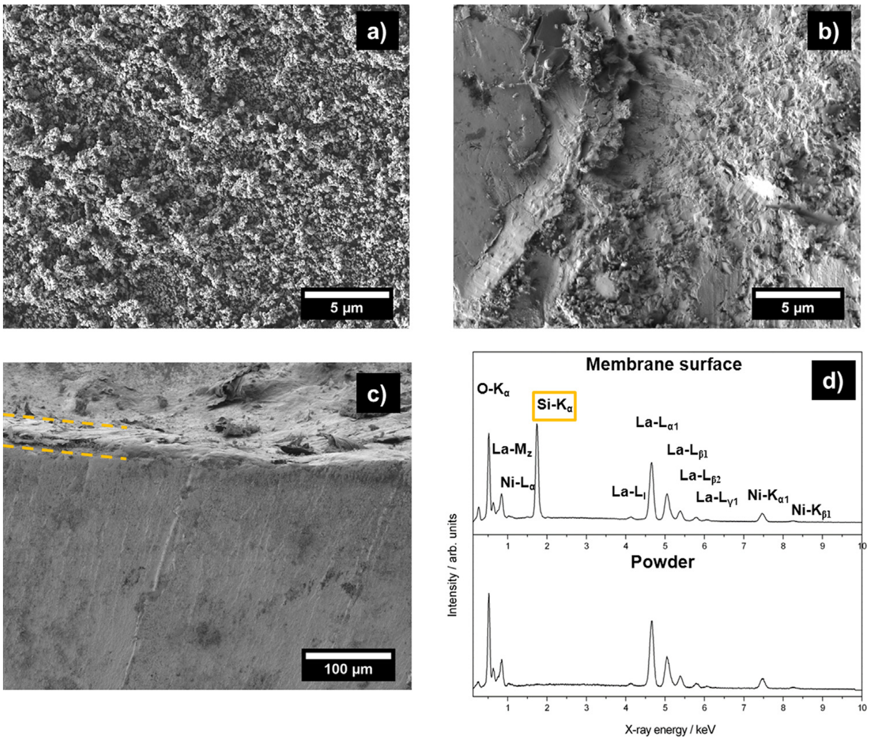

Fig. 1. Secondary electron micrograph of La_2NiO_4 ceramic, which was FAST/SPS sintered at 1423 K: (a) as-received powder, (b) membrane surface layer, (c) fractured membrane cross-section. The outer surface layer is labeled with orange dotted lines. (d) EDX spectrum of membrane surface layer and as-received powder. (For interpretation of the references to color in this figure legend, the reader is referred to the web version of this article.)

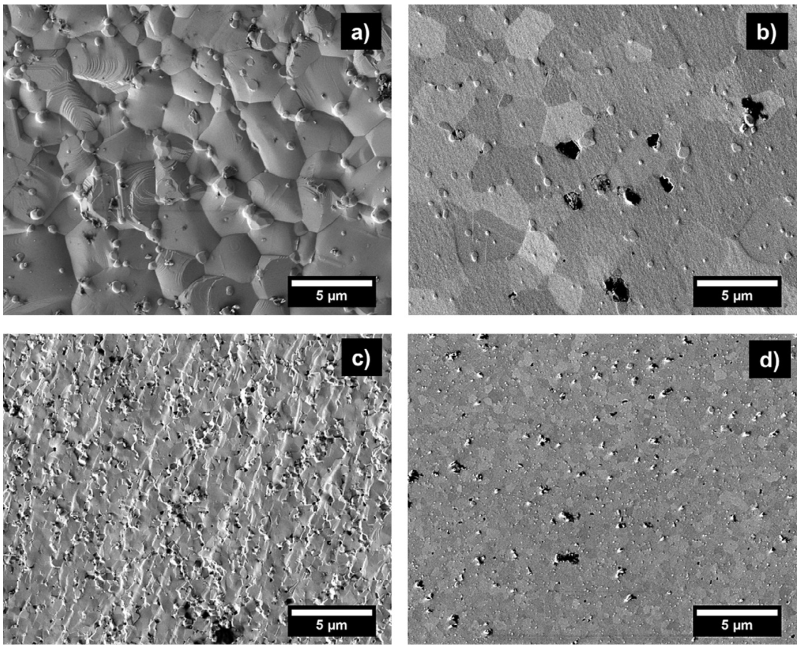

Fig. 2. Secondary electron micrograph of La_2NiO_4 ceramics: (a) membrane surface, produced by pressing and pressureless sintering at 1623 K. (b) Backscattered-electron channeling micrograph of vibration-polished membrane cross-section after pressureless sintering, (c) fractured cross-section of FAST/SPS-sintered membrane. (d) Backscattered-electron channeling micrograph of vibration-polished FAST/SPS-sintered membrane cross-section. Both membranes show some precipitation of ca. 100 nm–1 µm in diameter.

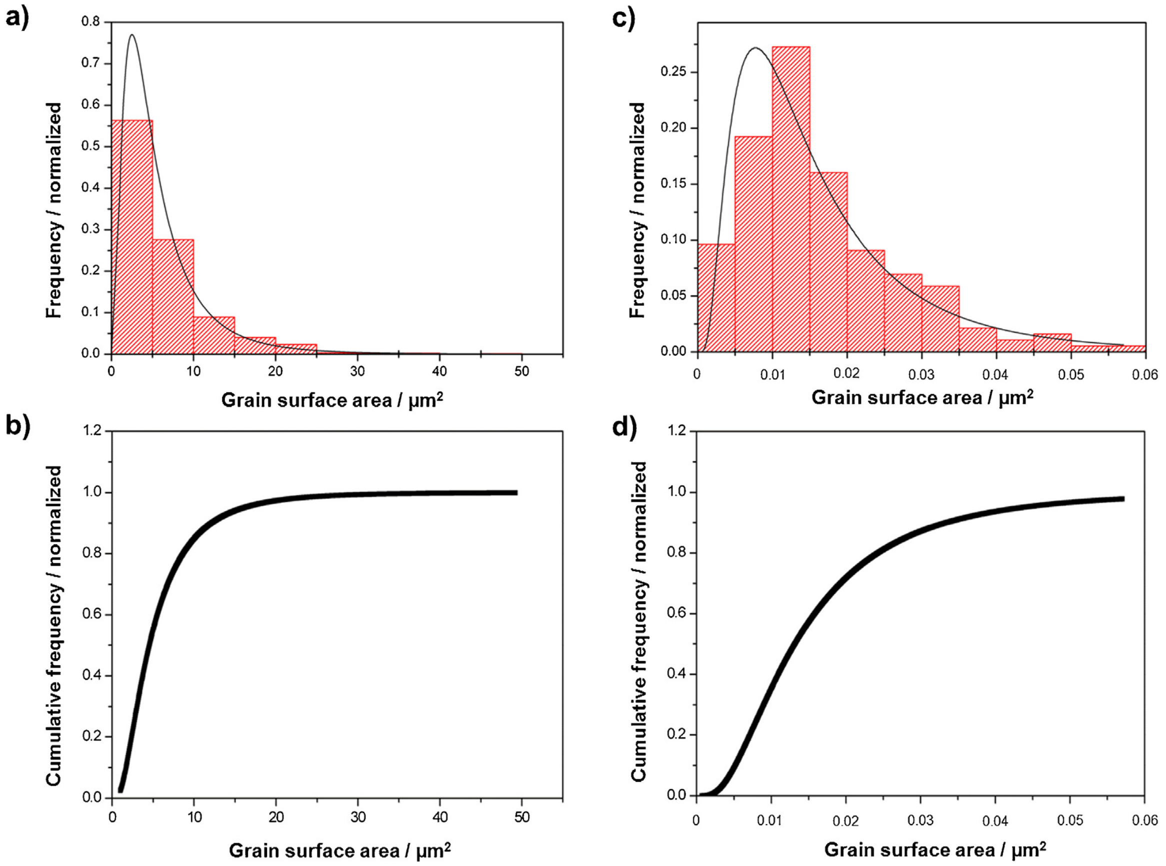

Fig. 3. Grain surface area distribution of conventionally pressureless sintered La_2NiO_4 membrane: (a) log-normal density function (b) cumulative distribution function. Grain surface area distribution of FAST/SPS-sintered La_2NiO_4 membrane: (c) log-normal density function (d) cumulative distribution function. Note scale (µm^2) on the abscissa.

was recorded between room temperature and 423 K, that was detected by in situ high-temperature neutron powder diffraction [32]. They suggest a transition between orthorhombic *Fmmm* and tetragonal *I4/mmm* modifications for $\delta = 0.17$. However, this phase transition does not influence the mixed ionic-electronic properties and the oxygen flux respectively, because the oxygen-permeation performance of the $La_2NiO_{4+\delta}$ membrane is conducted in the temperature range $T = 773–1273$ K.

Beside the crystal structure, the microstructure of the oxygen-transporting membranes can have a great influence on the functional properties of the materials [32–36]. There is no general trend, which would describe the dependence of the oxygen flux from the grain-size distribution. A lot of different studies for a variety of materials are reported in the literature. Klande et al. have investigated perovskite-type BSCF and $SrCo_{0.8}Fe_{0.2}O_{3-\delta}$ (SCF) and found no dependence of oxygen permeation flux on BSCF of grain size in the range from 24 to 42 µm [37]. For the SCF membrane, a decrease in permeation flux with larger grains was observed. Also Diethelm et al. reported lower oxygen permeation performance with larger grain size [38]. Analogous results were published for $La_{0.6}Sr_{0.4}Fe_{0.9}Ga_{0.1}O_{3-\delta}$ by Erchegoyen et al. [39]. For the Ruddlesden–Popper phase $La_2NiO_{4+\delta}$, a decrease of oxygen permeation flux with larger grains was observed by Klande et al. and explained by a faster grain boundary diffusion, which may be preferential in case of the anisotropic interstitialcy mechanism of oxygen ion transport through $La_2NiO_{4+\delta}$ [4]. However, the grain size reported by Klande et al. of $La_2NiO_{4+\delta}$ was controlled by dwelling time during the annealing at 1723 K. The average grain diameter achieved by this preparation method was 4.6 µm for 140 h and 1.8 µm for 10 h dwell time, which is rather big.

The sintering method often is important for the performance of ceramic materials. The characteristics of the membrane microstructure and density of the material can be influenced by choice of the sintering technique [40–42]. Ricote et al. have investigated the spark plasma sintering (SPS) technique to analyze $BaCe_{0.9-x}Zr_xY_{0.1}O_{3-\delta}$ ceramics [43]. They obtained samples with a much higher density compared to the conventional sintering technique. Furthermore, higher values of ionic conductivity for the SPS pellets were reported. El Horr et al. have investigated the microstructure of $Ba_{1-x}La_xTiO_{3-\delta}$ ceramics, that were sintered by the SPS method. It was shown that dense ceramic with an average diameter in the range from 330 to 36 nm at 1323 K can be produced by vary the La-doping level [44].

The present work is focused on microstructure investigation of $La_2NiO_{4+\delta}$ membranes, which were produced by field-assisted sintering technique/spark-plasma sintering (FAST/SPS) or by conventionally pressureless sintering. Furthermore, the influence of the sintering technique on the phase composition is analyzed. Moreover, the influence of impurities on the material properies is reported.

2. Experimental procedure

2.1. Preparation of dense membranes

As starting material, a commercial $La_2NiO_{4+\delta}$ powder (Marion Technologies, France) with an average particle diameter of 0.18 μm (±10%) was used. The crystal structure of the powder was analyzed by X-ray diffraction (XRD) using a Bruker-AXS D8 Advance diffractometer with Cu Kα radiation. Rietveld refinement shows a good match with a tetragonal *I4/mmm* space group with cell parameters: $a = 3.85$ Å and $c = 12.68$ Å.

For conventionally sintered material, green body of the membrane was obtained by uniaxial compression of the powders at 150 MPa for 30 min. The sintering process was conducted pressureless at 1623 K in ambient air atmosphere for 10 h. Heating and cooling rates of 2 K min^{-1} were used. As the result, a 1 mm thick perovskite ceramic membrane with a diameter of 16 mm was obtained.

Spark-plasma sintering (SPS) was carried out in a HHPD25 equipment (FCT Systeme GmbH, Frankenblick, Germany). The powder was placed in graphite die with an inner diameter of 20 mm and a die thickness of 10 mm and sintered under vacuum. A uniaxial force of 16 kN (pressure of 50 MPa) was applied before sintering started and was maintained constant for the whole experiment until the end of isothermal dwell time. The heating rate for experiment was set to 100 K min^{-1}. The experiment was done at 1423 K for 5 min. After that, the pressure was released and the sample was cooled down to the room temperature. A 5 mm thick pellet with a diameter of 20 mm was obtained which for further investigation was polished to a thickness of 1 mm and was bored out to a diameter of 16 mm.

The relative densities of produced membranes were measured via the Archimedes method on a Sartorius balance model BP 211D with a resolution of 0.01 mg.

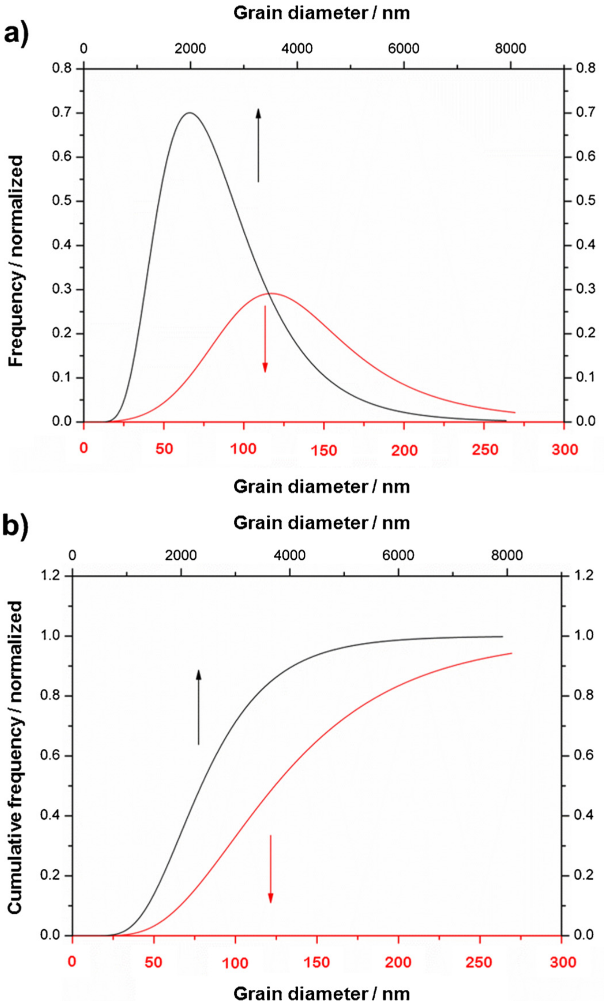

Fig. 4. Grain diameter distribution (black curve: conventionally sintered La_2NiO_4, red curve: FAST/SPS-sintered La_2NiO_4): (a) log-normal density function (b) cumulative distibution function. Note scale (nm) on the abscissa. (For interpretation of the references to color in this figure legend, the reader is referred to the web version of this article.)

2.2. Structural and microstructural characterization

X-ray diffraction analysis was conducted at room temperature using a Bruker-AXS D8 Advance diffractometer equipped with a Cu Kα radiation source. Data sets were recorded in step-scan mode in the angular 2θ range of 20–80°. High-temperature measurements were performed in an in situ cell (HTK-1200N, Anton Paar) between 30 °C and 1000 °C under synthetic air atmosphere (20% oxygen, 80% nitrogen) in 100 °C steps. The heating rate was 12 K min^{-1} with an equilibration time of 30 min before each measurement.

Scanning electron microscopy (SEM) studies were carried out on a JEOL JSM-6700F field-emission scanning electron microscope using a secondary electron detector at an accelerating voltage of 2 kV. For backscattered-electron channeling contrast imaging at a higher excitation voltage (15 kV), the membrane was vibration-polished using a Buehler VibroMet 2 vibratory polisher to preserve the crystallinity to the very surface. In order to investigate the microstructure and the grain size distribution, several micrographs of each membrane were analyzed using the Image J particle analyzer [45]. For each membrane more than 1000 grains were evaluated.

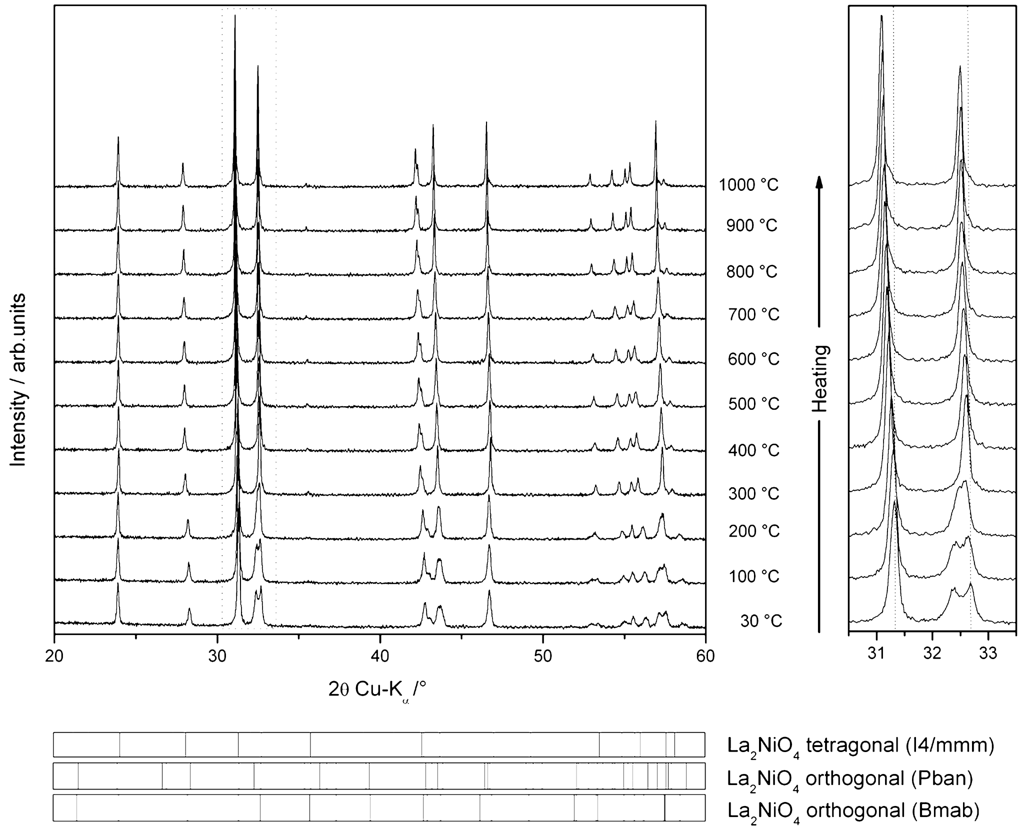

Fig. 5. Temperature-dependent XRD powder pattern in synthetic air (20% oxygen and 80% nitrogen) of crushed FAST/SPS-sintered La_2NiO_4 membrane after removal of the surface layer.

To analyze the microstructure in detail, transmission electron microscopy (TEM) was conducted at 200 kV with a JEOL JEM-2100F-UHR field-emission instrument, which was equipped with a Gatan GIF 2001 energy filter and a charge-coupled device (CCD) camera in order to obtain energy energy-loss (EEL) spectra. The microscope was operated in bright-field mode, and a scanning TEM (STEM) was used in a high-angle annular dark-field (HAADF). An energy-dispersive X-ray spectrometer (EDXS), Oxford Instruments INCA-300, with an ultra-thin window was used for elemental analysis at an excitation voltage of 200 kV.

Specimens for TEM investigations were prepared by cutting a 1 mm × 1 mm × 2 mm block of the membrane. The membrane pieces were then polished with polymer-embedded diamond lapping films down to 0.015 mm thickness. After the specimens were supported on a copper slot grid, the electron transparency was achieved by argon-ion sputtering at 3 kV with incident angles of 6° (Gatan, model 691 PIPS).

2.3. Oxygen permeation

The oxygen permeation experiments were carried out on a home-made high-temperature permeation cell, which has been described elsewhere [46]. Before measurement, both sides of the membranes were carefully polished with 800 mesh emery paper to obtain a uniform surface. Membranes were then sealed into a ceramic tube with gold paste (conducting paste, Heraeus) at 1223 K for 10 h. After sealing, gas flow rates were delivered to the reactor by mass flow controllers (Bronckhorst). The feed side of the membrane was fed with synthetic air (20 vol% O_2/80 vol% N_2) at a rate of 150 mL min^{-1}. The sweep side was flushed with He (29 mL min^{-1}, 99.995%). An online-coupled Agilent 7890 gas chromatograph with a Carboxen 1000 column was employed to analyze the gas mixture. The absolute flow rates of the effluents were calculated using neon (1 mL min^{-1}, 99.995%) as an internal standardization. By measuring the N_2 concentration, the total O_2 leakage was calculated and subtracted from the total oxygen flux.

3. Results and discussion

3.1. Characterization of membrane microstructure

The starting powder was investigated by SEM, combined with EDXS, to analyze the purity of the starting material. Fig. 1a shows a SEM micrograph of the as-received powder. The particles are arranged to loose aglomerates and the grain

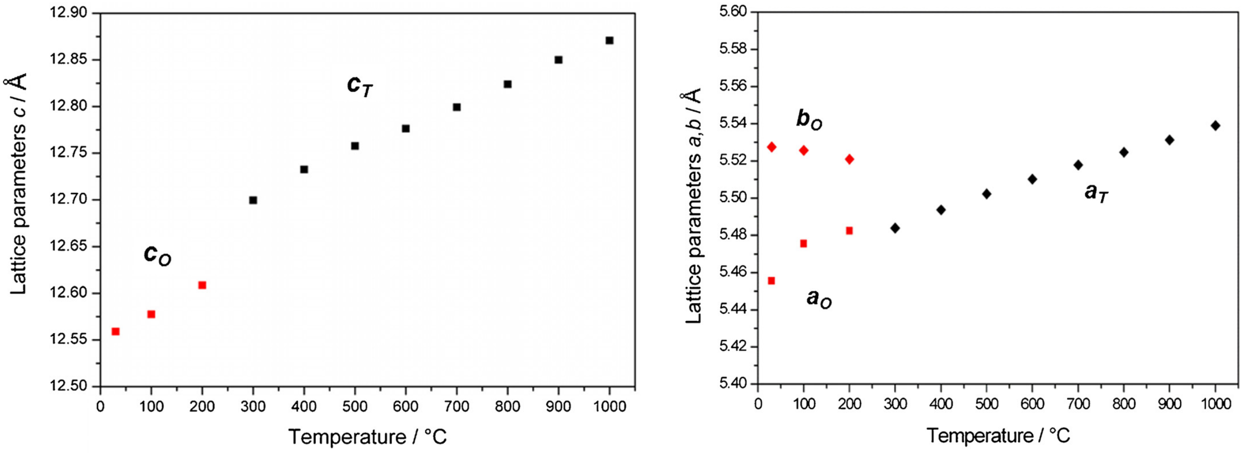

Fig. 6. FAST/SPS-sintered La_2NiO_4 membrane. Lattice parameters of tetragonal (*F4/mmm*) structure: a_T and c_T. Lattice parameters of orthorhombic structure (Bmab) structure: a_O, b_O and c_O.

size of single particle corresponds to the specification from the suplier (0.18 μm ± 10%). The EDX spectrum of the powder is shown in Fig. 1c. The ratio of La:Ni is 2:1 that is in good agreement with the stoichiometry of La_2NiO_4. Nevertheless, about 1 mol% silica impurity was detected in the powder, probably resulting from the fabrication process, e.g. contamination due to synthesis of different compounds on same equipment. Similar impurities can be also caused by ball-milling of the powder. The reason for applying the commercial powder was that small particles up to 200 nm are required for the FAST/SPS experiment, to achieve membranes with small grains. From our experience, the alternative synthesis using modified Pechini-methode delivers pre-calcined powders with particles up to 1 μm. Fig. 1b shows the membrane surface after FAST/SPS. The cross-section of the fractured membrane is presented in Fig. 1c. It can be seen that an outer surface layer with a thickness below 10 μm is formed during the sintering on the contact surface of powder and graphite die. The EDX spectrum of that layer is shown in Fig. 1d. It is distinct, that concentration of silica on the surface is much higher than in the powder. Furthermore, the XRD results from the surface does not correspond to the tetragonal *I4/mmm* structure, which was found

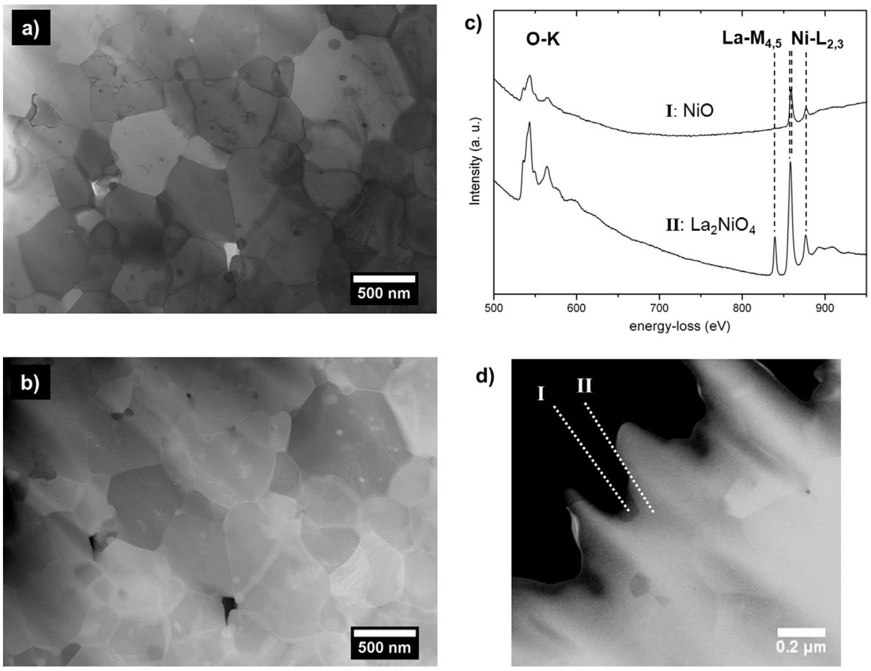

Fig. 7. FAST/SPS-sintered membrane: (a) STEM bright-field micrograph. (b) STEM high-angle annular dark-field micrograph. (c) EEL spectrum in the energy-loss range from 500 to 950 eV of La_2NiO_4 (II) and NiO (I). (d) TEM micrograph showing corresponding area (I) and (II) for the EELS.

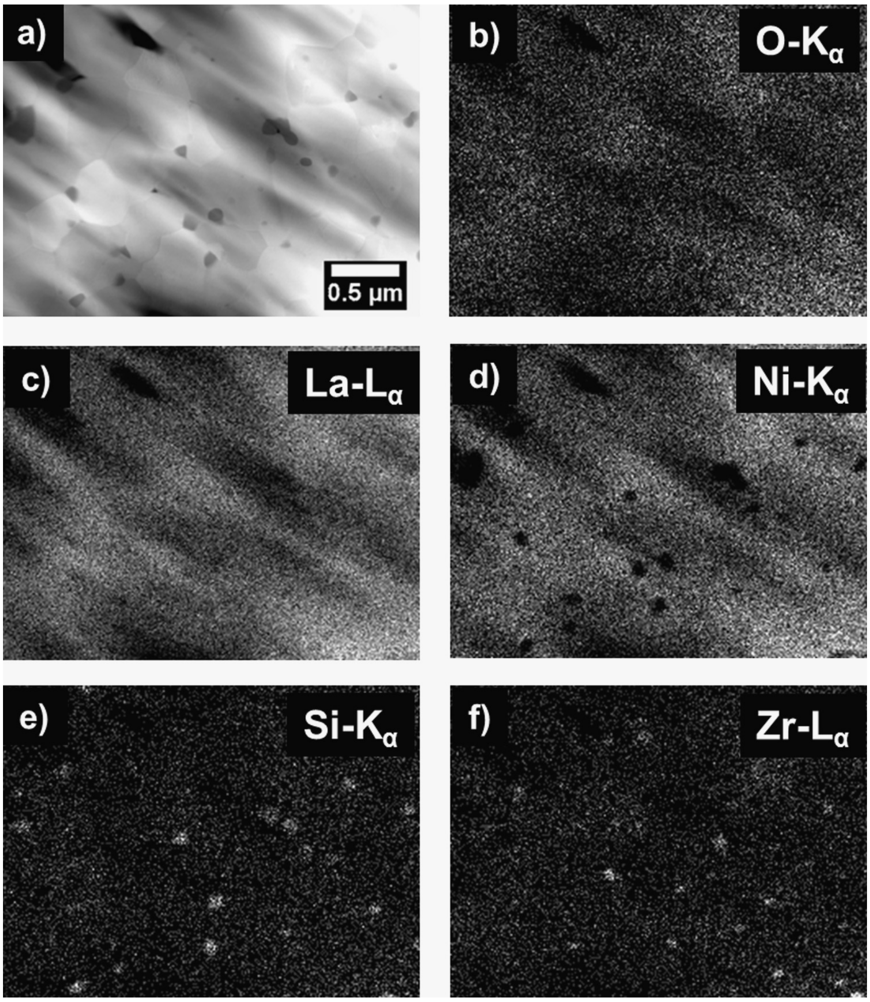

Fig. 8. FAST/SPS-sintered membrane: (a) STEM high-angle annular dark-field micrograph; EDXS elemental distribution showing: (b) O-K_α, (c) La-L_α, (d) Ni-K_α, (e) Si-K_α, and (f) Zr-L_α.

for the powder. For further experiments, both outer surface layers of the FAST/SPS membrane were removed by polishing.

To judge the quality and gas-tightness of the membranes, the relative density of FAST/SPS and conventionally sintered membranes was estimated by Archimedes method. A slight difference of density was found. The FAST/SPS membrane showed 99% and conventionally sintered membrane 95% density from the theoretical value. However, both membranes have have very low porosity and are dense.

Fig. 2 shows the SEM secondary electron micrographs of La_2NiO_4 ceramic membranes, which were prepared by different sintering techniques. The surface of pressureless sintered membrane and the fractured surface of FAST/SPS membrane are presented in Fig. 2a and c. The correspondig cross-sections are shown in Fig. 2b and d. The cross-sections of the membranes were vibration-polished to preserve the crystallinity of the material. A significant difference of the grain size can be seen. Furthermore, some precipitation is present.

To obtaine the grain surface area distribution for each membrane, more than 1000 grains were analyzed. The results for the grain areas were plotted as histograms and fitted with log-normal distribution density function and cumulative distribution function. Fig. 3 shows the corresponding grain surface area distributions. The slope of the cumulative distribution function shows spreading round the mean value. The avarage grain area increases from 0.015 μm^2 for FAST/SPS sintered ceramic to 6.11 μm^2 for conventionally pressureless produced membrane. The grain area for pressureless sintered membrane is in the range of 1–50 μm^2 (Fig. 3a). However, the grain area distribution is inhomogeneous. Above 50% of grains have grains in the range from 1 to 5 μm^2 and all the other are spread in the range from 5 to 50 μm^2. The slope of the corresponding cumulative distribution (Fig. 3b) shows steep ascent of the

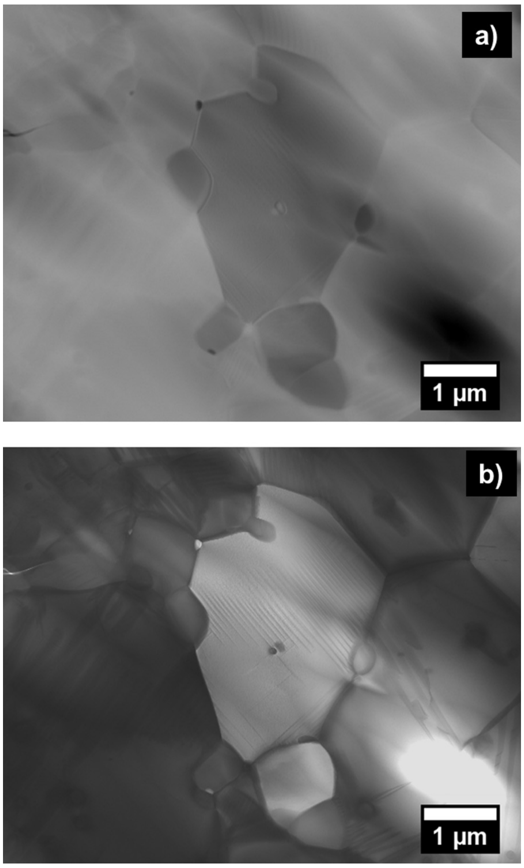

Fig. 9. Conventionally sintered membrane: (a) STEM high-angle annular dark-field micrograph. (b) STEM bright-field micrograph.

curve, which represent the smaller variation of the grain area. Below 80% of grains lie in the range between 1 and 10 μm^2. The grain area for FAST/SPS membrane is in the range of 0.0001–0.06 μm^2 (Fig. 3c) with the majority of grains between 0.01 and 0.02. The grain area is uniformly distributed, which is shown by flat ascent of the cumulative distribution curve (Fig. 3d). Below 80% of grains lie in the range between 0.001 and 0.02 μm^2.

For better comparability with the literature data, the grain diameter of the grains was estimated. It was assumed the grains are circular. Using the formula for circle area, the grains diameters for each membrane were calculated. This conversion can lead to small error, but it is the common way to estimate the grain diameter. Fig. 4a shows the log-normal density functions for both membranes with respect to the grain diameter. The corresponding cumulative distribution functions are shown in Fig. 4b. The avarage grain diameter for FAST/SPS membrane is 130 nm and 2500 nm for the conventionally sintered membrane. The particles in the starting powder were with an average particle diameter of 180 nm (±10%). The smaller grain size of the FAST/SPS sample can be explained by partial agglomeration of the as received powder. After FAST/SPS almost no grain growth was observed. The grain distribution stays homogeneous according to the particle distribution in the powder. In contrast, the average grain diameter in the conventionally sintered sample increased during the sintering from 180 nm to 2500 nm.

3.2. Structure and phase transition of FAST/SPS ceramic

The conventionally sintered sample have a tetragonal structure *I4/mmm* like the starting powder. The structure of the FAST/SPS membrane deviates from it. Temperature-dependent XRD powder pattern in synthetic air of crushed membrane after removal of the outer surface layers is shown in Fig. 5. From room temperature until 200 °C the orthorhombic lanthanum nickelate structure is detected. According to the Rietveld refinement even a mixture of orthorhombic Bmab and orthorhombic Pban structures is formed. After further heating above 200 °C, a phase transition occurs and formation of the tetragonal *I4/mmm* phase can be seen. After cooling down to room temperature, the structure remains tetragonal. Up to now, the formation of the orthorhombic phase was reported for lower temperatures and in dependence on the oxygen overstoichiometry [23–32]. Rice and Buttrey [23] reported the formation of Bmab orthorhombic structure for stoichiometric $La_2NiO_{4+\delta}$ by analyzing single crystals. Jorgensen et al. [25] concluded, that the solubility for excess oxygen in the Bmab phase is not zero, and that the Bmab phase exists for $0 < \delta < 0.02$. Rodriquez-Carvajal et al. [27] define the boundary for the Bmab phase at $\delta \approx 0.9$. Due to vacuum condition during the sintering process, FAST/SPS can cause an oxygen deficiency as reported by Valdez-Nava et al. [47]. During the temperature-dependent experiment in synthetic air, the oxygen excess can be incorporated in the structure, which results in the phase transition to the tetragonal structure. Rice and Buttrey proposed a dependence of lattice parameters $2c/(a+b)$ to the oxygen excess δ [23]. Applying this equation for room-temperature orthorhombic Bmab phase, the oxygen excess of $\delta \approx 0.007$ can be calculated. Almost a stoichiometric $La_2NiO_{4+\delta}$ compound is produced by FAST/SPS. The lattice parameters of the orthorhombic Bmab phase and the tetragonal *I4/mmm* phase are plotted in Fig. 6. For better comparison of the lattice parameters, the tetragonal unit cell was transformed to tetragonal *F4/mmm* unit cell applying $\sqrt{2}a \times \sqrt{2}b \times c$. It is convenient to index all phases on the basis of $\sqrt{2}a \times \sqrt{2}b \times c$ supercell, relative to the parent K_2NiF_4 cell [31]. From room temperature until 200 °C, the orthorhombic structure is presented. The lattice parameters $\boldsymbol{a_O}$, $\boldsymbol{b_O}$ and $\boldsymbol{c_O}$ are shown in red in Fig. 5. After the phase transition between 200 °C and 300 °C only the lattice parameters $\boldsymbol{a_T}$ and $\boldsymbol{c_T}$ are presented, because $\boldsymbol{a_T} = \boldsymbol{b_T}$ for the tetragonal structure. The increase of lattice parameters with temperature is due to thermal expansion of the lattice on heating.

3.3. TEM investigation on sintered ceramics

FAST/SPS membrane was analyzed by TEM. The STEM bright-field micrograph is shown in Fig. 7a and the STEM high-angle annular dark-field micrograph is presented in Fig. 7b. The

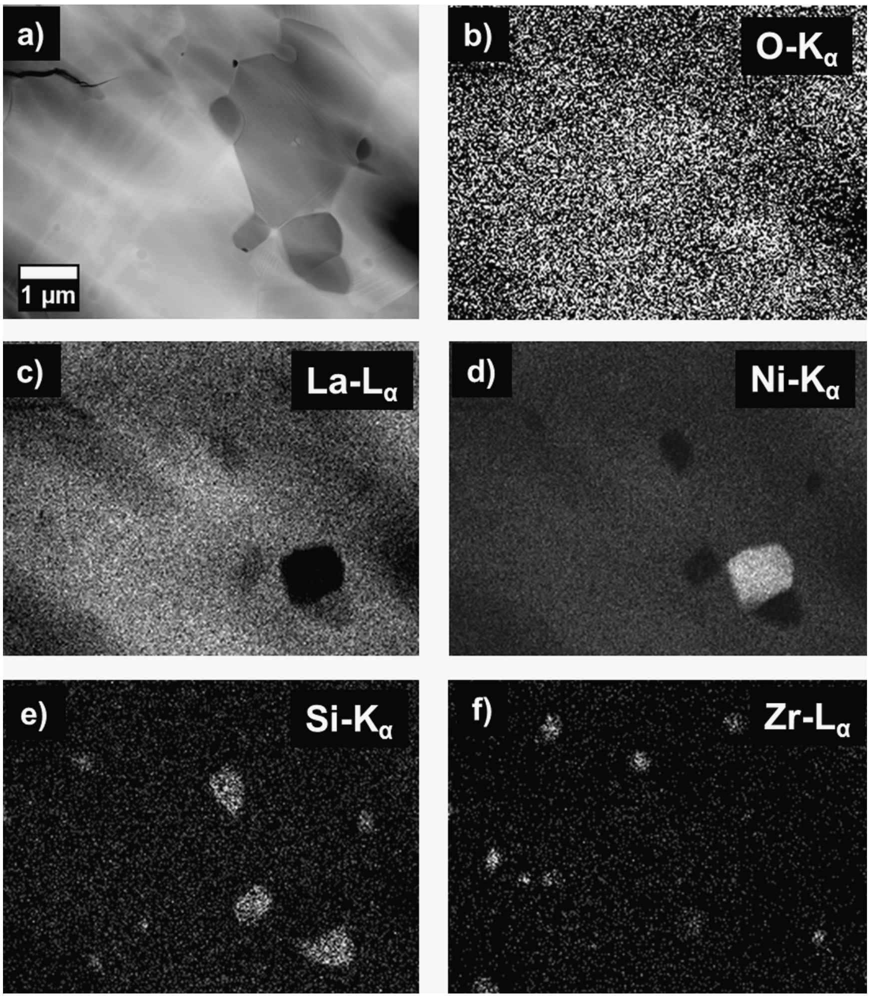

Fig. 10. Conventionally sintered membrane: (a) STEM high-angle annular dark-field micrograph; EDXS elemental maps showing: (b) O-K_α, (c) La-L_α, (d) Ni-K_α, (e) Si-K_α and (f) Zr-L_α.

precipitation, that also are shown by SEM in Fig. 2, are confirmed by STEM micrographs. To obtain more information about the phase composition, EELS was conducted. By this method, different phases can be distinguished by the specific fine structure. The results are shown in Fig. 7c. The corresponding areas (I) and (II) are labeled on the TEM micrograph in Fig. 7d. The EEL spectrum in Fig. 7c is shown in the energy-loss range of 500–1000 eV. The lanthanum nickelate phase (II) exhibits ionization edges of La-$M_{4.5}$ (832 and 850 eV [48]), Ni-$L_{2,3}$ (852 and 870 eV [49,50]), and O-K. Moreover, NiO precipitation is also present (I) and shows Ni-$L_{2.3}$ and O-K fine structures. The EDXS analysis completes the phase investigation. Fig. 8 shows the elemental distribution in the material. Beside the expected elements lanthanum, nickel and oxygen, silica- and also zirconia-rich regions were found. The impurities are homogeneously distributed all over the sample and do not form a solution with lanthanum nickelate or with each other. The diameter of the silica or zirconia-rich grains is below 50 nm. Klande et al. [4] investigated the effect of doping on microstructure of $La_2NiO_{4+\delta}$ ceramic. They have found that Zr-doping leads to formation of a secondary by-phase pyrochlore-type $La_2Zr_2O_7$. That means, that zirconia ions do not incorporate in the structure of lanthanum nickelate. The formation of the secondary by-phase yield depleting of the main phase on lanthanum. That could be the possible explanation of the NiO precipitation in our experiments.

Similar results were found for the pressureless high-temperature sintered sample. Fig. 9a shows the STEM high-angle annular dark-field micrograph and Fig. 9b the corresponding STEM bright-field micrograph. Again, some inclusions can be seen as well in the grain as in the grain boundaries. The elemental distribution is presented in Fig. 10. NiO segregation can clearly be seen in Fig. 10d. Silica-rich and zirconia-rich areas are discretly widely spread over the sample. The grain diameter of the impurity phases is between 100 nm and 500 nm. The amount of the impurity phase increases corresponding to the grain growth of the lanthanum nickelate grains.

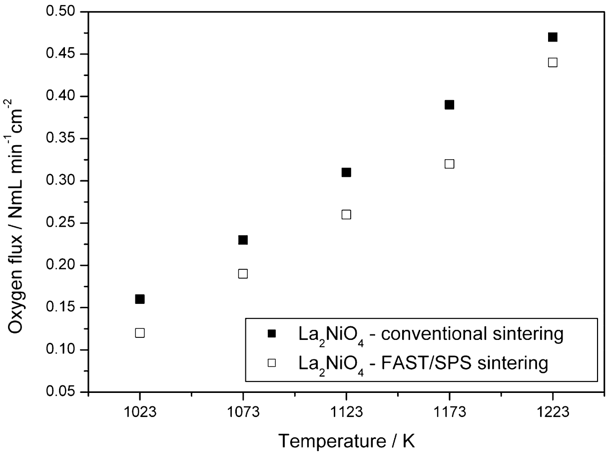

Fig. 11. Oxygen permeation measurements in the range of 1023–1223 K. Conditions: feed flow rates 150 NmL min^{-1} synthetic air (20% oxygen, 80% nitrogen); sweep flow rates He 29 NmL min^{-1}, Ne 1 NmL min^{-1}.

3.4. Oxygen permeation measurements

Oxygen permeation experiments were conducted in the range from 1023 K to 1223 K for membranes, that were prepared by different sintering techniques. The results are shown in Fig. 11. The oxygen permeation flux for the conventionally pressureless sintered membrane at 1223 K is 0.46 Nml min^{-1} cm^{-2} and for the FAST/SPS membrane is 0.43 Nml min^{-1} cm^{-2}. The relative deviation between the oxygen flux of this two membranes in the measured temperature range is in the scope of 7–30%. Both are not inside the measurement uncertainty. We can conclude, that the decrease of the grain size results in the decrease of the oxygen permeation flux. Concerning the oxygen permeation, the conventionally sintered membranes show better performance. The decrease of the oxygen permeation can be explained by disfavored grain boundary diffusion. The bulk diffusion of oxygen ions seems to be more important in this material.

The presence of impurities with this low concentration have obviously no effect on the oxygen permeation flux. The results for the pressureless sintered membrane are almost equal to the oxygen permeation values reported by Klande et al. [4] for the same experiment procedure. Nevertheless, the impurities might have strong influence on the electrochemical performance of such materials in e.g. solid oxide fuel cells. Oishi et al. [51] investigated the effect of minor elements in cathodes on oxygen reduction reaction. According to their report the minor elements such as Al or Si have a negative effect on chemical diffusion coefficient and surface exchange coefficient.

4. Conclusions

The microstructural properties of FAST/SPS and pressureless sintered $La_2NiO_{4+\delta}$ ceramics were investigated. The distribution of the grain size for each membrane was conducted. The grains of FAST/SPS material were found to be smaller with the avarage grain area of 0.015 μm^2 compared to the avarage grain area of conventionally sintered membrane 6.11 μm^2. However, it was shown, that small grain have negative effect on the oxygen permeation performance of the lanthanum nickelate membrane. Furthermore, the structure of the material can be controlled by the sintering technique during the sintering. Lanthanum nickelate membrane produced by FAST/SPS had the orthorhombic structure with very low oxygen excess caused by vacuum conditions. The conventionally sintered membrane has the tetragonal structure like the starting powder material. The quality and purity of the powder is very important. Even very small amounts of impurities in the powder (i.e. 1 mol% of silica) form widely spread impuritiy clusters, that can disadvantage the performance of the material.

Acknowledgements

The authors greatly acknowledge financial support from the Chinese-German Centre for Science (GZ676) and the Deutsche Forschungsgemeinschaft (FE 928/4-1) as well as fruitful discussions with Prof. Jürgen Caro.

References

[1] Satyalakshmi KM, Mallya RM, Ramanathan KV, Wu XD, Brainard B, Gautier C. Epitaxial metallic. $LaNiO_3$ thin-films grown by pulsed laser deposition. Appl Phys Lett 1993;62:1233–5.
[2] Ryll T, Reibisch P, Schlagenhauf L, Bieberle-Huetter A, Döbeli M, Rupp JLM, et al. Lanthanum nickelate thin films deposited by spray pyrolysis: crystallization, microstructure and electrochemical properties. J Eur Ceram Soc 2012;32:1701–9.
[3] Raj ES, Pratt KFE, Skinner SJ, Parkin IP, Kilner JA. High conductivity $La_{2-x}Sr_xCu_{1-y}(Mg,Al)_yO_4$ solid state metal oxide gas sensors with the K_2NiF_4 structure. Chem Mater 2006;18:3351.
[4] Klande T, Efimov K, Cusenza S, Becker K-D, Feldhoff A. Effect of doping, microstructure, and CO_2 on $La_2NiO_{4+\delta}$-based oxygen-transporting materials. J Solid State Chem 2011;184:3310–8.
[5] Atkin FT, Lin YS. Selective oxidation of ethane to ethylene in a dense tubular membrane reactor. J Membr Sci 2002;209:457–67.
[6] Chen C, Feng S, Ran S, Zhu D, Liu W, Boumeester HJM. Conversion of methane to syngas by a membrane-based oxidation-reforming process. Angew Chem Int Ed 2003;42:5196–8.
[7] Kharton VV. Solid state electrochemistry II Electrodes. Interfaces and ceramic membranes, vol. 2. Germany: Wiley-VCH; 2011.
[8] Shao Z, Haile SM. A high-performance cathode for the next generation of solid-oxide fuel cells. Nature 2004;431:170–3.
[9] Bredesen R, Jordal K, Bolland O. High-temperature membranes in power generation with CO_2 capture. Chem Eng Process 2004;43:1129–58.
[10] Stadler H, Beggel F, Habermehl M, Persigehl P, Kneer R, Modigell M, et al. Oxyfuel coal combustion by efficient intergration of oxygen transport membranes. Int J Greenh Gas Control 2011;5:7–15.
[11] Grielen D, Podkanski J. Prospect for CO_2 capture and storage. Paris, France: OECD/IEA; 2004.
[12] Tan XY, Li K, Thursfield A, Metcalfe IS. Oxyfuel combustion using a catalytic ceramic membrane reactor. Catal Today 2008;131:292–304.
[13] Smith A, Klosek J. A review of air separation technologies and their integration with energy conversion process. Fuel Process Technol 2001;70:115–34.
[14] International Energy Agency. World energy outlook 2011. Paris: OECD; 2011.
[15] Shao Z, Haile S. A high-performance cathode for the next generation of solid-oxide fuel cells. Nature 2004;431:170.
[16] Arnold M, Wang H, Feldhoff A. Influence of CO_2 on the oxygen permeation performance and the microstructure of perovskite-type

$(Ba_{0.5}Sr_{0.5})(Co_{0.8}Fe_{0.2})O_{3-\delta}$ membranes. J Membr Sci 2007;293: 44–52.

[17] Czuprat O, Arnold M, Schirrmeister S, Schiestel T, Caro J. Influence of CO_2 on the oxygen permeation performance of perovskite-type $BaCo_xFe_yZr_zO_{3-\delta}$ hollow fiber membranes. J Membr Sci 2010;364:132–7.

[18] Yi JX, Schroeder M, Weirich T, Mayer J. Behavior of $Ba(Co,Fe,Nb)O_{3-\delta}$ perovskite in CO_2-containing atmospheres: degradation mechanism and materials design. Chem Mater 2010;22:132–7.

[19] Ram MRA, Ganapathi L, Ganguly P, Rao CNR. Evolution of three-dimensional character across $La_{n+1}Ni_nO_{3n+1}$ homologous series with increase in n. J Solid State Chem 1986;63:139–47.

[20] Hiroi Z, Obata T, Takano M, Bando Y, Taked Y, Yamamoto O. Ordering of interstitial oxygen atoms in $La_2NiO_{4+\delta}$ observed by transmission electron microscopy. Phys Rev B 1990;41:11665–8.

[21] Naumovich EN, Kharton VV. Atomic-scale insight into the oxygen ionic transport mechanism in La_2NiO_4 materials. J Mol Struct: Theochem 2010;946:57–64.

[22] Chroneos A, Parfitt D, Kilner JA, Grimes RW. Anisotropic oxygen diffusion in tetragonal $La_2NiO_{4+\delta}$: molecular dynamics calculation. J Mater Chem 2010;20:266–70.

[23] Rice DE, Buttrey J. An X-ray diffraction study of the oxygen content phase diagram of $La_2NiO_{4+\delta}$. J Solid State Chem 1993;105:197–210.

[24] Tranquada JM, Kong Y, Lorenzo JE, Buttrey DJ, Rice DE, Sachan V. Oygen intercalation, stage ordering, and phase separation in $La_2NiO_{4+\delta}$ with $0.05 \le \delta \le 0.11$. Phys Rev B 1994;50:6340–51.

[25] Jorgensen JD, Dabrowski B, Pei A, Richards DR, Hinks DG. Structure of interstitial oxygen defect in $La_2NiO_{4+\delta}$. Phys Rev B 1989;40: 2187–99.

[26] Fernandez-Diaz MT, Martinez JL, Rodriquez-Carvajal J. High-temperature phase transformation of oxidized $R_2NiO_{4+\delta}$ (R = La, Pr and Nd) under vacuum. Solid State Ionics 1993;63–65:902–6.

[27] Rodriguez-Carvajal J, Fernandez-Diaz MT, Martinez JL. Neutron diffraction study on structural and magnetic properties of La_2NiO_4. J Phys: Condens Matter 1991;3:3215–34.

[28] Sayers R, Skinner SJ. Evidence for the catalytic oxidation of $La_2NiO_{4+\delta}$. J Mater Chem 2011;21:414–9.

[29] Faucheux V, Pignard S, Audier M. Structural study of lanthanum nickelate thin films deposited on different single crystal substrates. J Solid State Chem 2004;177:4616–25.

[30] Tranquada JM, Buttrey DJ, Rice DE. Phase separation charge-density waves, and magnetism in $La_2NiO_{4+\delta}$ with $\delta = 0.105$. Phys Rev Lett 1993;70:445–8.

[31] Hücker M, Chung K, Chand M, Vogt T, Tranquada JM, Buttrey DJ. Oxygen and strontium codoping of $La_2NiO_{4+\delta}$: room-temperature phase diagrams. Phys Rev B 2004;70:064105–64111.

[32] Skinner SJ. Characterisation of $La_2NiO_{4+\delta}$ using in-situ high temperature neutron powder diffraction. Solid State Sci 2003;5:419–26.

[33] Baumann S, Schulze-Küppers F, Roitsch S, Betz M, Zwick M, Pfaff EM, et al. Influence of sintering conditions on microstructure and oxygen permeation of $Ba_{0.5}Sr_{0.5}Co_{0.8}Fe_{0.2}O_{3-\delta}$ (BSCF) oxygen transport membranes. J Membr Sci 2010;359:102–9.

[34] Tan L, Gu XH, Yang L, Jin WQ, Zhang LX, Xu NP. Influence of powder synthesis methods on microstructure and oxygen permeation performance of $Ba_{0.5}Sr_{0.5}Co_{0.8}Fe_{0.2}O_{3-\delta}$ perovskite-type membranes. J Membr Sci 2003;212:1–157.

[35] Mori M, Sammes NM, Tompsett GA. Fabrication processing condition for dense sintered $La_{0.6}AE_{0.4}MnO_3$ perovskite synthesized by the coprecipitation method (AE = Ca and Sr). J Power Sources 2000;395:1–2.

[36] Martynczuk J, Arnold M, Feldhoff A. Influence of grain size on the oxygen permeation performance of perovskite-type $(Ba_{0.5}Sr_{0.5})(Co_{0.8}Zn_{0.2})O_{3-\delta}$ membranes. J Membr Sci 2008;322:375–82.

[37] Klande T, Ravkina O, Feldhoff A. Effect of microstructure on oxygen permeation of $Ba_{0.5}Sr_{0.5}Co_{0.8}Fe_{0.2}O_{3-\delta}$ and $SrCo_{0.8}Fe_{0.2}O_{3-\delta}$ membranes. J Eur Ceram Soc 2013;33:1129–36.

[38] Diethelm S, Van Herle J, Sfeir J, Buffat P. Correlation between oxygen transport properties and microstructure in $La_{0.5}Sr_{0.5}FeO_{3-\delta}$. J Eur Ceram Soc 2005;25:2191–6.

[39] Erchegoyen G, Chartier T, Del-Gallo P. Oxygen permeation in $La_{0.6}Sr_{0.4}Fe_{0.9}Ga_{0.1}O_{3-\delta}$ dense membrane: effects of surface microstructure. J Solid State Electrochem 2006;10:597–603.

[40] Guillon O, Gonzalez-Julian J, Dargatz B, Kessel T, Schierning G, Räthel J, et al. Field-assisted sintering technology/spark plasma sintering: mechanisms, materials, and technology developments. Adv Eng Mater 2014:1–20.

[41] Raj R, Cologna M, Francis JS. Infulence of externally imposed and internally generated electrical fields on grain growth, diffusion creep, sintering and related phenomena in ceramics. J Am Ceram Soc 2011;94: 1941–65.

[42] Ghosh S, Chokshi AH, Lee P, Raj R. A huge effect of weak dc electrical fields on grain growth in zirconia. J Am Ceram Soc 2009;92:1856–9.

[43] Ricote S, Caboche G, Estournes Bonanos C. Synthesis, sintering, and electrical properties of $BaCe_{0.9-x}Zr_xY_{0.1}O_{3-\delta}$. J Nanomater 2008:1–5.

[44] El Horr N, Valdez-Nava Z, Tenailleau C, Guillemet-Fritsch S. Microstructure of $Ba_{1-x}La_xTiO_{3-\delta}$ ceramics sintered by Spark Plasma Sintering. J Eur Ceram Soc 2011;31:1087–96.

[45] Abramof MD, Magelhaes PJ, Ram RJ. Image processing with image. J Biophotonics Int 2004;11:36–42.

[46] Wang H, Tablet C, Feldhoff A, Caro J. Investigation of phase structure, sintering, and permeability of perovskite-type $Ba_{0.5}Sr_{0.5}Co_{0.8}Fe_{0.2}O_{3-\delta}$ membranes. J Membr Sci 2005;262:20–6.

[47] Valdez-Nava Z, Guillemet-Fritsch S, Tenailleau C, Lebey T, Durand B, Chance-Ching JY. Colossal dielectric permittivity of $BaTiO_3$-based nanocrystalline ceramics sintered by spark plasma sintering. J Electroceram 2009;22:238–44.

[48] Belliere V, Joorst G, Stephan O, de Groot FMF, Weckhuysen BM. Phase segregation in cerium-lanthanum solid solution. J Phys Chem B 2006;110:9984–90.

[49] Mitterbauer C, Kothleitner G, Grogger W, Zandbergen H, Freitag B, Tiemeijer P, et al. Electron energy-loss near-edge structure of 3d transition metal oxides recorded at high-energy resolution. Ultramicroscopy 2003;96:469–80.

[50] Krivanek OL, Paterson JH. ELNES of 3d transition-metal oxides. Ultramicroscopy 1990;32:313–8.

[51] Oishi J, Otomo J, Oshima Y, Koyama M. The effect of minor elements in $La_{0.6}Sr_{0.4}Co_{0.8}Fe_{0.2}O_{3-\delta}$ cathodes on oxygen reduction reaction. J Power Sources 2015;277:44–51.

3.3 Effect of microstructure on oxygen permeation of $Ba_{0.5}Sr_{0.5}Co_{0.8}Fe_{0.2}O_{3-\delta}$ and $SrCo_{0.8}Fe_{0.2}O_{3-\delta}$ membranes

---

Reprinted with kind permission from Elsevier:
Tobias Klande, Olga Ravkina and Armin Feldhoff
Journal of the European Ceramic Society **33** (2013) 1129-1136.
doi:10.1016/j.jeurceramsoc.2012.11.023

Available online at www.sciencedirect.com
SciVerse ScienceDirect
Journal of the European Ceramic Society 33 (2013) 1129–1136
www.elsevier.com/locate/jeurceramsoc

Effect of microstructure on oxygen permeation of $Ba_{0.5}Sr_{0.5}Co_{0.8}Fe_{0.2}O_{3-\delta}$ and $SrCo_{0.8}Fe_{0.2}O_{3-\delta}$ membranes

Tobias Klande*, Olga Ravkina, Armin Feldhoff

Institute of Physical Chemistry and Electrochemistry, Leibniz Universität Hannover, Callinstr. 3a, D-30179 Hannover, Germany

Received 25 July 2012; received in revised form 23 November 2012; accepted 26 November 2012
Available online 27 December 2012

Abstract

The effect of grain size on oxygen permeation properties of $Ba_{0.5}Sr_{0.5}Co_{0.8}Fe_{0.2}O_{3-\delta}$ (BSCF) and $SrCo_{0.8}Fe_{0.2}O_{3-\delta}$ (SCF) membranes was investigated by variation of the dwell time. The membrane microstructure was examined by field-emission scanning microscopy (FE-SEM) and then evaluated using a statistical approach. With longer dwell times the grain growth was stimulated and leaded to grains with a narrower size distribution. The grains of SCF (average size from 11.3 to 19.9 μm) were found to be smaller than those of BSCF (average size from 13.9 to 41.3 μm). The oxygen permeation flux of BSCF membranes was found to be independent of grain size in the range from 24 to 42 μm. However, membranes with smaller grains (13.9 μm) show a decreased oxygen permeation flux. For the SCF membranes a decrease in permeation flux with larger grains was observed for average grain sizes between 11.3 and 19.9 μm. By transmission electron microscopy (TEM) formation of an oxygen ordered $SrCo_{0.8}Fe_{0.2}O_{2.5}$ brownmillerite by-phase could be observed at the oxygen-depleted sweep side of the membrane.

Keywords: Microstructure; Grain size; Oxygen permeation; Scanning electron microscopy; Transmission electron microscopy

1. Introduction

The emission of green-house gases from fossil power plants can be reduced by sequestration of CO_2 by oxyfuel combustion.[1] In this process the fuel is directly combusted with pure oxygen and the reaction products, water and CO_2, can be easily separated from each other by condensation. The required oxygen for this technology can be produced by the use of mixed ionic–electronic conductors (MIECs) as oxygen-transporting membranes (OTMs).[2] For this application, ceramic membrane materials with good oxygen-ionic and electronic conductivities are advantageous, which are often classic ABO_3 perovskite materials. Other structures such as fluorites or perovskite-related structures like $La_2NiO_{4+\delta}$ are known to possess slightly lower oxygen permeation properties.[3] Among the perovskite materials $Ba_{0.5}Sr_{0.5}Co_{0.8}Fe_{0.2}O_{3-\delta}$ (BSCF) is known to posses the highest stable oxygen permeability under long-term conditions at high temperatures ($T > 1123$ K).[4] To obtain further optimized membranes the focus is on: (i) technical improvements such as asymmetric membrane design[5]; (ii) optimization of microstructure and processing parameters.[6] In fact, the influence of microstructure on membrane properties has to be understood but it is discussed controversially throughout a lot of different studies and materials. For $(La_{0.5}Sr_{0.5})FeO_{3-\delta}$, Diethelm et al. reported lower oxygen permeation performance with larger grain size.[7] This matches with measurements by Kusaba et al. and Etchegoyen et al. who reported analogous results for $La_{0.1}Sr_{0.9}Co_{0.9}Fe_{0.1}O_{3-\delta}$ and $La_{0.6}Sr_{0.4}Fe_{0.9}Ga_{0.1}O_{3-\delta}$ perovskite material.[8,9] Watanabe et al. observed this behavior for $Ba_{0.95}La_{0.05}FeO_{3-\delta}$.[10] For the perovskite-related anisotropic oxygen conductor $La_2NiO_{4+\delta}$ as well, a decrease of oxygen permeation with larger grains, thus fewer grain boundaries, was reported.[11] Also for so called dual-phase membranes a decrease of oxygen flux was found for larger grains for $Ce_{0.85}Sm_{0.15}O_{3-\delta}$–$Sm_{0.6}Sr_{0.4}FeO_{3-\delta}$.[12] Other groups showed a increase of oxygen flux for larger grains – therefore a negative impact of grain boundaries – for $(Ba_{0.5}Sr_{0.5})(Fe_{0.8}Zn_{0.2})O_{3-\delta}$,[13] $Ca(Ti_{0.8}Fe_{0.2})O_{3-\delta}$,[14] $LaCoO_{3-\delta}$[15,16] $(La_{0.6}Sr_{0.4})(Co_{0.2}Fe_{0.8})O_{3-\delta}$,[17] $La_{0.3}Sr_{0.7}CoO_{3-\delta}$,[18] $Sr(Co,Fe,Cu,Cr)O_{3-\delta}$,[19] and $SrFe(Al)O_{3-\delta}$–$SrAl_2O_4$ composites.[20] However, for the system $(Ba_{1-x}Sr_x)(Co_{0.8}Fe_{0.2})O_{3-\delta}$ contradicting results were reported. For the end member $SrCo_{0.8}Fe_{0.2}O_{3-\delta}$ larger

---

* Corresponding author. Tel.: +49 511 762 2943; fax: +49 511 762 19121.
E-mail address: tobias.klande@pci.uni-hannover.de (T. Klande).

0955-2219/$ – see front matter © 2012 Elsevier Ltd. All rights reserved.
http://dx.doi.org/10.1016/j.jeurceramsoc.2012.11.023

oxygen permeation with decreasing grain size was reported.[21] Grain size of BSCF was reported to have a strong influence,[22] small influence[23] or no influence.[24,25] In this study on BSCF and SCF we prepared different membranes with different microstructure by changing the dwell time during sintering. All samples were investigated using X-ray diffraction (XRD) to ensure phase purity. The microstructure was investigated by field-emission scanning electron microscopy (FE-SEM) and the obtained micrographs were analyzed to obtain the grain sizes. The different membranes were investigated by oxygen permeation measurements to observe the influence of different grain sizes. Transmission electron microscopy (TEM) was used to investigate the microstructure after permeation experiments.

2. Experimental

Powders of $SrCo_{0.8}Fe_{0.2}O_{3-\delta}$ (SCF) and $Ba_{0.5}Sr_{0.5}Co_{0.8}Fe_{0.2}O_{3-\delta}$ (BSCF) were prepared via a combined citrate and ethylene-diamine-tetraacetic acid (EDTA) complexing method as described elsewhere.[26] Stoichiometric amounts of metal oxides were dissolved in water with subsequent addition of complexing agents and $NH_3{\cdot}(H_2O)$. The obtained aqueous solution was changed into a gel by continuous stirring and heating. After combustion in a heating mantle, the powders were precalcined at 1173 K in air for 10 h with heating and cooling rates of $2\,K\,min^{-1}$. The ground powders were uniaxially presses into 16 mm green bodies at 150 kN for 20–30 min. The final sintering process was conducted at 1373 K with a heating and cooling rate of $1\,K\,min^{-1}$ in ambient air atmosphere with different dwell times of 2, 4, 8, 16, and 32 h. The relative densities were measured via the Archimedes method on a Sartorius balance model BP 211D with a resolution of 0.01 mg. X-ray diffraction (XRD) analysis was performed using a Bruker AXS D8 Advance diffractometer equipped with a Cu Kα radiation source. Data sets were recorded in a step-scan mode in the 2θ range of $20° \leq 2\theta \leq 90°$ at an interval of 0.02°. All powders, membranes, and ground membranes were investigated to ensure phase purity. The microstructure of the different membranes was investigated in a JEOL JSM-6700 F field-emission instrument at a low excitation voltage of 2 kV. Several micrographs of each membrane were taken and then analyzed using the Image J particle analyzer.[27] Effective grain diameters were estimated from measured grain areas in μm^2 by assuming circle-shaped grains. For each membrane between 400 and 500 grains were evaluated. Oxygen permeation was measured in a custom-made high-temperature permeation cell, as described elsewhere.[13] Both sides of each membrane were carefully polished with 800 mesh emery paper and then sealed on an alumina tube with a gold cermet (Heraeus). The feed side was fed with synthetic air (20 vol.% O_2/80 vol.% N_2) at a rate of $150\,mL\,min^{-1}$, whereas Ne ($1.0\,mL\,min^{-1}$, 99.995%) and He ($29.0\,mL\,min^{-1}$, 99.995%) were fed to the sweep side. An Agilent 7890 gas chromatograph with a Carboxen 1000 column was employed to analyze the gas mixture. The absolute flux rate was calculated using neon as an internal standard. A possible O_2 leakage was calculated and subtracted from the total O_2 flux after the N_2 concentration was measured. TEM investigations were performed at an accelerating voltage of 200 kV on a JEOL JEM-2100 F-UHR field-emission instrument ($C_s = 0.5$ mm, $C_c = 1.2$ mm). The microscope was operated as a high-resolution TEM (HRTEM) and in selected area electron diffraction (SAED) mode. The preparation method of TEM specimen is described in detail elsewhere.[28]

3. Results

All produced powders and crushed membranes were investigated by XRD. The post-calcination process at 1223 K was sufficient to form single-phase material. However, to achieve gas-tight membranes higher sintering temperatures of 1373 K were necessary. The XRD analysis confirmed formation of single-phase cubic perovskite structure (s.g. $Pm\bar{3}m$) as can be seen for example in Fig. 1. The cell parameter for BSCF with $a = 3.986$ Å and for SCF with $a = 3.872$ Å are in agreement with literature data (ICSD no. 109462 and 79022).[29,30] The decrease of the cell parameter with decreasing barium content is in accordance with the cation radii of Ba^{2+} (161 pm) and Sr^{2+} (144 pm).[31]

To judge the quality and gas-tightness of the membranes, the relative density was determined by Archimedes method on sintered membranes. Only membranes with low porosity, which means not more than 10% deviation from the theoretical density, were taken into investigation of the permeation properties (Table 1).

In order to increase the grain size of the material, several membranes were sintered with different dwell times. As expected the average grain size increased with increasing time. Fig. 2 shows surface of all BSCF membranes with corresponding grain size distributions. The slope of the cumulative distribution function shows the spreading around the mean value. A steeper curve represents a smaller variation. By the shape of the curve the amount of grains below a certain grain size can be determined.

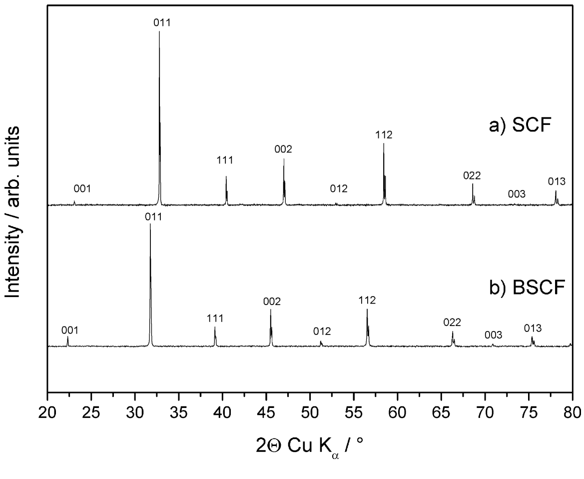

Fig. 1. Room-temperature XRD powder patterns of (a) $SrCo_{0.8}Fe_{0.2}O_{3-\delta}$ (SCF, $a = 3.872$ Å) and (b) $Ba_{0.5}Sr_{0.5}Co_{0.8}Fe_{0.2}O_{3-\delta}$ (BSCF, $a = 3.986$ Å). Miller indices are given for cubic symmetry (s.g. $Pm\bar{3}m$).

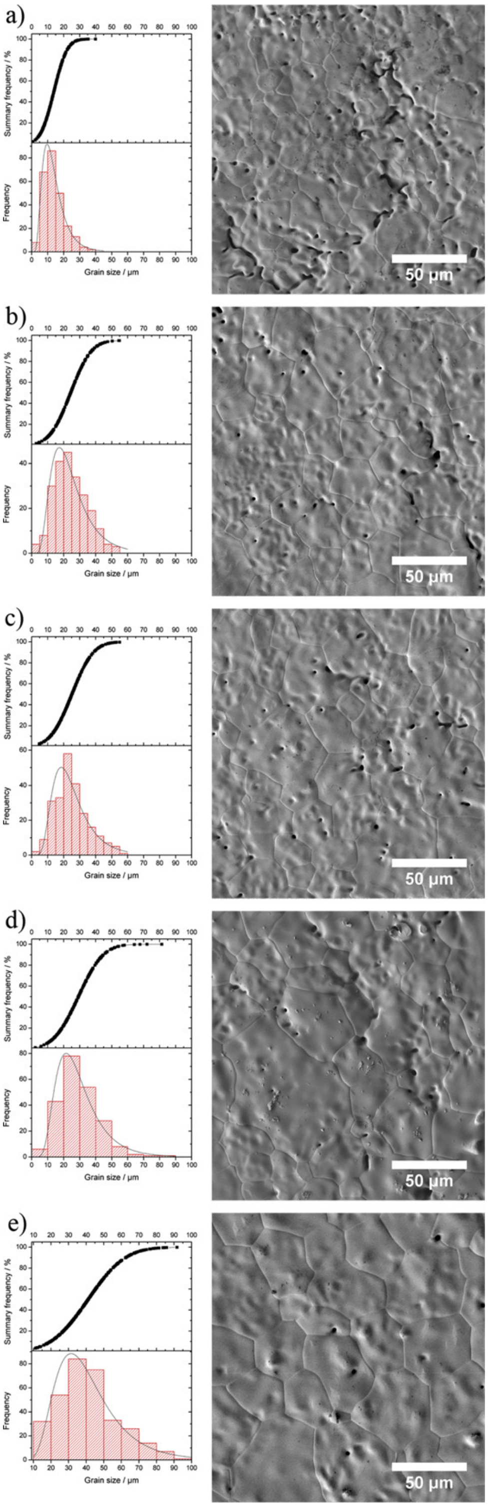

Fig. 2. Cumulative distribution function, log-normal density function, and surface view of $Ba_{0.5}Sr_{0.5}Co_{0.8}Fe_{0.2}O_{3-\delta}$ membranes after sintering at 1373 K with different dwell times: (a) 2 h, (b) 4 h, (c) 8 h, (d) 16 h, and (e) 32 h.

Table 1
Overview of samples according to sintering time, density, average grain size, and activation energy.

Sample	Sintering time (h)	Density (% theoretical)	Average grain size (μm)	Act. energy O_2permeation (kJ mol^{-1})
BSCF 1	2	90.7	13.9	29.7
BSCF 2	4	92.8	24.1	34.9
BSCF 3	8	92.2	25.2	34.8
BSCF 4	16	92.0	29.1	33.5
BSCF 5	32	91.4	41.3	34.5
SCF 1	8	94.2	11.3	46.8
SCF 2	16	94.1	15.1	46.6
SCF 3	32	94.3	19.9	55.8

The obtained grain sizes were plotted as histograms. Then, they were fitted with log-normal distribution density function. For each sintering time more than 400 different grains were analyzed and the spreading correlates to a log-normal distribution.

The average grain size as estimated by SEM micrographs increases from 13.9 to 41.3 μm. The grain size for BSCF sintered for 2 h is in the range of 1–40 μm whereby most of the grains are between 5 and 16 μm. With longer dwell times the growth of bigger grains was stimulated. The membrane sintered for 4 h exhibited grains in the range of 3–55 μm with the majority of grains between 15 and 25 μm. When sintered for 8 h the grain size spans from 5 to 60 μm with a lot of grains between 20 and 30 μm. A dwell time of 16 h leads to a grain size distribution between 6 and 90 μm with many grains between 20 and 40 μm. When sintered for 32 h the grain sizes distribute between 10 and 90 μm with most of the grains are around 30–50 μm. The slope of the cumulative distribution function shows an inhomogeneous distribution of grains for the BSCF 2 h sample. With increasing dwell time the grain size distribution is shifted to larger grains with smaller scatter around the mean value, as can be seen in Fig. 2. The grain size of all BSCF samples plotted as a function of dwell time is shown in Fig. 3. The grain growth follows a

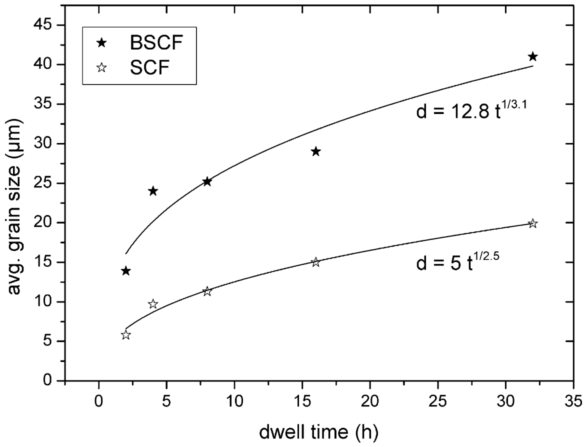

Fig. 3. Dependence of the average grain size on dwell time during sintering at 1373 K for $Ba_{0.5}Sr_{0.5}Co_{0.8}Fe_{0.2}O_{3-\delta}$ and $SrCo_{0.8}Fe_{0.2}O_{3-\delta}$. Fitting was performed using the power law $d = kt^{1/n}$.[32]

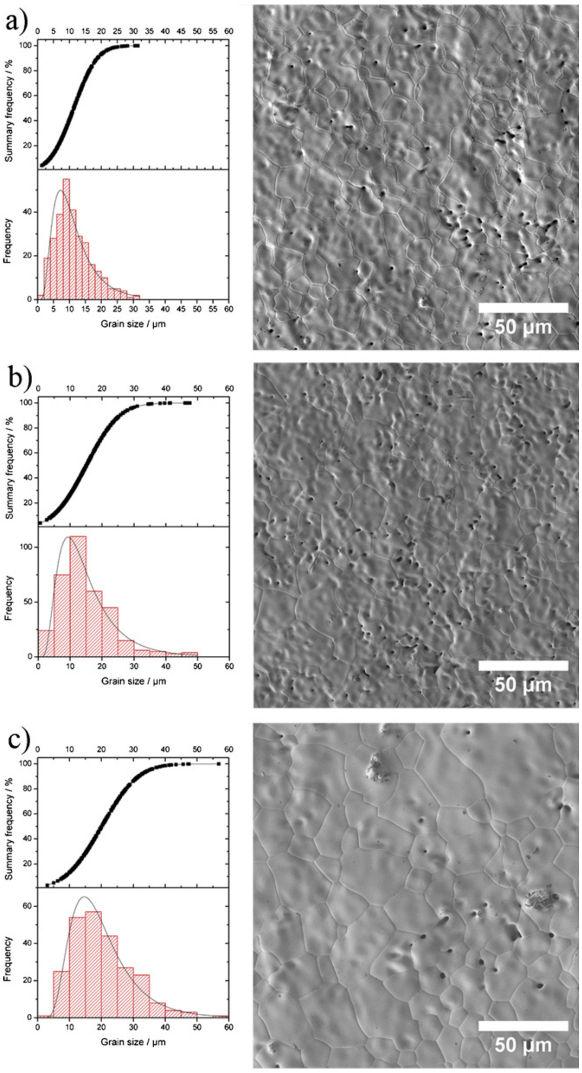

Fig. 4. Cumulative distribution function, log-normal density function, and surface view of $SrCo_{0.8}Fe_{0.2}O_{3-\delta}$ membranes after sintering at 1373 K with different dwell times: (a) 8 h, (b) 16 h, and (c) 32 h.

power law $d = kt^{1/n}$, [32] where k is the grain growth constant and n the grain growth exponent. Experimental results show a variation for metals and ceramics for *n* between 2 and 4.[33] The grain growth constant and the grain growth exponent for BSCF were estimated to be 12.8 and 3.1. The change in porosity was insignificant for the different dwell times.

For SCF analogous behavior was observed with an increase of the grain size from 11.3 to 19.9 µm (Fig. 4). The grain size of SCF sintered for 8 h ranges from 1 to 34 µm with most of the grains between 7 and 11 µm. When sintered for 16 h, grains between 2 and 48 µm with a dominant fraction between 10 and 15 µm were found. For the sample sintered for 32 h the grain size spans from 2 to 58 µm with the majority of grains around 12–18 µm. The variation of grain sizes around the mean value, obtained by cumulative distribution function, behaves similarly as reported for BSCF above. However, the grains in the SCF membranes compared to the BSCF membranes were much smaller at same dwell times and temperatures. The grain size increased, as expected, by a power law dependence with dwell time (Fig. 3). The grain growth constant and the grain growth exponent for SCF were estimated to be 5 and 2.5. This is in contrast to the findings by Zhang et al., who reported before, that grain size for SCF does not depend on sintering time at 1327 K.[21] Sintering times of 2 and 4 h in case of SCF did not lead to gas-tight ceramics, so that these samples were excluded in this study.

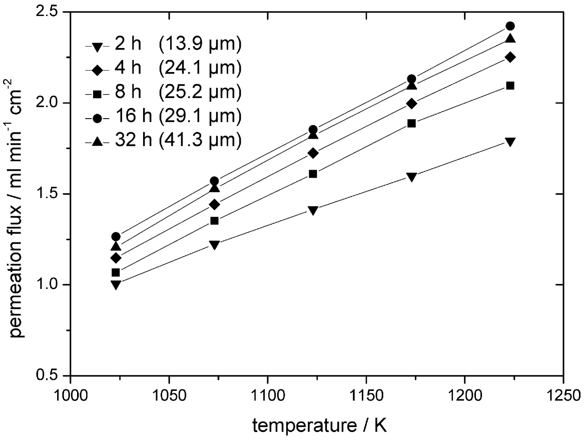

Fig. 5. Oxygen-permeation flux of $Ba_{0.5}Sr_{0.5}Co_{0.8}Fe_{0.2}O_{3-\delta}$ membranes after sintering at 1373 K for different dwell times. Average grain sizes are indicated as estimated from Fig 2.

The oxygen permeation measurements for the BSCF system are shown in Fig. 5. The membrane sintered for 2 h with an average grain size of 13.9 µm exhibited the lowest permeation flux of 1.6 mL min^{-1} cm^{-2} at 1173 K. With further increase of the grain size the permeation rate remained identically at around 2 mL min^{-1} cm^{-2}. The relative deviation between the oxygen flux of the samples sintered for 4 and 8 h is 5.5%. For the samples sintered for 16 and 32 h it is 1.8%. Both are inside the measurement uncertainty. The deviation of the sample sintered for 2 h compared to the sample sintered for 4 h is 20.1%. The activation energies calculated by Arrhenius representation are around 35 kJ mol^{-1} for membranes sintered between 4 and 32 h. The membrane sintered for 2 h exhibited a slightly decreased activation energy of 29 kJ mol^{-1}. However, this is in accordance with earlier reported values for BSCF membranes of 25–30 kJ mol^{-1} in the temperature range of 973–1173 K[24] and 40.9 kJ mol^{-1} in the temperature range of 1048–1223 K.[4]

For SCF the membrane with the smallest grains of 11.3 µm exhibited the highest flux of 1.92 mL min^{-1} cm^{-2}. However, with increasing grain size the permeation flux decreases (Fig. 6), which is opposite behavior to that of BSCF as described before. The relative deviation between the oxygen permeation fluxes for the samples sintered for 8 and 16 h is 6.8% and for the samples sintered for 16 and 32 h 20.7%. The activation energy for the oxygen permeation estimated by Arrhenius representation was around 46 kJ mol^{-1} for the membranes sintered for 8 and

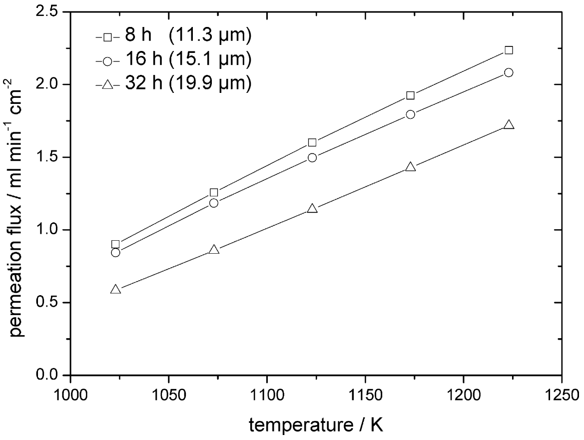

Fig. 6. Oxygen-permeation flux of $SrCo_{0.8}Fe_{0.2}O_{3-\delta}$ after sintering at 1373 K for different dwell times. Average grain sizes are indicated as estimated from Fig. 4. For short dwell times (2 h, 4 h) no dense membranes for oxygen permeation measurements could be obtained.

16 h. The membrane sintered for 32 h exhibited slightly higher activation energy of 55.7 kJ mol^{-1}. Fig. 7a shows a bright-field TEM micrograph of the sweep side of the SCF 32 h membrane. The insets show the sample regions, which were investigated by high-resolution TEM (Fig. 7b–d). The determination of the zone axis for each grain was performed by two-dimensional fast Fourier transformation shown as insets on each corresponding grain. The grain boundaries were atomically thin without any interface phases between orthorhombic brownmillerite grains I and II, as well as between brownmillerite grain II and cubic perovskite grain III.

4. Discussion

Some groups reported about the influence of microstructure on functional properties of oxygen-transporting materials, e.g. BSCF and SCF. It is hard to determine the dominating oxygen-transport paths for materials because they can change with composition. The main mechanisms for oxygen diffusion are bulk and grain boundary diffusion. The diffusion through

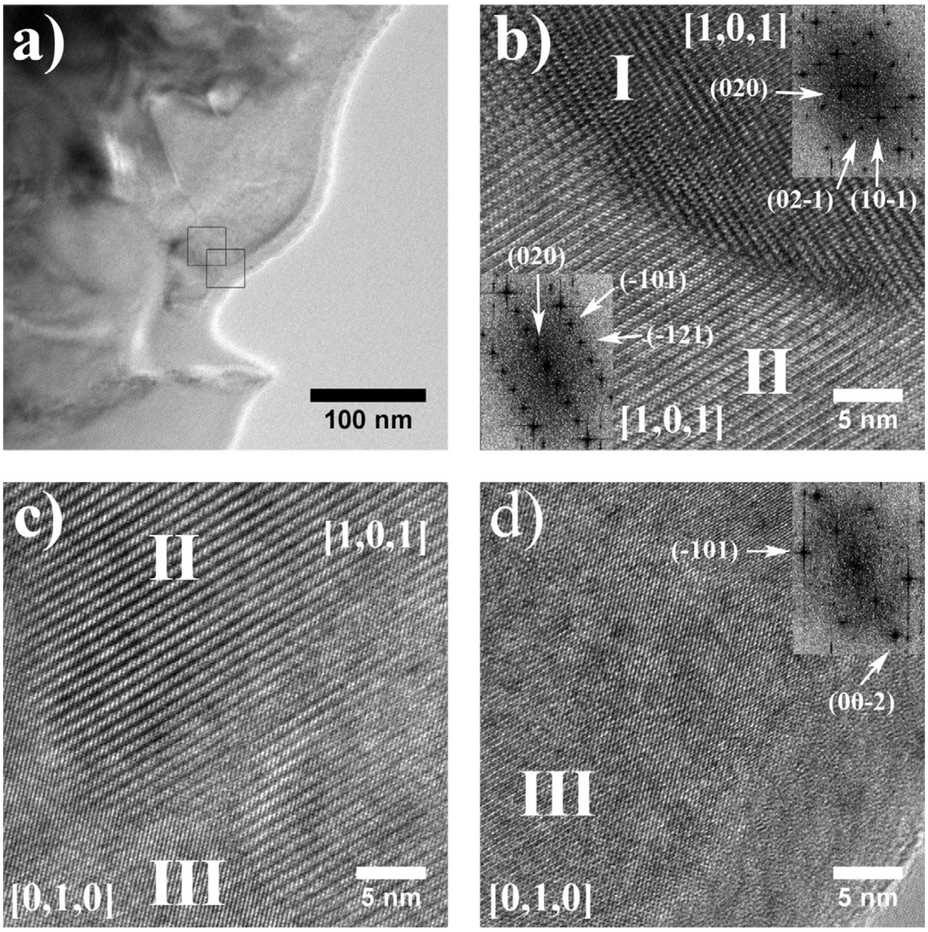

Fig. 7. (a) Bright-field TEM of the sweep side of the $SrCo_{0.8}Fe_{0.2}O_{3-\delta}$ membrane, (b) grain boundary between two brownmillerite grains I and II, which are both viewed along [1 ,0 ,1] zone axis, but with different in-plane rotation (c) interface between brownmillerite II and perovskite III and (d) perovskite III viewed along zone axis [0 ,1 ,0]. Insets showing the two-dimensional fast Fourier transformed of the corresponding grains.

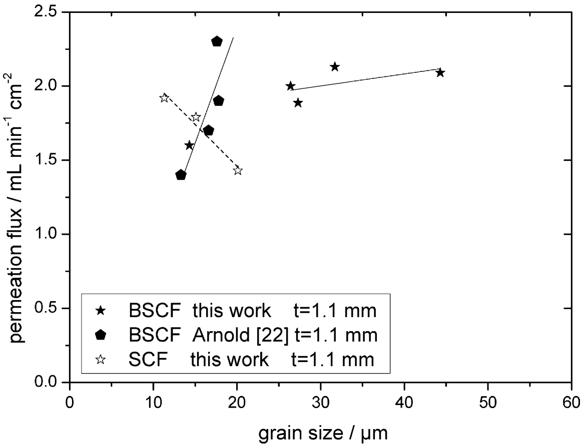

Fig. 8. Dependence of oxygen-permeation flux on the average grain size for $Ba_{0.5}Sr_{0.5}Co_{0.8}Fe_{0.2}O_{3-\delta}$ and $SrCo_{0.8}Fe_{0.2}O_{3-\delta}$ at 1173 K. The data points are taken from this work (Figs. 5 and 6) and from Arnold et al.[22]

pores may have an additional effect. However, Bauman et al. already showed low influence of porosity up to 15% in samples of BSCF.[24]

If grain-boundary diffusion is predominant, small grains are favorable. Otherwise, if bulk diffusion is the major contribution, large grains are favorable. The third possibility is no effect in the observed grain size spectrum. Grain growth can be easily induced by increasing the dwell time and sintering temperature for the BSCF and SCF membranes. Furthermore, a possible influence of the microstructure on surface exchange rates has to be kept in mind. By reducing the thickness below a characteristic value the oxygen flux is predominantly controlled by surface exchange reactions. With increasing thickness the ionic transport is governed by a combination of both processes and will be finally controlled predominantly by bulk diffusion for thick membranes. The ratio of grains and grain boundaries therefore affects both surface exchange rates and bulk diffusion coefficients. Which transport mechanism is significant, depends on membrane thickness, temperature, oxygen partial pressure gradients and possibly phase instability and/or demixing.[34]

In Fig. 8 an overview of our measured data for BSCF and the results of Arnold et al. is given.[22] In previous publications Wang et al. observed a slight increase of permeation flux with increasing grain size between 55 and 80 µm,[23] whereby the work of Baumann et al. showed a small decrease of permeation flux in the range of 10–45 µm,[24] and the result from Salehi et al. indicate no effect on permeation flux in the grain size range of 3–18 µm.[25] These results give raise to the assumption that there is no significant contribution of the grain size in the observed grain size regiment. However, according to the data from Arnold et al., who found a strong dependence for small grain sizes, i.e. predominant bulk diffusion, which is in favor of large grains, was observed in the range of 12–18 µm.[22] The small grain sizes were achieved by using boron nitride as sintering aid. By HRTEM investigations of the grain boundaries and electron-energy loss spectroscopy of the grains no boron containing phase could be detected after sintering of the membranes. The results of Arnold et al. are in agreement with our findings for a membrane with an average grain size of 13.9 µm. However, with further increase in the average grain size beyond 24 µm the variation of permeation flux is not significantly changed. A significant influence of larger grains on oxygen permeation in the grain size range of 24.1–41.3 µm could not be observed.

For SCF membranes, the oxygen permeation flux was decreased with larger grain sizes, which is in agreement with results of Zhang et al.[21] This leads to the assumption that the grain boundaries provide a faster path for oxygen transport. The increase in grain boundaries may affect the surface exchange and diffusion processes. The grain boundaries, which exhibit a higher defect concentration than the bulk material, should promote oxygen transport. Zhang et al. observed this behavior and a decrease of permeation flux on 2 mm thick membranes in the grain size regiment from 4 to 15 µm. Our measurements, which were extended to the range of 11.3–19.9 µm, could confirm this trend (Fig. 8). However, due to the low oxygen partial pressure in the used helium gas ($p(O_2) \approx 10^{-4}$ atm) a partial formation of a small amount of brownmillerite by-phase at the sweep side of the membrane, which leads to lower oxygen conductivity[35] would be another possible explanation. The increase in oxygen permeation by smaller grains may then be additionally attributed to stabilization of an oxygen-disordered phase, as observed for cobalt-substituted bismuth vanadate.[36] As shown in our TEM investigations at the sweep side of the SCF membrane sintered for 32 h an orthorhombic brownmillerite phase could be identified (Fig. 7). The XRD patterns taken from the sweep side showed single-phase cubic perovskite material. Also EDXS measurements performed on brownmillerite and perovskite grains give no evidence of difference in chemical composition, which leads to the conclusion that ordering of oxygen between $SrCo_{0.8}Fe_{0.2}O_{3-\delta}$ and $SrCo_{0.8}Fe_{0.2}O_{2.5}$ phases occurs. This is also indicated by Fig. 7c, which shows a sluggish transition between the brownmillerite II and perovskite III. A biphasic reversible transition of brownmillerite to perovskite was also found for $SrCoO_{3-\delta}$ ($\delta = 0.25$–0.5) material by Toquin et al. who did electrochemical oxygen intercalation with simultaneous in situ neutron powder diffraction.[37] As was reported by Bouwmeester et al.[34] and Qiu et al.[35] the surface exchange rates play a decisive role in SCF materials. The overall transport kinetics are probably not completely governed by the surface exchange reaction due to relative thick membranes. However, a formation of oxygen ordered by-phases like brownmillerites can cause the observed decrease in permeation flux. This may also explain the increase in activation energy for the sample sintered for 32 h compared to the samples sintered at 8 and 16 h.

5. Conclusions

The microstructural properties of BSCF and SCF membranes, which were sintered for different dwell times, were investigated in order to elucidate a possible influence on the oxygen-transport performance. The distribution of the grain size

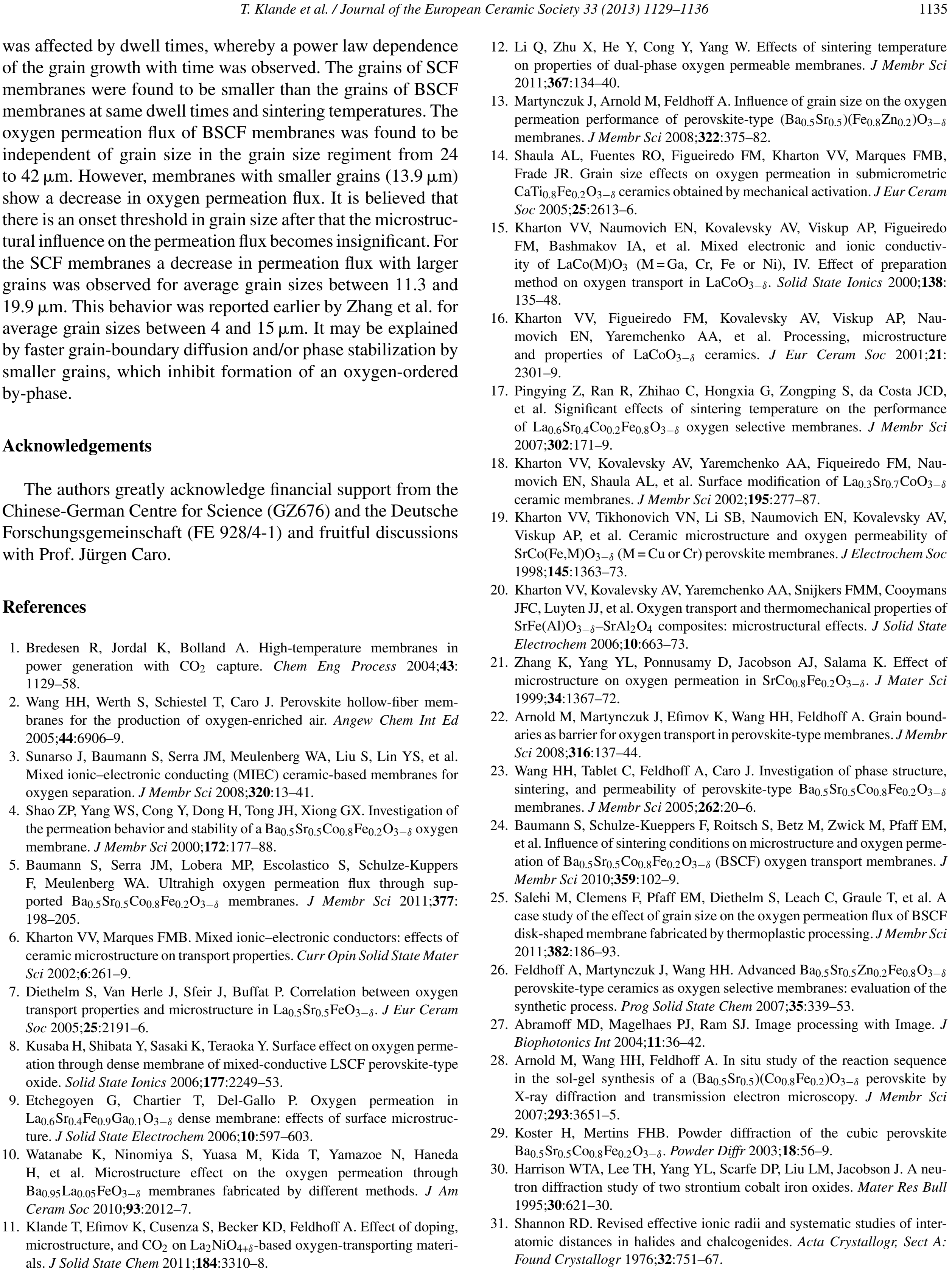

was affected by dwell times, whereby a power law dependence of the grain growth with time was observed. The grains of SCF membranes were found to be smaller than the grains of BSCF membranes at same dwell times and sintering temperatures. The oxygen permeation flux of BSCF membranes was found to be independent of grain size in the grain size regiment from 24 to 42 μm. However, membranes with smaller grains (13.9 μm) show a decrease in oxygen permeation flux. It is believed that there is an onset threshold in grain size after that the microstructural influence on the permeation flux becomes insignificant. For the SCF membranes a decrease in permeation flux with larger grains was observed for average grain sizes between 11.3 and 19.9 μm. This behavior was reported earlier by Zhang et al. for average grain sizes between 4 and 15 μm. It may be explained by faster grain-boundary diffusion and/or phase stabilization by smaller grains, which inhibit formation of an oxygen-ordered by-phase.

Acknowledgements

The authors greatly acknowledge financial support from the Chinese-German Centre for Science (GZ676) and the Deutsche Forschungsgemeinschaft (FE 928/4-1) and fruitful discussions with Prof. Jürgen Caro.

References

1. Bredesen R, Jordal K, Bolland A. High-temperature membranes in power generation with CO_2 capture. *Chem Eng Process* 2004;**43**:1129–58.
2. Wang HH, Werth S, Schiestel T, Caro J. Perovskite hollow-fiber membranes for the production of oxygen-enriched air. *Angew Chem Int Ed* 2005;**44**:6906–9.
3. Sunarso J, Baumann S, Serra JM, Meulenberg WA, Liu S, Lin YS, et al. Mixed ionic–electronic conducting (MIEC) ceramic-based membranes for oxygen separation. *J Membr Sci* 2008;**320**:13–41.
4. Shao ZP, Yang WS, Cong Y, Dong H, Tong JH, Xiong GX. Investigation of the permeation behavior and stability of a $Ba_{0.5}Sr_{0.5}Co_{0.8}Fe_{0.2}O_{3-\delta}$ oxygen membrane. *J Membr Sci* 2000;**172**:177–88.
5. Baumann S, Serra JM, Lobera MP, Escolastico S, Schulze-Kuppers F, Meulenberg WA. Ultrahigh oxygen permeation flux through supported $Ba_{0.5}Sr_{0.5}Co_{0.8}Fe_{0.2}O_{3-\delta}$ membranes. *J Membr Sci* 2011;**377**:198–205.
6. Kharton VV, Marques FMB. Mixed ionic–electronic conductors: effects of ceramic microstructure on transport properties. *Curr Opin Solid State Mater Sci* 2002;**6**:261–9.
7. Diethelm S, Van Herle J, Sfeir J, Buffat P. Correlation between oxygen transport properties and microstructure in $La_{0.5}Sr_{0.5}FeO_{3-\delta}$. *J Eur Ceram Soc* 2005;**25**:2191–6.
8. Kusaba H, Shibata Y, Sasaki K, Teraoka Y. Surface effect on oxygen permeation through dense membrane of mixed-conductive LSCF perovskite-type oxide. *Solid State Ionics* 2006;**177**:2249–53.
9. Etchegoyen G, Chartier T, Del-Gallo P. Oxygen permeation in $La_{0.6}Sr_{0.4}Fe_{0.9}Ga_{0.1}O_{3-\delta}$ dense membrane: effects of surface microstructure. *J Solid State Electrochem* 2006;**10**:597–603.
10. Watanabe K, Ninomiya S, Yuasa M, Kida T, Yamazoe N, Haneda H, et al. Microstructure effect on the oxygen permeation through $Ba_{0.95}La_{0.05}FeO_{3-\delta}$ membranes fabricated by different methods. *J Am Ceram Soc* 2010;**93**:2012–7.
11. Klande T, Efimov K, Cusenza S, Becker KD, Feldhoff A. Effect of doping, microstructure, and CO_2 on $La_2NiO_{4+\delta}$-based oxygen-transporting materials. *J Solid State Chem* 2011;**184**:3310–8.
12. Li Q, Zhu X, He Y, Cong Y, Yang W. Effects of sintering temperature on properties of dual-phase oxygen permeable membranes. *J Membr Sci* 2011;**367**:134–40.
13. Martynczuk J, Arnold M, Feldhoff A. Influence of grain size on the oxygen permeation performance of perovskite-type $(Ba_{0.5}Sr_{0.5})(Fe_{0.8}Zn_{0.2})O_{3-\delta}$ membranes. *J Membr Sci* 2008;**322**:375–82.
14. Shaula AL, Fuentes RO, Figueiredo FM, Kharton VV, Marques FMB, Frade JR. Grain size effects on oxygen permeation in submicrometric $CaTi_{0.8}Fe_{0.2}O_{3-\delta}$ ceramics obtained by mechanical activation. *J Eur Ceram Soc* 2005;**25**:2613–6.
15. Kharton VV, Naumovich EN, Kovalevsky AV, Viskup AP, Figueiredo FM, Bashmakov IA, et al. Mixed electronic and ionic conductivity of $LaCo(M)O_3$ (M = Ga, Cr, Fe or Ni), IV. Effect of preparation method on oxygen transport in $LaCoO_{3-\delta}$. *Solid State Ionics* 2000;**138**:135–48.
16. Kharton VV, Figueiredo FM, Kovalevsky AV, Viskup AP, Naumovich EN, Yaremchenko AA, et al. Processing, microstructure and properties of $LaCoO_{3-\delta}$ ceramics. *J Eur Ceram Soc* 2001;**21**:2301–9.
17. Pingying Z, Ran R, Zhihao C, Hongxia G, Zongping S, da Costa JCD, et al. Significant effects of sintering temperature on the performance of $La_{0.6}Sr_{0.4}Co_{0.2}Fe_{0.8}O_{3-\delta}$ oxygen selective membranes. *J Membr Sci* 2007;**302**:171–9.
18. Kharton VV, Kovalevsky AV, Yaremchenko AA, Fiqueiredo FM, Naumovich EN, Shaula AL, et al. Surface modification of $La_{0.3}Sr_{0.7}CoO_{3-\delta}$ ceramic membranes. *J Membr Sci* 2002;**195**:277–87.
19. Kharton VV, Tikhonovich VN, Li SB, Naumovich EN, Kovalevsky AV, Viskup AP, et al. Ceramic microstructure and oxygen permeability of $SrCo(Fe,M)O_{3-\delta}$ (M = Cu or Cr) perovskite membranes. *J Electrochem Soc* 1998;**145**:1363–73.
20. Kharton VV, Kovalevsky AV, Yaremchenko AA, Snijkers FMM, Cooymans JFC, Luyten JJ, et al. Oxygen transport and thermomechanical properties of $SrFe(Al)O_{3-\delta}$–$SrAl_2O_4$ composites: microstructural effects. *J Solid State Electrochem* 2006;**10**:663–73.
21. Zhang K, Yang YL, Ponnusamy D, Jacobson AJ, Salama K. Effect of microstructure on oxygen permeation in $SrCo_{0.8}Fe_{0.2}O_{3-\delta}$. *J Mater Sci* 1999;**34**:1367–72.
22. Arnold M, Martynczuk J, Efimov K, Wang HH, Feldhoff A. Grain boundaries as barrier for oxygen transport in perovskite-type membranes. *J Membr Sci* 2008;**316**:137–44.
23. Wang HH, Tablet C, Feldhoff A, Caro J. Investigation of phase structure, sintering, and permeability of perovskite-type $Ba_{0.5}Sr_{0.5}Co_{0.8}Fe_{0.2}O_{3-\delta}$ membranes. *J Membr Sci* 2005;**262**:20–6.
24. Baumann S, Schulze-Kueppers F, Roitsch S, Betz M, Zwick M, Pfaff EM, et al. Influence of sintering conditions on microstructure and oxygen permeation of $Ba_{0.5}Sr_{0.5}Co_{0.8}Fe_{0.2}O_{3-\delta}$ (BSCF) oxygen transport membranes. *J Membr Sci* 2010;**359**:102–9.
25. Salehi M, Clemens F, Pfaff EM, Diethelm S, Leach C, Graule T, et al. A case study of the effect of grain size on the oxygen permeation flux of BSCF disk-shaped membrane fabricated by thermoplastic processing. *J Membr Sci* 2011;**382**:186–93.
26. Feldhoff A, Martynczuk J, Wang HH. Advanced $Ba_{0.5}Sr_{0.5}Zn_{0.2}Fe_{0.8}O_{3-\delta}$ perovskite-type ceramics as oxygen selective membranes: evaluation of the synthetic process. *Prog Solid State Chem* 2007;**35**:339–53.
27. Abramoff MD, Magelhaes PJ, Ram SJ. Image processing with Image. *J Biophotonics Int* 2004;**11**:36–42.
28. Arnold M, Wang HH, Feldhoff A. In situ study of the reaction sequence in the sol-gel synthesis of a $(Ba_{0.5}Sr_{0.5})(Co_{0.8}Fe_{0.2})O_{3-\delta}$ perovskite by X-ray diffraction and transmission electron microscopy. *J Membr Sci* 2007;**293**:3651–5.
29. Koster H, Mertins FHB. Powder diffraction of the cubic perovskite $Ba_{0.5}Sr_{0.5}Co_{0.8}Fe_{0.2}O_{3-\delta}$. *Powder Diffr* 2003;**18**:56–9.
30. Harrison WTA, Lee TH, Yang YL, Scarfe DP, Liu LM, Jacobson J. A neutron diffraction study of two strontium cobalt iron oxides. *Mater Res Bull* 1995;**30**:621–30.
31. Shannon RD. Revised effective ionic radii and systematic studies of interatomic distances in halides and chalcogenides. *Acta Crystallogr, Sect A: Found Crystallogr* 1976;**32**:751–67.

32. El-Khozondar R, El-Khozondar H, Gottstein G, Rollet A. Microstructural simulation of grain growth in two-phase polycrystalline materials. *Egypt J Solids* 2006;**72**:35–47.
33. Anderson MP, Srolovitz DJ, Grest GS, Sahni PS. Computer simulation of grain growth. I. Kinetics. *Acta Metall* 1984;**32**: 783–91.
34. Bouwmeester HJM, Kruidhof H, Burggraf AJ. Importance of the surface exchange kinetics as rate limiting step in oxygen permeation through mixed-conducting oxides. *Solid State Ionics* 1994;**72**: 185–94.
35. Qiu L, Lee TH, Liu LM, Yang YL, Jacobson AJ. Oxygen permeation studies of $SrCo_{0.8}Fe_{0.2}O_{3-\delta}$. *Solid State Ionics* 1995;**76**: 321–9.
36. Steil MC, Fouletier J, Kleitz M, Labrune P. BICOVOX: Sintering and grain size dependence of the electrical properties. *J Eur Ceram Soc* 1999;**93**:815–8.
37. Le Toquin R, Paulus W, Cousson A, Prestipino C, Lamberti C. Time-resolved in situ studies of oxygen intercalaction into $SrCoO_{2.5}$, performed by neutron diffraction and X-ray absorption spectroscopy. *J Am Chem Soc* 2006;**128**:13161–74.

3.4 Phase separation in BSCF perovskite under elevated oxygen pressures from 1 to 50 bar

---

Olga Ravkina, Aleksey Yaremchenko and Armin Feldhoff

Submitted to Journal of Membrane Science (2016).

Phase separation in BSCF perovskite under elevated oxygen pressures ranging from 1 to 50 bar

Olga Ravkina[a,*], Aleksey Yaremchenko[b], Armin Feldhoff [a]

[a]Institute of Physical Chemistry and Electrochemistry, Leibniz Universität Hannover, Callinstraße 3A, D-30167 Hannover, Germany

[b]CICECO – Aveiro Institute of Materials, Department of Materials and Ceramic Engineering, University of Aveiro, 3810-193 Aveiro, Portugal

KEYWORDS: $Ba_{0.5}Sr_{0.5}Co_{0.8}Fe_{0.2}O_{3-\delta}$, phase decomposition, high oxygen pressure, oxygen nonstoichiometry, electron microscopy.

ABSTRACT: The influence of elevated oxygen pressure (from 1 to 50 bar) on phase separation in $Ba_{0.5}Sr_{0.5}Co_{0.8}Fe_{0.2}O_{3-\delta}$ cubic perovskite was investigated in the range of 300 to 1300 K. X-ray diffraction and thermogravimetric analysis revealed two separation processes occurring in the high temperature (HT), ~1043 K, and low temperature (LT), ~713 K, ranges. Increasing oxygen pressure shifts slightly the LT phase separation to lower temperature, but has a rather minor effect on the volume fraction growth of the secondary phase. Phase transformation in the HT range is a slow process and the degree of decomposition is strongly influenced by the cooling rate from higher temperatures. The LT separation is relatively fast and is essentially independent of the cooling rate. The BSCF ceramics thermally treated at $p(O_2)$=50 bar was analyzed by different electron microscopy techniques. The structures of separation products were identified as trigonal $Ba_3Co_{10}O_{17}$-like lamellae and 2H-hexagonal $Ba_{0.5\pm x}Sr_{0.5\pm x}CoO_{3-\delta}$ perovskite, respectively.

INTRODUCTION

The oxide ceramics $Ba_{0.5}Sr_{0.5}Co_{0.8}Fe_{0.2}O_{3-\delta}$ (BSCF) with cubic perovskite structure is one of the prominent mixed ionic-electronic conductors. The oxygen-transporting properties of BSCF open up broad areas of energy-relevant applications, for example as a cathode material for solid oxide fuel cells (SOFCs)[1-2] or as an oxygen separation membrane material[3-6]. BSCF demonstrates the highest known oxygen permeation flux under long-term conditions at temperatures above 1123 K[7]. Moreover, the formation of an oxygen vacancy-ordered brownmillerite structure, which was reported for $SrCo_{0.8}Fe_{0.2}O_{3-\delta}$ (SCF) at lower partial pressures of oxygen, was successfully inhibited by introduction of larger Ba cations into the cubic perovskite lattice[8-10]. The result of this substitution is an enhanced phase stability of BSCF coinciding with a high concentration of mobile oxygen vacancies and high oxygen permeation flux[11-14].

Nevertheless, economically feasible application of BSCF membrane materials require operating in the intermediate temperature range (773-1123 K)[1,15-16]. Several groups investigated the phase stability of BSCF in the intermediate temperature regime. Shao et al.[2] and van Veen at al.[17] demonstrated, that a stable and constant oxygen flux can only be realized at temperatures above 1123 K. Efimov et al.[18] confirmed these results and showed a drop of oxygen flux to about 50% of the starting value after 240 h of operation time at 1023 K. This decline of oxygen flux can be explained by degradation of the cubic perovskite structure and formation of noncubic phases, which hinder the transport of oxygen ions through the material. X-ray diffraction (XRD) investigation of BSCF after annealing in the intermediate temperature range, as performed by Rebeillieau-Dassonneville et al.[19], confirmed the formation of secondary noncubic phases. Švarcová et al.[20] described the occurrence of hexagonal 2H or 4H perovskite structures in samples annealed for 24 h at 1023 K in ambient air. Mueller et al.[21] showed by electron microscopy that BSCF samples annealed at 1073 K for 8 days resulted in the formation of 2H barium and cobalt ion rich hexagonal perovskite. They also proposed a simplistic phase diagram of BSCF at 1073 K which includes the presence of a miscibility gap in the region of BSCF composition, which could explain the decomposition into cubic and hexagonal polymorphs of the starting material. More detailed transmission electron microscopy (TEM) analyses subsequently carried out by several groups expanded the understanding of the degradation processes in the intermediate temperature range. Efimov et al.[18] first presented the formation of Co-rich 15R-related lamellar-shaped $Ba_{1-x}Sr_xCo_{2-y}Fe_yO_{5-\delta}$ complex oxide in addition to the hexagonal phase. Further investigations performed by Müller et al.,[22] who studied BSCF decomposition products after annealing periods ranging from 10 to 1350 h between 973 and 1273 K by XRD and various electron microscopy techniques, arrived at similar results. They described that, beside the hexagonal phase, a second phase with a trigonal symmetry and a plate-like morphology was formed between 973 and 1173 K. Additionally, fast formation kinetics of the trigonal phase were concluded from the absence of correlation between the annealing time and volume fraction. On the contrary, the hexagonal phase was found only in the samples annealed for 1350 h at temperatures up to 1103 K, which demonstrates a slow formation mechanism. Similar findings were reported by Liang et al.[23], who used a dead-end membrane reactor geometry with highly pressurized air (1-5 bar) and vacuum extraction. Using XRD and transmission electron microscopy the hexagonal phase was described as the cobalt-rich $Ba_{0.5\pm x}Sr_{0.5\pm x}CoO_{3-\delta}$. Lamellae were proposed to have a trigonal structure, which can be indexed in space group $R3m$, which is structurally related to the $Ba_3Co_{10}O_{17}$ layered structure as first described by Sun et al.[24-26] Furthermore, pronounced formation of secondary phases was observed at the feed side of the membrane under more oxidizing conditions. Continuing investigations concerning trigonal lamellae formation as one of the BSCF degradation products in the temperature range of 973 to 1173 K performed by Müller et al.[27] revealing the structure as $Ba_{n+1}Co_nO_{3n+3}(Co_8O_8)$ with n ≥ 2, with additional iron in the cobalt position.

The degradation of the functional properties of BSCF can be explained primarily by the change of the oxidation state of the cobalt ion. The decrease of concentration of oxygen vacancies in the intermediate temperature range requires a higher valence state of cobalt for charge compensation. Arnold et al.[28] determined the absolute value of Co(2.6+) in the cubic BSCF. Müller et al.[29] estimated the valence state of cobalt in BSCF by applying a new fasr mapping technique based on electron energy loss spectroscopy (EELS), and found that the valency increases form 2.2+ in the cubic phase to 2.8+ in the hexagonal phase. This result corresponds to the findings of Efimov et al.[18] who defined the Co valence state of 3+ in the lamellae by comparing the cobalt L_3-edge of cubic BSCF with that of well-known materials by EELS. The oxidation state of the cobalt ion influences its ionic radius. Considering Goldschmidt`s tolerance factor[30], a rough estimation of cubic perovskite phase formation criteria can be given. Based on the approach by Švarcová et al.[20] to substitute the cobalt ion with a cation of fixed valence state and ionic radius close to that of Co(2+), several groups have reported on successful partial doping with Y(3+)[31,32], Zr(4+)[33,34] or Nb(5+)[35]. However, the cubic structure stabilization effect correlates strongly with a decrease of the oxygen transport performance of BSCF.

DFT calculations performed by Kuklja et al.[36-38] show that a high concentration of oxygen vacancies stabilizes the cubic perovskite structure. Beside the temperature, the amount of oxygen vacancies is affected also by the partial pressure of oxygen. The reductive decomposition of BSCF was investigated by Mueller et al.[39], who described the material degradation at $p(O_2)$ of 10^{-12} and 10^{-10} bar at 1173 and 1273 K. A decrease of $p(O_2)$ for reductive decomposition from 10^{-13} to 10^{-15} bar with a decline of the temperature from 1173 to 973 K was described by Wagner et al.[40] and Niedrig et al[41].

Sahini et al.[42] observed a correlation between the transformation of cubic BSCF to hexagonal polymorphs and the partial pressure of oxygen by analyzing BSCF samples via in situ high temperature powder X-ray diffraction and thermo-gravimetric analysis under $p(O_2)$ ranging from inert atmosphere (10^{-4} bar) to 10 bar. The decomposition process was reported to be driven by oxidation in air and in oxygen. They detected only the formation of the hexagonal phase, while the trigonal lamellae phase separation was not described.

Recently, another phase separation process occurring in pure oxygen atmosphere at lower temperatures was reported by Yaremchenko et al.[43] and by Wang et al.[44,45]. The nature of low-temperature precipitates was not studied in detail yet, though Wang et al. suggested such precipitates can be a monoclinic Ba_2CoO_4 phase[45].

This study reports on the impact of elevated oxygen pressures on the phase separation of the cubic perovskite BSCF as investigated by XRD, thermogravimetric analysis (TGA) and differential scanning calorimetry (DSC). The formed secondary phases are analyzed by different electron microscopy techniques.

SAMPLE PREPARATION AND EXPERIMENTAL TECHNIQUES

Powders of BSCF were prepared by the glycine-nitrate self-combustion technique using metal nitrates as oxidants and glycine as fuel and chelating agent. Appropriate proportions of $Ba(NO_3)_2$ (≥ 99.0%, Sigma Aldrich), $Sr(NO_3)_2$ (≥ 99.0%, Sigma Aldrich), $Fe(NO_3)_3{*}9H_2O$ (≥ 98%, Sigma Aldrich), $Co(NO_3)_2{*}6H_2O$ (98%, Sigma Aldrich) and glycine (≥ 99%, SAFC) were dissolved in distilled water. The solution was stirred at room temperature for several hours, and then heated on a hot plate until auto-ignition. The foam-like combustion product was ground and annealed in air at 1173 K for 2 h in order to burn out organic residues. Disk-shaped samples were pressed uniaxially at 40 MPa and sintered in air at 1373 K for 5 h. The density of sintered ceramics, calculated from the mass and the geometric dimensions of the samples, was 5.13 g/cm^3 (91% of the theoretical density).

Sintered ceramic samples were cut into rectangular bars and polished. Powdered samples for thermal analysis and structural studies were prepared by grinding sintered ceramics in a mortar. Before the experiments, all samples were fired in air at 1223 K for 5 h and cooled at 5 K/min. According to the XRD results, thus-prepared samples were of a single-phase with a cubic perovskite structure (space group $Pm3m$).

X-ray diffraction (XRD) patterns were recorded at room temperature using a Rigaku D/Max-B (CuK_α, 2θ=20-80°, step 0.02°, exposition 3-5 s) diffractometer.

Thermogravimetric analysis (TGA, Setaram SetSys 16/18 instrument, sensitivity 0.4 μg) was carried out in flowing air or oxygen from 298 to 1273 K with a constant heating/cooling rate of 1-5 K/min or with isothermal equilibration steps. Initial sample mass was ~0.16 g for the samples after high-pressure DSC and ~ 0.50 g in other cases. All thermogravimetric data were corrected for buoyancy effects by subtracting corresponding baselines recorded under identical conditions using an inert alumina reference. The measurement cycle for each sample included an equilibration step in air at 1223 K for 5 h followed by cooling at 5 K/min. The absolute oxygen content at this reference state (air, 1223 K) was determined thermogravimetrically via in-situ reduction to metallic Co and Fe, coexisting with SrO and BaO, in flowing dry 10% H2-N2 gas mixture at 1273-1373 K, as described by Yaremchenko et al[43]. Thermogravimetric data were recalculated into overall oxygen content (3-δ) per formula unit of nominal $Ba_{0.5}Sr_{0.5}Co_{0.8}Fe_{0.2}O_{3-\delta}$ (BSCF) composition.

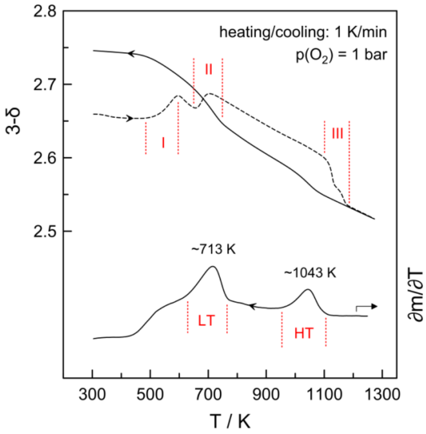

Figure 1. Thermogravimetric data for powdered air-equilibrated BSCF ceramics at $p(O_2)$ = 1 bar: (top) variations of overall oxygen content in one heating/cooling cycle, and (bottom) differential thermogravimetric curve on cooling. Marked regions: (I) re-equilibration of cubic perovskite lattice with the gas phase on heating; (II) separation of LT phase on heating or cooling; (III) recovery of single-phase cubic perovskite on heating; (HT) and (LT) – precipitation of high-temperature and low-temperature phases on cooling.

Differential scanning calorimetry (DSC) studies were performed using a Netzsch 204HP instrument under controlled oxygen pressures (10, 20 or 50 bar) at 298-873 K at a constant heating/cooling rate of 2 K/min or with isothermal steps. After the DSC runs, the samples were analyzed by XRD and TGA. Small bar-shaped ceramic samples for scanning electron microscopy (SEM) and TEM studies were annealed using the same equipment under one heating/cooling cycle (2 K/min) at *p*(O2) = 50 bar.

SEM studies were carried out on a JEOL JSM-6700F field-emission scanning electron microscope using an accelerating voltage of 2 kV. For backscattered-electron channeling contrast imaging at the higher excitation voltage of 15 kV, the ceramic sample was vibration-polished using a Buehler VibroMet 2 vibratory polisher to preserve the crystallinity of the surface.

In order to obtain a TEM sample, the ceramics was epoxy-glued between two pieces of silicon and was cut into a 1 mm × 1 mm × 2 mm block. The protected ceramics was than polished with polymer-embedded diamond lapping films down to approximately 0.015 mm thickness. After the specimen was supported on a copper slot grid, the electron transparency was achieved by argon-ion sputtering at 3 kV (Gatan, model 691 PIPS, precision ion polishing system) with incident angles in the range of 4-10°.

TEM was conducted at 200 kV with a JEOL JEM-2100F-UHR field-emission instrument, which was equipped with a Gatan GIF 2001 energy filter. TEM imaging and selected area electron diffraction (SAED) were performed on the charge-coupled device (CCD) camera of the GIF. Scanning transmission electron microscopy (STEM) was used in high-angle annular dark-field mode. A light element energy dispersive X-ray (EDX) spectrometer, Oxford Instruments INCA-200 TEM, was used for elemental analysis.

RESULTS AND DISCUSSION

1. Phase separation under *p*(O2) = 1 bar

Analysis of thermogravimetric data obtained upon temperature cycling in oxygen atmosphere (Figures 1 and 2) in combination with subsequent XRD (Figure 3) confirmed the existence of two major phase separation processes in BSCF ceramics occurring in different temperature ranges. The sequence of phase transformations is well illustrated by the TGA curves.

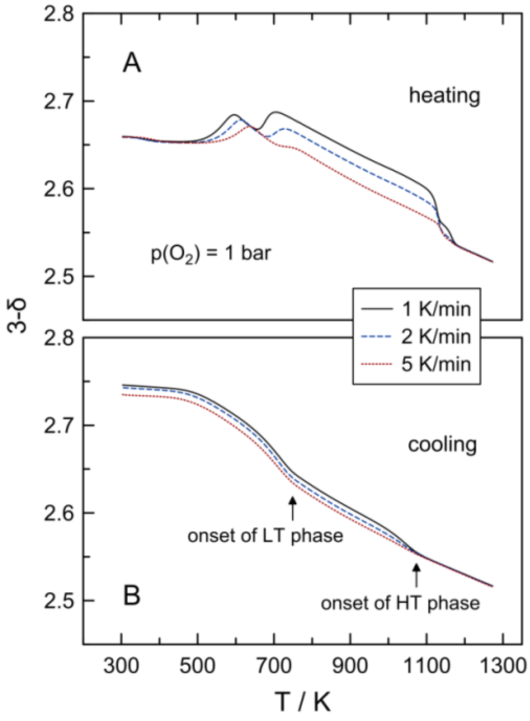

Figure 2. Thermogravimetric results for powdered BSCF ceramics at *p*(O2) = 1 bar: variations of overall oxygen content on heating (A) and cooling (B) at different rates. Before the experiment, BSCF powder was equilibrated with air at 1223 K for 5 h and then cooled at 5 K/min.

At first, heating of air-equilibrated BSCF samples in oxygen atmosphere ($p(O_2)$ = 1 bar) is accompanied by an oxygen uptake associated with the re-equilibration of the cubic perovskite lattice with the gas phase between 480 and 640 K. A second oxygen uptake on heating occurs at ~660-750 K and is assigned to a low-temperature (LT) phase separation process. Increasing the heating rate shifts the onset of this process to a higher temperature and results in a lower degree of transformation. Further heating is accompanied with a high-temperature (HT) phase separation process occurring at ~900-1050 K. Restoration of a single cubic perovskite phase on heating is a two-step process. The shape of the thermogravimetric curves obtained at different heating rates suggests that the dissolution of the LT phase occurs first and is immediately followed by elimination of the HT phase (Figure 2). A single cubic perovskite phase seems to exist above ~1200 K. These observations are generally in agreement with the high-temperature XRD data reported by Wang et al.[45].

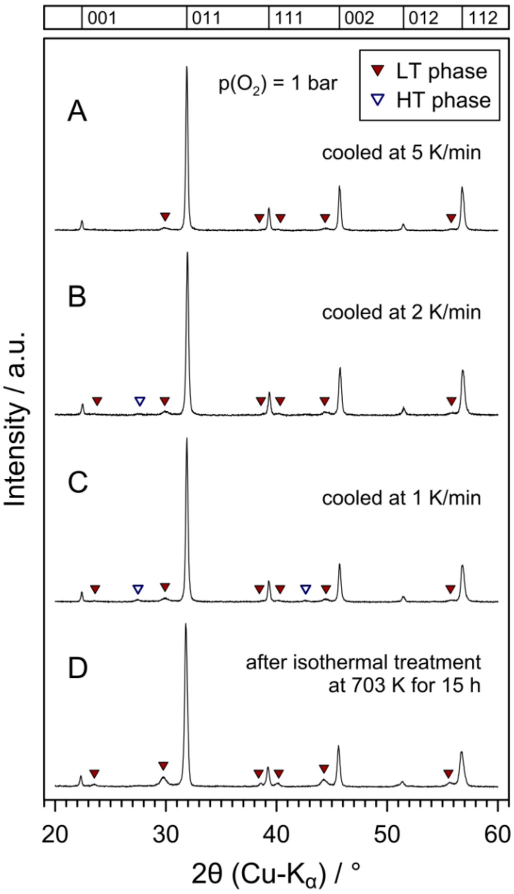

Figure 3. Room-temperature XRD patterns of BSCF powdered ceramics after treatment at $p(O_2)$ = 1 bar: (A-C) after heating/cooling cycle up to 1273 K at different rates; (D) after isothermal treatment at 703 K for 15 h. Before treatments, BSCF powder was equilibrated with air at 1223 K for 5 h and then cooled at 5 K/min. Bragg positions of the cubic BSCF are shown on top.

The phase separation processes are reversed on cooling. Distinguishable separation of the HT phase starts at approximately 1100-1120 K and achieves a maximum rate at ~ 1043 K (at 1 K/min). This is a comparatively slow process, and the degree of phase transformation depends on the cooling rate (Figure 2). On the contrary, the degree of phase transformation in the LT process is apparently independent of the cooling rate; it starts at ~ 770 K and attains a maximum rate at ~ 713 K (at 1 K/min).

XRD analysis of the sample after thermogravimetric experiments revealed the presence of two sets of impurity peaks assigned to precipitated LT and HT phases (Figures 3A-C). The relative intensity of the LT phase reflections was rather independent of the heating rate, which was in agreement with the thermogravimetric data. Although the phase could not be identified due to a low fraction volume, its reflections did not coincide with those of Ba_2CoO_4 phase (e.g., JCPDS PDF # 74-2679) as suggested by Wang et al.[45] However, taking the literature data into account, we assume that the LT phase has a trigonal symmetry[18,23,27]. The amount of HT phase was below the XRD detection limit after cooling at 5 K/min; small reflections of this phase can be distinguished in XRD patterns of the samples obtained at slower cooling rates (Figures 3B and C). At first glance, the HT phase can be identified as a hexagonal phase identical to the one formed during long-term annealing of cubic perovskite BSCF in air at 973-1123 K[18,23].

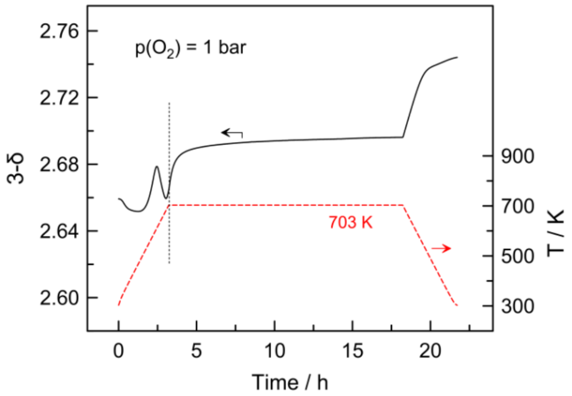

Figure 4. Thermogravimetric results for powdered BSCF ceramics at $p(O2)$ = 1 bar: variations of overall oxygen content upon heating/cooling cycles with an isothermal dwell for 15 h at 703 K. Before the experiment, BSCF powder was equilibrated with air at 1223 K for 5 h and then cooled at 5 K/min.

Figure 4 shows a thermogravimetric curve of a BSCF sample obtained using a heating/cooling cycle in oxygen flow with an isothermal step at 703 K. Longer annealing results in a somewhat larger amount of the LT phase (Figure 3D). However, its fraction increases only slightly with time after initial precipitation indicating that the cubic perovskite and LT phases tend to co-exist under these conditions.

Summarizing, one can draw the following conclusions based on the TGA and XRD data:

(i) Cubic perovskite BSCF undergoes two major phase separation processes at *p*(O2) = 1 bar;

(ii) The HT process is identical to that taking place in air, occurs at ~900-1120 K, and results in a segregation of the hexagonal phase. Once formed, the HT hexagonal phase is stable until ~ 1170 K.

(iii) The LT phase separation occurs at ~630-770 K, is faster compared to the HT process, and results in precipitation of an unidentified LT phase. The LT phase co-exists with the cubic perovskite and is stable up to ~1125 K.

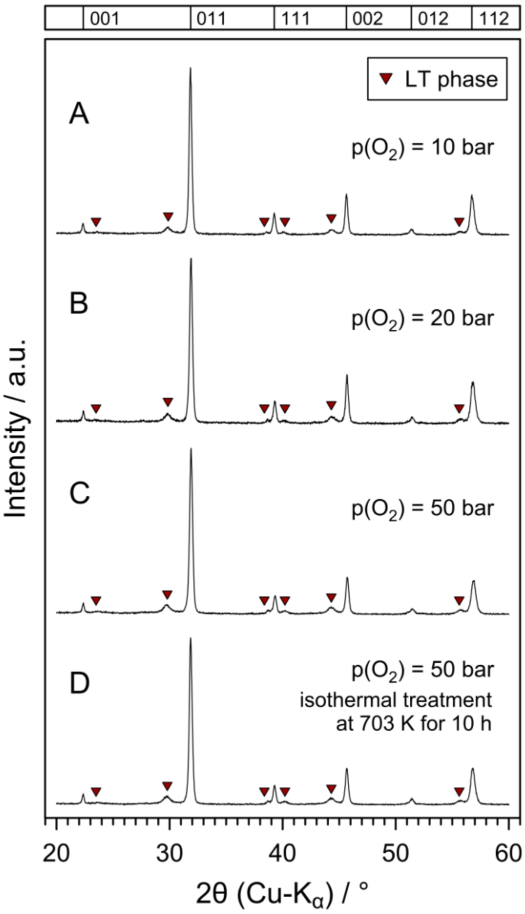

Figure 5. XRD patterns of BSCF powdered ceramics: (A-C) after heating/cooling cycles up to 873 K under different *p*(O2); (D) after isothermal treatment at 703 K for 10 h under *p*(O2) = 50 bar. In all cases, the heating/cooling rate was 2 K/min. Before treatment, the BSCF powder was equilibrated in air at 1223 K for 5 h and then cooled at 5 K/min. Bragg positions of the cubic BSCF are shown on top.

2. Effect of high oxygen pressure on LT phase separation

High-pressure DSC studies in the range of 298 to 873 K demonstrated that the LT phase separation on heating is an exothermic process. Increasing the oxygen pressure resulted in a minor shift of the phase separation to lower temperatures: from ~680-735 K at *p*(O2) = 10 bar to ~660-715 K at *p*(O2) = 50 bar. XRD analysis demonstrated, however, that the fraction of the LT phase after thermal cycling was nearly unaffected by *p*(O2) (Figure 5). This result was further confirmed by subsequent thermogravimetric analysis in air (Figure 6). Overall oxygen content per formula unit of BSCF increased only from ~2.74 atoms after treatment at *p*(O2) = 1 bar to ~2.81 atoms after treatment at *p*(O2) = 50 bar. This suggests, again, that LT phase separation is limited, and that the LT phase tends to co-exist with the major cubic perovskite phase.

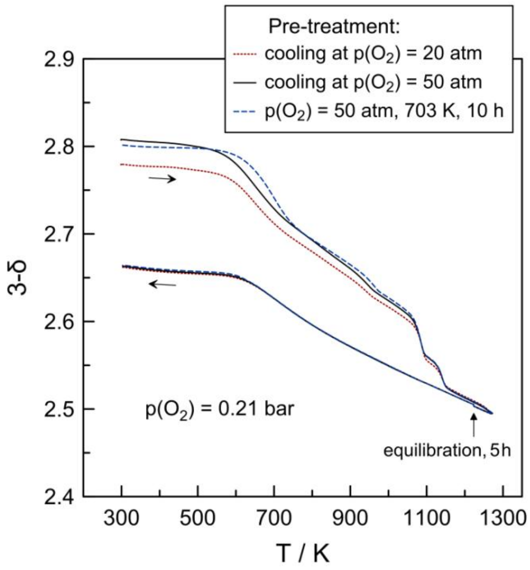

Figure 6. Thermogravimetric results for powdered BSCF ceramics at *p*(O2) = 0.21 bar: variations of overall oxygen content upon cycling of heating/cooling after treatments at elevated oxygen pressure.

3. Electron microscopy analysis

To further study the phase separation in BSCF under elevated oxygen pressures by electron microscopy, dense BSCF ceramics samples were annealed in the DSC equipment at *p*(O2) = 50 bar for one heating/cooling cycle (T_{max} = 873 K). Preliminary inspection by SEM clearly showed the formation of precipitates on the surface and in the bulk in the near-surface region of BSCF ceramics (Figure 7a). The inclusions exhibited an average diameter of 500 nm. The elemental distribution performed in scanning transition electron microscopy mode (Figure 7b-7h) demonstrated the presence of cobalt oxide particles not only on the surface of the material but also in the bulk. It is known from literature that CoO is easily formed by decomposition of Co_3O_4 spinel at temperatures above 1123 K in air[46]. Moreover, the compounds containing cobalt ions with a high valence state are not stable under standard conditions and tend to decompose to stable Co_3O_4 and CoO[47]. There is presently no thermodynamic data about the stability of more complex cobaltite materials such as BSCF. However, the formation of CoO during annealing was also reported by Müller et al[22,27]. Due to its small ionic radius compared to other ions present in

BSCF, cobalt cations exhibit a high mobility and diffusibility. However, the volume fraction ratio of cobalt oxide is low and could not be detected by XRD (Figures 3 and 5).

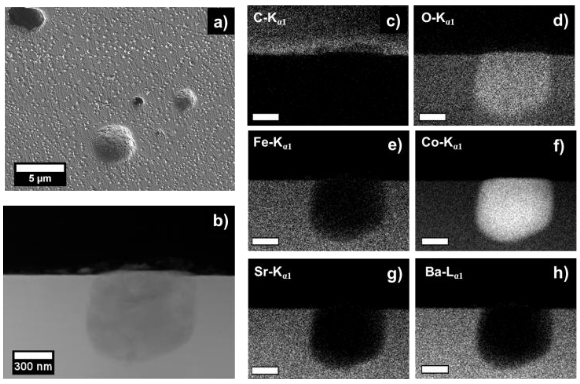

Figure 7. (a) SEM image of polished BSCF ceramics near the surface showing many inclusions with an average diameter of 500 nm. (b) Annular-dark-field STEM of the inclusion near the membrane surface. (c-h) EDXS elemental distribution. Carbon elemental distribution demonstrates the border of the membrane surface to the epoxy glue, used during specimen preparation.

Additionally, the formation of faceted pore walls was observed in the near-surface regions of the ceramics. Figure 8a demonstrates one such pore, which was opened during the TEM sample preparation and filled with epoxy glue. The closed isolated pore is shown in Figure 8b. The EDXS results revealed an identical elemental composition of the pore wall with the matrix of BSCF material. Due to the high oxygen pressure, which was conducted into the BSCF bulk material, a faceted BSCF pore wall was formed on the interface between solid ceramics and gas. Similar observations stemming from the surface investigations of ceramic materials have been reported.

The STEM micrograph in Figure 9a taken from the bulk of the BSCF specimen demonstrates the formation of oriented lamellae. The same lamellae can also be seen by SEM in the fractured membrane surface (Figure 9b).

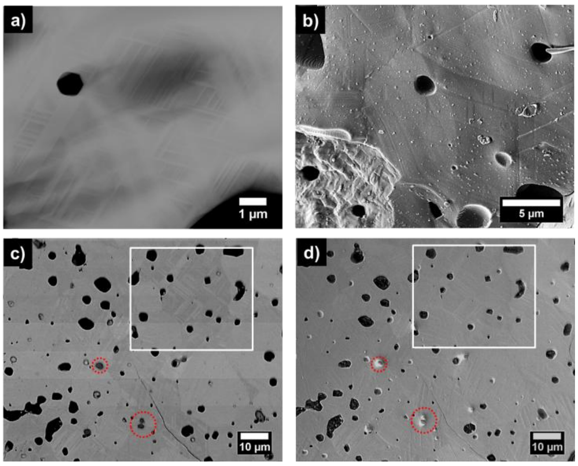

Figure 9. BSCF ceramics cross-section (heated and cooled at 873 K in 50 bar oxygen): (a) annular-dark-field STEM showing lamella-type secondary phase. (b) Lamellae in fractured membrane. Vibration-polished specimen: (c) BSE SEM showing the formation of oriented lamellae highlighted by white rectangles. (d) SE SEM. Red circles mark the further secondary phase.

To obtian a more detailed insight into the microstructure of the material vibration-polished BSCF ceramics cross-sections were analyzed by backscattered electron (BSE) and secondary electron (SE) SEM (Figures 9c and 9d, respectively). The area highlighted by the white rectangles exhibit the oriented lamellae, which show different contrast in the BSE SEM micrograph compared to the matrix material. In addition to the differences in the orientation of the grains, the disparity of contrast correlates with the average atomic number Z in the material[48].

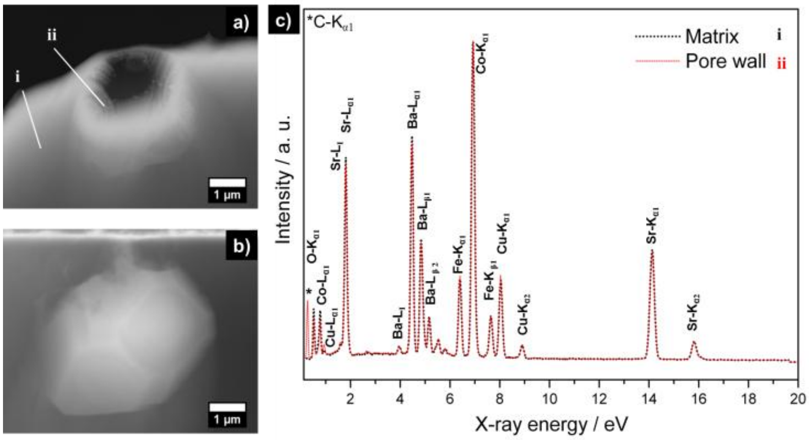

Figure 8. Formation of faceted oriented pore walls. (a, b) Annular dark-field STEM images taken near the sample surface. (c) EDX spectra of the pore wall (ii) and matrix material (i), taken from the location labeled in (a), exhibit the same elemental composition. Carbon and copper signals do not belong to the specimen.

The brighter BSE intensity of the lamellae can be explained by the greater average atomic number in this region. Assuming, that the Ba and Sr ion concentrations do not vary, the higher Co ion concentration in the lamellae might be responsible for the increase in Z. Similarly, the red encircled areas in Figures 9c and 9d show darker BSE intensities, which suggest a decrease of the average atomic number in this region. As the Z value of cobalt oxide is small compared to BSCF, we expect that cobalt oxide particles would exhibit a similarly dark BSE intensity in Figure 9c.

The oriented lamellae were analyzed by TEM in HRTEM and SAED mode. Figure 10a shows a representive bright-field TEM micrograph with crossing lamellae. The lamellae are formed in two directions and the crossing angle is 70° as evident from the HRTEM micrographs in Figures 10 b and 10c. The matrix area **i** consists of a cubic perovskite structure viewed along the $[1,1,0]_{cubic}$ direction (Figure 10d). The lamellae shown in the region **ii** contain areas with different structures. In addition to the cubic structure, viewed along the $[1,1,0]_{cubic}$ direction, a superstructure with a double cubic cell parameter is formed (Figure 10e). Similar observations were made by Efimov et al.[18], who found alternating cubic and 15R-related structures inside a lamella. Additionally, formation of stacking faults can be observed in the HRTEM images, which also results in streaking of the reflections in the SAED pattern in Figure 10e. The crossing angle of 70° displayed along the $[1,1,0]_{cubic}$ direction corresponds to the angle, that is formed by crossing of the close-packed layers of the cubic structure (Figure 10f).

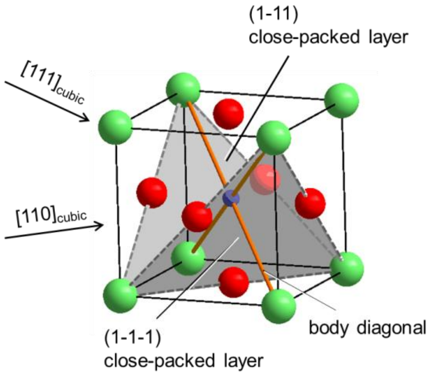

Figure 11. Face-centered unit cell of cubic ABO_3 perovskite (A cations – green balls, B cations – blue balls, O anions – red balls). Gray triangular surfaces represent two close-packed layers oriented perpendicular to the body diagonals (orange lines). The [111] zone axis along a further body diagonal and the [110] zone axis along a face diagonal are shown with arrows.

Figure 11 demonstrates the face-centered ABO_3 unit cell of the ideal cubic perovskite structure. This structure can also be described by a close-packed array of anions, with one quarter of these replaced by larger A cations in an ordered manner[49]. The close-packed layers (gray triangular surfaces in Figure 11) run parallel to the {111} planes or perpendicular to the body diagonal of the cube. Therefore, there are four different orientations of such close-packed layers.

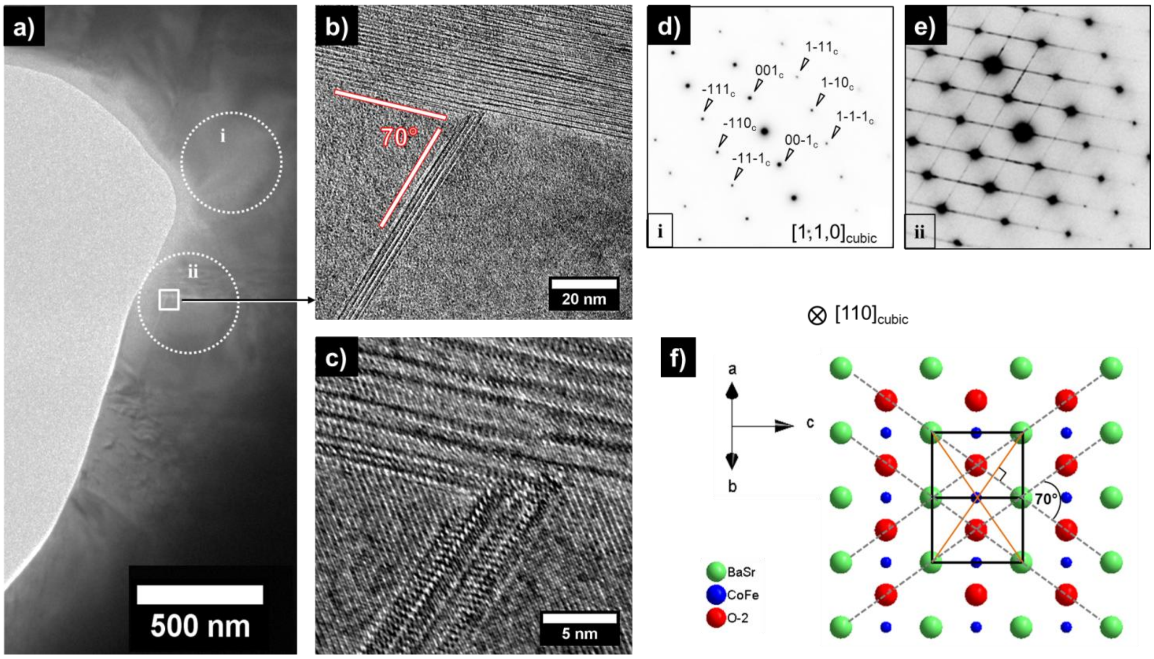

Figure 10. (a) TEM bright-field micrograph. (b, c) HRTEM of lamellae and stacking faults, which are formed in two directions with an angle of 70°. (d) SAED pattern of encircled area i showing the cubic structure along $[110]_{cubic}$. (e) SAED pattern of encircled area ii showing the formation of super cell structure. (f) Scheme of cubic perovskite structure along $[110]_{cubic}$. The unit cell is shown by black lines. The close-packed layers (only two can be seen here), represented by dotted gray lines, form by crossing at an angle of 70°. The body diagonals of the unit cell are colored orange.

For a better overview, only two of four close-packed layers, plane (1-11) and plane (1-1-1), are shown in Figure 11. The angle that is formed between these two planes is 70°. This indicates that the new superstructure is built along the close-packed layers of the cubic perovskite.

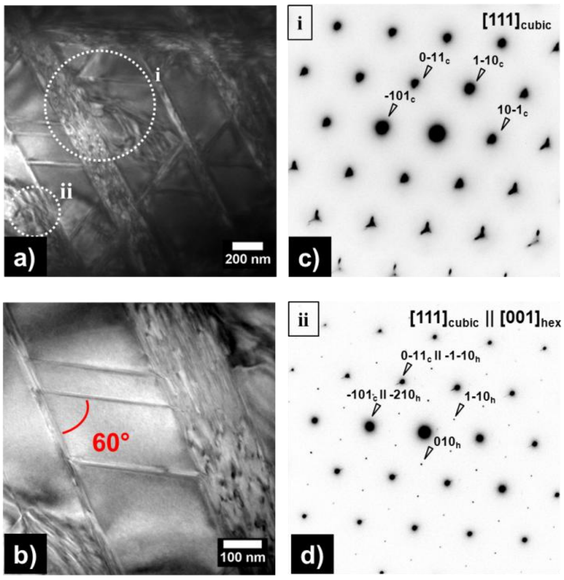

Figure 12. (a, b) TEM bright-field micrographs. (c, d) Corresponding SAED patterns. Hexagonal lamellae are formed in cubic BSCF along $[111]_{cubic}$.

Müller et al.[27] have shown in a previous investigation that the formation of a hexagonal secondary phase is pronounced in the grain boundaries. In this work we observed the 2H hexagonal phase lamellae with a thickness between approximately 20 and 200 nm running through the grain as demonstrated in Figure 12. Indexing the SAED pattern in Figure 12c, the structure of the matrix material can be estimated as cubic viewed along the $[111]_{cubic}$ direction. The SAED pattern in Figure 12d shows reflections from cubic BSCF as well as hexagonal perovskite. The close-packed layers of cubic and hexagonal perovskite are arranged parallel, $[111]_{cubic} \parallel [001]_{hex}$. Similar results were reported by Liang et al.[23], who reported hexagonal lamellae growing mostly along the cubic <110> direction. However, as shown in Figure 12a and 12b the hexagonal lamellae grow along different directions and form crossing angles of 60°, which corresponds to the angle between the cubic planes (-101) and (0-11) viewed along the $[111]_{cubic}$ direction.

Figure 13a shows a dark-field TEM micrograph of the sample in a region near the surface. At first, according to the elemental distribution and as already presented in Figure 7 and Figure 9, two grains of cobalt oxide can be seen (Figures 13b,13f). Moreover, lamellae with different orientation and size are formed near to the cobalt oxide. We can confirm the observations of Müller et al.[27] who found that the plate-like regions are favorably formed at cobalt oxide precipitates.

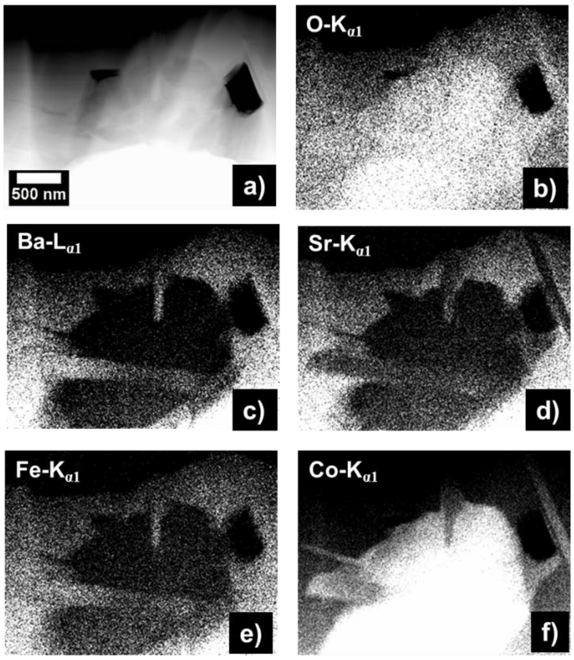

Figure 13. (a) TEM investigation close to specimen surface. (a) Annular dark-field STEM. (b-f) EDXS elemental distributions.

The Sr content varies within the lamellae shown (Figure 13d). One explanation for this observation can be the formation of alternating cubic and noncubic structures inside individual lamellae. For further investigations, the lamella shown in the top right corner of Figure 13a was chosen. The detailed EDX elemental distribution of this lamella is presented in Figure 14. The lamella contained no strontium and was Co-, Ba- and oxygen-rich. The iron concentration did not differ from that of the matrix material. The absence of strontium agrees well with the barium cobaltite series $Ba_{n+1}Co_nO_{3n+1}(Co_8O_8)$ described by Sun et al.[24] and investigated in detail by Müller et al[22,27].

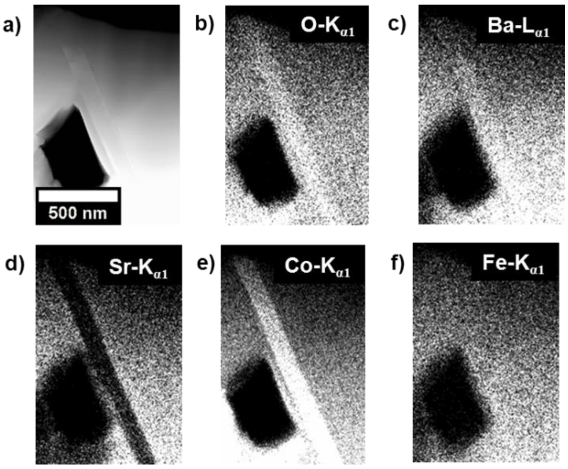

Figure 14. (a) TEM investigation of lamellar area corresponding to the top right corner of Figure 13. (a) Annular-dark-field STEM. (b-f) EDXS elemental distributions.

Figures 15a and 15b show the STEM and corresponding dark-field TEM images of the lamella from Figure 14. The structure can be indexed as $Ba_3Co_{10}O_{17}$, which is a member of the $Ba_{n+1}Co_nO_{3n+1}(Co_8O_8)$ series with n=2, or one with a double perovskite layer. This structure is an intergrowth cobaltite, which contains alternating CdI_2-type layers and perovskite layers. $Ba_3Co_{10}O_{17}$ was reported to be metastable and to transform into a 2H hexagonal oxide at high temperature[24]. However, according to the EDXS elemental distribution in Figure 14, the lamella contains iron in the same concentration as the cubic BSCF matrix material. We assume that the perovskite layer as well as CdI2-type layer inside the $Ba_3Co_{10}O_{17}$ structure can accommodate iron ions in octahedral coordination. The lamella is formed in the cubic perovskite BSCF matrix (Figure 15c), which also shows the presence of iron cations. In contrast, the hexagonal phase is characterized by the absence of iron ions, which are too large for the structure. The HRTEM micrographs, shown in Figure 15d and 15f show the stacking sequences of the corresponding perovskite and CdI_2-type layers inside the trigonal $Ba_3Co_{10}O_{17}$ lamella, as viewed along the $[-110]_{trig}$ direction.

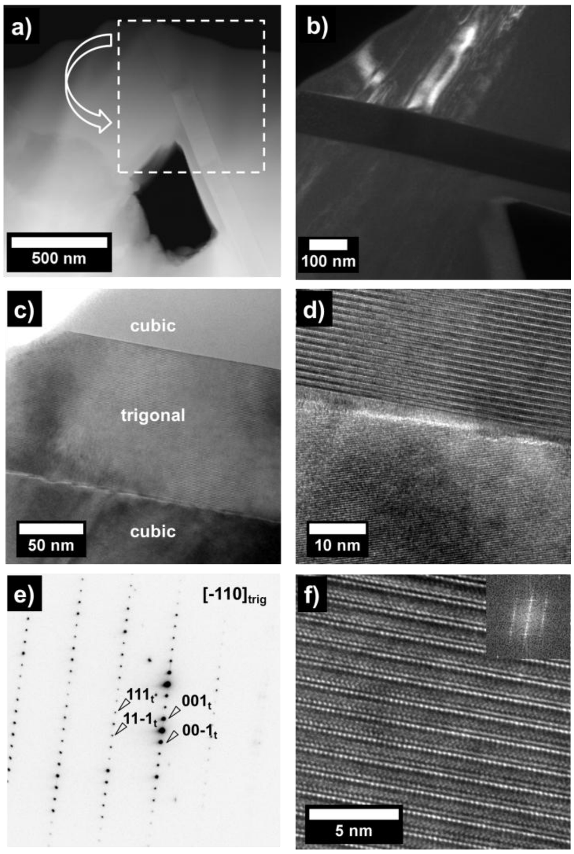

Figure 15. TEM investigation of the lamella shown in Figure 14. (a) Annular-dark-field STEM. The dashed square shows the area represented in b), which is rotated by approx. 60°. (b) Annular dark-field TEM. (c, d) HRTEM of the lamella and the surrounding matrix. (e) SAED pattern of trigonal lamella (e) HRTEM of lamella with FFT pattern.

SUMMARY

The influence of elevated oxygen pressure (from 1 to 50 bar) on decomposition process of $Ba_{0.5}Sr_{0.5}Co_{0.8}Fe_{0.2}O_{3-\delta}$ (BSCF) ceramics with cubic perovskite structure was investigated in the range from 300 to 1300 K. Based on the TGA and XRD results, we can conclude that two major phase separation processes occur at $p(O2)$ = 1 bar. High-temperature (HT) segregation, which results in the formation of the 2H hexagonal phase, takes place between 900-1200 K and, if compared to the LT separation, is a slow process. The degree of decomposition into the HT phase is strongly influenced by the cooling rate from higher temperatures. The low-temperature (LT) separation of the trigonal $Ba_3Co_{10}O_{17}$ phase occurs between 630 and 670 K. The LT phase co-exists with the cubic perovskite phase and is stable up to ~1125 K. Moreover, it was shown that the LT phase separation is a fast process and is almost unaffected by the cooling rate or oxygen pressure in the studied range of conditions. Electron microscopy analyses, performed on BSCF samples at $p(O2)$ = 50 bar after one heating/cooling cycle (T_{max} = 873 K), showed the pronounced formation of cobalt oxide precipitates not only close to the surface of the investigated specimen, but also in the bulk. These cobalt oxide particles can serve as a nucleation agent for the formation of cobalt-rich $Ba_3Co_{10}O_{17}$ lamellae, which consists of alternating perovskite-type and CdI_2-type layers. It was shown, that this structure can accommodate a large amount of iron, most likely at cobalt-sites with octahedral coordination. Additionally, a mixture of the cubic perovskite phase and a superstructure phase (with a double cell parameter) were found inside of a single lamella. This superstructure is formed on the close-packed layers of the cubic structure. Furthermore, the formation of stacking faults is favored in this area. We hypothesize that the formation of $Ba_3Co_{10}O_{17}$ lamellae start with a change of the valence state and interdiffusion of Co ions. This leads to the ordering of oxygen in the cubic structure and reduction of concentration of oxygen vacancies in this region, which destabilizes the cubic structure. The observed superstructure might be a transition state between the cubic and noncubic phase. Because the iron concentration remains constant in the cubic and trigonal phase, it can be concluded that the diffusibility of iron is small compared to that of the Co cation. However, the formation of a hexagonal phase also requires the diffusion of iron, because the Fe cation is too large for the B-sites of the hexagonal phase.

In addition to the trigonal lamellae (the LT phase), hexagonal lamellae (the HT phase) were found in the specimen. Contrary to earlier reports, the hexagonal phase was not found in the grain boundaries, but in the grains themselves, as lamellae with different orientations.

AUTHOR INFORMATION

Corresponding Author

* E-mail: olga.ravkina@pci.uni-hannover.de

Author Contributions

The manuscript was written through contributions of all authors. All authors have given approval to the final version of the manuscript.

ACKNOWLEDGMENT

O.R. and A.F. acknowledge financial support by the Deutsche Forschungsgemeinschaft (DFG) under grant FE928/7-1. We also acknowledge Frank Steinbach for his support during TEM investigations and fruitful discussions. A. Y. would like to acknowledge support from the FCT, Portugal (project IF/01072/2013/ CP1162/CT0001 and project CICECO - Aveiro Institute of Materials POCI-01-0145-FEDER-007679 (FCT ref. UID/CTM/50011/2013) financed by national funds through the FCT/MEC and when applicable co-financed by FEDER under the PT2020 Partnership Agreement).

ABBREVIATIONS

BSCF, $Ba_{0.5}Sr_{0.5}Co_{0.8}Fe_{0.2}O_{3-\delta}$; BSE, backscattered electron; EELS, electron energy loss spectroscopy; EDXS, energy dispersive X-ray spectroscopy; DSC, differential scanning calorimetry; HAADF, high angle annular dark field; HRTEM, high resolution transmission electron microscopy; FFT, fast Fourier transformation; SEM, scanning electron microscopy; SE, secondary electron; SAED, selected area electron diffraction; STEM, scanning transmission electron microscopy; TEM, transmission electron microscopy; TGA, thermogravimetric analysis; XRD, X-ray diffraction.

REFERENCES

[1] Zhou, W.; Ran, R.; Shao, Z. Progress in understanding and development of $Ba_{0.5}Sr_{0.5}Co_{0.8}Fe_{0.2}O_{3-\delta}$-based cathodes for intermediate temperature solid-oxide fuel cell: a review. *J. Power Sources* **2009**, 192, 231-246.

[2] Shao, Z.; Haile, S.M.; A high-performance cathode for the next generation of solid-oxide fuel cell, *Nature* **2004**, 431, 170-173.

[3] Chen, C.; Feng, S.; Ran, S.; Zhu, D.; Liu, W.; Boumeester, H.J.M. Conversion of methane to syngas by a membrane-based oxidation–reforming process. *Angew. Chem. Inter. Ed.* **2003**, 42, 5196.

[4] Sunarso, J.; Baumann, S.; Serra, J.M.; Meulenberg, W.A.; Liu, S.; Lin, Y.S.; da Costa, J.D. Mixed ionic-electronic conducting (MIEC) ceramic-based membranes for oxygen separation. *J. Membr. Sci.* **2008**, 320, 13-41.

[5] Shao, Z.; Yang, W.; Cong, Y.; Dong, H.; Tong, J.; Xiong, G. Investigation of the permeation behavior and stability of a $Ba_{0.5}Sr_{0.5}Co_{0.8}Fe_{0.2}O_{3-\delta}$ oxygen membrane. *J. Membr. Sci.* **2000**, 172, 177-178.

[6] Kovalevsky, A.V.; Yaremchenko, A.A.; Kolotygin, V.A.; Shaula, A.L.; Kharton, V.V.; Snijkers, F.M.M.; Buekenhoudt, A.; Frade, J.R.; Naumovich, E.N. Processing and oxygen permeation studies of asymmetric multilayer $Ba_{0.5}Sr_{0.5}Co_{0.8}Fe_{0.2}O_{3-\delta}$ membranes. *J. Membr. Sci.* **2011**, 380, 68-80.

[7] McIntosh, S.; Vente, J.F.; Haije, W.G.; Blank, D.H.A.; Bouwmeester, H.J.M. Oxygen stoichiometry and chemical expansion of $Ba_{0.5}Sr_{0.5}Co_{0.8}Fe_{0.2}O_{3-\delta}$ measured by in situ neutron diffraction. *Chem. Mater.* **2006**, 18, 2187-2193.

[8] Grundbaum, N.; Mogni, L.; Prado, F.; Caneiro, A.J.; Phase equilibrium and electrical conductivity of $Sr(Co_{0.8}Fe_{0.2})O_{3-\delta}$. *J. Solid State Chem.* **2004**, 177, 2350-2357.

[9] Liu, L.M.; Lee, T.H.; Qui, L.; Yang, Y.L.; Jacobson, A.J. A thermogravimetric study of the phase diagram of strontium cobalt iron oxide $Sr(Co_{0.8}Fe_{0.2})O_{3-\delta}$. *Mater. Res. Bull.* **1996**, 31, 29-35.

[10] Harrison, W.T.A.; Lee, T.H.; Yang, Y.L.; Scarfe, D.P.; Liu, L.M.; Jacobson, A.J. Neutron diffraction study of two strontium cobal iron oxides. *Mater. Res. Bull.* **1995**, 30, 621-630.

[11] Zeng, P.; Chen, Z.; Gu, H.; Shao, Z.; Liu, S. Re-evaluation of $Ba_{0.5}Sr_{0.5}Co_{0.8}Fe_{0.2}O_{3-\delta}$ perovskite as oxygen semi-permeable membrane. *J. Membr. Sci.* **2007**, 291, 148-156.

[12] Shao, Z.; Xiong, G.; Tong, J.; Dong, H.; Yang, W. Ba effect in doped $Sr(Co_{0.8}Fe_{0.2})O_{3-\delta}$ on the phase structure and oxygen permeation properties of the dense ceramic membranes. *Sep. Purif. Technol.* **2001**, 25, 419-429.

[13] McIntosh, S.; Vente, J.F.; Haije, W.G.; Blank, D.H.A.; Bouwmeester, H.J.M. Phase stability and oxygen non-stoichiometry of $SrCo_{0.8}Fe_{0.2}O_{3-\delta}$ measured by in situ neutron diffraction. *Solid State Ionics*. **2006**, 177, 833-842.

[14] Kriegel, R.; Kircheisen, R.; Töpfer, J. Oxygen stoichiometry and expansion behavior of $Ba_{0.5}Sr_{0.5}Co_{0.8}Fe_{0.2}O_{3-\delta}$. *Solid State Ionics.* **2010**, 181, 64-70.

[15] Steele, B.C.H.; Heinzel, A. Materials for fuel-cell technologies. *Nature*. **2001**, 345-352.

[16] Brett, D.J.L.; Atkinson, A.; Brandon, N.P.; Intermediate temperature solid oxide fuel cells. *Chem. Soc. Rev*. **2008**, 37, 1568-1578.

[17] van Veen, A.C.; Reveilleau, M.; Farruseng, D.; Mirodatos, C.; Studies on the performance stability of mixed conducting BSCFO membranes in medium temperature oxygen permeation. *Chem. Commun*. **2003**, 32-33.

[18] Efimov, K.; Xu, Q.; Feldhoff, A. Transmission microscopy study of $Ba_{0.5}Sr_{0.5}Co_{0.8}Fe_{0.2}O_{3-\delta}$ perovskite decomposition at intermediate temperatures. *Chem. Mater*. **2010**, 5866-5875.

[19] Rebeilleau-Dassonneville, M.; Rosini, S.; van Veen, A.C.; Farrusseng, D.; Mirodatos, C. Oxidative activation of ethane on catalytic modified dense ionic oxygen conducting membranes. *Catal. Today* **2005**, 104, 131-137.

[20] Švarcová, S., Wiik, K.; Tolchard, J.; Bouwmeester, H.J.M.; Grande, T.; Structural instability of cubic perovskite $Ba_xSr_{1-x}Co_{1-y}Fe_yO_{3-\delta}$. *Solid State Ionics* **2008**, 178, 1787-1791.

[21] Mueller, D.N.; De Souza, R.A.; Weirich, T.E.; Roehrens, D.; Mayer, J.; Martin, M. A kinetic study of the decomposition of the cubic perovskite-type oxide $Ba_xSr_{1-x}Co_{1-y}Fe_yO_{3-\delta}$ (BSCF) (x=0.1 and 0.5). *Phys. Chem. Chem. Phys*. **2010**, 12, 10320-10328.

[22] Müller, P.; Störmer, H.; Dieterle, L.; Niedrig, C.; Ivers-Tiffée, E.; Gerthsen, D. Decomposition pathway of cubic $Ba_{0.5}Sr_{0.5}Co_{0.8}Fe_{0.2}O_{3-\delta}$ between 700 °C and 1000 °C analyzed by electron microscopy techniques. *Solid State Ionics* **2012**, 57-66.

[23] Liang, F.; Jiang, H.; Luo, H.; Caro, J.; Feldhoff, A. Phase stability and preparation behavior of a dead-end $Ba_{0.5}Sr_{0.5}Co_{0.8}Fe_{0.2}O_{3-\delta}$ tube membrane in high-purity oxygen production. *Chem. Mater*. **2011**, 23, 4765-4772.

[24] Sun, J.; Yang, M.; Li, G.; Yang, T.; Liao, F.; Wang, Y.; Xiong, M.; Lin, J. New barium cobaltite series $Ba_{n+1}Co_nO_{3n+3}(Co_8O_8)$: intergrowth structure containing perovskite and CdI2-type layers. *Inorg. Chem*. **2006**, 45, 9151-9153.

[25] Ehora, D.; Daveiro-Minaud, S.; Colmont, M.; André, G.; Metré, O. $Ba_2Co_9O_{14}$: new inorganic building blocks with magnetic ordering through super-super exchanges only. *Chem. Mater*. **2007**, 19, 2180-2188.

[26] David, R.; Pautrat, A.; Kabbour, H.; Sturza, M.; Curelea, S.; André, G.; Pelloquin, D.; Metré, O. $[BaCoO_3]_n[BaCo_8O_{11}]$ modular intergrowths: singularity of the n = 2 Term. *Chem. Mater*. **2011**, 23, 5191-5199.

[27] Müller, P.; Störmer, H.; Meffert, M.; Dieterle, L.; Niedrig, C.; Wagner, S.F.; Ivers-Tiffée, E.; Gerthsen, D. Secondary phase formation in $Ba_{0.5}Sr_{0.5}Co_{0.8}Fe_{0.2}O_{3-\delta}$ studied by electron microscopy. *Chem. Mater*. **2013**, 25, 564-573.

[28] Arnold, M.; Xu, Q.; Tichelaar, F.D.; Feldhoff, A.; Local charge disproportion in a high-performance perovskite. *Chem. Mater*. **2009**, 21, 635-640.

[29] Müller, P.; Meffert, M.; Störmer, H.; Gerthsen, D. Fast mapping of the cobalt-valence state in $Ba_{0.5}Sr_{0.5}Co_{0.8}Fe_{0.2}O_{3-\delta}$ by

electron energy loss spectroscopy. *Microsc. Microanal.* **2013**, 19, 1595-1605.

[30] Goldschmidt, V.M.; Barth, T.; Lunde, G.; Zachariasen, W. Geochemische Verteilungsgesetze der Elemente: 7, Die Gesetze der Kristallchemie, Oslo, I Kommission Hos Jacob Dybwad 1926, 58-74.

[31] Haworth, H.; Smart, S.; Glasscock, J.; Diniz da Costa, J.C. Yttrium doped BSCF membranes for oxygen separation. *Sep. Purif. Techol.* **2011**, 81 (1), 88-93.

[32] Haworth, H.; Smart, S.; Glasscock, J.; Diniz da Costa, J.C. High performance yttrium-doped BSCF hollow fibre membranes. *Sep. Purif. Techol.* **2012**, 94, 16-22.

[33] Yakovlev, S.; Yoo, C.-Y.; Fang, S.; Bouwmeester, H.J.M. Phase transformation and oxygen equilibration kinetics of pure and Zr-doped $Ba_{0.5}Sr_{0.5}Co_{0.8}Fe_{0.2}O_{3-\delta}$ perovskite oxide probed by electrical conductivity relaxation. *Appl. Phys. Lett.* **2010**, 96 (25), 254101.

[34] Ravkina, O.; Klande, T.; Feldhoff, A. Investigation of Zr-doped BSCF perovskite membrane for oxygen separation in the intermediate temperature range. *J. Solid State Chem.* **2013**, 101-106.

[35] Fang, S.M.; Yoo, C.-Y. Bouwmeester, H.J.M; Performance and stability of niobium-substituted $Ba_{0.5}Sr_{0.5}Co_{0.8}Fe_{0.2}O_{3-\delta}$ membranes. *Solid State Ionics* **2011**, 1-6.

[36] Kuklja, M.M.; Mastrikov, Y.A.; Jansang, B.; Kotomin, E.A. The intrinsic defects, disordering, and structural stability of $Ba_xSr_{1-x}Co_yFe_{1-y}O_{3-\delta}$ perovskite solid solutions. *J. Phys. Chem. C.* **2012**, 116, 18605-18611.

[37] Kuklja, M.M.; Mastrikov, Y.A.; Rashkeev, S.; Kotomin, E.A. The structural disorder and lattice stability of BSCF complex perovskites. *ECS Trans.* **2011**, 35(1), 2077.

[38] Kuklja, M.M.; Mastrikov, Y.A.; Jansang, B.; Kotomin, E.A. First principles calculations of $(Ba,Sr)(Co,Fe)O_{3-\delta}$ structural stability. *Solid State Ionics* **2013**, 230, 21-26.

[39] Mueller, D.N.; De Souza, R.A.; Yoo, H.-I.; Martin, M. Phase stability and oxygen nonstoichiometry of highly oxygen-deficient perovskite-type oxides: a case study of $(Ba,Sr)(Co,Fe)O_{3-\delta}$. *Chem. Mater.* **2012**, 24, 269-274.

[40] Wagner, S.F.; Taufall, S.; Niedrig, C.; Götz, H.; Menesklou, W.; Baumann, S.; Ivers-Tiffée, E. pO_2 stability of $Ba_{0.5}Sr_{0.5}Co_{0.8}Fe_{0.2}O_{3-\delta}$. *Mater. Res. Soc. Symp. Proc.* **2011**, 1309, 57-64.

[41] Niedrig, C.; Menesklou, W.; Wagner, S.F.; Ivers-Tiffée, E. High-Temperature pO2 Stability of Metal Oxides Determined by Amperometric Oxygen Titration. *J. Electrochem. Soc.* **2013**, 160(2), F135-F140.

[42] Sahini, M.G., Tolchard, J.R., Wiik, K., Grande, T., High-temperature diffraction and thermogravimetrical analysis of the cubic perovskite $Ba_{0.5}Sr_{0.5}Co_{0.8}Fe_{0.2}O_{3-\delta}$ in different atmospheres. *Dalton Trans.* **2015**, 44, 10875-10881.

[43] Yaremchenko, A.A.; Mikhalev, S.M.; Kravchenko, E.S.; Frade, J.R. Thermochemical expansion of mixed-conducting $(Ba,Sr)Co_{0.8}Fe_{0.2}O_{3-\delta}$ ceramics. *J. Eur. Ceram. Soc.* **2014**, 34, 703-715.

[44] Wang, F.; Yashiro, K.; Amezawa, K.; Mizusaki, J. Chemical stability of $Ba_{0.5}Sr_{0.5}Co_{0.8}Fe_{0.2}O_{3-\delta}$ under different oxygen partial pressure, In Proceedings of the 13th Asian Conference on Solid State Ionics; Chowdari, B.V.R.; Kawamura, J.; Mizusaki, J.; Amezawa, K. Eds.; World Scientific Publishing Co.: Singapore, 2013, pp 228-234.

[45] Wang, F.; Nakamura, T.; Yashiro, K.; Mizusaki, J.; Amezawa, K.; The crystal structure, oxygen nonstoichiometry and chemical stability of $Ba_{0.5}Sr_{0.5}Co_{0.8}Fe_{0.2}O_{3-\delta}$ (BSCF). *Phys. Chem. Chem. Phys.* **2014**, 16, 7307-7314.

[46] Tanga, C.-W.; Wang, C.-B.; Chien, S.-H. Characterization of cobalt oxides studied by FT-IR, Raman, TPR and TG-MS. *Thermochimica Acta* **2008**, 473, 68–73.

[47] Chen, M.; Hallstedt, B.; Gauckler, L.J. Thermodynamic Assessment of the Co-O System. *Journal of Phase Equilibria.* **2003**, 24(3), 212-227.

[48] Williams, D.B.; Carter, C.B. Transmission electron microscopy. A textbook for materials science, Springer, New York, 2. Edition, 2009.

[49] Mitchell, R.H. *Perovskites. Modern and Ancient*, Almaz Press, Thunder Bay, 2002.

Scientific publications

Publications included in the thesis

1. **Investigation of carbonates in oxygen-transporting membrane ceramics**
   Olga Ravkina, Tobias Klande, Armin Feldhoff,
   Journal of Membrane Science **480** (2015) 31-38.

2. **Effect of A-site lanthanum doping on the CO_2 tolerance of $SrCo_{0.8}Fe_{0.2}O_{3-\delta}$ oxygen-transporting membranes**
   Tobias Klande, Olga Ravkina, Armin Feldhoff,
   Journal of Membrane Science **437** (2013) 122-130.

3. **Effect of CO_2 and SO_2 on oxygen permeation and microstructure of $(Pr_{0.9}La_{0.1})_2(Ni_{0.74}Cu_{0.21}Ga_{0.05})O_{4+\delta}$ membranes**
   Yanying Wei, Olga Ravkina, Tobias Klande, Armin Feldhoff,
   Journal of Membrane Science **429** (2013) 147-154.

4. **Influence of different sintering techniques on microstructure and phase composition of oxygen-transporting ceramic**
   Olga Ravkina, Jan Räthel, Armin Feldhoff,
   Journal of the European Ceramic Society **35** (2015) 2833-2843.

5. **Effect of microstructure on oxygen permeation of $Ba_{0.5}Sr_{0.5}Co_{0.8}Fe_{0.2}O_{3-\delta}$ and $SrCo_{0.8}Fe_{0.2}O_{3-\delta}$ membranes**
   Tobias Klande, Olga Ravkina, Armin Feldhoff,
   Journal of the European Ceramic Society **33** (2013) 1129-1136.

6. **Phase separation in BSCF perovskite under elevated oxygen pressures from 1 to 50 bar**
   Olga Ravkina, Aleksey Yaremchenko, Armin Feldhoff,
   Journal of Membrane Science (2016), submitted.

Publications not included in the thesis

7. **Investigation of Zr-doped BSCF perovskite membrane for oxygen separation in the intermediate temperature range**
   Olga Ravkina, Tobias Klande, Armin Feldhoff,
   Journal of Solid State Chemistry **201** (2013) 101-106.

8. **Novel CO_2-stable dual phase membrane with high oxygen permeability**
   Fangyi Liang, Huixia Luo, Kaveh Partovi, Olga Ravkina, Zhengwen Cao, Yi Liu, Jürgen Caro,
   Chemical Communications **50** (2014) 2451-2454.

9. **High-flux oxygen transporting membrane $Pr_{0.6}Sr_{0.4}Co_{0.5}Fe_{0.5}O_{3-\delta}$: CO_2 stability and microstructure**
   Kaveh Partovi, Fangyi Liang, Olga Ravkina, Jürgen Caro,
   Applied Materials and Interfaces **6** (2014) 10274-10282.

Contributions to conferences

1. **Influence of different sintering techniques on microstructure and phase composition of oxygen-transporting ceramic**
   Olga Ravkina, Jan Räthel, Armin Feldhoff,
   14th International Conference of the European Ceramic Society, 21-26 June 2015, Toledo, Spain. (Keynote Speech)

2. **Impact of partial cationic substitution on the CO_2-tolerance of oxygen-transporting membrane ceramics**
   Armin Feldhoff, Olga Ravkina,
   90th DKG Annual Meeting and Symposium on High-Performance Ceramics 2015, 15-18 March 2015, Bayreuth, Deutschland. (Talk)

3. **Investigation of carbonates in oxygen-transporting membrane ceramics**
   Olga Ravkina, Tobias Klande, Armin Feldhoff,
   Electroceramics XIV Conference, 16-20 June 2014, Bucharest, Romania. (Talk)

4. **Effect of cation deficiency on microstructure, electrical conductivity and oxygen transport properties of $(\mathrm{Pr}_{0.9}\mathrm{La}_{0.1})_2(\mathrm{Ni}_{0.74}\mathrm{Cu}_{0.21}\mathrm{Ga}_{0.05})\mathrm{O}_{4+\delta}$**
   Jian Xue, Olga Ravkina, Benjamin Geppert, Wei Fang, Haihui Wang, Armin Feldhoff,
   Electroceramics XIV Conference, 16-20 June 2014, Bucharest, Romania. (Talk)

5. **Ca-containing and cobalt-free CO_2-tolerant perovskite materials for oxygen separation**
   Wei Fang, Olga Ravkina, Benjamin Geppert, Jian Xue, Armin Feldhoff,
   Electroceramics XIV Conference, 16-20 June 2014, Bucharest, Romania. (Talk)

6. **Thermoelectric oxides for thermoelectric high-temperature energy harvesting**
   Armin Feldhoff, Olga Ravkina, Benjamin Geppert,
   14th International Conference on Thermoelectrics ICT, 6-10 June 2014, Nashville, USA. (Poster)

7. **Investigation of carbonates in oxygen-transporting membrane ceramics by analytical transmission electron microscopy**
   Armin Feldhoff, Olga Ravkina, Tobias Klande,
   Microscopy Conference 2013, 25-30 August 2013, Regensburg, Germany. (Talk)

8. **Investigation of phase stability in the intermediate temperature range of the zirconium-doped BSCF perovskite membrane for oxygen separation**
   Olga Ravkina, Tobias Klande, Armin Feldhoff,
   13th International Conference of the European Ceramic Society, 23-27 June 2013, Limoges, France. (Talk)

9. **Investigation of phase stability in the intermediate temperature range of the zirconium-doped BSCF perovskite membrane for oxygen separation**
   Armin Feldhoff, Olga Ravkina, Tobias Klande,
   13th International Conference of the European Ceramic Society, 23-27 June 2013, Limoges, France. (Talk)

10. **Partial cation substitution to enhance chemical stability of oxygen-transporting membranes**
    Armin Feldhoff, Olga Ravkina, Tobias Klande,
    The 19th International Conference on Solid State Ionics, 2-7 June 2013, Kyoto, Japan. (Talk)

11. **Investigation of Zr-doped BSCF perovskite membrane for oxygen separation in the intermediate temperature range**
    Olga Ravkina, Tobias Klande,Armin Feldhoff,
    Electroceramics XIII Conference, 24-27 June 2012, Twente-Enschede, Netherlands. (Poster)

Curriculum Vitae

Personal Data

Name	Olga Ravkina
Date of birth	19.07.1983
Place of birth	Charkow (Ukraine)
Martial status	unmarried, no children

Higher education

02/2016	**Submission of doctoral thesis** Gottfried Wilhelm Leibniz Universität Hannover, Germany ”Investigation on the chemical and the thermodynamic stability of oxygen-transporting membranes”
2012-2015	**Scientific co-worker** Gottfried Wilhelm Leibniz Universität Hannover, Germany Institute of Physical Chemistry and Electrochemistry in the group of Prof. Dr. Armin Feldhoff
2003-2012	**Chemistry degree: Diplom-Chemikerin** Gottfried Wilhelm Leibniz Universität Hannover, Germany Diploma thesis: ”Untersuchungen zur Verbesserung der Stabilität von perowskitartigen Gemischtleitern”

Education

1997-2003	**Abitur** Johannes Kepler Gymnasium, Garbsen, Germany.